Determination of Kinetic Parameters of the Thermal Dissociation of Methane

Von der Fakultät für Maschinenwesen der Rheinisch-Westfälischen Technischen Hochschule Aachen zur Erlangung des akademischen Grades eines Doktors der Ingenieurwissenschaften genehmigte Dissertation

vorgelegt von

Michael Wullenkord

Berichter: Univ.-Prof. Dr.-Ing. Robert Pitz-Paal
Direktor Dr. Gilles Flamant

Tag der mündlichen Prüfung: 08.04.2011

Acknowledgments

This work was compiled at the Institute of Technical Thermodynamics (Solar Research) of the German Aerospace Center in Cologne in the context of the European project SOLHYCARB. I would like to thank the European Commission for co-funding this project in the sixth framework program (SES6 019770).

I would also like to thank Prof. Dr. Robert Pitz-Paal (First Examiner), head of Solar Research, for supervising this work, for critical discussions, and for meaningful suggestions as well as Dr. Gilles Flamant (Second Examiner), Director of PROMES-CNRS, for coordinating SOLHYCARB and allowing inspiring conversation.

I am grateful for the motivating working atmosphere offered by colleagues of Solar Research. Especially the guidance and support provided by Dr. Karl-Heinz Funken and Dr. Christian Sattler is highly acknowledged. I appreciate that Peter Rietbrock and Lamark de Oliveira have assisted me with their comprehensive competence in laboratory issues. I gladly honor the helpful discussions with Nicole Janotte concerning the expression of uncertainty and the companionship of Dr. Martina Neises who has shared office with me for several years. I would like to thank the SOLHYCARB group for successful team work and particularly Dr. Eusebiu Grivei for BET measurements and useful comments. I esteem the important laboratory work of Elena Albermann, Beatrice Förster as well as Tom Maibauer and their contributions to the project. I am indebted to Janine Schneider for manufacturing perfect thermocouples, which functioned much longer than any bought devices, as well as to Claus-Jürgen Kröder for calibrating them and providing advice.

This thesis would not have been possible without the grand encouragement that has been given by my family and especially by my wife Nathalie Wullenkord who has had to demonstrate much patience during the last years.

Contents

List of Figures

List of Tables

Abstract

The solar thermal decomposition of methane could be an economically and ecologically beneficial process to produce hydrogen and particulate carbon. Aiming at the determination of general kinetic laws and parameters the thermal dissociation of methane was examined employing an alumina tubular reactor situated in an electric tube furnace. Nominal furnace temperatures in the range between 1200 °C and 1600 °C were set. Gas mixtures containing argon or helium as dilution gas and methane with a molar fraction between 2 % and 10 % were introduced into the reactor at an absolute pressure around 1 bar. The residence times ranged from 0.0115 s to 1.47 s. Temperature profiles along the reactor were measured with a thermocouple type S. Experimental results concerning the conversion of methane practically cover the full range from minor to total progress. Hydrogen was the main product of the decomposition. However, significant amounts of ethane, ethene, and especially ethyne formed part of the product flow. Seeding with carbon black featuring a specific surface similar to generated particles result in a significant increase of both, conversion of methane and yield of hydrogen.

The laminar flow conditions at the inlet of and inside the reactor were assessed by means of simulations employing ANSYS and COMSOL Multiphysics. Diverse reactor models based on nested tube reactors were employed. The models either disregarded radial diffusion or implied ideal radial diffusion. A simplified kinetic model which takes the considered species into account and respects forward dehydrogenation reactions was engaged. Kinetic parameters were varied in order to minimize the model errors. Best agreement between the calculations and experimental findings was achieved for a reactor model featuring five nested tube reactors and neglecting radial diffusion. The respective decay of methane is characterized by a reaction order regarding methane of 1.283 and an activation energy of 510.1 kJ/mol. Low standard uncertainties of estimated parameter values were derived from the covariance matrix. Except for quantities associated with the same reaction, parameters showed only marginal correlation. Radial diffusion was found to be a key phenomenon difficult to assess properly. The probable presence of not considered high molecular intermediates and differing properties of generated carbon have been identified as limiting issues concerning a comprehensive kinetic approach including heterogeneous effects.

1 Introduction

Energy systems have to be transformed substantially in order to preserve Earth and to allow subsequent generations to benefit from our planet equitably. Today processes involved in the provision of energy are mainly based on the combustion of fossil energy carriers or on nuclear fission and thus not compatible with the idea of sustainability. Fossil and fissionable feedstocks are finite and their mining involves a grave interference of landscape and healthiness. The products of their use are either relevant for the greenhouse effect (especially carbon dioxide – CO_2) or radioactive what directly leads to the question how to dispose them reasonably. An unrestricted discharge of CO_2 to the atmosphere is not acceptable any more. According to the IPCC[1], respective emissions have to be reduced significantly in the near future in order to avoid the risk of an incalculable climate change combined with numerous threats to mankind and ecosystems.[2]

A possible resort is the establishment of the hydrogen society in which hydrogen (H_2) plays the key role as energy carrier. Hydrogen represents the ultimate species of the transition from solid energy carriers with a high C/H-ratio (such as coal) via liquid energy carriers with moderate C/H-ratio (such as oil) to gaseous energy carriers with low C/H-ratio (such as methane). The usage of hydrogen in highly efficient fuel cells or internal combustion engines features a reaction with oxygen to water and does practically not involve any emissions of harmful substances or matters with relevance for climate change.[3] Since hydrogen is a secondary energy carrier, it has to be produced before being applied. Consequently, the application of hydrogen can only be as clean as the method of its production. Nowadays the most important processes for the production of hydrogen are steam reforming of methane and naphtha (38 %), partial oxidation of heavy fuel oil (24 %), reforming of benzine (H_2 as byproduct, 18 %), and coal gasification (H_2 as byproduct, 10 %), whereas minor fractions are allotted to the ethylene production and other chemical industries as well as to the chloralkali electrolysis.[4] In their current configuration they cause massive emissions of CO_2 and are thus not suitable for a carbon neutral hydrogen system. Either the aforementioned processes have to be modified that way that CO_2-drawbacks are avoided (e. g. CCS[5], renewable energy and feedstocks) or alternative, environmentally acceptable methods have to be employed. Amongst others potential processes could be the electrolysis of water, water splitting (in thermochemical cycles or photobiological), reforming and

[1] Intergovernmental Panel on Climate Change
[2] cp. [IPCC, 2007]
[3] cp. [Ausubel, 2000], [Hefner, 2002], [Dunn, 2002], [Muradov, 2005 a], [Marbán, 2007]
[4] cp. [Geitmann, 2002], p. 27, providing data from DWV
[5] carbon capture and storage

gasification of biomass, fermentation of biomass (thermophilic or photo fermentation) and cracking of hydrocarbons (thermal or in thermal plasma).[6]

Concentrating solar power (CSP) offers the greatest potential for electricity production in the EUMENA[7] region taking renewable sources into account.[8] Consequently, the employment of solar power is also particularly interesting for the production of hydrogen and has been discussed intensively.[9] The solar thermal dissociation of methane, which is the main component of natural gas (and biogas) still featuring great resources[10], could be an ecologically and economically beneficial method of hydrogen generation representing an intermediate step from fossil fuel based to entirely regenerative hydrogen production. The heat input needed for the cracking reactions is here provided by solar radiation. Since oxygen is not included in the decomposition process, the formation of CO_2 is avoided. The final products of the thermal dissociation of methane are hydrogen and solid carbon. This allows the storage of a part of the introduced solar energy in an advantageous energy carrier. Depending on its quality generated carbon could be sold as an industrial commodity or landfilled without difficulty. As a result the process does not involve drawbacks of CO_2-emissions although the fossil (if not from biogas) energy carrier methane is engaged.[11] The recently completed European project SOLHYCARB has been concerned with the solar thermal dissociation of methane.[12]

For a proper design and cost-efficient construction of suitable solar operated plants it is essential to know about the kinetics of the cracking reactions. Although the kinetics of the thermal dissociation of methane has been considered for several decades, comprehensive information has not been reported in literature yet. Published kinetic parameters cover a wide range of values. They are partly associated with special types of reactors or determined based on vague reaction conditions, e. g. concerning reaction temperatures as well as diffusive effects, and therefore refuse a universal character. Moreover, the uncertainty of estimated values is often unclear. As a consequence the application of such kinetic findings to arbitrary systems involves an unknown ambiguity. The aim of this work was the determination of general kinetic parameters for the thermal decomposition of methane employing a tubular reactor and a practically assessable kinetic model based on net forward reactions. Reaction conditions should be investigated in detail in order to allow a reliable approximation of the circumstances of the reactions. Special attention should be turned on the uncertainty in measurement and related

[6] see e. g. [Steinberg, 1989], [Geitmann, 2002], p. 27 et seqq., [Stolten, 2010], p. 169 et seqq.
[7] Europe, Middle East, North Africa
[8] cp. [DLR, 2005], p. 56
[9] see e. g. [Steinfeld, 2001], [Hirsch, 2001], [Fletcher, 2001], [Kodama, 2003], [Steinfeld, 2004], [Steinfeld, 2005], [Zedtwitz, 2006], [Muradov, 2008], [Ozalp, 2009], [Pregger, 2009]
[10] resources of non-conventional natural gas equivalent to 103364 EJ estimated for 2008, cp. [Rempel, 2009], p. 11
[11] cp. [Spath, 2003]
[12] cp. [Flamant, 2007] (description of SOLHYCARB)

propagation in the kinetic evaluation. A suitable test facility had to be developed and assembled before experiments could be carried out. Appropriate simulation tools had to be identified and utilized with the purpose of clarification of flow characteristics and finally of definition of an accurate reactor model for the kinetic evaluation.

After introducing some basic terms related to data preparation, reaction kinetics, and uncertainty in measurement as well as of model parameters in Chapter 2, general information about the thermal splitting of methane including an overview about the state of kinetic research is provided in Chapter 3. The experimental setup, procedures and results are presented in Chapter 4, whereas the kinetic evaluation, which features the creation of a realistic reactor model and the application of a simplified kinetic model taking the main components of the product flow into account, is described in Chapter 5. Findings are summarized and an outlook is given in Chapter 6.

2 Fundamental terms and issues

This chapter provides the explanation of fundamental terms important for following considerations as well as data preparation. Furthermore, the expressions of uncertainty in measurement and of model parameters being part of this work are illustrated.

2.1 Conversion, yield and further basic figures

An ideal gas follows the ideal gas law which is usually written as

$$p \cdot V = n \cdot \Re \cdot T \quad , \qquad \textbf{Equation 1}$$

where $\Re$ is the universal gas constant, p and T stand for the absolute pressure and the temperature, respectively, while n represents the amount of substance and V is the related volume. Consequently, conditions in a flow system, comprising a volume flow $\dot{V}$ and a flow of amount of substance $\dot{n}$, change in compliance with

$$p \cdot \dot{V} = \dot{n} \cdot \Re \cdot T \quad . \qquad \textbf{Equation 2}$$

The standard volume flow $\dot{V}_{\mathrm{N}}$ corresponding to a certain flow of amount of substance $\dot{n}$ refers to standard conditions, defined by the standard temperature T_{N} and the standard pressure p_{N}, and arises from

$$\dot{V}_{\mathrm{N}} = \dot{n} \cdot \frac{\Re \cdot T_{\mathrm{N}}}{p_{\mathrm{N}}} \quad . \qquad \textbf{Equation 3}$$

The total initial standard volume flow of a gas mixture, containing methane and an inert dilution gas (DG), entering a reactor $\dot{V}_{\mathrm{N,tot,0}}$ can be calculated employing the initial standard volume flow of methane $\dot{V}_{\mathrm{N,CH_4,0}}$ and the initial standard volume flow of the dilution gas $\dot{V}_{\mathrm{N,DG,0}}$ by

$$\dot{V}_{\mathrm{N,tot,0}} = \dot{V}_{\mathrm{N,DG,0}} + \dot{V}_{\mathrm{N,CH_4,0}} \quad .$$ **Equation 4**

The initial molar fraction of methane $x_{\mathrm{CH_4,0}}$ can be determined via

$$x_{\mathrm{CH_4,0}} = \frac{\dot{V}_{\mathrm{N,CH_4,0}}}{\dot{V}_{\mathrm{N,tot,0}}} \quad .$$ **Equation 5**

Respecting Equation 3 the molar flow of methane at the inlet of a reactor $\dot{n}_{\mathrm{CH_4,0}}$ arises from

$$\dot{n}_{\mathrm{CH_4,0}} = \dot{V}_{\mathrm{N,CH_4,0}} \cdot \frac{p_{\mathrm{N}}}{\Re \cdot T_{\mathrm{N}}} \quad .$$ **Equation 6**

Given that the dilution gas is an inert gas, it does not serve as a reactant. Then the molar flow of the dilution gas $\dot{n}_{\mathrm{DG}}$ equals the molar flow of the dilution gas at the outlet of the reactor $\dot{n}_{\mathrm{DG,P}}$ and the molar flow of the dilution gas at the inlet of the reactor $\dot{n}_{\mathrm{DG,0}}$:

$$\dot{n}_{\mathrm{DG}} = \dot{n}_{\mathrm{DG,P}} = \dot{n}_{\mathrm{DG,0}} = \dot{V}_{\mathrm{N,DG,0}} \cdot \frac{p_{\mathrm{N}}}{\Re \cdot T_{\mathrm{N}}} \quad .$$ **Equation 7**

Employing the molar fraction of the dilution gas in the product gas $x_{\mathrm{DG,P}}$ the molar flow of the product gas $\dot{n}_{\mathrm{tot,P,g}}$ can be calculated using

$$\dot{n}_{\mathrm{tot,P,g}} = \frac{\dot{n}_{\mathrm{DG}}}{x_{\mathrm{DG,P}}}$$ **Equation 8**

and moreover the molar flows of other gaseous species i of the product flow by

$$\dot{n}_{i,\mathrm{P}} = x_{i,\mathrm{P}} \cdot \dot{n}_{\mathrm{tot,P,g}} \qquad i = \mathrm{CH_4}, \mathrm{H_2}, \mathrm{C_2H_6}, \mathrm{C_2H_4}, \mathrm{C_2H_2}, \ldots \quad . \qquad \textbf{Equation 9}$$

With $\dot{n}_{\mathrm{CH_4,0}}$ and $\dot{n}_{\mathrm{CH_4,P}}$, the molar flow of methane at the outlet of the reactor, the conversion of methane $X_{\mathrm{CH_4}}$

$$X_{\mathrm{CH_4}} = \frac{\dot{n}_{\mathrm{CH_4,0}} - \dot{n}_{\mathrm{CH_4,P}}}{\dot{n}_{\mathrm{CH_4,0}}} \qquad \textbf{Equation 10}$$

can be determined, while the yield of hydrogen $Y_{\mathrm{H_2}}$ arises from

$$Y_{\mathrm{H_2}} = \frac{1}{2} \cdot \frac{\dot{n}_{\mathrm{H_2,P}}}{\dot{n}_{\mathrm{CH_4,0}}} \qquad \textbf{Equation 11}$$

considering the overall decomposition reaction[13] and employing $\dot{n}_{\mathrm{H_2,P}}$, the molar flow of hydrogen at the outlet of the reactor. Introducing the formal reaction equations yielding in C_2-hydrocarbons

$$2\,\mathrm{CH_4\,(g)} \rightarrow \mathrm{C_2H_6\,(g)} + \mathrm{H_2\,(g)} \quad ,$$

$$2\,\mathrm{CH_4\,(g)} \rightarrow \mathrm{C_2H_4\,(g)} + 2\,\mathrm{H_2\,(g)} \quad \text{, and}$$

$$2\,\mathrm{CH_4\,(g)} \rightarrow \mathrm{C_2H_2\,(g)} + 3\,\mathrm{H_2\,(g)}$$

the yields of the different C_2-hydrocarbons $Y_{\mathrm{C_2H_6}}$, $Y_{\mathrm{C_2H_4}}$, and $Y_{\mathrm{C_2H_2}}$

[13] see Chapter 3.1

$$Y_i = 2 \cdot \frac{\dot{n}_{i,\mathrm{P}}}{\dot{n}_{\mathrm{CH_4},0}} \qquad i = \mathrm{C_2H_6}, \mathrm{C_2H_4}, \mathrm{C_2H_2}$$ **Equation 12**

can be determined. The factors $F_{\mathrm{P},i,q}$ occurring in Equation 11 (0.5) and Equation 12 (2), respectively, result from the ratio of the absolute values of the stoichiometric coefficients of methane $\nu_{\mathrm{CH_4},q}$ and the considered product $\nu_{\mathrm{P},i,q}$ concerning reaction q:

$$F_{\mathrm{P},i,q} = \frac{\left|\nu_{\mathrm{CH_4},q}\right|}{\nu_{\mathrm{P},i,q}} \quad .$$ **Equation 13**

Finally the yield of C_2-hydrocarbons $Y_{\mathrm{C_2-HC}}$ arises from

$$Y_{\mathrm{C_2-HC}} = Y_{\mathrm{C_2H_6}} + Y_{\mathrm{C_2H_4}} + Y_{\mathrm{C_2H_2}} \quad .$$ **Equation 14**

2.2 Reaction kinetics

Reaction kinetics deals with the analysis of the reaction rate and the dependencies on the influencing factors, which are

- the reaction temperature T_{R},
- the concentration of different reactants i c_i,
- the total pressure p_{R}, at which the reaction proceeds, and
- catalysts as well as the amount of reaction sites on surfaces.

The concentration of component i c_i can be calculated by

$$c_i = \frac{n_i}{V} = \frac{\dot{n}_i}{\dot{V}} \quad , \qquad \textbf{Equation 15}$$

where n_i is the amount of substance i in a certain volume V, while for a flow system the consideration of the molar flow of component i $\dot{n}_i$ in the volume flow $\dot{V}$ is more suitable.

In homogeneous reactions only substances with the same state of aggregation are involved, whereas heterogeneous reactions comprise at least two states of aggregation. The equivalent reaction rate of a homogeneous reaction r_{hom} is defined as

$$r_{\text{hom}} = \frac{1}{\nu_i \cdot V} \cdot \frac{\mathrm{d}\, n_i}{\mathrm{d}\, t}\Big|_{\text{hom}} = \frac{r_{\text{hom},i}}{\nu_i} \quad , \qquad \textbf{Equation 16}$$

where ν_i is the stoichiometric coefficient of component i, n_i is the amount of substance of component i, t is the time, and V is the considered volume. Directly connected to r_{hom} is $r_{\text{hom},i}$, the reaction rate of the homogeneous reaction regarding component i. Contrariwise, the equivalent reaction rate of a heterogeneous reaction r_{het} refers to a relevant surface S

$$r_{\text{het,surface}} = \frac{1}{\nu_i \cdot S} \cdot \frac{\mathrm{d}\, n_i}{\mathrm{d}\, t}\Big|_{\text{het}} = \frac{r_{\text{het,surface},i}}{\nu_i} \quad , \qquad \textbf{Equation 17}$$

or a relevant mass m

$$r_{\text{het,mass}} = \frac{1}{\nu_i \cdot m} \cdot \frac{\mathrm{d}\, n_i}{\mathrm{d}\, t}\Big|_{\text{het}} = \frac{r_{\text{het,mass},i}}{\nu_i} \quad , \qquad \textbf{Equation 18}$$

with the reaction rates of the heterogeneous reaction regarding component i $r_{\text{het,surface},i}$ and $r_{\text{het,mass},i}$. For a homogeneous reaction a common approach to analyze the relation between the reaction rate and the influencing factors is that the reaction rate equals a product of two terms, the first only depending on the temperature and the second only depending on the concentrations of the reactants:

$$r = k(T) \cdot f(c_i) \quad .^{14}$$ **Equation 19**

While the first term $k(T)$ is called rate constant and depends on the temperature T following an Arrhenius law in accordance with

$$k(T) = k_0 \cdot e^{-\frac{E_a}{\Re \cdot T}}$$ **Equation 20**

the second term $f(c_i)$ is often assumed to be an exponential function appropriate to

$$f(c_i) = \prod_i c_i^{m_i} \quad .$$ **Equation 21**

Here three important parameters, the kinetic parameters, can be identified: the pre-exponential factor k_0, the activation energy E_a, and the reaction order regarding component i m_i. Strictly speaking, the pre-exponential factor itself is a function of the temperature. It may be proportional to the temperature to the power of 0.5 following collision theory or proportional to the temperature to the power of another exponent resulting from transition state theory. However, this dependency of the pre-exponential factor on the temperature is usually weak compared to the dependency of the exponential term of Equation 20.[15] Thus, the pre-exponential factor is considered as a constant. Usually for a heterogeneous reaction the relation between the reaction rate and the influencing factors is more complex, especially when the second phase does not have constant properties.

2.3 Uncertainty in measurement

In this work special attention was turned to the assessment of uncertainty of determined figures, such as conversions, yields, and temperatures. Two different expressions of uncertainty can be found. The first one is the maximum (positive and negative) uncertainty, whereas the second one results from an attempt to state the standard uncertainty according to GUM[16]. Diverse types of evaluation of standard uncertainty have to be distinguished: the Type A evaluation of uncertainty, a “method of evaluation of uncertainty by statistical analysis of series of

[14] cp. [Hagen, 2004], p. 31 et seqq.
[15] cp. [Chorkendorff, 2003], p. 36, p. 100 et seqq., p. 108 et seqq., [Ebbing, 2005], p. 581 et seqq.
[16] Guide to the expression of uncertainty in measurement, see [ISO, 2008]

observations", and the Type B evaluation of uncertainty, a "method of evaluation of uncertainty by means other than the statistical analysis of series of observations".[17]

In this work mainly the Type B evaluation of uncertainty was employed. Usually manufacturers of used measuring devices state uncertainty of a measured value x by upper and lower limits a^+ and a^-, respectively. Consequently, the maximum positive uncertainty of x $u^+_{\max}(x)$ arises from

$$u^+_{\max}(x) = a^+ - x \qquad \textbf{Equation 22}$$

and the maximum negative uncertainty of x $u^-_{\max}(x)$ from

$$u^-_{\max}(x) = a^- - x \quad . \qquad \textbf{Equation 23}$$

In absence of further information, the assumption of a rectangular probability distribution is admissible. If not otherwise stated, a symmetric situation corresponding to

$$x = 0.5 \cdot \left(a^+ + a^-\right) \qquad \textbf{Equation 24}$$

was postulated in agreement to the specification of used instruments. Employing a, the half width of the interval defined by a^+ and a^-, calculated from

$$a = 0.5 \cdot \left(a^+ - a^-\right) \qquad \textbf{Equation 25}$$

the standard uncertainty of x $u(x)$ can be calculated by

[17] cp. [ISO, 2008], p. 3

$$u(x) = \frac{a}{\sqrt{3}} \quad .^{18}$$ **Equation 26**

The maximum positive and negative uncertainty of a quantity y being a function of N other quantities x_i congruent to

$$y = f(x_1, x_2, ..., x_N)$$ **Equation 27**

arises from severest combinations of values of influencing quantities in the range of their limits given by maximum uncertainties. Contrariwise, the combined standard uncertainty of y $u_c(y)$ can be estimated from

$$u_c(y) = \sqrt{\sum_{i=1}^{N} \left(\frac{\partial f}{\partial x_i} \right)^2 \cdot u^2(x_i)} \quad .^{19}$$ **Equation 28**

To simplify matters, the index c is eliminated in the following and $u(y) = u_c(y)$ is called the standard uncertainty of y.

2.4 Uncertainty and correlation of model parameters

Given a situation of multidimensional Chi-Square fitting involving a nonlinear model following

$$y = y(\boldsymbol{x}_i, \boldsymbol{\psi}) \quad ,$$ **Equation 29**

where $\boldsymbol{x}_i$ is a vector of variables defining condition i influencing the function y, the merit function to be minimized is

[18] cp. [ISO, 2008], p. 11 et seqq.
[19] cp. [ISO, 2008], p. 18 et seq. Assumptions: input quantities are uncorrelated and nonlinearity of the considered function is not significant (higher-order terms neglected).

$$\chi^2 = \sum_{i=1}^{N_{\text{data points}}} \left[\frac{y_i - y(\boldsymbol{x}_i, \boldsymbol{\psi})}{\sigma_i} \right]^2 \quad , \qquad \textbf{Equation 30}$$

with $\boldsymbol{\psi}$ accounting for the set of model parameters to be varied and σ_i characterizing the standard deviation of y_i. The covariance matrix of $\boldsymbol{\psi}$ $Cov(\boldsymbol{\psi})$ provides information about the standard uncertainty of estimated parameters (square root of diagonal elements) and covariance between components of $\boldsymbol{\psi}$. $Cov(\boldsymbol{\psi})$ can be assessed via

$$Cov(\boldsymbol{\psi}) = \boldsymbol{\alpha}^{-1} \quad , \qquad \textbf{Equation 31}$$

where the components of matrix $\boldsymbol{\alpha}$ are defined by

$$\alpha_{kl} = \sum_{i=1}^{N_{\text{data points}}} \frac{1}{\sigma_i^2} \left[\frac{\partial y(\boldsymbol{x}_i, \boldsymbol{\psi})}{\partial \psi_k} \cdot \frac{\partial y(\boldsymbol{x}_i, \boldsymbol{\psi})}{\partial \psi_l} \right] \quad .[20] \qquad \textbf{Equation 32}$$

If

$$\tilde{y}_i = \frac{y_i - y(\boldsymbol{x}_i, \boldsymbol{\psi})}{\sigma_i} \quad , \qquad \textbf{Equation 33}$$

it is obvious that

$$\frac{\partial \tilde{y}_i}{\partial \psi_k} = -\frac{1}{\sigma_i} \cdot \frac{\partial y(\boldsymbol{x}_i, \boldsymbol{\psi})}{\partial \psi_k} \qquad \textbf{Equation 34}$$

and consequently

[20] cp. [Press, 2007], p. 788 et seqq. (in particular p. 790, p. 798, p. 800 et seq.)

$$\alpha_{kl} = \sum_{i=1}^{N_{\text{data points}}} \left[\frac{\partial \tilde{y}_i}{\partial \psi_k} \cdot \frac{\partial \tilde{y}_i}{\partial \psi_l} \right] \quad . \qquad \textbf{Equation 35}$$

Introducing the matrix $\boldsymbol{A}$ with

$$\boldsymbol{A} = \begin{bmatrix} \frac{\partial \tilde{y}_1}{\partial \psi_1} & \frac{\partial \tilde{y}_1}{\partial \psi_2} & \cdots & \frac{\partial \tilde{y}_1}{\partial \psi_{N_{\text{parameters}}}} \\ \frac{\partial \tilde{y}_2}{\partial \psi_1} & \frac{\partial \tilde{y}_2}{\partial \psi_2} & \cdots & \frac{\partial \tilde{y}_2}{\partial \psi_{N_{\text{parameters}}}} \\ \vdots & \vdots & \ddots & \vdots \\ \frac{\partial \tilde{y}_{N_{\text{data points}}}}{\partial \psi_1} & \frac{\partial \tilde{y}_{N_{\text{data points}}}}{\partial \psi_2} & \cdots & \frac{\partial \tilde{y}_{N_{\text{data points}}}}{\partial \psi_{N_{\text{parameters}}}} \end{bmatrix} \qquad \textbf{Equation 36}$$

it becomes clear that

$$Cov(\boldsymbol{\psi}) = \boldsymbol{\alpha}^{-1} = \left(\boldsymbol{A}^{\mathrm{T}} \cdot \boldsymbol{A} \right)^{-1} \quad . \qquad \textbf{Equation 37}$$

The matrix of correlation coefficients $Corr(\boldsymbol{\psi})$ arises from

$$Corr(\psi_k, \psi_l) = \frac{Cov(\psi_k, \psi_l)}{\sigma(\psi_k) \cdot \sigma(\psi_l)} \quad , \qquad \textbf{Equation 38}$$

where $\sigma(\psi_k)$ and $\sigma(\psi_l)$ represent square roots of respective components of $Cov(\boldsymbol{\psi})$.[21]

[21] cp. e. g. [ISO, 2008], p. 47

3 Thermal splitting of methane

In Chapter 3.1 basics about the thermal splitting of methane that are important for general understanding are given, before the current extent of CO_2-free applications is presented in Chapter 3.2. Thermodynamic considerations and calculations can be found in Chapter 3.3, whereas Chapter 3.4 provides information about the state of research concerning the kinetics of the thermal decomposition of methane.

3.1 Basics

The overall reaction of the thermal decomposition of methane, which needs an energy input to proceed respecting the positive standard reaction enthalpy, can be written as

$$\mathrm{CH_4\,(g) \rightarrow "C"(s) + 2\,H_2\,(g)} \qquad \Delta H_R^0 = +74.8 \frac{\mathrm{kJ}}{\mathrm{mol}}$$

and summarizes numerous elementary reactions included in a complex reaction mechanism. An accepted sequence of cracking reactions finally forming molecular hydrogen and particulate carbon (“C”) is the stepwise dehydrogenation considering the intermediates ethane (C_2H_6), ethene (C_2H_4), and ethyne (C_2H_2):

$$2\,\mathrm{CH_4} \xrightarrow{-\mathrm{H_2}} \mathrm{C_2H_6} \xrightarrow{-\mathrm{H_2}} \mathrm{C_2H_4} \xrightarrow{-\mathrm{H_2}} \mathrm{C_2H_2} \rightarrow \ldots \xrightarrow{-\mathrm{H_2}} \ldots \rightarrow 2\,\mathrm{"C"}$$ [22]

The formation of methyl radicals (CH_3) according to

$$\mathrm{CH_4 \rightarrow CH_3 + H}$$

was proven to be the initial and rate determining step of the dissociation of methane, whereas the formation of methylene radicals (CH_2) was rejected.[23] Reactions of ethene may beside the formation of ethyne also lead to the formation of propene and subsequently of propadiene and 1-butene, whereas methylation of ethyne could explain the occurrence of propyne.[24] Models for the reaction mechanism of the thermal dissociation of methane with different levels of sophistication – partly respecting high molecular hydrocarbons such as benzene and polycyclic aromatic hydrocarbons (PAHs) – have been suggested and applied.[25]

[22] cp. [Khan, 1970] and [Back, 1983], p. 2
[23] cp. [Back, 1983], p. 5, p. 12 et seq.
[24] cp. [Billaud, 1989]
[25] see. e. g. [Sundaram, 1977 a], [Sundaram, 1977 b], [Sundaram, 1978], [Roscoe, 1985], [Stewart, 1989], [Grenda, 2003], [Matheu, 2003]; including benzene: see e. g. [Billaud, 1992], [Guerét, 1994],

The general situation of a reactor with entering gases and additional leaving reaction products is shown in Figure 3-1. Cracking reactions inside the reactor consume the provided heat and lead to the formation of the final products as well as of C_2-hydrocarbons and of not further specified hydrocarbons (C_mH_n).

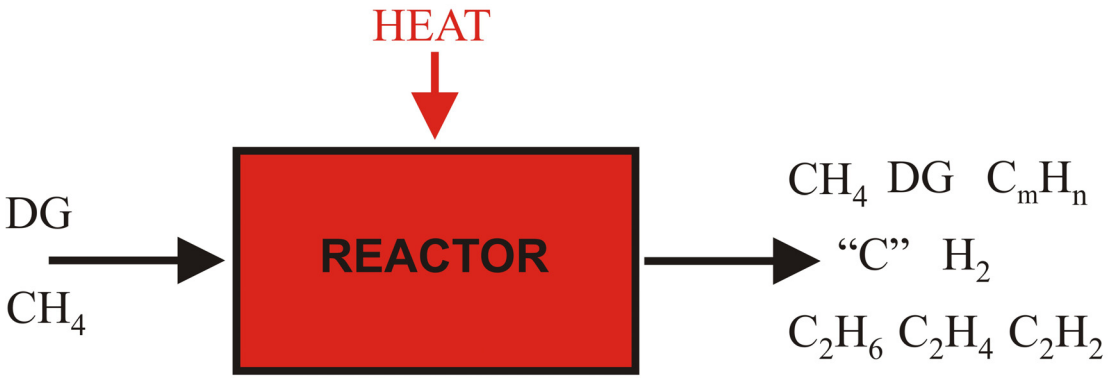

Figure 3-1: General situation of a reactor for the thermal splitting of methane with methane (CH_4) as well as the dilution gas (DG) at the inlet of the reactor and additional reaction products at the outlet of the reactor, which are particulate carbon ("C"), hydrogen (H_2), ethane (C_2H_6), ethene (C_2H_4), and ethyne (C_2H_2) as well as further hydrocarbons (C_mH_n).

3.2 Applications with CO_2-free heat supply

The thermal dissociation of methane offers the possibility of simultaneous CO_2-emission free production of hydrogen and carbon when the heat necessary to run the cracking reactions is provided without the release of CO_2. A possibility of CO_2-free heat supply – however, up to now without practical demonstration – is the combustion of a part of the produced hydrogen introduced by Kreysa as "The Carbon Moratorium".[26] Another option is the use of concentrated solar radiation. Several solar operated reactors in laboratory and prototype scales have already been constructed and tested. Concepts of indirect heating have to be distinguished from those of direct solar irradiation of the reactants. Steinfeld produced filamentous carbon and hydrogen in a small scale solar irradiated reactor implying a fluidized bed of Ni catalyst and Al_2O_3 grains.[27] Weimer and Dahl reported the construction and operation of a fluid-wall aerosol flow reactor irradiated with concentrated solar power at maximum levels of 10 kW.[28] Tornado flow conditions were simulated and applied to a reactor, which was operated with a solar radiation input in the range of 2 kW and allowed a volumetric absorption of solar radiation as soon as the first carbon particles were formed. Additionally, Kogan introduced an apparatus for seeding targeting an increase of radiative heat transfer into the gas/particle-mixture.[29] A reactor configuration in the

[Olsvik, 1994], [Olsvik, 1995], [Holmen, 1995], [Tynnukov, 2002]; including PAHs: see e. g. [Lucas, 1990], [Dean, 1990], [Richter, 2000], [Younessi-Sinaki, 2009]

[26] see [Kreysa, 2009] (extended and translated version of [Kreysa, 2008])

[27] see [Steinfeld, 1997]

[28] see [Weimer, 2001], [Dahl, 2001], [Dahl, 2002], [Dahl, 2004]

[29] see [Kogan, 2003], [Kogan, 2004], [Kogan, 2005], [Kogan, 2007]

5 kW class based on a particle laden vortex flow acting as a volumetric absorber was presented and examined with respect to the radiative heat transfer by Hirsch. Trommer investigated respective kinetics, whereas Maag carried out further experiments after modifying the reactor.[30] Abanades conducted experiments with a 1 kW reactor that featured different graphite nozzles which absorbed solar radiation and lead heat energy into the passing flow of reactants.[31] A reactor in the 10 kW scale consisting of four units of concentric graphite tubes situated in a graphite cavity was presented and examined by Abanades and Rodat.[32] Seven straight and horizontally oriented graphite tubes placed in a graphite cavity form the key parts of a reactor working at an extended nominal power level of 50 kW.[33] The latter configuration represents the most advanced solar operated reactor for the thermal decomposition of methane demonstrated up to now. Its construction and operation was one of the final objectives of the European project SOLHYCARB.

3.3 Thermodynamics

Materials conversion can be interpreted as a balancing process which dissipates the differences of driving potentials and finally leads to the mechanical, thermal, material, and chemical equilibrium. Temperature and pressure represent the reference for the thermal and mechanical potential, respectively. The material equilibrium and chemical equilibrium are related to the chemical potential. The material equilibrium is reached as soon as the chemical potential of component i μ_i is equal in all involved phases. μ_i is defined as the partial derivative of the Gibbs energy with respect to the amount of substance of component i at constant temperature, pressure, and amounts of substance of components other that i :

$$\mu_i = \left(\frac{\partial G}{\partial n_i} \right)\Bigg|_{T,p,n_{j \neq i}} .[34] \qquad \textbf{Equation 39}$$

The free enthalpy of reaction ΔG_R arises from

[30] see [Hirsch, 2004 a], [Hirsch, 2004 b], [Trommer, 2004], [Maag, 2009]
[31] see [Abanades, 2005], [Abanades, 2006], [Abanades, 2007]
[32] see [Abanades, 2009], [Rodat, 2009], [Rodat, 2010 b]
[33] see [Rodat, 2010 a]
[34] cp. [Lucas, 2008], p. 431 et seqq.

$$\Delta G_{\mathrm{R}} = \sum_i \nu_i \cdot \mu_i \quad , \qquad \textbf{Equation 40}$$

where ν_i is the stoichiometric coefficient of component i. Introducing the standard free enthalpy of reaction ΔG_{R}^0 with

$$\Delta G_{\mathrm{R}}^0 = \sum_i \nu_i \cdot \mu_i^0 \qquad \textbf{Equation 41}$$

and the activity of component i a_i, it can be shown that

$$\Delta G_{\mathrm{R}} = \Delta G_{\mathrm{R}}^0 + \Re \cdot T \cdot \ln \prod_i a_i^{\nu_i} \quad . \qquad \textbf{Equation 42}$$

Regarding a heterogeneous equilibrium involving a gaseous phase treated as an ideal gas mixture as well as a solid phase containing pure substances, the activity of a component i in the ideal gas phase a_i^{ig} can be calculated employing the partial pressure p_i and the standard reference pressure p^0 following

$$a_i^{\mathrm{ig}} = \frac{p_i}{p^0} \quad , \qquad \textbf{Equation 43}$$

whereas a_i^{s}, the activity of a pure solid component i, can be treated as a constant according to

$$a_i^{\mathrm{s}} = 1 \quad . \qquad \textbf{Equation 44}$$

The chemical equilibrium is characterized by $\Delta G_{\mathrm{R}} = 0$.[35]

Equilibrium compositions were calculated for different temperatures and pressures employing HSC 5[36]. The program routines determine stable compositions of chosen species using the

[35] cp. [Atkins, 2010], p. 190, p. 214 et seqq. and [Weingärtner, 2003], p. 155 et seqq.

"Gibbs energy minimization method". Gaseous species comprising methane, hydrogen, all hydrocarbons with up to 8 carbon atoms available in the HSC 5 database, and selected higher hydrocarbons, especially polycyclic aromatic hydrocarbons (PAHs)[37], as well as solid carbon were considered. A complete table of respected species can be found in Appendix A. Figure 3-2 represents the amounts of substances in the equilibrium at 1 bar higher than $1 * 10^{-8}$ kmol based on an initial amount of methane of 1 kmol. Small amounts of the C_2-hydrocarbons ethane, ethene, and ethyne as well as of propadiene, 1-propyne, butadiyne, and 1-heptene can be found in the equilibrium composition, but practically only hydrogen, carbon, and methane are the relevant species at temperatures up to 1700 °C. At 783 °C still 10 % of the initial amount of methane remains unconverted, whereas at 1114 °C the equilibrium is almost completely shifted to the side of products.

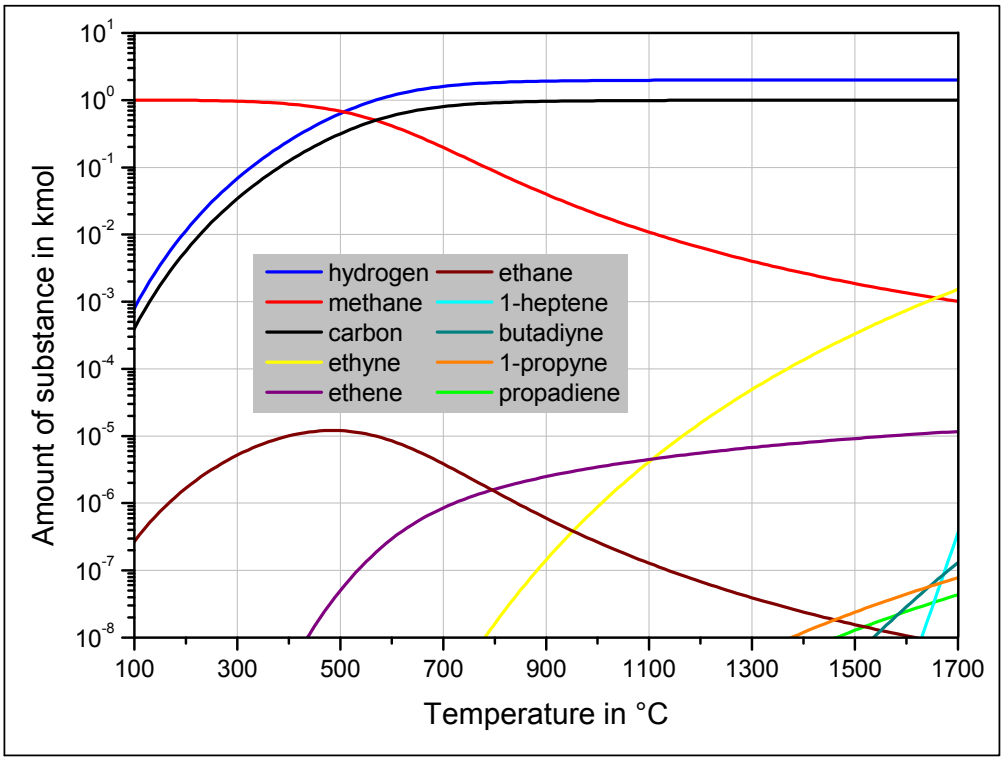

Figure 3-2: Equilibrium compositions at 1 bar as a function of the temperature (based on an initial amount of 1 kmol methane)

Ideally, two moles of hydrogen are formed per mole of methane. Consequently, according to the principle of Le Chatelier and Braun an increase of pressure results in a shift of the equilibrium to the side of methane as can be seen in Figure 3-3. Complete figures for 0.5 bar and 2 bar corresponding to Figure 3-2 can be found in Appendix A.

[36] HSC Chemistry 5: Calculation of Equilibrium Composition v. 5.0 (Outokumpu Research Oy, 2002).
[37] The thermal decomposition of methane involves the presence of PAHs, e. g. naphthalene and benzo[a]pyrene, cp. e. g. [Hu, 2003]. Albermann presented a comprehensive review of literature as well as own experimental results in [Albermann, 2007]. Most of identified PAHs are part of the HSC 5 database and were respected for equilibrium calculations.

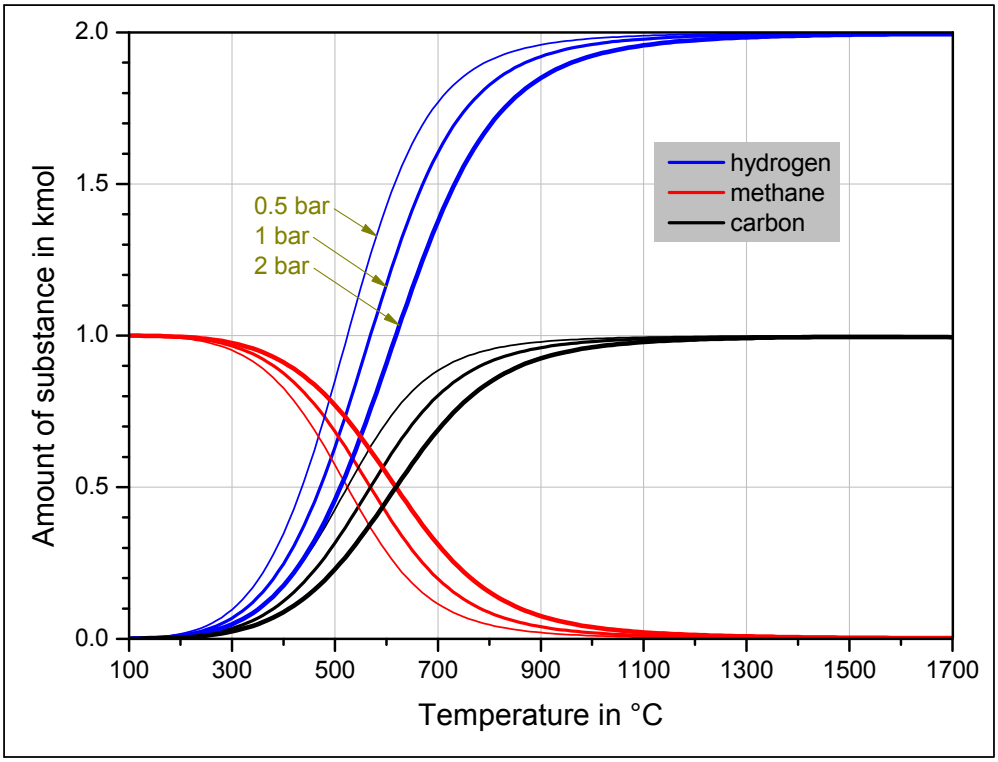

Figure 3-3: Amount of substance of the main components of the equilibrium composition as a function of the temperature and the pressure (based on an initial amount of 1 kmol methane)

3.4 Kinetics

The thermal splitting of hydrocarbons has been a frequently addressed topic in research for more than a hundred years. For instance, the French chemist M. Berthelot presented some basic findings in the second half of the 19th century.[38] The thermal decomposition of methane has been investigated employing different ways to heat up the reactants. Very common is the heat supply via hot reactor walls influencing the temperature of the reactants by convection and in presence of absorbers also by radiation. As presented in Chapter 3.2 the direct solar irradiation of particles in contact to the reactants is possible too. Moreover, high temperature of reactants can be achieved by compression in shock tubes. In addition, applications employing thermal plasma, microwaves, and molten metal baths can be found.[39] However, the latter applications form part of special fields and are excluded from subsequent considerations.

Kinetic experiments have been carried out under various conditions differing for instance in temperature and pressure. Furthermore, experiments conducted in presence of catalysts other than those formed by the reaction itself have to be distinguished from experiments carried out without the employment of additional substances. Influences of carbon based catalysts as well as of metal based catalysts were examined. Abbas has recently presented a respective review

[38] see e. g. [Berthelot, 1866]
[39] see e. g. [Fincke, 2002], [Fulcheri, 2002] (thermal plasma); [Tanashev, 1998] (microwaves); [Serban, 2003] (molten metal)

article.[40] Although the present work principally deals with the simplest reaction system, which corresponds to the situation without any added catalyst, the consideration of literature providing information about reaction rates found for the presence of carbon material is useful, since findings could help to understand the influence of formed carbon particles on the reaction rates. Contrariwise, metal based catalysts may involve additional effects and are consequently excluded in the following.

According to the general information provided in Chapter 3.1, many species are involved in the thermal dissociation of methane. However, on the path from the reactant methane to the final products hydrogen and carbon, C_2-hydrocarbons feature particular importance as intermediates and byproducts with significant fractions in the product flow. The reliability of kinetic data derived from experiments respecting the individual species as reactants is not guaranteed when transferred to reactions as intermediates, since alternative reaction mechanism could become relevant. Nevertheless, some examples are presented in Chapter 3.4.3.

3.4.1 Kinetic experiments without seeding

Kinetic experiments concerning the thermal decomposition of methane were carried out in shock tubes, in tube reactors and in static systems. In spite of the long-lasting consideration there exists a remarkable lack of clarity regarding involved reactions, kinetics and mechanisms. Scientists reported numerous – and partly inconsistent – observations in these fields along with approaches to explain them. Most researchers agree that ethane is the primary product of the decomposition followed by ethene and ethyne. Controversial results concerning the pressure dependence of the dissociation[41], the relevance of surface effects[42], and the influence of decomposition products such as hydrogen[43], ethane, and ethyne[44] were reported. Palmer observed induction, acceleration, and deceleration periods and suggested that shock tube experiments refer to conditions before acceleration.[45] Comprehensive overviews about respective up-to-date information were compiled in 1970 by Khan and Crynes[46], in 1983 by Back and Back[47], and in 1989 by Billaud, Baronnet et al.[48] Table 3-1 provides information about

[40] see [Abbas, 2010 a]
[41] cp. [Hartig, 1971] (“pressure dependence of *k*“) and [Napier, 1972] (“results were not sensitive to pressure“)
[42] cp. [Shantarovich, 1962] (“The relationship R ~ s/v […] and […] indicate that cracking is a heterogeneous reaction.“) and [Palmer, 1968] (“the rate is not appreciably affected by the *S*/*V* ratio“)
[43] cp. [Kevorkian, 1960] (“homogeneous reaction is not hydrogen inhibited“) and [Kassel, 1932] (“rate […] very greatly retarded by hydrogen“)
[44] cp. [Eisenberg, 1967] (”rate is accelerated by ethane”), [Gordon, 1948] (“acetylene was a catalyst for the decomposition of methane”), and [Skinner, 1959] (“methane decomposition is not much affected by the presence of the decomposition products”)
[45] cp. [Palmer, 1968]
[46] see [Khan, 1970]
[47] see [Back, 1983]
[48] see [Billaud, 1989]

the scope of applied reaction conditions and determined kinetic parameters along with utilized temperature measurement techniques.

Table 3-1: Kinetic experiments concerning the thermal decomposition of methane and determined kinetic parameters

Reference / reactor / dilution gas **Temperature in °C / measurement technique** **Pressure in bar / residence time in ms** **Initial molar fraction of methane in % / conversion in %**	**Reaction** E_a in $\frac{kJ}{mol}$ $\log(k_0)$ in $\log\left[\frac{1}{s}\cdot\left(\frac{mol}{m^3}\right)^{(1-m)}\right]$ m in –
[Kassel, 1932] / quartz vessel / - 700 °C – 850 °C / Pt-Pt/Rh TC (outer contact) 0.017 – 0.51 / up to 40 min 100 / a few	CH_4 → products 332.4 12 1
[Skinner, 1959] / shock tube / Ar 1157 – 1512 / calculation 5.1 / < 15 12 (and 1) / < 10	CH_4 → products 422.9 14.71 1
[Glick, 1959] / shock tube / He and Ar 1227 – 2627 / calculation not specified (n. s.) / several ms 10 / 0 – 100	CH_4 → products 355.9 12.96 1
[Kevorkian, 1960] / shock tube / Ar 1383 – 1692 / calculation 3.4 – 12.0 / 1.4 – 2.4 2 and 10 / 7.6 – 86.2	CH_4 → products 389.4 14.12 1
[Shantarovich, 1962] / porcelain tube / He 1293 – 1373 / n. s. 0.023 – 0.027 / 5 – 42 1.2 – 20 / 0.12 – 1.02	CH_4 → products 376.8 11.60 1
[Kozlov, 1962] / shock tube / Ar 1397 – 1777 / calculation 2.0 – 8.1 / n. s. 2 and 5 / n. s.	CH_4 → products 381.0 13.65 1 (based on own data and other works)
[Palmer, 1963] / annular reactor / He 890 – 1078 / n. s. n. s. / n. s. n. s. (variation by factor 20) / n. s.	CH_4 → products 422.9 14.1 1
[Palmer, 1968] / porcelain tube / He 1050 – 1250 / Pt-Pt/10Rh TC moved through reactor 0.99 / 100 – 900 1 – 20 / up to 85	CH_4 → products 431.2 14.6 1 (based on own data and other works)
[Hartig, 1971] / shock tube / Ar 1577 – 2227 / calculation 5.1 – 222.9 / less than Kozlov, Kevorkian, and Skinner 0.2 – 1 / n. s.	CH_4 (+ Ar) → CH_3 + H (+ Ar) 368.4 11.30 2 (low pressure limit) / 435.4 15.10 1 (high pressure limit)

Reference / reactor / dilution gas **Temperature in °C / measurement technique** **Pressure in bar / residence time in ms** **Initial molar fraction of methane in % / conversion in %**	**Reaction** E_a in $\frac{\text{kJ}}{\text{mol}}$ $\log(k_0)$ in $\log\left[\frac{1}{\text{s}}\cdot\left(\frac{\text{mol}}{\text{m}^3}\right)^{(1-m)}\right]$ m in –
[Napier, 1972] / shock tube / Ar 1477 – 2427 / sodium-line reversal and C_2 reversal methods 5.2 – 20.7 / 0.1 – 2.5 10 / 34.7 – 97	CH_4 → products 391.9 13.58 1
[Gardiner, 1975] / shock tube / Ar + Kr + Ne 1727 – 2427 / calculation 0.2 – 1.6 / n. s. 0.4 / n. s.	CH_4 → products 312.0 9.927 1
[Chen, 1975] / quartz vessel / - 722 – 830 / TC in center 0.033 – 0.99 / up to 2.5 100 / n. s.	CH_4 → CH_3 + H 450.5 16.45 1
[Holmen, 1976] / graphite tube reactor / H_2 1500 – 2005 / pyrometer (outer reactor wall) 0.13 / 2 – 22 50 / 10 – 100	CH_4 → products 371.4 29.29 1
[Tabayashi, 1979] / shock tube / Ar 1677 – 2497 / calculation 20.7 – 34.5 / 0.5 µs – 50 µs 10 and 20 / n. s.	CH_4 + M → CH_3 + H + M M = all collision partners (Ar, CH_4, …) 359.2 11.00 2
[Kiefer, 1993] / shock tube / Kr and Ar 2527 – 4127 / calculation 0.31 – 0.88 / n. s. 0.5 – 2 / n. s.	CH_4 + M → CH_3 + H + M 406.2 28.376 - 4.830 * log(T / K) 2
[Steinberg, 1998] / Inconel 617 tubular reactor / - 700 – 900 / n. s. 28.6 – 56.8 / up to 103 s 100 / up to 35	CH_4 → C + 2 H_2 131.0 3.732 1
[Koike, 2000] / shock tube / Ar 1127 – 2227 / calculation 0.41 – 0.83 / n. s. 1.32 / n. s.	CH_4 + M → CH_3 + H + M 339.1 10.48 2
[Sutherland, 2001] / shock tube / Kr 1465 – 1796 / calculation 0.0212 / n. s. n. s. / very low	CH_4 + Kr → CH_3 + H + Kr 182.6 -12.97 2

Most researchers agree that the thermal dissociation of methane follows a first order reaction. Activation energies in the range from 312 kJ/mol to 450.5 kJ/mol were reported, whereas pre-exponential factors between $8.46 * 10^9$ 1/s and $2.8 * 10^{16}$ 1/s can be found. An exceptionally high pre-exponential factor could be extracted from figures presented in [Holmen, 1976], while remarkably low values for both activation energy and pre-exponential factor were reported in [Steinberg, 1998]. The first elementary dissociation reaction could be a second order reaction

involving present collision partners. Respective results differ in part significantly as can be obtained from the table. Simplified kinetic models taking C_2-hydrocarbons into account were applied by Happel and Kramer as well as by Schulz, Klotz et al. Results of data fitting are provided in Table 3-2. Happel and Kramer suggested the consideration of three reactions and chose first and second order approaches in order to assess their rates, whereas Schulz, Klotz et al. considered five second order reactions – amongst them four forward reactions as well as one backward reaction which takes possible methane formation from the products into account.

Table 3-2: Kinetic experiments concerning the thermal decomposition of methane and determined kinetic parameters employing simplified kinetic models

Reference / reactor / dilution gas **Temperature in °C / measurement technique** **Pressure in bar / residence time in ms** **Initial molar fraction of methane in % / conversion in %**	**Reaction** E_a in $\frac{\text{kJ}}{\text{mol}}$ $\log(k_0)$ in various units m in –
[Happel, 1967] / annular alumina reactor / H_2 1074 – 1783 / Pt-Pt/10Rh TC (center) + pyrometer (outer wall) 0.092 – 0.94 / less than 1 21.5 – 100 / 38.4 – 100 (parameters fitted to data) $r_{CH_4,1} = k_{0,1} \cdot e^{-\frac{E_{a,1}}{\Re \cdot T}} \cdot p_{CH_4}$ $r_{CH_4,2} = k_{0,2} \cdot e^{-\frac{E_{a,2}}{\Re \cdot T}} \cdot p_{CH_4}$ $r_{C_2H_2,3} = k_{0,3} \cdot e^{-\frac{E_{a,3}}{\Re \cdot T}} \cdot \frac{p_{C_2H_2}^2}{1+\tilde{k}_3 \cdot p_{H_2}}$	$CH_4 \rightarrow C + 2\ H_2$ {1} 67.83 4.392 log[mol/(s m^3 bar)] 1
	$CH_4 \rightarrow 1/2\ C_2H_2 + 3/2\ H_2$ {2} 361.9 13.50 log[mol/(s m^3 bar)] 1
	$C_2H_2 \rightarrow 2\ C + H_2$ {3} 74.11 6.329 log[mol/(s m^3 bar^2)] 2 ($\tilde{k}_3$ = 1.515 / bar)
[Schulz, 1985] / shock tube / Ar 1507 – 2257 / calculation 2.6 / 0.5 – 4 2 / 30 – 100 (parameters fitted to data)	$CH_4 + M \rightarrow 1/2\ C_2H_6 + H_2 + M$ 130 5.500 log[m^3/(s mol)] 2
	$C_2H_6 + M \rightarrow C_2H_4 + H_2 + M$ 283 11.36 log[m^3/(s mol)] 2
	$C_2H_4 + M \rightarrow C_2H_2 + H_2 + M$ 172.3 7.450 log[m^3/(s mol)] 2
	$C_2H_2 + M \rightarrow 2\ C + H_2 + M$ 17.2 1.660 log[m^3/(s mol)] 2
	$P + M \rightarrow CH_4 + M$ ($c_P = c_{CH_4,0} - c_{CH_4}$) 38.3 1.800 log[m^3/(s mol)] 2

3.4.2 Kinetic experiments in presence of carbon based catalysts

The influence of different types of carbonaceous material, such as carbon black and activated carbon, was studied mainly in fixed bed reactors and in fluidized bed reactors. Muradov for example examined the influence of numerous carbon based catalysts with a mass of about 0.03 g in a fixed bed reactor at 850 °C and a residence time of about 1 s. Under these conditions only hydrogen and carbon as well as very small fractions of C_2-hydrocarbons were produced. It was found that disordered kinds – like activated carbon (AC) and the amorphous forms carbon black (CB) and acetylene black (AB) – show a higher catalytic activity than ordered ones – like graphite and diamond. The catalytic activity of examined CBs and ABs was linearly related to the surface area, whereas the activity of ACs was apparently independent from surface area and method of activation. Usually a deactivation was observed as a function of time. CBs and ABs were initially less active than ACs; however, the decomposition process employing the amorphous forms showed better sustainability.[49] The dependency of the reaction rate on the specific surface of CBs is controversial. Lee et al. reported that no respective trends could be identified.[50]

Table 3-3 gives an overview about kinetic parameters derived in cracking experiments in presence of activated carbon, carbon black or coal char (CC). According to Equation 18, the initial rate of methane decomposition was mostly defined as

$$r_{\text{initial}} = k_0 \cdot e^{-\frac{E_a}{\Re \cdot T}} \cdot p_{CH_4}^{m} = \frac{1}{\nu_{CH_4} \cdot m_{\text{cat}}} \cdot \frac{\mathrm{d}\, n_{CH_4}}{\mathrm{d}\, t} \qquad \textbf{Equation 45}$$

based on the overall reaction of the decomposition. Most researchers agree that the reaction order is about 0.5, but also higher values were reported. Activation energies in the range from 117 kJ/mol to 201 kJ/mol, from 143 kJ/mol to 236 kJ/mol, and from 89 kJ/mol to 105 kJ/mol were estimated for ACs, CBs and CCs, respectively. Results shown here exemplarily are in good agreement with findings of other workers.[51]

[49] cp. [Muradov, 2001 a]; similar results were presented in [Muradov, 2001 b]
[50] cp. [Lee, 2004 b]
[51] cp. [Pinilla, 2008], [Ashok, 2008], [Lee, 2008], [Abbas, 2009] extracted from [Abbas, 2010 a]

Table 3-3: Kinetic experiments concerning the thermal decomposition of methane in the presence of carbon based catalysts and determined kinetic parameters

Reference / reactor / dilution gas **Temperature in °C / measurement technique** **Pressure in bar / residence time in s / catalyst mass in g** **Initial molar fraction of methane in % / conversion in %**	**Catalysts / specific surface in m^2/g** E_a in $\frac{kJ}{mol}$ $\log(k_0)$ in $\log\left[\frac{mmol}{min \cdot g_{cat} \cdot bar^m}\right]$ m in –
[Kim, 2004] / fixed bed quartz tube reactor / Ar 750 – 900 / TC n. s. / 0.6 / 0.2 – 0.8 up to 100 / up to 15	AC / 725, 912, 966 (725, 912) 194, 186, 198 n. s. ~ 0.5 (0.51, 0.49)
[Lee, 2004 a] / fluidized bed quartz tube reactor / - 700 – 900 / TC in middle of bed n. s. / n. s. / 20 100 / up to 45	AC / 966 138.9 (MFR) – 147.4 (PFR) 13.54 (MFR) – 14.28 (PFR) ~ 0.5
[Lee, 2004 b] / fixed bed quartz tube reactor / Ar 750 – 1050 / TC 1.01 / n. s. / 0.1 up to 100 / up to 70	CB / 79, 1475 183, 143 7.920, 6.401 ~ 1 (0.919, 0.984)
[Trommer, 2004] / vortex flow reactor / Ar 627 – 800 / TC type K up to 1.1 / 9 / 1.9 g/min 15 / up to 46	AC / 900 147 (PFR) – 162 (MFR) 6.029 (PFR) log(1/s) – 6.877 (MFR) log(1/s) 1
[Muradov, 2005 b] / quartz microreactor with fixed bed / - 850 / TC type K 1.01 / 0.1 / 0.03 – 0.1 100 / n. s. (20 – 70)	AC / 650 – 3370 (650) 160 – 201 n. s. ~ 0.5 (0.6)
	CB / 25 – 1500 (1500) 205 – 236 n. s. ~ 0.5 (0.5)
[Bai, 2005] / fixed bed quartz tube reactor / N_2 750 – 900 / n. s. 1.01 / n. s. / 1 up to 100 / up to 35	AC / n. s., 783, 735, 738 116.9, 133.6, 140.0, 184.9 n. s. 0.5
[Bai, 2006] / fixed bed quartz tube reactor / N_2 750 – 900 / n. s. 1.01 / n. s. / 1 up to 100 / up to 35	CC / 22, 41, 127 (22, 127) 105, 98, 89 n. s. ~ 0.5 (0.54, 0.52)
[Jung, 2007] / fluidized bed quartz tube reactor / - 800 – 925 / TC in middle of bed 1.01 / n. s. / 20 100 / up to 50	AC / n. s. 140 n. s. n. s.
[Abbas, 2010 b] / fixed bed stainless steel tube reactor / - 775 – 850 / TC type K 1.01 / 2 – 12.2 / 20 – 120 100 / 24.2 – 68.6	AC / n. s. 163 7.409 log[$dm^6/(g_{cat}$ mol min)] 2

3.4.3 Kinetic experiments concerning the pyrolysis of C_2-hydrocarbons

Table 3-4 shows some examples for works dealing with the thermal dissociation of C_2-hydrocarbons. Orders of initial stage or overall reactions were found to equal one or two. By trend, the activation energy increases with the number of H-atoms in the reactant.

Table 3-4: Kinetic experiments concerning the thermal decomposition of C_2-hydrocarbons and determined kinetic parameters

Reference / reactor / dilution gas Temperature in °C / measurement technique Pressure in bar / residence time in ms Initial molar fraction of reactant in % / conversion in %	**Reaction** E_a in $\frac{\text{kJ}}{\text{mol}}$ $\log(k_0)$ in $\log\left[\frac{1}{\text{s}}\cdot\left(\frac{\text{mol}}{\text{m}^3}\right)^{(1-m)}\right]$ m in –
[Kozlov, 1962] / shock tube / Ar 887 – 1307 / calculation 2.03 – 6.08 / 0.8 1 and 5 / 2 – 90	$C_2H_6 \rightarrow C_2H_4 + H_2$ 334.9 16.65 1 (based on own data and other works)
	$C_2H_6 \rightarrow C_2H_4 + H_2$ 288.9 14 1 (based on own data and other works)
[Hidaka, 1985] / shock tube / Ar 927 – 1427 / calculation 1.72 – 2.53 / n. s. 1 – 5 / n. s.	$C_2H_6 \rightarrow 2\ CH_3$ 334.9 14.85 1
[Kozlov, 1962] / shock tube / Ar 977 – 1577 / calculation 2.03 – 6.08 / n. s. 1 and 5 / whole range	$C_2H_4 \rightarrow C_2H_2 + H_2$ 167.5 8.410 1
[Pilla, 2010] / shock tube / Ar 1117 – 1597 / calculation 2.23 – 3.14 / 1 1 / n. s.	$C_2H_4 \rightarrow C_2H_2 + H_2$ 227.0 8.740 2
[Kozlov, 1962] / shock tube / Ar 1327 – 2227 / calculation 4.05 / 0.8 1 and 5 / up to 98	$C_2H_2 \rightarrow 2\ C + H_2$ 125.6 6.230 1 (suggested for high temperatures)
	$C_2H_2 \rightarrow 2\ C + H_2$ 167.5 7.330 2 (suggested for low temperatures)
[Wu, 1987] / shock tube / Ne + Ar 1627 – 2227 / calculation 0.3 – 0.56 / up to 0.75 1 – 6.2 / n. s.	$2\ C_2H_2 \rightarrow C_4H_3 + H$ 186.3 7.301 2

4 Experimental

In order to investigate the kinetics of the thermal dissociation of methane, numerous experiments were accomplished based on a wide range of reaction conditions. The feed flow contained methane as well as an inert dilution gas, which allowed studying the influence of methane concentration at a constant pressure level and damped the temperature change due to reaction. Furthermore, the risk of clogging was decreased. After presenting the experimental setup, the covered reaction conditions are introduced before the adopted procedure of the experiments is explained. General results based on the conversion of methane and the yields of considered products are shown subsequently.[52] The next chapter deals with the measurement of the temperature, one of the main influencing factors of reaction rates. At last additional experiments, which were carried out in order to gain further knowledge about the repeatability of results, location and character of formed carbon, balances of H- and C-atoms, as well as the influences of added carbon particles, are respected.[53]

4.1 Experimental setup

The kinetic experiments were carried out employing an aluminum oxide tube reactor[54] with an inner/outer diameter of 8/12 mm situated in a tube furnace[55] as can be seen in Figure 4-1. This tube furnace contains molybdenum disilicide ($MoSi_2$) heating elements which allow the provision of heat at temperatures up to 1800 °C. The inlet gas composed of methane and a dilution gas, either argon (Ar) or helium (He), was prepared by mass flow controllers[56]. Depending on the conditions inside the reactor cracking reactions proceeded generating the desired products hydrogen (H_2) and carbon (C) as well as intermediates. The composition of the product gas was analyzed by a gas chromatograph (GC)[57] respecting argon, methane, hydrogen, and C_2-hydrocarbons. There were two particle filters which guaranteed a high efficiency of filtration: the main filter and the GC filter with a nominal pore diameter of 1 µm and 0.5 µm, respectively.[58] The main filter removed particles from the product flow before it left the systems toward the flue, whereas the GC filter removed particles from the sample flow toward the GC. A two filter configuration permits the usage of large filter elements in the main filter going hand in hand with an increase of operating time due to a lower risk of clogging without drawbacks for the GC

[52] Brief descriptions of the experimental setup as well as preliminary experimental results can be found in [Wullenkord, 2008], [Wullenkord, 2009 a], [Wullenkord, 2009 b], and [Wullenkord, 2010 a].
[53] Respective results were partly presented in [Wullenkord, 2010 a] and [Wullenkord, 2010 b].
[54] Manufacturer: FRIATEC AG, Mannheim, Germany.
[55] Manufacturer: Gero Hochtemperaturöfen GmbH & Co. KG, Neuhausen, Germany.
Type HTRV 40-250-18 SO.
[56] Manufacturer: MKS Instruments Deutschland GmbH, München, Germany.
[57] Manufacturer / provider: SRI Instruments Inc., Las Vegas, NV, USA. Schambeck SFD GmbH, Bad Honnef, Germany. Type SRI Multiple Gas Analyzer #2 8610C.
[58] Manufacturer / provider: CONTEC GmbH, Bad Honnef, Germany (filter body AVPP20 with filter element AX1-20) and B.E.S.T. Fluidsysteme GmbH, Kaarst, Germany (Swagelok).

measurement resulting from a larger dead volume of the filter. The water coolers at the inlet and outlet of the reactor ensured almost constant as well as low temperatures of the gas or gas mixture at the respective positions.

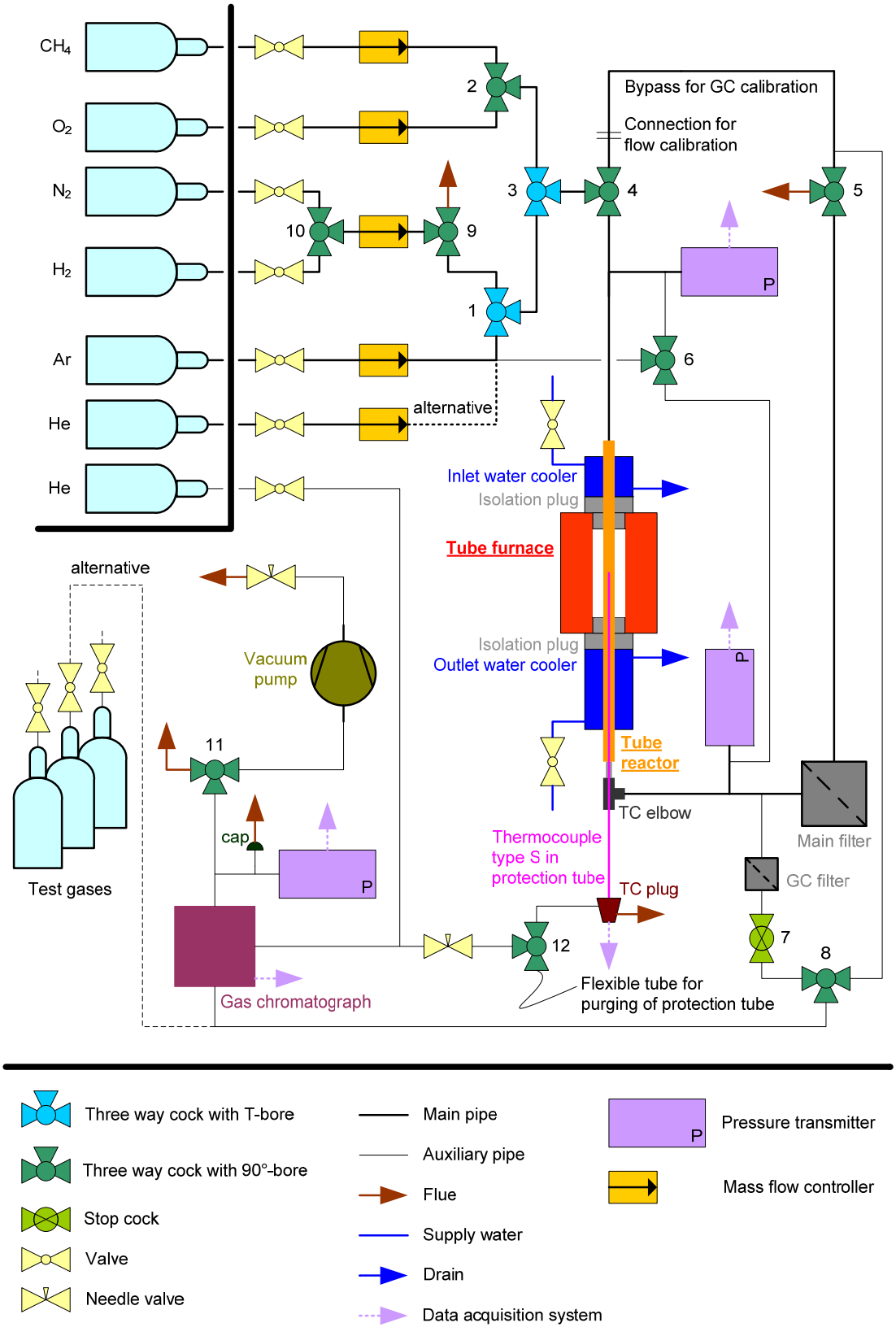

Figure 4-1: Sketch of the experimental setup for the kinetic analysis of the thermal decomposition of methane

The measurement of axial temperature profiles inside the tube reactor took place using a self-made thermocouple type S[59] described in detail later (see Chapter 4.5). Finally, the pressure was measured at both sides of the reactor tube.[60] All metal parts were grounded. Figure 4-2 shows a picture of the experimental setup including stop cock and three way cocks[61] as well as fittings and connections[62].

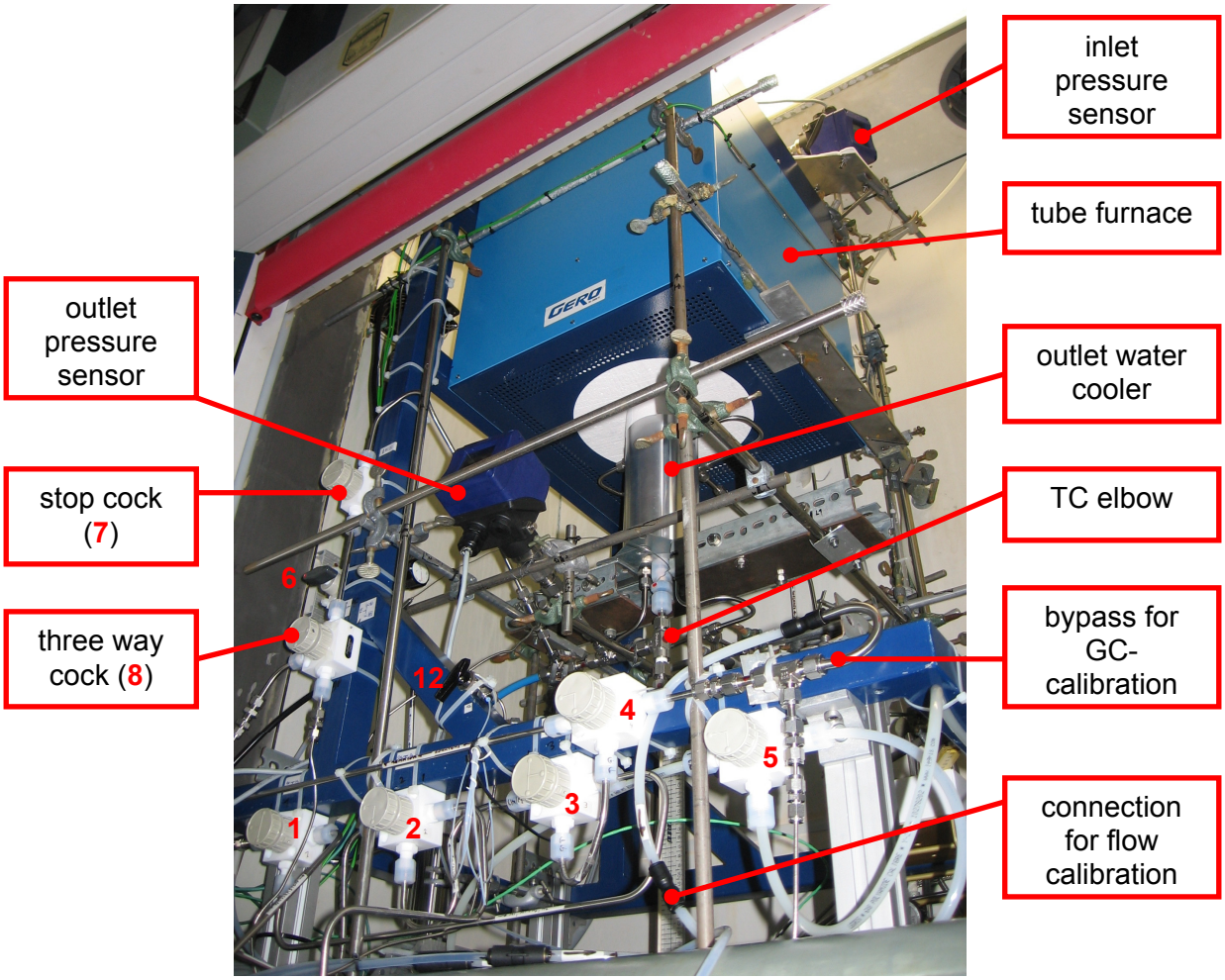

Figure 4-2: Picture of the experimental setup with some main components as well as additional parts like two and three way cocks (numbers in red) and connections

The diameters of the reactor tube and the protection tube of the thermocouple have a maximum uncertainty of +/- 5 %, which means that the tolerance for the inner diameter of the reactor equals 0.4 mm, whereas the outer diameter of the protection tube may vary by 0.2 mm.[63] Different dimensions as well as axial positions of the experimental setup relevant for illustration and later calculations are shown in Figure 4-3. In the following the position - 213 mm, which

[59] Provider of thermo wires: E&S METRONIC Meß- und Regeltechnik GmbH, Werne, Germany.
[60] Manufacturer of pressure transmitters: WIKA Alexander Wiegand GmbH & Co. KG, Klingenberg, Germany.
[61] Manufacturer / provider: EM-TECHNIK GmbH, Maxdorf, Germany. B.E.S.T. Fluidsysteme GmbH, Kaarst, Germany (Swagelok).
[62] Manufacturer / provider: B.E.S.T. Fluidsysteme GmbH, Kaarst, Germany (Swagelok). PTS MARQUARDT GmbH Automatisierungstechnik, Pulheim, Germany (Legris).
[63] cp. [FRIATEC, 2003], p. 14

corresponds to the upper edge of the inlet water cooler, accounts for the inlet of the reactor. The heated length of the tube furnace equals 250 mm. The manufacturer states that the temperature homogeneity inside the work tube reaches +/- 10 K in 50 % of the heated length.[64]

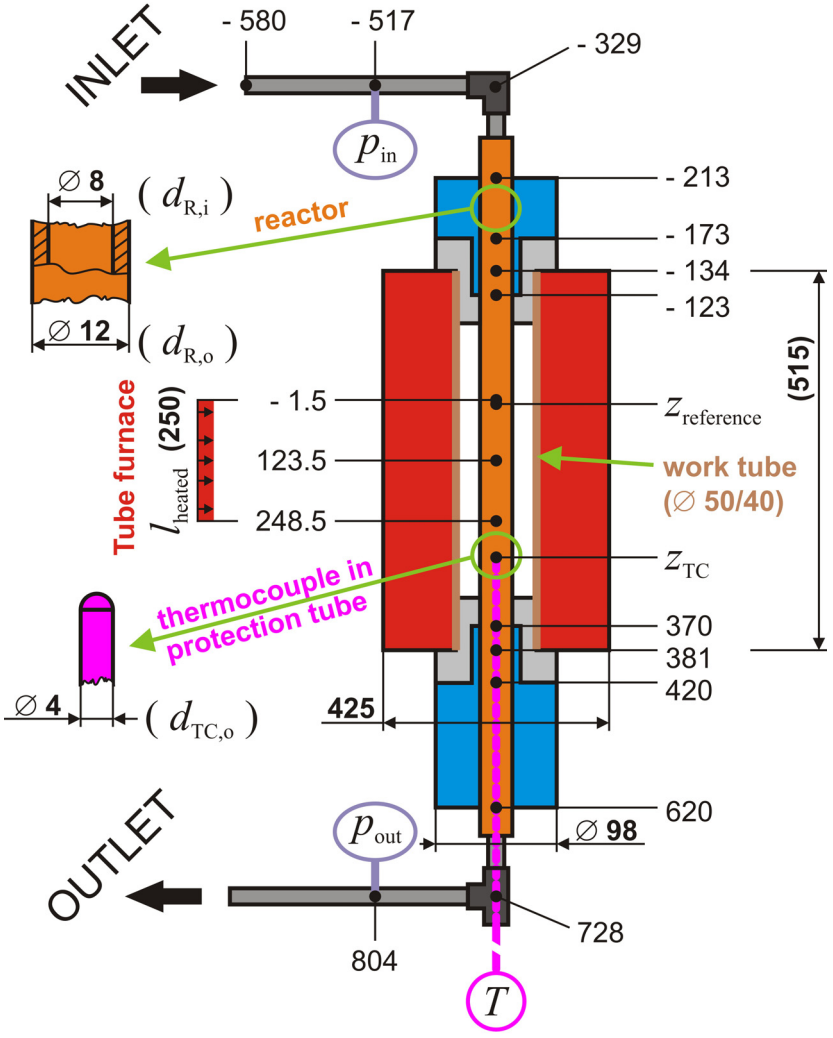

Figure 4-3: Basic dimensions and axial positions of the experimental setup for the kinetic analysis of the thermal decomposition of methane in mm

Some components of the experimental setup will be described in detail in the following chapters.

4.1.1 Mass flow controllers

For the preparation of gas mixtures, either as inlet gas or calibration gas for the gas chromatograph, mass flow controllers (MFCs) manufactured by MKS were employed. Table 4-1 provides information about the MFCs implemented in the experimental setup and used gases.

[64] [Gero, 2006]

Table 4-1: Information about used mass flow controllers and gases (GCF = Gas Correction Factor)

Gas[65] Quality Purity	Type of MFC (produced) Nominal range and gas Range for selected gas (GCF)	Accuracy Repeatability
Ar 4.8 99.998 %	1179 (2003) 500 sccm N_2 685.0 sccm Ar (1.37)	1.0 % of FS (full scale) +/- 0.2 % of FS → +/- 1.37 sccm
	1259 (1999) 2000 sccm N_2 2740 sccm Ar (1.37)	0.8 % of FS n. s. (not specified)
	1179 (2007) 15 SLM CO_2 approximated by 20 SLM N_2 (due to control unit) 27.40 SLM Ar (1.37, originally 1.986)	0.5 % of reading + 0.2 % of FS +/- 0.2 % of FS → +/- 0.0548 SLM
	1179 (2007) 20 SLM N_2 27.40 SLM Ar (1.37)	0.5 % of reading + 0.2 % of FS +/- 0.2 % of FS → +/- 0.0548 SLM
CH_4 4.5 99.995 %	1179 (2007) 10 sccm CH_4 10.00 sccm (1.00)	0.5 % of reading + 0.2 % of FS +/- 0.2 % of FS → +/- 0.02 sccm
	1259 (1996) 100 sccm N_2 72.00 sccm (0.72)	0.8 % of FS n. s.
	1259 (1996) 500 sccm N_2 360.0 sccm (0.72)	0.8 % of FS n. s.
He 5.0 99.999 %	1179 (2003) 500 sccm N_2 725.0 sccm (1.45)	1.0 % of FS +/- 0.2 % of FS → +/- 1.45 sccm
	1259 (1999) 2000 sccm N_2 2900 sccm (1.45)	0.8 % of FS n. s.
	1179 (2007) 20 SLM N_2 29.00 SLM (1.45)	0.5 % of reading + 0.2 % of FS +/- 0.2 % of FS → +/- 0.058 SLM
O_2 2.5 99.5 %	1259 (1998) 50 sccm N_2 50.00 sccm (1.00)	0.8 % of FS n. s.
H_2 5.0 99.999 %	1179 (2007) 10 sccm H_2 10.00 sccm (1.00)	0.5 % of reading + 0.2 % of FS +/- 0.2 % of FS → +/- 0.02 sccm
N_2 2.8 99.8 %	1179 (2007) 10 sccm H_2 10.00 sccm (1.00)	0.5 % of reading + 0.2 % of FS +/- 0.2 % of FS → +/- 0.02 sccm
all	Multigas Controller 647BE (1996)	+/- 1 digit

The measurement technique of the MFCs is based on the temperature rise of part of the controlled gas flow with known heat capacity resulting from the import of a certain amount of

[65] Provider: Praxair Deutschland GmbH, Hürth, Germany.

heat energy.[66] Since a high purity of used gases was requested, any uncertainties related to respective impurities were neglected.

4.1.2 Gas chromatograph

A gas chromatograph equipped with a thermal conductivity detector (TCD) and a helium ionization detector (HID) was used for the analysis of the composition of the product gas. The TCD shows good performance for high molar fractions up to 100 %. It was used for the evaluation of molar fractions of argon and methane (with molar fractions above 0.8 %). Contrariwise, the HID provides high functionality for low concentrations and for hydrogen. Hydrogen could hardly be detected with the TCD because hydrogen has quite similar thermal conductivity characteristics compared to the carrier gas helium. Two packed columns were utilized for the separation of the sample components: a molecular sieve column (MS) for hydrogen, argon, and methane as well as a HayeSep A column for the C_2-hydrocarbons and higher hydrocarbons. Figure 4-4 shows the setup of the GC.

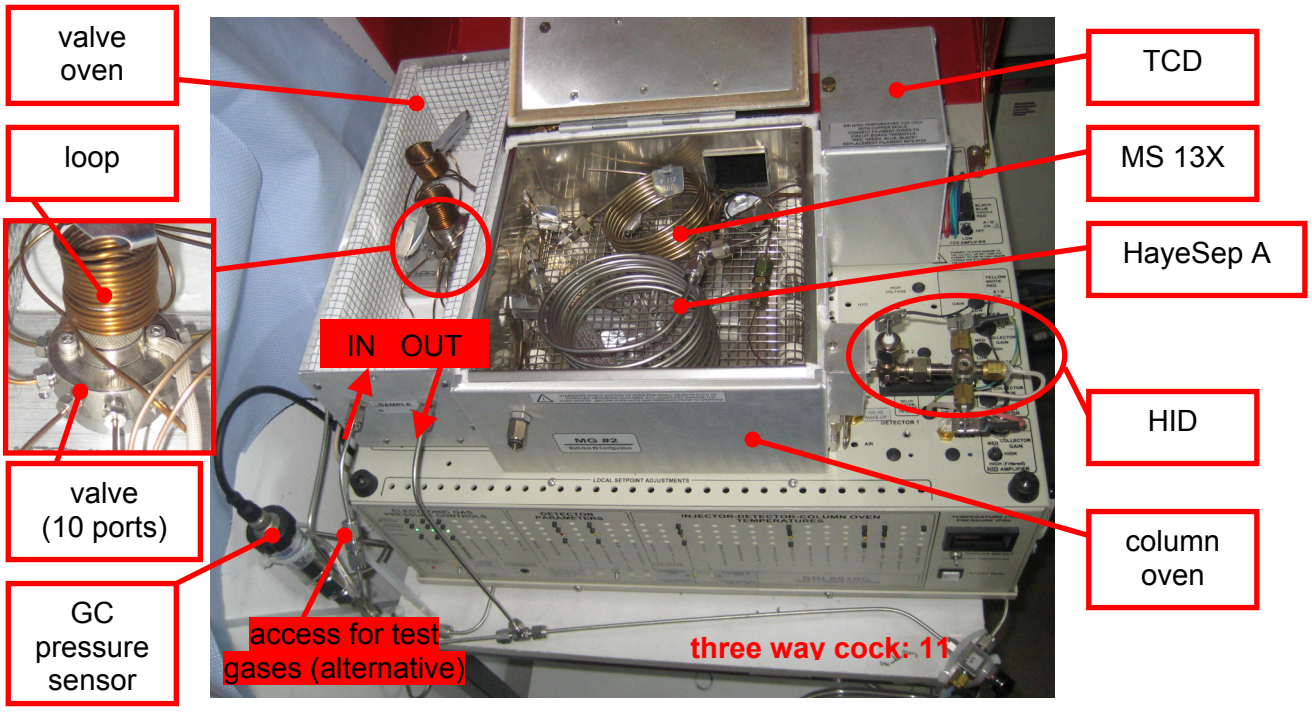

Figure 4-4: Configuration of gas chromatograph

Basic information about the GC and its periphery can be found in Table 4-2. Additional information about the adjusted parameters of the GC as well as examples for chromatograms of the product gas are provided in Appendix B.

[66] Further information may be found on http://www.mksinst.com.

Table 4-2: Basic information about the gas chromatograph

Detectors	Helium ionization detector (HID) Thermal conductivity detector (TCD)
Sample loops	2 x 1 ml
Packed columns	Molecular sieve MS 13X, length: 6' HayeSep A, length: 3 m
Load and inject device	Automated gas sample valve with 10 ports
Sample carrier gas	Helium 5.0 (purity: 99.999 %, further purification by moisture trap[67] → hydrocarbon trap[68] → oxygen trap[69], overpressure at GC inlet: 4 bar)
Operating gas of HID and TCD	
Length of HID electric arc	0.8 mm … 0.9 mm
Special features of HID	• enhanced collector electrode • inert glass tube inserted in metal tube between electric arc and collector electrode
Power supply	Variable transformer: 230 V (+/- 5 %)[70]

Gas samples were fed into the loops either by underpressure at the sample outlet (vacuum pump) or by overpressure at the sample inlet (pressurized test gases). According to the ideal gas law, the amount of injected substance n_{loop} depends on the conditions inside the loop before injection following

$$n_{\text{loop}} = \frac{p_{\text{loop}} \cdot V_{\text{loop}}}{\Re \cdot T_{\text{loop}}} \quad . \qquad \textbf{Equation 46}$$

Since the loop's volume V_{loop} and T_{loop} keep constant (the loops are situated in the tempered valve oven), n_{loop} is only a function of the pressure inside the loop before injection p_{loop}, which depends on the ambient pressure and the pressure inside the reactor. It was measured by a pressure transmitter at the sample outlet of the GC.

Actually, the area of a peak $A_{i,\text{peak}}$ is a function of the amount of substance of the particular component i approaching the detector $n_{i,\text{detector}}$, which equals the amount of substance of the particular component i inside the loop $n_{i,\text{loop}}$ arising from

[67] Manufacturer: Restek GmbH, Bad Homburg, Germany.
[68] Manufacturer: SGE Europe Ltd., Kiln Farm Milton Keynes, United Kingdom.
[69] Manufacturer: see above
[70] Manufacturer: BLOCK Transformatoren-Elektronik GmbH, Verden, Germany. Type: BR2200.

$$n_{i,\mathrm{loop}} = x_{i,\mathrm{loop}} \cdot n_{\mathrm{loop}} \quad , \qquad \textbf{Equation 47}$$

with the molar fraction of component i in the loop $x_{i,\mathrm{loop}}$, because there is no reduction of the amount of substance between the loops and the detectors concerning the considered species.

The aim of GC measurement is the analysis of the composition of the sample in terms of molar fractions $x_{i,\mathrm{loop}}$. Considering a sample with a molar fraction of component i $x_{i,\mathrm{loop}}$ different pressures inside the loop result in different peak areas $A_{i,\mathrm{peak}}$, since n_{loop} depends on p_{loop}. In order to compensate this effect and allow comparability of different measurements, a normal peak area $A_{i,\mathrm{peak,N}}$ was calculated by

$$A_{i,\mathrm{peak,N}} = A_{i,\mathrm{peak}} \cdot \frac{p_{\mathrm{N}}}{p_{\mathrm{loop}}} \quad , \qquad \textbf{Equation 48}$$

assuming that $A_{i,\mathrm{peak}}$ is proportional to $n_{i,\mathrm{loop}}$. $A_{i,\mathrm{peak,N}}$ corresponds to the theoretic peak area resulting from $x_{i,\mathrm{loop}}$ at standard pressure p_{N}. Although linear relationships could not be verified generally, $x_{i,\mathrm{loop}}$ can be well approximated as a function of $A_{i,\mathrm{peak,N}}$. An overview about components, the measurement of their molar fractions, and determined calibration curves is given in Table 4-3.

Table 4-3: Employed detectors and calibration curves for the measurement of molar fractions of the main sample components

Component	HID	TCD	Calibration curve
H_2	✓	✗	2nd order polynomial
CH_4	✓ $(x_{CH_4} < 0.8\,\%)$	✓ $(x_{CH_4} \geq 0.8\,\%)$	2nd order polynomial (HID), line (TCD)
Ar	✗	✓	line
C_2H_6	✓	✗	2nd order polynomial
C_2H_4	✓	✗	2nd order polynomial
C_2H_2	✓	✗	2nd order polynomial

As can be seen in Table 4-3, calibration curves do not have a uniform shape. Linear fit functions as well as 2nd order polynomials can be found. Figure 4-5 (a) and (b) show examples of calibration curves for hydrogen and methane. Approaches for the curves are valid for a wide range of molar fractions covering more than one order of magnitude. Further examples for calibration curves can be found in Appendix B.

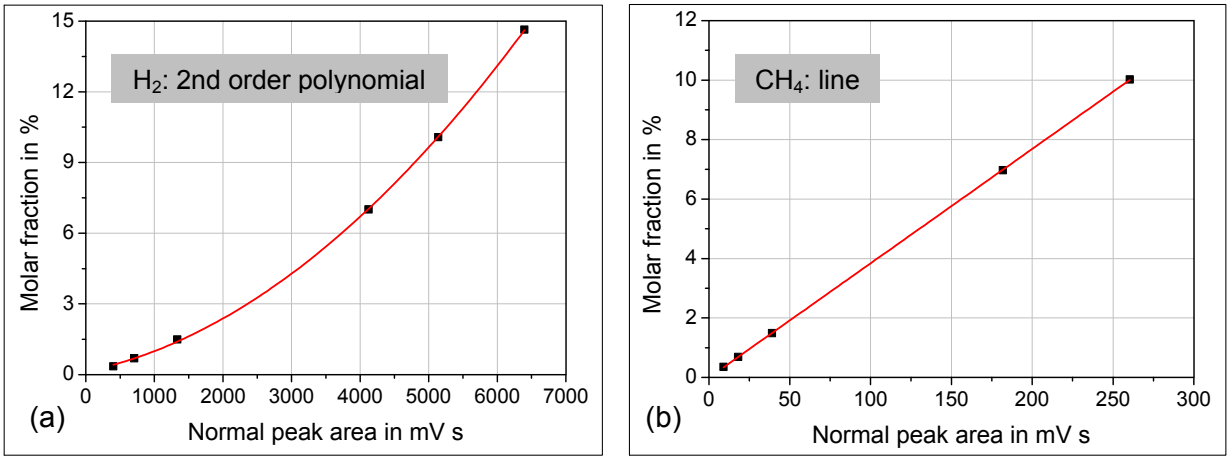

Figure 4-5: Examples for GC calibration curves: the molar fraction of hydrogen detected by the HID (a) and the molar fraction of methane detected by the TCD (b) as a function of the normal peak area

The needle valve downstream the vacuum pump of the GC was installed in order to allow the adjustment of the sample volume flow. Preliminary tests showed that practically complete purging of the GC inlet pipes could be achieved with about 60 s operating time of the vacuum pump at about 50 ml/min. For this volume flow the difference of the pressure at the GC sample outlet at the end of and during the operation of the vacuum pump lies in the range of 35 mbar. An increase of the vacuum pump volume flow due to a decrease of the flow resistance in the needle valve downstream the vacuum pump causes a higher pressure difference (about 75 mbar at 100 ml/min and about 180 mbar at 200 ml/min). Tests were carried out in order to check whether measurement results are affected by the sample volume flow e. g. due to a possibly favored transport of hydrogen. An influence of the pressure difference on the measurement result exceeding the uncertainty of GC measurement and of composition of the test gas mixture could not be observed.

In order to quantify the uncertainty of GC measurements, test gases were injected in the GC repeatedly. Different numbers of runs N_i were performed respecting component i in the considered test gas. For every session $s_{\mathrm{rel}}(A_{i,\mathrm{peak,N}})$, the experimental standard deviation of j normal peak areas $A_{i,\mathrm{peak,N}}$ relative to the mean $\overline{A}_{i,\mathrm{peak,N}}$, calculated by

$$\overline{A}_{i,\mathrm{peak,N}} = \frac{1}{N_i} \cdot \sum_{j=1}^{N_i} A_{i,\mathrm{peak,N},j} \quad , \qquad \textbf{Equation 49}$$

was determined according to

$$s_{\mathrm{rel}}(A_{i,\mathrm{peak,N}}) = \frac{1}{\overline{A}_{i,\mathrm{peak,N}}} \cdot \sqrt{\frac{\sum_{j=1}^{N_i} \left(A_{i,\mathrm{peak,N},j} - \overline{A}_{i,\mathrm{peak,N}}\right)^2}{N_i - 1}} \quad . \qquad \textbf{Equation 50}$$

Additionally, maximum positive deviations relative to the mean $s^{+}_{\mathrm{rel,max}}$ were calculated employing

$$s^{+}_{\mathrm{rel,max}}(A_{i,\mathrm{peak,N}}) = \frac{\max_j\left(A_{i,\mathrm{peak,N},j}\right) - \overline{A}_{i,\mathrm{peak,N}}}{\overline{A}_{i,\mathrm{peak,N}}} \qquad \textbf{Equation 51}$$

and similarly maximum negative deviations relative to the mean $s^{-}_{\mathrm{rel,max}}$ following

$$s^{-}_{\mathrm{rel,max}}(A_{i,\mathrm{peak,N}}) = \frac{\min_j\left(A_{i,\mathrm{peak,N},j}\right) - \overline{A}_{i,\mathrm{peak,N}}}{\overline{A}_{i,\mathrm{peak,N}}} \quad . \qquad \textbf{Equation 52}$$

Depending on the test day determined values for the standard deviation, maximum positive deviation, and maximum negative deviation relative to the mean differ in part significantly. Extreme deviations observed in practice are summarized in Table 4-4 for considered gases and molar fractions. Maximum positive and negative deviations do not always show symmetric behavior. Compared to hydrogen and methane somewhat higher deviations have to be reported for the C_2-hydrocarbons. Greatest deviations could be found for ethyne, mainly resulting from drifting during the particular test day. Complete information respecting results of particular test days is provided in Appendix B.

Table 4-4: Extreme values for standard deviations, maximum positive deviations, and maximum negative deviations relative to mean normal peak areas determined in GC measurements for different gases and molar fractions

Gas	Molar fraction	s_{rel} in %	$s^{+}_{rel,max}$ in %	$s^{-}_{rel,max}$ in %
H_2	100 ppm	7.29	7.09	-7.41
	1 %	1.38	2.14	-2.48
	10 %	0.39	0.62	-0.70
CH_4 (HID)	100 ppm	3.06	2.35	-4.13
	1 %	1.07	1.58	-2.11
CH_4 (TCD)	1 %	0.77	1.68	-1.21
Ar	98.8 %	0.64	1.05	-0.68
C_2H_6	100 ppm	3.76	3.71	-3.75
	490 ppm	1.20	1.28	-1.48
	1 %	2.49	1.67	-4.31
C_2H_4	100 ppm	3.06	3.34	-3.00
	1040 ppm	1.74	1.05	-3.10
	1 %	2.44	1.57	-4.28
C_2H_2	100 ppm	14.49	16.38	-13.59
	0.5 %	4.89	3.19	-8.57
	1.01 %	5.78	8.33	-9.45

In the following the procedure of determining the estimated maximum relative deviation for different molar fractions based on extreme values – presented in Table 4-4 – is exemplarily explained for ethyne. According to Figure 4-6, molar fractions considered in the experiments (here 100 ppm, 0.5 %, and 1.01 %) were embedded in a basic scheme of order of magnitudes (0.001 %, 0.01 %, etc.), substituting a particular order of magnitude when appropriate (here in case of 1.01 %). Measured maximum relative deviations are multiplied by the safety factor 1.1 leading to an extended maximum relative deviation. Maximum relative deviations for orders of magnitude of molar fractions not covered experimentally were estimated either by interpolation on a logarithmic scale or by multiplication of the nearest extended value with a worst case factor based on experimental experience. It is postulated that the determined maximum relative deviations can be applied to a certain interval around respected molar fractions. These intervals are defined according to the equation given in Figure 4-6. As a result, the multiplication of a considered molar fraction with a certain constant leads to the upper bound of the interval. Multiplying the upper bound, which is also the lower bound of the next interval, with the same constant leads to the next considered molar fraction.

Corresponding information about extended and estimated maximum relative deviations for other components can be found in Appendix B.

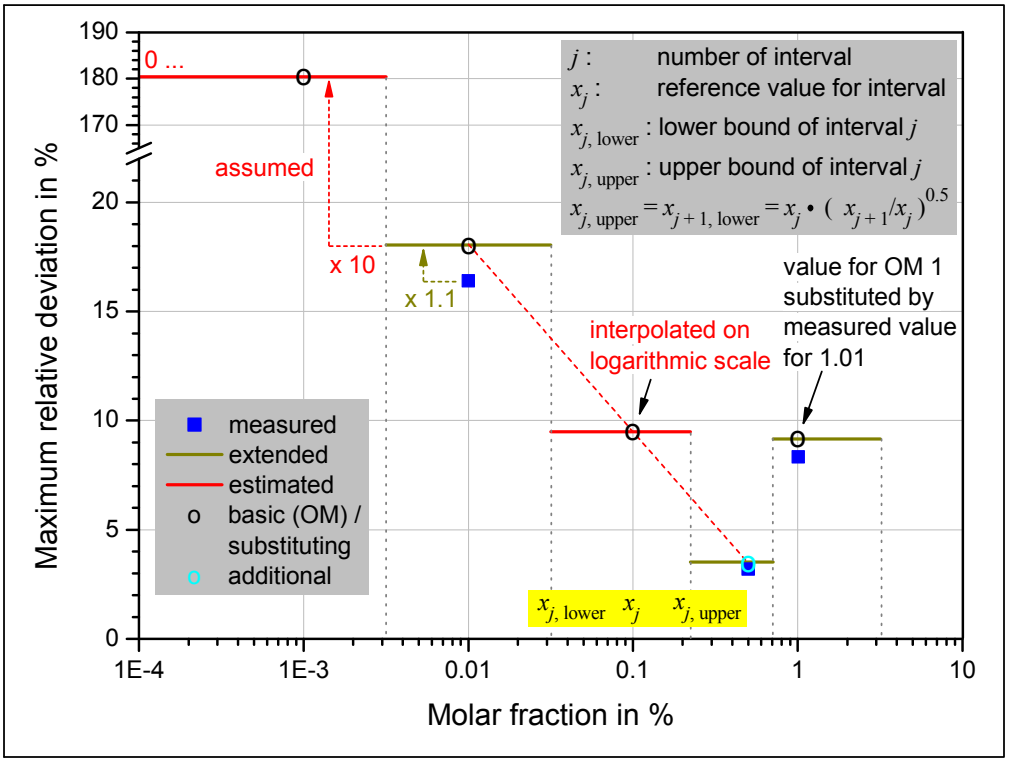

Figure 4-6: Maximum relative positive deviation of GC measurements for ethyne: measured, extended and estimated levels (OM = order of magnitude)

Be it that a certain normal peak area $A_{i,\mathrm{peak,N}}$ was determined for the component i of a gas mixture. If no further data is available, $A_{i,\mathrm{peak,N}}$ is the best estimate for subsequent calculations. However, the measured value could just lie on the upper or lower bound of the interval of possible values around the theoretical average of a collectivity of not executed measurements. It is consequently admissible to calculate the extreme values $A_{i,\mathrm{peak,N,max}}$ and $A_{i,\mathrm{peak,N,min}}$, the limits of an interval, in which the theoretical average should be found with a probability of practically 100 %, according to

$$A_{i,\mathrm{peak,N,max}} = \frac{A_{i,\mathrm{peak,N}}}{s^{-}_{\mathrm{rel,max}} + 1} \qquad \textbf{Equation 53}$$

and

$$A_{i,\mathrm{peak,N,min}} = \frac{A_{i,\mathrm{peak,N}}}{s^{+}_{\mathrm{rel,max}} + 1} \quad . \qquad \textbf{Equation 54}$$

4.1.3 Pressure transmitters

Pressures at the inlet and the outlet of the reactor as well as at the sample outlet of the GC were determined by pressure transmitters manufactured by WIKA. The measurement chain is shown in Figure 4-7.

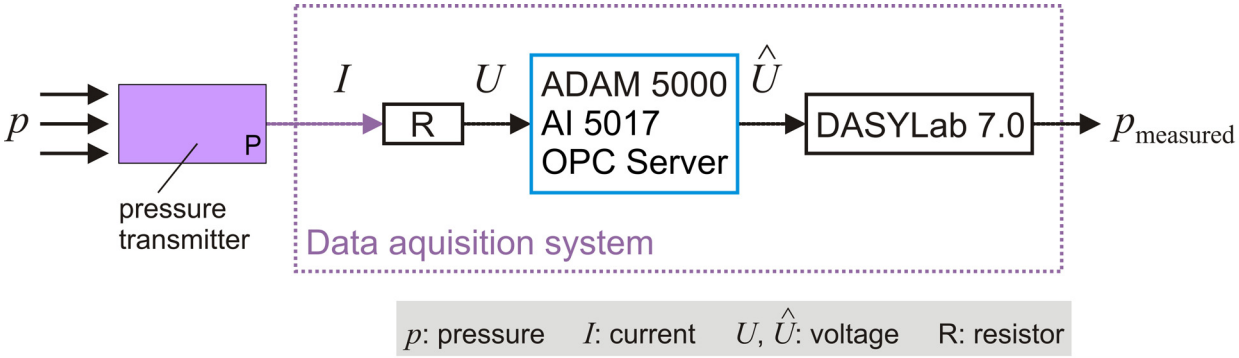

Figure 4-7: Measurement chain of the measurement of pressures

Depending on the pressure affecting the membrane of the pressure transmitter, an electric current is available at the signal output. Via a resistor the electric current was converted into a voltage signal which was interpreted by further components of the data acquisition system[71]. Information about the employed pressure transmitters, the subsequent measurement chain, and estimated maximum as well as standard uncertainties is provided in Table 4-5.

[71] Manufacturer / provider: Advantech Co., Ltd., Milpitas, USA and National Instruments Germany GmbH, München, Germany.

Table 4-5: Information about pressure transmitters and the subsequent measurement chain

Position of pressure transmitter →	Inlet of reactor	Outlet of reactor	Sample outlet of GC
Pressure transmitter model	UT-11	UT-11	S-10
Pressure range (absolute pressure)	0 bar … 1.5 bar (turn down, originally 0 bar … 6 bar)		0 bar … 1.6 bar
Output signal	4 mA … 20 mA		
Accuracy[72]	+/- 0.15 % of span: +/- 0.024 mA (increased due to gold coating on membrane)		+/- 0.25 % of span: +/- 0.04 mA
Assumed probability distribution	rectangular		
Resistor	120.01 Ω	120.00 Ω	120.50 Ω
Accuracy[73]	+/- 0.16 Ω		
Assumed probability distribution	rectangular		
ADAM 5000 module	AI 5017		
Input range	- 5 V … + 5 V		
Accuracy[74]	+/- 0.1 % of range: +/- 0.01 V		
Assumed probability distribution	rectangular		
Estimated maximum uncertainty	+/- 12 mbar	+/- 12 mbar	+/- 15 mbar
Estimated standard uncertainty (type B)	+/- 5 mbar	+/- 5 mbar	+/- 6 mbar

4.2 Reaction conditions

All experiments were carried out at a pressure around 1 bar. Three parameters were varied in order to study a wide range of reaction conditions:

- nominal temperature of the tube furnace T_{furnace} (somehow corresponding to the reaction temperature T_{R} inside the reactor)
- initial total standard volume flow $\dot{V}_{\text{N,tot,0}}$ (and consequently the residence time τ)
- initial molar fraction of methane $x_{\text{CH}_4,0}$

[72] cp. [WIKA, 2005], p. 9 et seqq. and [WIKA, 2006], p. 2
[73] resulting from accuracy of Fluke 189 True RMS Multimeter concerning measurement of electric resistance up to 500 Ω: +/- (0.05 % of measured value + 0.1 Ω), cp. [Fluke, 2002], p. 7-8
[74] cp. [Advantech, 2007], p. 10

Experiments with argon as the diluent have been carried out at five levels of nominal temperature of the tube furnace: 1200 °C, 1300 °C, 1400 °C, 1500 °C, and 1600 °C. For every nominal furnace temperature five (in case of 1600 °C four) residence times were applied. Each set of nominal furnace temperature and residence time comprises three (in one case four) initial molar fractions of methane, regularly in the range between 2 % and 10 %. An overview of the reaction conditions finally covered in the experiments using argon as the dilution gas is given in Table 4-6.

Table 4-6: Reaction conditions covered in experiments with argon as dilution gas

Ar		**Level of**		
T_{furnace} / τ **-set**	T_{furnace} in °C	$\dot{V}_{\mathrm{N,tot,0}}$ in sccm	τ in s	$x_{\mathrm{CH_4,0}}$ in %
1	1200	95	1.46	2, 5, 10
2		200	0.696	2, 5, 10
3		350	0.396	2, 5, 10
4		685	0.203	2, 5, 10
5		2000	0.0697	2, 5, 10, 20
6	1300	340	0.378	2, 5, 10
7		650	0.200	2, 5, 10
8		1300	0.100	2, 5, 10
9		2600	0.0501	2, 5, 10
10		4800	0.0275	2, 5, 10
11	1400	700	0.174	2, 5, 10
12		1400	0.0885	2, 5, 10
13		2600	0.0487	2, 5, 10
14		3800	0.0324	2, 5, 10
15		6500	0.0198	2, 5, 7.1
16	1500	1600	0.0707	2, 5, 10
17		2800	0.0415	2, 5, 10
18		4600	0.0256	2, 5, 10
19		7200	0.0162	2, 5, 6.3
20		9800	0.0119	2, 3.1, 5
21	1600	2000	0.0547	2, 5, 10
22		3350	0.0335	2, 5, 10
23		6500	0.0176	2, 5, 7.1
24		9800	0.0115	2, 3, 5

Moreover, a reduced number of experiments with helium as diluent were executed. Here only three nominal furnace temperatures were considered, namely 1300 °C, 1400 °C, and 1500 °C, applying one or three residence times, respectively. As also done in experiments with argon as

dilution gas, the initial molar fraction of methane was varied between 2 % and 10 %. A corresponding summary can be found in Table 4-7.

Table 4-7: Reaction conditions covered in experiments with helium as dilution gas

He		Level of		
$T_{furnace}$ / τ **-set**	$T_{furnace}$ in °C	$\dot{V}_{N,tot,0}$ in sccm	τ in s	$x_{CH_4,0}$ in %
25	1300	3800	0.0344	2, 5, 10
26	1400	2800	0.0443	2, 5, 10
27		3800	0.0328	2, 5, 10
28		6500	0.0190	2, 5, 7.1
29	1500	3800	0.0303	2, 5, 10

The residence time in the reactor τ – introduced before – is defined as

$$\tau = \frac{V_{heated}}{\dot{V}_{reference}} = \frac{\frac{\pi}{4} \cdot d_{R,i}^2 \cdot l_{heated}}{\dot{V}_{N,tot,0} \cdot \frac{T_{furnace}}{T_N} \cdot \frac{p_N}{\overline{p}_{R,inlet}}} \quad . \qquad \textbf{Equation 55}$$

V_{heated} is the volume in the reactor that is actively heated by the tube furnace and which can be calculated employing the inner diameter of the tube reactor $d_{R,i}$ and the heated length of the tube furnace l_{heated}. $\dot{V}_{reference}$ is a reference volume flow depending on the initial total standard volume flow $\dot{V}_{N,tot,0}$, the nominal furnace temperature $T_{furnace}$, and the average pressure at the inlet of the reactor $\overline{p}_{R,inlet}$, calculated as the mean of the pressures at the inlet of the reactor at the start and the end of the GC-procedure. T_N represents the standard temperature, whereas p_N stands for the standard pressure.

4.3 Procedure

At the beginning of each test day the mass flow controllers were calibrated with respect to standard volume flows needed later on during the calibration of the GC and the cracking experiments employing a primary flow calibrator[75]. By now, the tube furnace should have reached the nominal furnace temperature, because a timer was set which allowed a controlled start of the heating process taking into account that the heating rate must not exceed 300 K/h

[75] Manufacturer: Bios International Corporation, Butler, USA. DCL-L and DCL-H in combination with DCNS.

due to material restrictions. Subsequently, the GC was calibrated with gas mixtures characterized by different molar fractions of hydrogen and / or methane in argon or helium (cock 4 and cock 5 opened toward bypass). Usually a 3-point-calibration was achieved for hydrogen and methane, whereas the number of molar fractions of argon varied depending on the number of gas mixtures used for the GC calibration concerning hydrogen and methane. The GC could not be calibrated with respect to helium as explained before.

As soon as the calibration of the GC, employing gas mixtures produced by mass flow controllers, was finished, the pressure transmitters at the inlet and outlet of the reactor were purged for several minutes with a pure flow of dilution gas (cock 1 and 4 closed, cock 5 connecting reactor outlet and flue, cock 6 opened leading dilution gas in respective direction). Then the standard volume flow of dilution gas through the reactor was increased successively ensuring that maximum temperature changes inside the reactor did not reach a critical extend taking the mechanical and thermal properties of the reactor material into account. Finally the total standard volume flow of the particular experiment was attained. In order to avoid a contamination of the dilution gas with methane before a thermal equilibrium inside the reactor was accomplished, cock 2 remained closed and cock 3 only connected the pipes coming from cock 1 with the reactor. However, for standard volume flows above 2000 sccm cock 3 was brought in central position connecting all ways after the final total standard volume flow was reached in order to prevent a shock pressure afterwards, when cock 3 would have to be turned to allow methane feed. The volume between cock 2 and 3 filled with methane is negligibly low compared to the volume flow of dilution gas passing cock 3. While a thermal equilibrium inside the reactor was approached – this usually took about an hour – the GC was calibrated with at least one ready-to-use test gas containing the C_2-hydrocarbons ethane, ethene, and ethyne. It was assumed that the temperatures inside the reactor could be considered to be constant, when the temperature at position 320 mm measured by the thermocouple reached constant levels. Some minutes after a steady temperature at position 320 mm was observed, cock 2 was opened toward methane and the respective mass flow controller was actuated to introduce the required standard volume flow of methane. Simultaneously, the standard volume flow of the dilution gas was reduced guaranteeing a stable residence time and finally resulting in the projected molar fraction of methane at the inlet of the reactor. After introducing methane, a temperature variation could be noted. The temperature change never exceeded 31.3 K and averaged 10.5 K, comprising absolute values of temperature drops up to 4.9 K which occurred in few cases. The establishment of a constant temperature at position 320 mm after the addition of methane took a different amount of time depending on the reaction conditions. In most cases three to five minutes were needed, whereas this period of time exceptionally lasted up to 29 minutes. The GCs measurement was started as soon as the criterion of a constant temperature at position 320 mm was satisfied. Reference experiments were executed providing

different periods of time between the initialization of the methane flow and the activation of the GC vacuum pump. It was found that the dependencies of the measurement results on the duration of methane flow until starting the GC-procedure were negligible within a certain interval of time around the moment the temperature at position 320 mm reached a constant level. As a consequence this moment provides a representative experimental situation. It guarantees that transient conditions directly after applying methane were not considered as well as conditions later on, when the deposition of carbon could have affected the reaction conditions.

The temperature at position at 320 mm could change during the operation of the vacuum pump responsible for the sample transport into the loops of the GC due to the progress of the reactions and the formation as well as deposition of carbon. However, temperatures and pressures did not change significantly as can be seen in Table 4-8. Thus, the reaction conditions were constant during the sample collection.

Table 4-8: Changes of pressures at reactor inlet and reactor outlet as well as change of temperature at position 320 mm during operation of the vacuum pump of the GC

Change	$p_{\mathrm{R,inlet}}$	$p_{\mathrm{R,outlet}}$	$T_{\mathrm{R,320\,mm}}$
average absolute	0.48 mbar	0.16 mbar	0.32 K
maximum positive	7 mbar	1 mbar	5.0 K
maximum negative	1 mbar	1 mbar	0.9 K

As soon as the sample collection procedure of the GC was finished, the methane flow was stopped, while the flow of the dilution gas was increased again in order to apply a practically constant standard volume flow at the inlet of the reactor. The dilution gas purged the reactor assuring that only traces of methane and reaction products remained in the system. After a few minutes between 5 sccm and 40 sccm oxygen (O_2) were added to the dilution gas by adjusting cock 2, while the standard volume flow of dilution gas was reduced slightly keeping the total standard volume flow constant. The oxygen reacted with carbon depositions inside the reactor when temperatures were high enough. A temperature increase at position 320 mm could usually be observed after a certain period of time depending on the amount of carbon deposit and the standard volume flow of oxygen indicating that the flame front caused by the endothermic reaction approached the tip of the thermocouple. Some minutes later, when also the region below the tip of the thermocouple was sufficiently treated with oxygen, the oxygen flow was stopped and the flow of dilution gas adapted to the required residence time. By doing so, the setup was prepared for the next run. Usually all three initial molar fractions of methane, which had to be applied for one set of nominal furnace temperature and residence time according to the schemes given in Table 4-6 and Table 4-7, were considered during one test day – partly more than one time.

After the last run was performed ending with the final burning off, the temperature of the furnace was reduced with a cooling rate of 450 K/h. While the standard volume flow through the reactor was reduced gradually, the GC was calibrated a second time with respect to C_2-hydrocarbons using ready-to-use test gases. Afterwards, a second calibration of the GC with respect to methane and hydrogen took place employing gas mixtures prepared with the mass flow controllers, as done previous to the cracking experiments. A test day closed with the programming of the controller of the tube furnace ensuring a proper progress of heating at the beginning of the next day and the initialization of the GC column bake-out procedure.

In the following chapters the calibration of mass flow controller, the calibration of the GC, and the determination of molar fractions in the product gas are explained in detail.

4.3.1 Calibration of mass flow controllers

Mass flow controllers were employed in order to produce GC calibration gas mixtures as well as inlet gas mixtures for the cracking experiments. The calibration of the MFCs took place with a volume flow calibration unit comprising a device, which measured the actual volume flow (DCL-L and DCL-H), as well as a device, which measured the temperature and the absolute pressure of the flow and finally calculated the standard volume flow passing the calibration unit. Respective nominal values at the MKS control unit were adjusted that way that $\dot{V}_{\mathrm{N},i,\mathrm{DC}}$, the output value for the standard volume flow of gas i of the flow calibration unit, equaled the required value. The measurement of the standard volume flow employing the calibration unit involves a certain uncertainty depending on the level of measured volume flow. Respective information can be extracted from Table 4-9.

Table 4-9: Stated, projected, and estimated accuracy of the volume flow calibration unit

Volume flow as percentage of lower limit of optimal flow range								Volume flow within optimal flow range
< 10 %	< 20 %	< 30 %	< 40 %	< 50 %	< 60 %	< 80 %	< 100 %	
5.8 %	3.0 %	2.1 %	1.7 %	1.4 %	1.3 %	1.1 %	1 %	1.0 %
8.12 %	4.20 %	2.94 %	2.38 %	1.96 %	1.82 %	1.54 %	1.40 %	1.4 %

Projected accuracy of DCL-L and DCL-H given in [Bios, 2006]
Accuracy of DCL-L and DCL-H stated in [ANALYT, 2006], p. 4, leakage neglected
Accuracy of DCL-L and DCL-H in combination with DCNS stated in [ANALYT, 2006], p. 13 and [Bios, 2009]
Estimated accuracy of DCL-L and DCL-H in combination with DCNS employing rule of proportion regarding stated and projected accuracies
Optimum flow range: DCL-L → 10 ml/min – 500 ml/min, DCL-H → 500 ml/min – 30 l/min
Operation temperature between 20 °C and 30 °C

$\dot{V}_{\mathrm{N},i,0}$, the standard volume flow of gas i leaving the respective mass flow controller, might have changed during the calibration and experiment because of imprecise repeatability. Therefore $\dot{V}_{\mathrm{N},i,0}$ arises from

$$\dot{V}_{\mathrm{N},i,0} = \dot{V}_{\mathrm{N},i,\mathrm{DC}} + \Delta\dot{V}_{\mathrm{N},i,\mathrm{MKS,repeatability}} \qquad \textbf{Equation 56}$$

featuring $\Delta\dot{V}_{\mathrm{N},i,\mathrm{MKS,repeatability}}$, a repeatability term nominally set to 0 but contributing to the uncertainty of $\dot{V}_{\mathrm{N},i,0}$ according to Table 4-1. For mass flow controllers, whose repeatability is not provided, the repeatability was approximated by the accuracy, which is definitely a worst case examination.

The nominal molar fraction of component i in a gas mixture used for calibration of the GC produced by mass flow controllers $x_{i,\mathrm{MFC}}$ arises from

$$x_{i,\mathrm{MFC}} = \frac{\dot{V}_{\mathrm{N},i,0}}{\sum_i \dot{V}_{\mathrm{N},i,0}} \quad . \qquad \textbf{Equation 57}$$

Due to incomplete mixing of the gaseous components and purging of the bypass pipes, the effective molar fraction of component i $x_{i,\mathrm{GC}}$ could differ slightly from $x_{i,\mathrm{MFC}}$. Experimental experience led to an approach following

$$x_{i,\mathrm{GC}} = x_{i,\mathrm{MFC}} + \Delta x_{i,\mathrm{bypass}} \quad , \qquad \textbf{Equation 58}$$

where $\Delta x_{i,\mathrm{bypass}}$ nominally equaled 0 but contributed to the uncertainty of $x_{i,\mathrm{GC}}$ with the extremes following

$$\Delta x_{i,\mathrm{bypass,max}} = b_{i,\mathrm{bypass}} \cdot x_{i,\mathrm{MFC}} \qquad \textbf{Equation 59}$$

and

$$\Delta x_{i,\mathrm{bypass,min}} = -b_{i,\mathrm{bypass}} \cdot x_{i,\mathrm{MFC}} \quad , \qquad \textbf{Equation 60}$$

with a component specific uncertainty factor $b_{i,\mathrm{bypass}}$. It was found that $b_{\mathrm{CH_4},\mathrm{bypass}} = 0.5\,\%$ and $b_{\mathrm{Ar,bypass}} = 0.15\,\%$ reasonably cover the maximum range of uncertainty and assumed that $b_{\mathrm{H_2},\mathrm{bypass}} = b_{\mathrm{CH_4},\mathrm{bypass}}$. It was postulated that the standard uncertainty of $\dot{V}_{\mathrm{N},i,\mathrm{DC}}$, $\Delta\dot{V}_{\mathrm{N},i,\mathrm{MKS,repeatability}}$, and $\Delta x_{i,\mathrm{bypass}}$ can be estimated based on a rectangular probability function.

4.3.2 Calibration of the gas chromatograph

Usually three different molar fractions of methane and hydrogen were applied for the determination of respective calibration curves of the GC. In few cases the pre- or post-experimental GC calibration only comprehended two normal peak areas. Then, based on the complete set of normal peak areas $A_{i,\mathrm{peak,N},1}$, $A_{i,\mathrm{peak,N},2}$, and $A_{i,\mathrm{peak,N},3}$ as well as the incomplete set $\hat{A}_{i,\mathrm{peak,N},1}$ and $\hat{A}_{i,\mathrm{peak,N},2}$, the missing normal peak area $\hat{A}_{i,\mathrm{peak,N},3}$ was estimated by

$$\hat{A}_{i,\mathrm{peak,N},3} = 0.5 \cdot \left(\frac{\hat{A}_{i,\mathrm{peak,N},1}}{A_{i,\mathrm{peak,N},1}} \cdot A_{i,\mathrm{peak,N},3} + \frac{\hat{A}_{i,\mathrm{peak,N},2}}{A_{i,\mathrm{peak,N},2}} \cdot A_{i,\mathrm{peak,N},3} \right) \qquad \textbf{Equation 61}$$

with the extremes

$$\hat{A}_{i,\mathrm{peak,N},3,\max} = 0.5 \cdot \left(\frac{\hat{A}_{i,\mathrm{peak,N},1,\max}}{A_{i,\mathrm{peak,N},1,\min}} \cdot A_{i,\mathrm{peak,N},3,\max} + \frac{\hat{A}_{i,\mathrm{peak,N},2,\max}}{A_{i,\mathrm{peak,N},2,\min}} \cdot A_{i,\mathrm{peak,N},3,\max} \right) \qquad \textbf{Equation 62}$$

and

$$\hat{A}_{i,\mathrm{peak,N},3,\min} = 0.5 \cdot \left(\frac{\hat{A}_{i,\mathrm{peak,N},1,\min}}{A_{i,\mathrm{peak,N},1,\max}} \cdot A_{i,\mathrm{peak,N},3,\min} + \frac{\hat{A}_{i,\mathrm{peak,N},2,\min}}{A_{i,\mathrm{peak,N},2,\max}} \cdot A_{i,\mathrm{peak,N},3,\min} \right) \quad . \qquad \textbf{Equation 63}$$

Concerning the C_2-hydrocarbons four ready-to-use test gases with three different levels of molar fractions had been used for the calibration of the GC as can be seen in Table 4-10. Test gas 1

was not only used for the GC calibration with respect to C_2-hydrocarbons but also with respect to argon. Taking into account that C_2H_6, C_2H_4, C_2H_2, and Ar with stated qualities of 2.0, 2.5, 2.6, and 4.8, respectively, were used for the production of the test gas, it can be shown that the molar fraction of argon in test gas 1 $x_{\mathrm{Ar,test\,gas\,1}}$ equals approximately 98.834 %[76] with conceivable extreme values $x_{\mathrm{Ar,test\,gas\,1,max}} = 98.860\,\%$ and $x_{\mathrm{Ar,test\,gas\,1,min}} = 98.809\,\%$.

Table 4-10: Information about ready-to-use test gases employed for GC calibration

Test gas	x_{CH_4}	$x_{C_2H_6}$	$x_{C_2H_4}$	$x_{C_2H_2}$	x_{H_2}	Accuracy	Balance / further components	Notes
1	-	490 ppm	1040 ppm	1.01 %	-	+/- 2 %	Ar / -	[77]
2	1 %	1 %	1 %	0.5 %	-	+/- 5 %	N_2 / CO, CO_2	[78]
3	100 ppm	100 ppm	-	-	-	+/- 2 %	He / C_3H_8, n-C_4H_{10}, i-C_4H_{10}	[79]
4	100 ppm	100 ppm	100 ppm	100 ppm	100 ppm	+/- 10 %	N_2 / O_2, CO, CO_2	see test gas 1

In order to reduce the duration of the calibration of the GC, in most cases only one or two test gases, mainly including test gas 1, were applied. However, in any case the determination of an appropriate calibration curve based on three nodes was possible, since the ratios of normal peak areas showed quite constant behavior allowing the calculation of the missing normal peak areas. An overview about respective ratios is provided in Table 4-11 along with determined average values, observed standard deviation, and extreme values.

For example the missing normal peak areas $A_{\mathrm{C_2H_2,peak,N,100\,ppm}}$ and $A_{\mathrm{C_2H_2,peak,N,0.5\,\%}}$ could be determined employing the measured normal peak area for 1.01 % C_2H_2 $A_{\mathrm{C_2H_2,peak,N,1.01\,\%}}$ following

$$A_{\mathrm{C_2H_2,peak,N,100\,ppm}} = A_{\mathrm{C_2H_2,peak,N,1.01\,\%}} \cdot \left(\frac{A_{\mathrm{C_2H_2,peak,N,100\,ppm}}}{A_{\mathrm{C_2H_2,peak,N,1.01\,\%}}} \right)_{\mathrm{average}} \qquad \textbf{Equation 64}$$

and

[76] Assumption: present value of molar fraction of the respective C_2-hydrocarbon in the raw gas lies in the center of the interval of possible molar fraction according to the quality of the raw gas. Impurities of Ar 4.8 were neglected.
[77] Manufacturer: Westfalen AG, Münster, Germany. Customer-specific test gas.
[78] Manufacturer: SIGMA-ALDRICH Chemie GmbH, Taufkirchen, Germany. Fluka 68811.
[79] Manufacturer: Linde AG, Pullach, Germany. Test gas in Minican.

$$A_{C_2H_2,peak,N,0.5\%} = A_{C_2H_2,peak,N,1.01\%} \cdot \left(\frac{A_{C_2H_2,peak,N,0.5\%}}{A_{C_2H_2,peak,N,1.01\%}} \right)_{average} , \qquad \textbf{Equation 65}$$

respectively. The maximum and minimum values of missing normal peak areas were determined employing extended maximum and minimum ratios.

Table 4-11: Determined ratios of normal peak areas corresponding to different molar fractions of C_2-hydrocarbons. Extended values are based on experimental results, but comprise a safety factor of 1.1 (maximum) and 0.9 (minimum).

Ratio	Average	# Particular ratios	Standard deviation related to average in %	Extended maximum	Extended minimum
$\frac{A_{C_2H_6,peak,N,100\,ppm}}{A_{C_2H_6,peak,N,490\,ppm}}$	0.2233	13	5.65	0.2705	0.1834
$\frac{A_{C_2H_6,peak,N,100\,ppm}}{A_{C_2H_6,peak,N,1\%}}$	0.01787	9	6.76	0.02294	0.01526
$\frac{A_{C_2H_6,peak,N_6,1\%}}{A_{C_2H_6,peak,N,490\,ppm}}$	12.45	27	5.05	14.60	9.018
$\frac{A_{C_2H_4,peak,N,100\,ppm}}{A_{C_2H_4,peak,N,1040\,ppm}}$	0.1200	8	6.96	0.1470	0.09990
$\frac{A_{C_2H_4,peak,N,100\,ppm}}{A_{C_2H_4,peak,N,1\%}}$	0.01845	5	4.57	0.02186	0.01589
$\frac{A_{C_2H_4,peak,N,1\%}}{A_{C_2H_4,peak,N,1040\,ppm}}$	6.437	27	3.40	7.413	5.109
$\frac{A_{C_2H_2,peak,N,100\,ppm}}{A_{C_2H_2,peak,N,1.01\%}}$	0.01044	8	18.96	0.01565	0.007423
$\frac{A_{C_2H_2,peak,N,100\,ppm}}{A_{C_2H_2,peak,N,0.5\%}}$	0.02013	5	26.79	0.03083	0.01380
$\frac{A_{C_2H_2,peak,N,0.5\%}}{A_{C_2H_2,peak,N,1.01\%}}$	0.5185	27	3.06	0.5958	0.4219

When two test gases were applied and consequently two normal peak areas were available for every C_2-hydrocarbon, the missing normal peak areas were calculated as the arithmetic mean of values resulting from the measured peak areas and ratios given in Table 4-11. Moreover, the respective greatest and lowest values based on extended maximum and minimum ratios were considered. Figure 4-8 illustrates the determination of a nominal calibration curve resulting from

a number (usually three) of pairs of known molar fractions $x_{i,\mathrm{GC}}$ and normal peak areas $A_{i,\mathrm{peak,N}}$. Additionally, an upper and a lower calibration curve were determined employing extreme values according to the diagram.

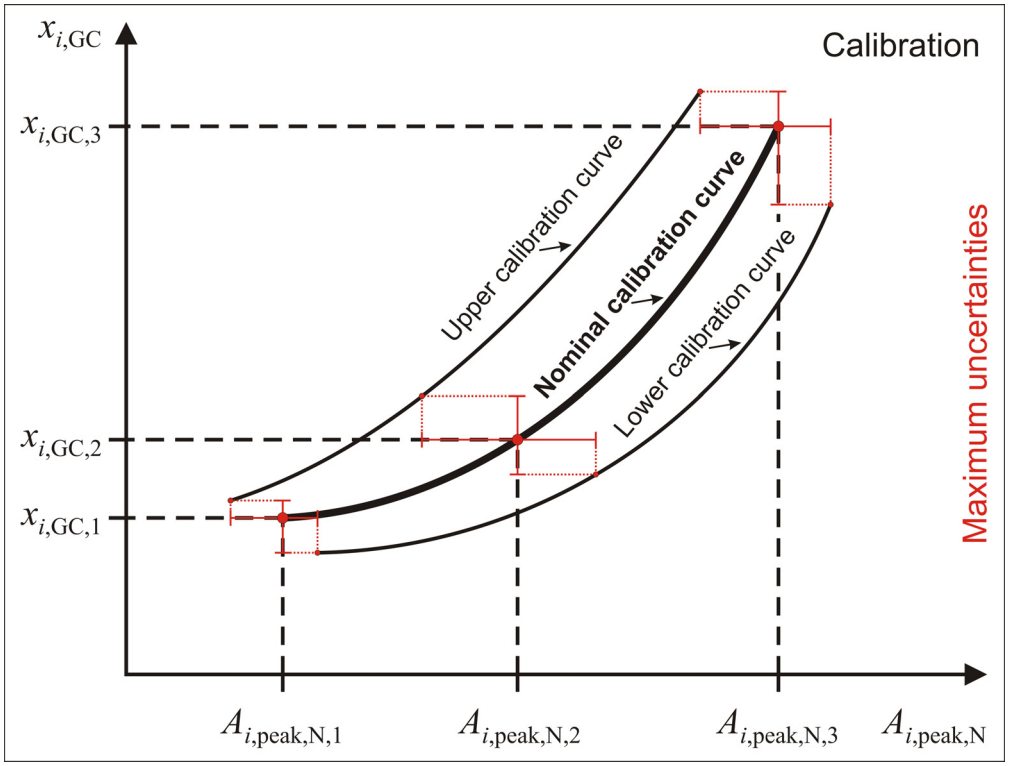

Figure 4-8: Illustration of the definition of calibration curves of the GC

4.3.3 Molar fractions in the product gas

The GC was calibrated at the beginning and the end of every test day in order to minimize the influence of possible changes of the GC characteristics during the experimental period on the results of the measurement. The timing of each test day started with the injection of the first calibration sample. All other injections related to this reference point of time. The time $t_{i,\mathrm{GC,before}}$, corresponding to the calibration of the GC before the cracking experiments with respect to component i, was defined as the average of times for all particular injections contributing to the respective calibration curve. Compatibly, $t_{i,\mathrm{GC,after}}$ refers to the average of times for all GC calibration injections associated with component i, that started after the termination of the last cracking experiment of the considered test day. The molar fraction of component i in the product gas at the outlet of the reactor $x_{i,\mathrm{P}}$ injected at the time $t_{i,\mathrm{GC}}$ was calculated by linear interpolation respecting the molar fractions $x_{i,\mathrm{P,before}}$ and $x_{i,\mathrm{P,after}}$ determined based on calibration curves referring to the situation before and after the cracking experiments following

$$x_{i,\mathrm{P}} = x_{i,\mathrm{P,before}} + \frac{x_{i,\mathrm{P,after}} - x_{i,\mathrm{P,before}}}{t_{i,\mathrm{GC,after}} - t_{i,\mathrm{GC,before}}} \cdot \left(t_{i,\mathrm{GC}} - t_{i,\mathrm{GC,before}}\right) \quad . \qquad \textbf{Equation 66}$$

Figure 4-9 illustrates the evaluation of a measured normal peak area of species i regarding experiment k using calibration curves defined for the situation before the experiments.

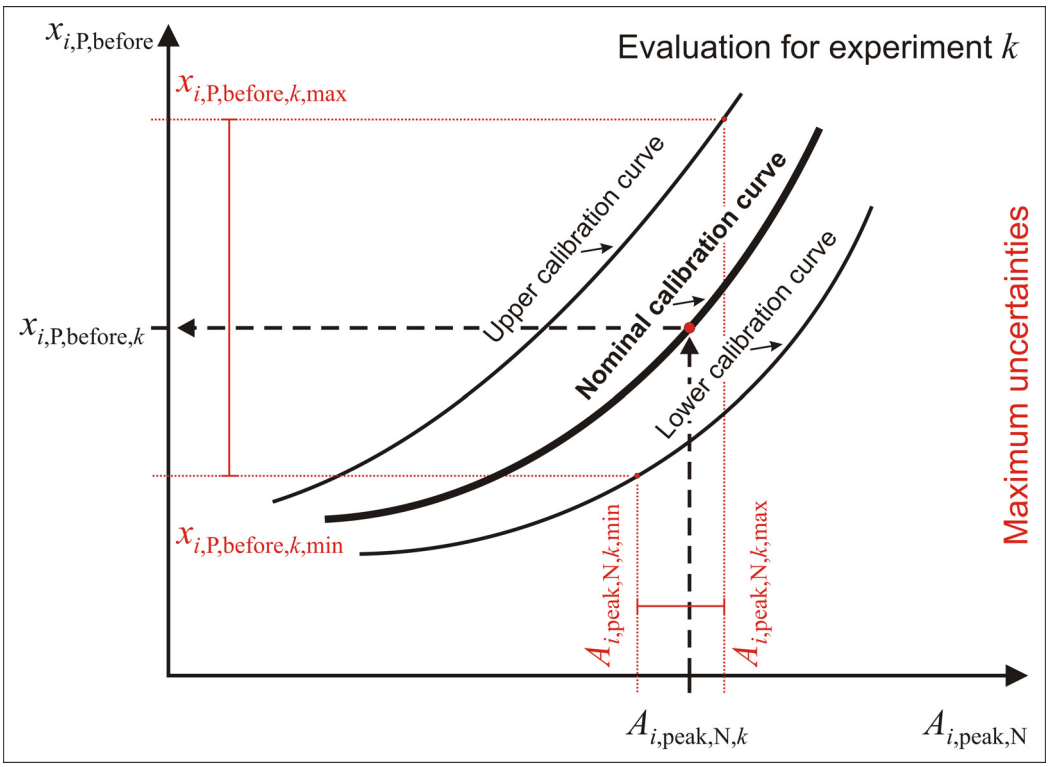

Figure 4-9: Illustration of the utilization of calibration curves of the GC which exemplarily refer to the situation before the experiments.

The maximum uncertainty of the measurement of time only accounts for approximately 6 s and was therefore neglected. Consequently, the extreme values for $x_{i,\mathrm{P}}$ were determined according to

$$x_{i,\mathrm{P,max}} = x_{i,\mathrm{P,before,max}} + \frac{x_{i,\mathrm{P,after,max}} - x_{i,\mathrm{P,before,max}}}{t_{i,\mathrm{GC,after}} - t_{i,\mathrm{GC,before}}} \cdot \left(t_{i,\mathrm{GC}} - t_{i,\mathrm{GC,before}}\right) \qquad \textbf{Equation 67}$$

and

$$x_{i,\mathrm{P,min}} = x_{i,\mathrm{P,before,min}} + \frac{x_{i,\mathrm{P,after,min}} - x_{i,\mathrm{P,before,min}}}{t_{i,\mathrm{GC,after}} - t_{i,\mathrm{GC,before}}} \cdot \left(t_{i,\mathrm{GC}} - t_{i,\mathrm{GC,before}}\right) \quad , \qquad \textbf{Equation 68}$$

calculating $x_{i,\mathrm{P},k,\max}$ – the maximum possible molar fraction of component i in the product gas regarding experiment k – by evaluating the maximum normal peak area $A_{i,\mathrm{peak,N},k,\max}$ employing the upper calibration curve and $x_{i,\mathrm{P},k,\min}$ – the minimum possible molar fraction of component i in the product gas regarding experiment k – by evaluating the minimum normal peak area $A_{i,\mathrm{peak,N},k,\min}$ employing the lower calibration curve.

When a reaction condition was applied more than one time, meaning that several experiments could be carried out at a particular test day with marginally different conditions regarding total standard volume flow and composition at the inlet of the reactor as well as measured pressures at the inlet and the outlet of the reactor, average values of determined molar fractions and pressures were used for further calculations. In these cases the minimum of calculated maximum molar fractions of component i was considered as the maximum possible molar fraction respecting the average and the maximum of calculated minimum molar fractions of component i was considered as the minimum possible molar fraction respecting the average.

The maximum positive uncertainty of the molar fraction of component i in the product gas arises from the difference of the determined maximum value and the nominal value following

$$u^{+}_{\max}(x_{i,\mathrm{P}}) = x_{i,\mathrm{P,max}} - x_{i,\mathrm{P}} \quad , \qquad \textbf{Equation 69}$$

whereas the respective maximum negative uncertainty arises from

$$u^{-}_{\max}(x_{i,\mathrm{P}}) = x_{i,\mathrm{P,min}} - x_{i,\mathrm{P}} \quad . \qquad \textbf{Equation 70}$$

In addition to the declaration of the maximum uncertainties of molar fractions in the product gas, the determination of a standard uncertainty was attempted. Therefore firstly an average maximum uncertainty $\overline{u}_{\max}(x_{i,\mathrm{P}})$ was calculated employing

$$\overline{u}_{\max}(x_{i,\mathrm{P}}) = 0.5 \cdot \left(u^{+}_{\max}(x_{i,\mathrm{P}}) + \left|u^{-}_{\max}(x_{i,\mathrm{P}})\right|\right) \quad , \qquad \textbf{Equation 71}$$

which is a reasonable measure of the maximum uncertainty because usually

$$\left|u^{+}_{\max}(x_{i,\mathrm{P}})\right| \approx \left|u^{-}_{\max}(x_{i,\mathrm{P}})\right| \quad . \qquad \textbf{Equation 72}$$

On average $\left|u^{+}_{\max}(x_{i,\mathrm{P}})\right|$ and $\left|u^{-}_{\max}(x_{i,\mathrm{P}})\right|$ differ from $\overline{u}_{\max}(x_{i,\mathrm{P}})$ about 4.2 % for hydrogen, 4.3 % for methane, 30.5 % for ethane, 15.1 % for ethene, 18.2 % for ethyne, and 6.1 % for argon.

The interval defined by the bounds $x_{i,\mathrm{P}} - \overline{u}_{\max}(x_{i,\mathrm{P}})$ and $x_{i,\mathrm{P}} + \overline{u}_{\max}(x_{i,\mathrm{P}})$ practically covers the region of 100 % probability. Assuming that the probability function regarding $x_{i,\mathrm{P}}$ resemble a normal distribution and that the interval $[x_{i,\mathrm{P}} - \overline{u}_{\max}(x_{i,\mathrm{P}}), x_{i,\mathrm{P}} + \overline{u}_{\max}(x_{i,\mathrm{P}})]$ corresponds to the confidence interval of 99 %, the standard uncertainty of $x_{i,\mathrm{P}}$ can be calculated from

$$u(x_{i,\mathrm{P}}) = \frac{\overline{u}_{\max}(x_{i,\mathrm{P}})}{k_p} \quad , \qquad \textbf{Equation 73}$$

with the coverage factor $k_p = 2.576$.[80] The assumption of a normal distribution of probability, in particular in contrast to a rectangular distribution, is admissible, since

- maximum and minimum normal peak areas used for calibration and for the determination of a corresponding molar fraction using the calibration curves were calculated presuming extreme deviations, which is a worst case estimation. Usually considerably smaller deviations could be reported.
- maximum uncertainties of molar fractions employed for the definition of calibration curves were calculated based on severest combinations of contributing uncertainties. Standard uncertainties calculated postulating rectangular probability distributions of contributing uncertainties are remarkably lower than the maximum uncertainties. Although rectangular probability distributions were considered for all input parameters,

[80] cp. [ISO, 2008], p. 70

the probability distribution of the molar fraction as the output parameter likely approaches a normal distribution following the Central Limit Theorem.[81]

- though theoretically possible, the combination of extreme normal peak areas and extreme molar fractions postulated for the determination of upper and lower calibration curves is improbable.

The confidence interval of practically 100 % was substituted by a confidence interval of 99 %, because levels of confidence higher than 99 % are practically unlikely to attain.[82]

The calibration curves did not cover the experimental findings in few cases, meaning that the respective calculated molar fraction of component i of the product gas $x_{i,\mathrm{P}}$ determined employing the calibration curves lies above the greatest ($x_{i,\mathrm{GC},3}$) or below the smallest ($x_{i,\mathrm{GC},1}$) molar fraction used for GC calibration. If $x_{i,\mathrm{P}} \leq 1.15 \cdot x_{i,\mathrm{GC},3}$ and $x_{i,\mathrm{P}} \geq 0.85 \cdot x_{i,\mathrm{GC},1}$ the regular procedure explained above was applied, whereas for other cases nominal, maximum, and minimum values were recalculated taking appropriate experimental observations into account.

A deviant recalculation was carried out for calculated molar fractions of C_2-hydrocarbons below 100 ppm ($x_{i,\mathrm{GC},1} = 100\ \mathrm{ppm} \quad i = \mathrm{C_2H_6}, \mathrm{C_2H_4}, \mathrm{C_2H_2}$). Here a linear approach for the calibration curves was employed as can be seen in Figure 4-10.

[81] cp. [ISO, 2008], p. 71 et seq.
[82] cp. [ISO, 2008], p. 70

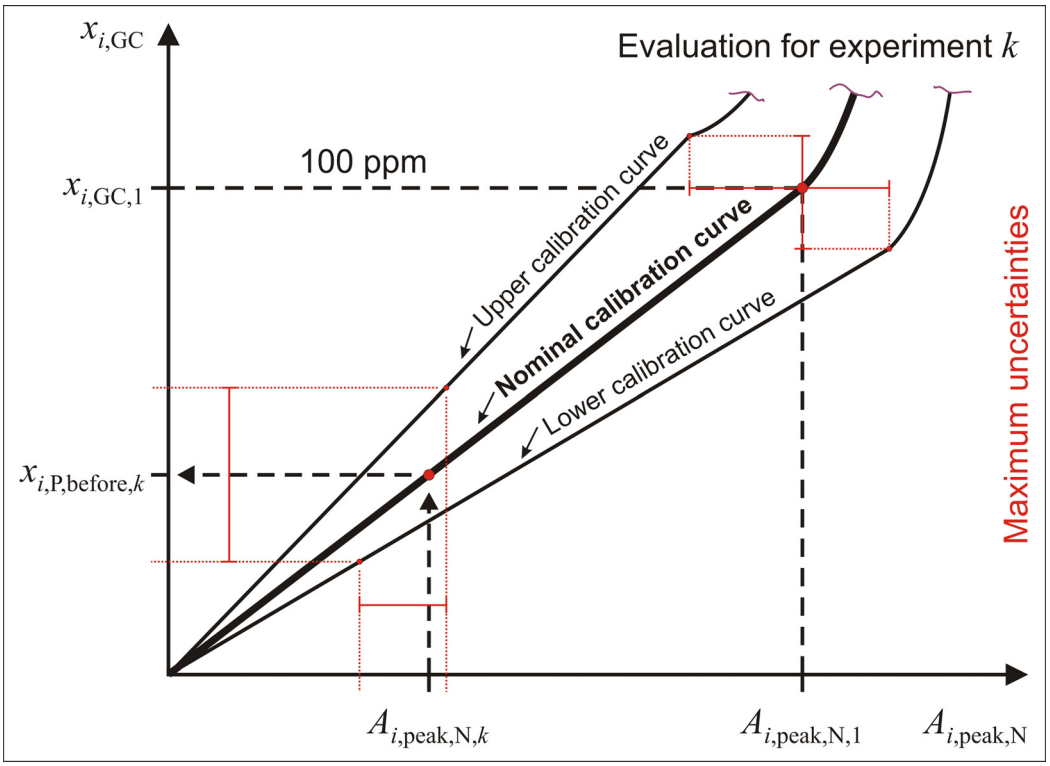

Figure 4-10: Illustration of the definition and the utilization of GC calibration curves for C_2-hydrocarbons which exemplarily refer to the situation before the experiments (molar fractions smaller than the lowest molar fractions employed for the determination of calibration curves).

4.4 General results

The following chapters provide general results of the executed experiments with argon and helium as dilution gas, respectively. Experimental findings are mostly provided in terms of conversion of methane and yield of hydrogen as well as of the C_2-hydrocarbons. Usually numerous graphs are shown in a particular diagram along with estimated standard uncertainties in order to allow a rough overview of results and trends. More detailed information can be found in Appendix C.

4.4.1 General results of experiments with argon as dilution gas

Experimental results concerning the conversion of methane practically cover the whole range between marginal and full advance. As can be seen in Figure 4-11 the conversion of methane clearly increases with residence time and nominal furnace temperature, which somehow corresponds to temperatures inside the reactor. A maximum conversion of 99.8 % was achieved at 1600 °C nominal furnace temperature and a residence time of 0.0547 s, whereas a minimum value of 1.20 % was obtained at 1300 °C and 0.0275 s, in both cases based on 2 % initial molar fraction of methane. The initial molar fraction of methane moderately influences the conversion of methane determined for 1200 °C nominal furnace temperature and medium

residence times; however, for all other considered conditions minor dependencies have to be reported respecting the applied range.

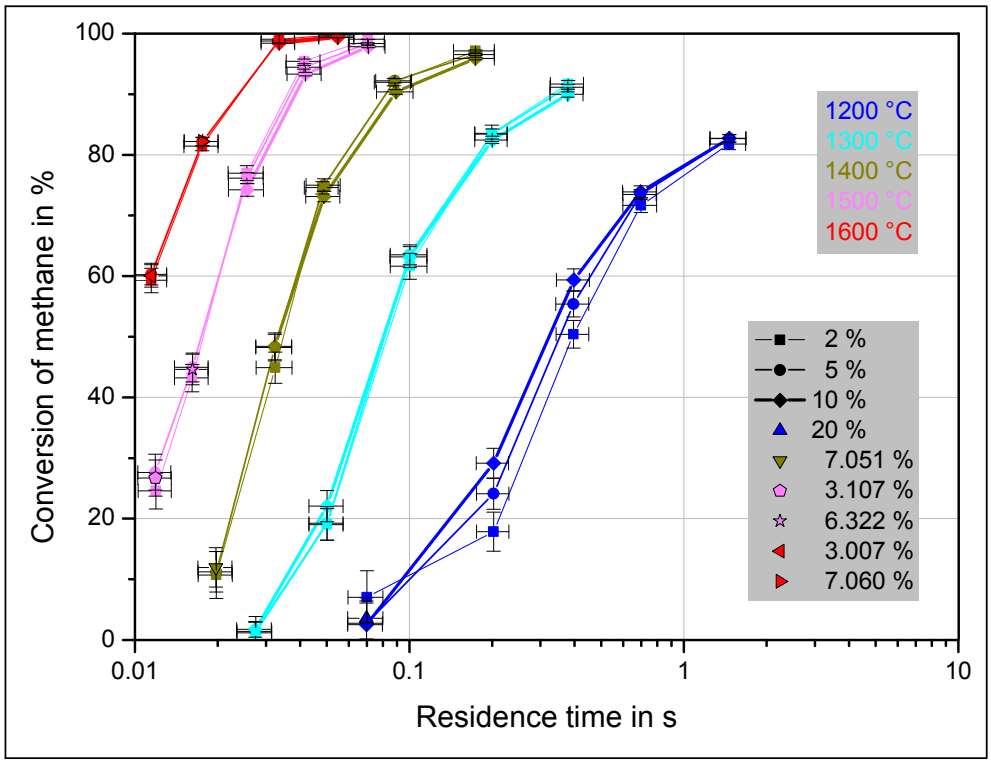

Figure 4-11: Conversion of methane as a function of the residence time, the nominal furnace temperature, and the initial molar fraction of methane. Dilution gas: argon. Indicators of uncertainty refer to maximum uncertainty for the residence time and to standard uncertainty for the conversion.

The yield of hydrogen is depicted in Figure 4-12 as a function of the residence time, the nominal furnace temperature, and the initial molar fraction of methane. Similar to the conversion of methane, the yield of hydrogen rises when the nominal furnace temperature or the residence time increases. The initial molar fraction of methane affects the yield of hydrogen more strongly than the conversion of methane but still at little extend. Obtained values lie between 0.546 % and 95.4 % characterized by lower levels compared to the conversion of methane due to the presence of byproducts at the outlet of the reactor.

Ethane, ethene, and ethyne are byproducts, whose portions of the product gas were analyzed by gas chromatography. Small fractions of ethane could be found in the outlet gas mixture. However, the yield of ethane never exceeds 0.927 % and considerably decreases with rising residence time and nominal furnace temperature, as can be extracted from Figure 4-13. By trend, higher initial molar fractions of methane lead to lower yields of ethane at otherwise identical reaction conditions.

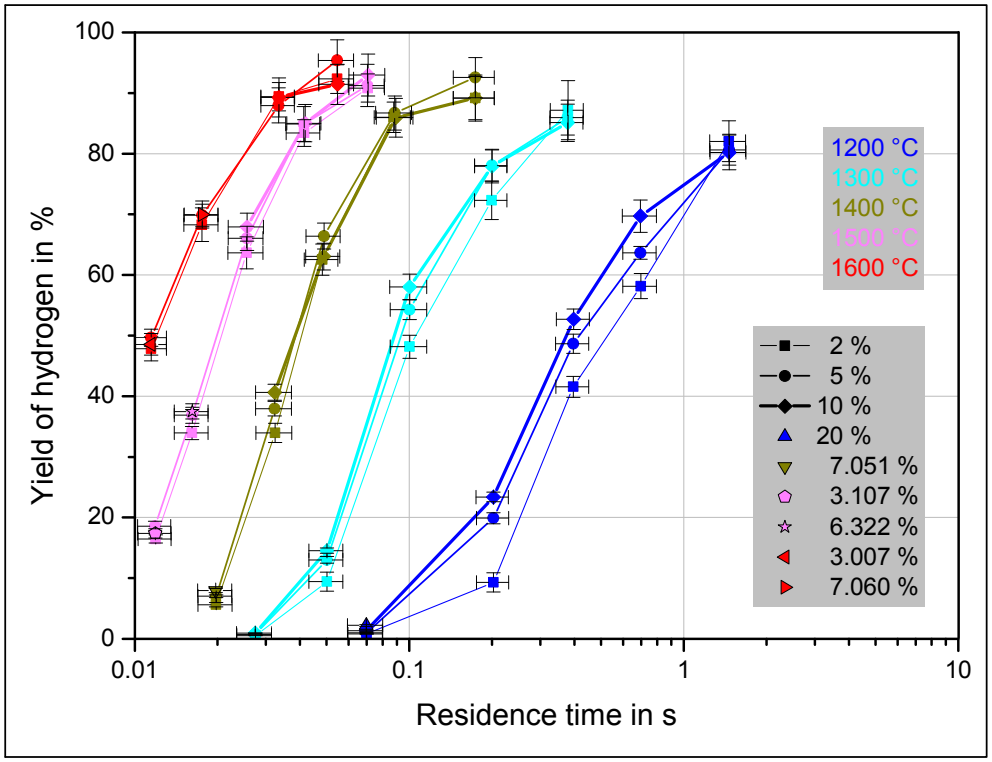

Figure 4-12: Yield of hydrogen as a function of the residence time, the nominal furnace temperature, and the initial molar fraction of methane. Dilution gas: argon. Indicators of uncertainty refer to maximum uncertainty for the residence time and to standard uncertainty for the yield.

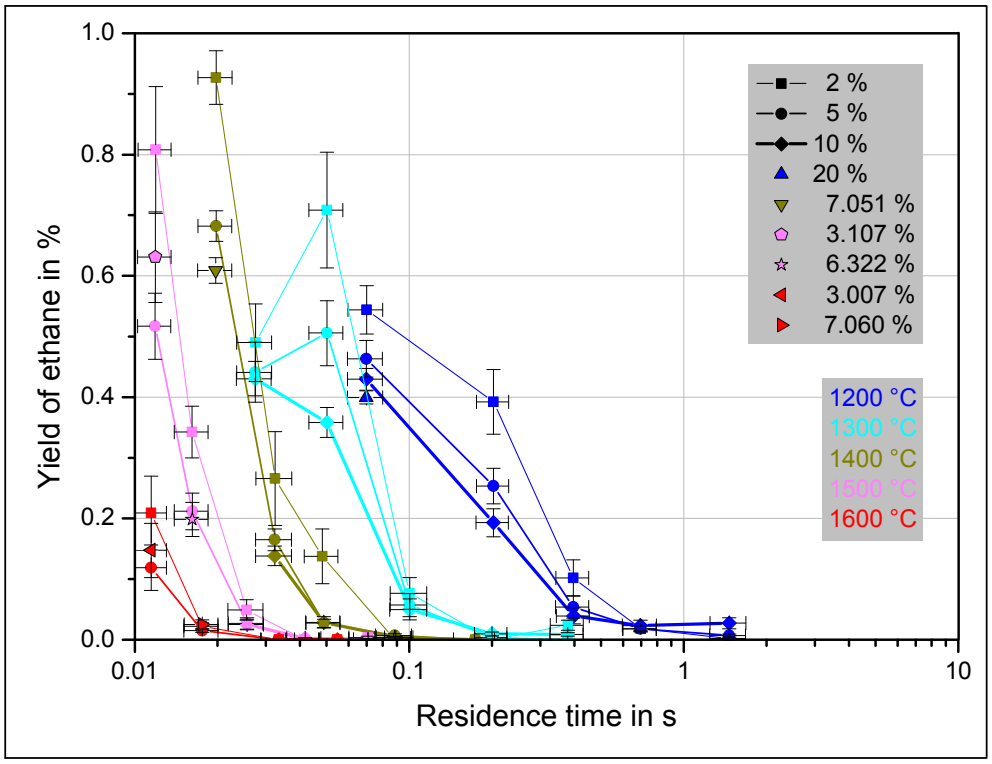

Figure 4-13: Yield of ethane as a function of the residence time, the nominal furnace temperature, and the initial molar fraction of methane. Dilution gas: argon. Indicators of uncertainty refer to maximum uncertainty for the residence time and to standard uncertainty for the yield.

A maximum yield of 4.71 % ethene was achieved at 1300 °C nominal furnace temperature and 2 % initial molar fraction of methane. Explicit dependencies of the yield of ethene on the residence time, the initial molar fraction of methane, and the nominal furnace temperature can not be identified as becomes clear in Figure 4-14. The graphs for 1200 °C, 1300 °C, and partly 1400 °C indicate that a local maximum may exist at moderate residence times and that values may stabilize at increased residence times, reaching higher levels when higher initial molar fractions of methane were applied. A local maximum is probably not shown by graphs for higher nominal furnace temperatures, because the applied residence times might not be low enough to reach that region.

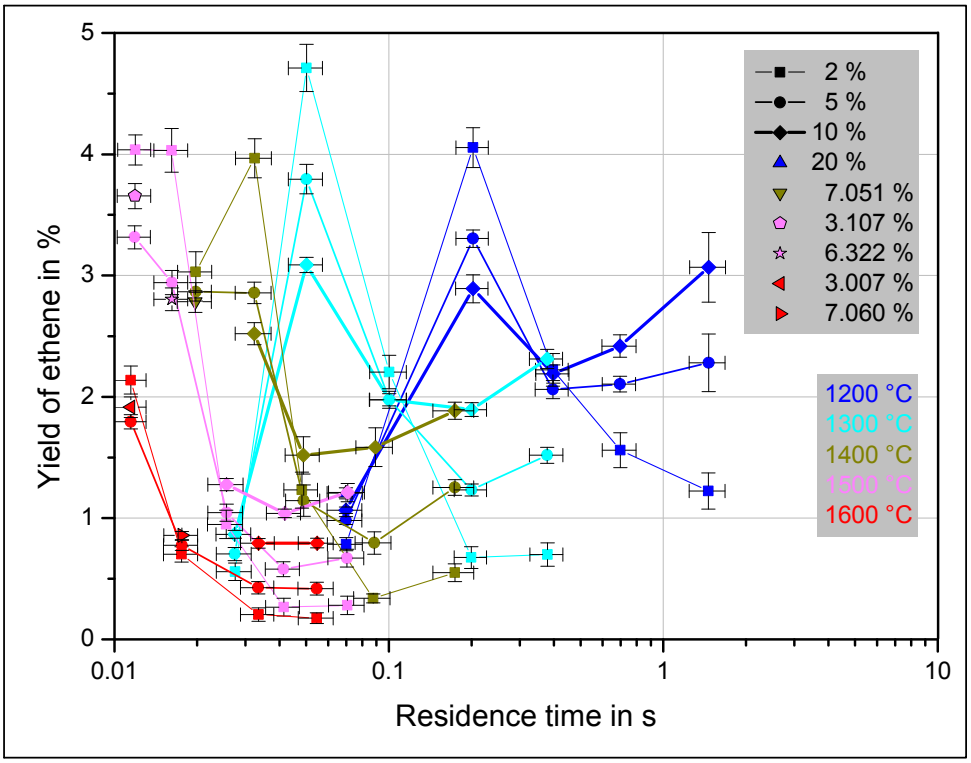

Figure 4-14: Yield of ethene as a function of the residence time, the nominal furnace temperature, and the initial molar fraction of methane. Dilution gas: argon. Indicators of uncertainty refer to maximum uncertainty for the residence time and to standard uncertainty for the yield.

Figure 4-15 depicts the yield of ethyne, which is by far the most important byproduct. After passing the initial stage of the splitting reactions at low residence times the yield of ethyne approaches remarkable high levels up to 59.5 %. Mostly also here a maximum is reached at moderate residence times. However, due to the slight slope of the graphs in the region right-hand the maximum, large amounts of ethyne form part of the product gas even at high residence times. Usually the yield of ethyne decreases with rising initial molar fraction of methane, presumably due to a better promotion of the final steps of the splitting reactions resulting from an increased probability of collision and somewhat higher concentrations of generated carbon providing reactive sites.

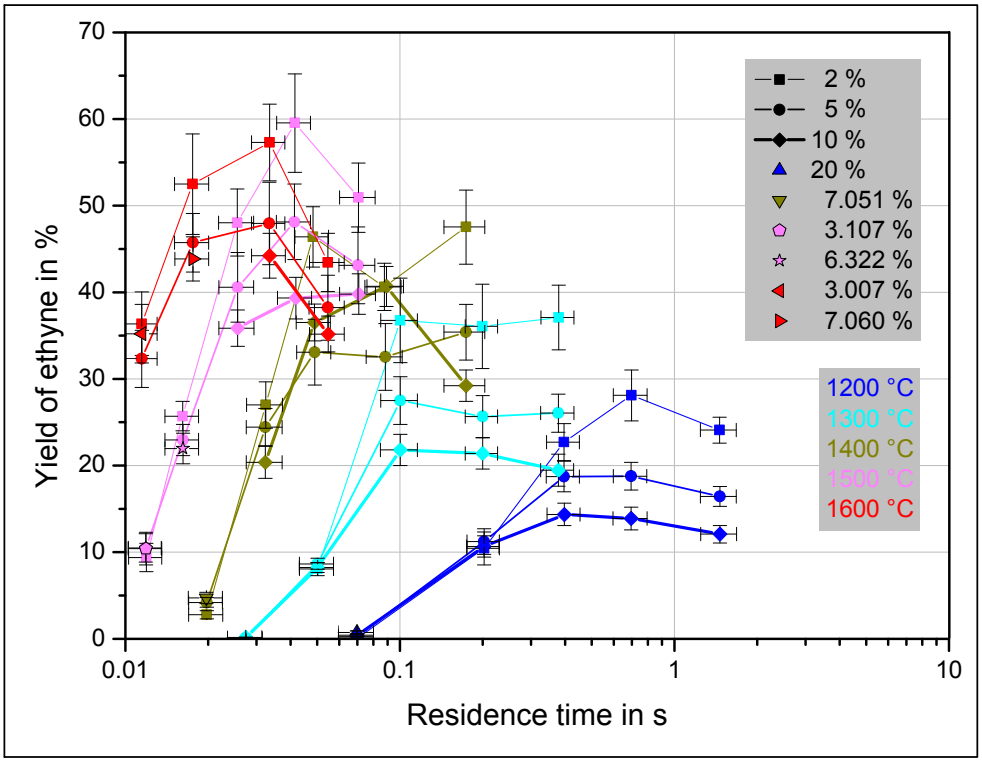

Figure 4-15: Yield of ethyne as a function of the residence time, the nominal furnace temperature, and the initial molar fraction of methane. Dilution gas: argon. Indicators of uncertainty refer to maximum uncertainty for the residence time and to standard uncertainty for the yield.

The conversion of methane and the yields of considered species are shown together in Figure 4-16 exemplarily for 1300 °C nominal furnace temperature and 10 % initial molar fraction of methane. Similar to results based on other reaction conditions, methane starts to decompose as soon as the residence time is high enough while hydrogen and C_2-hydrocarbons are generated. For lowest residence times the yield of ethane is higher than the yield of ethyne. The shapes of the graphs propose that the yield of ethane also exceeds the yield of ethene for residence times lower than the residence times considered here, suggesting that ethane is one of the first intermediates of a complex decomposition mechanism. While ethane disappears very fast, the yields of ethene and ethyne first reach a maximum and then fall slightly with residence time. Quite low levels of yield of ethene can be reported. Contrariwise, residence times considered in this work are not high enough for even nearly total conversion of ethyne. Accordingly, considerable fractions of hydrogen and carbon atoms form part of an intermediate, not of the final and desired products. In order to increase the amount of hydrogen and particulate carbon in the product flow, clearly longer residence times should be taken into consideration.

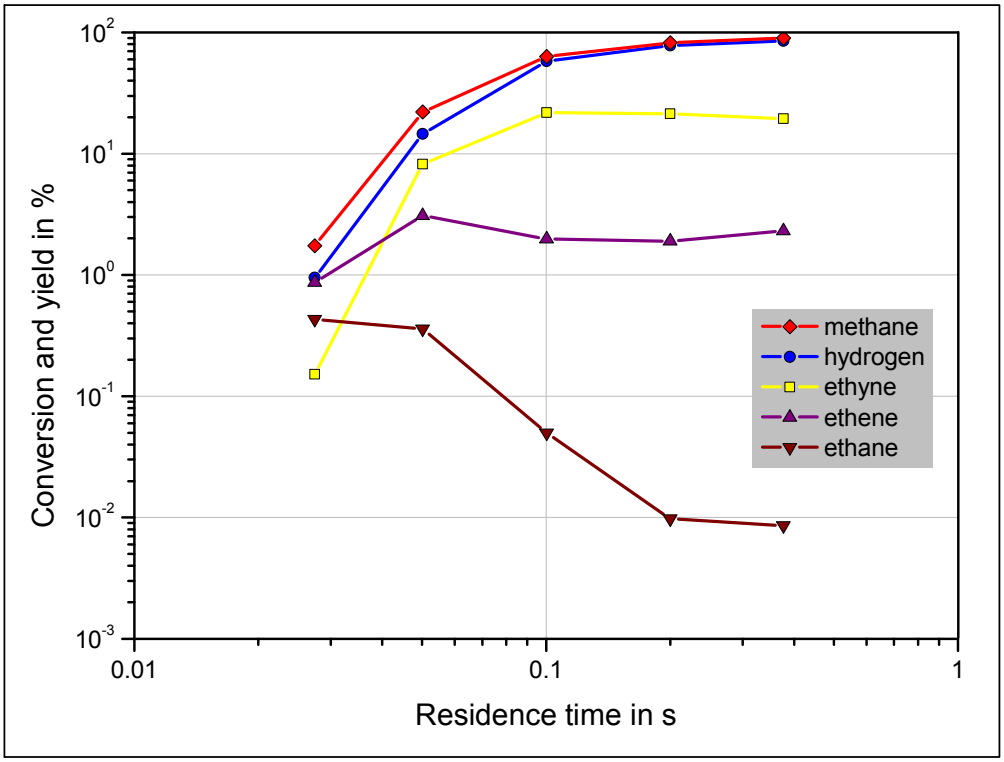

Figure 4-16: Conversion of methane as well as yields of hydrogen, ethane, ethene, and ethyne as a function of the residence time for 1300 °C nominal furnace temperature of and 10 % initial molar fraction of methane. Dilution gas: argon.

The fraction of recovered hydrogen atoms in the considered species $\Delta\dot{n}_{\mathrm{H,rel}}$ arising from

$$\Delta\dot{n}_{\mathrm{H,rel}} = \frac{\dot{n}_{\mathrm{H,P}} - \dot{n}_{\mathrm{H,0}}}{\dot{n}_{\mathrm{H,0}}} = \frac{4\cdot\dot{n}_{\mathrm{CH_4,P}} + 2\cdot\dot{n}_{\mathrm{H_2,P}} + 6\cdot\dot{n}_{\mathrm{C_2H_6,P}} + 4\cdot\dot{n}_{\mathrm{C_2H_4,P}} + 2\cdot\dot{n}_{\mathrm{C_2H_2,P}} - 4\cdot\dot{n}_{\mathrm{CH_4,0}}}{4\cdot\dot{n}_{\mathrm{CH_4,0}}} \qquad \textbf{Equation 74}$$

is a measure of the balance of H-atoms. Ideal agreement between ingoing and outgoing molar flows of H-atoms would lead to $\Delta\dot{n}_{\mathrm{H,rel}} = 0$. In opposition to the ideal case, determined values are distributed within an interval defined by the limits - 5.7 % and + 6.9 % as can be seen in Figure 4-17. Since a source of hydrogen atoms inside the reactor is rejected, positive values are a result of the uncertainty of initial molar flows of argon and methane. Moreover, perfect agreement lies in range of every determined value, when uncertainties are taken into account. Consequently, it becomes clear that the respected species are the most important carriers of H-atoms in the product flow and that the H-balance is practically satisfied.

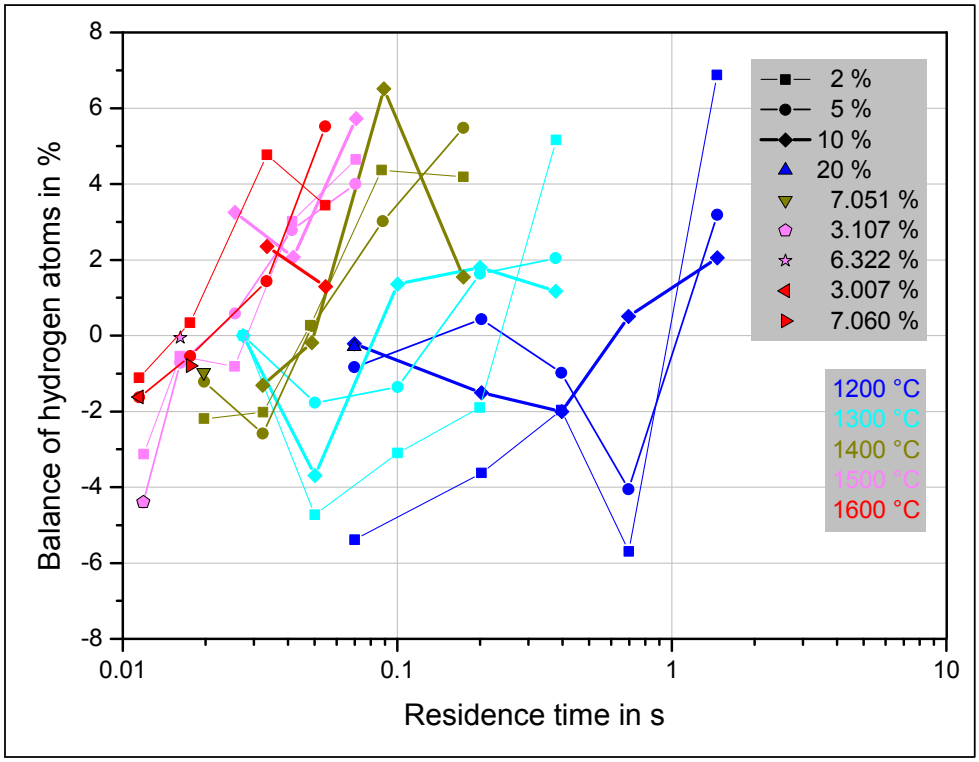

Figure 4-17: Balance of hydrogen atoms as a function of the residence time, the nominal furnace temperature, and the initial molar fraction of methane. Dilution gas: argon.

The approximated molar fraction of argon in the product gas $x_{\mathrm{Ar,P,approximated}}$ was calculated according to

$$x_{\mathrm{Ar,P,approximated}} = 1 - \sum_i x_{i,\mathrm{P}} \qquad i = \mathrm{CH_4}, \mathrm{H_2}, \mathrm{C_2H_6}, \mathrm{C_2H_4}, \mathrm{C_2H_2} \qquad \textbf{Equation 75}$$

assuming that argon, hydrogen, methane, and the C_2-hydrocarbons are the only components of the product gas. The relative discrepancy between the approximated and measured molar fraction of argon in the product gas $\Delta x_{\mathrm{Ar,P,rel}}$ was determined by

$$\Delta x_{\mathrm{Ar,P,rel}} = \frac{x_{\mathrm{Ar,P,approximated}} - x_{\mathrm{Ar,P}}}{x_{\mathrm{Ar,P}}} \qquad \textbf{Equation 76}$$

and gives information about the molar fraction of species not considered in this work at the reactor outlet. Although values range from - 1.0 % to + 1.3 % (see Figure 4-18), a good estimation of the relative difference is 0 % confirming that the considered species constitute major part of the gaseous product flow and that only low fractions of other compounds may be present at the outlet of the reactor. Considering maximum uncertainty, perfect agreement of

approximated and measured molar fraction of argon in the product gas is possible for every reaction condition.

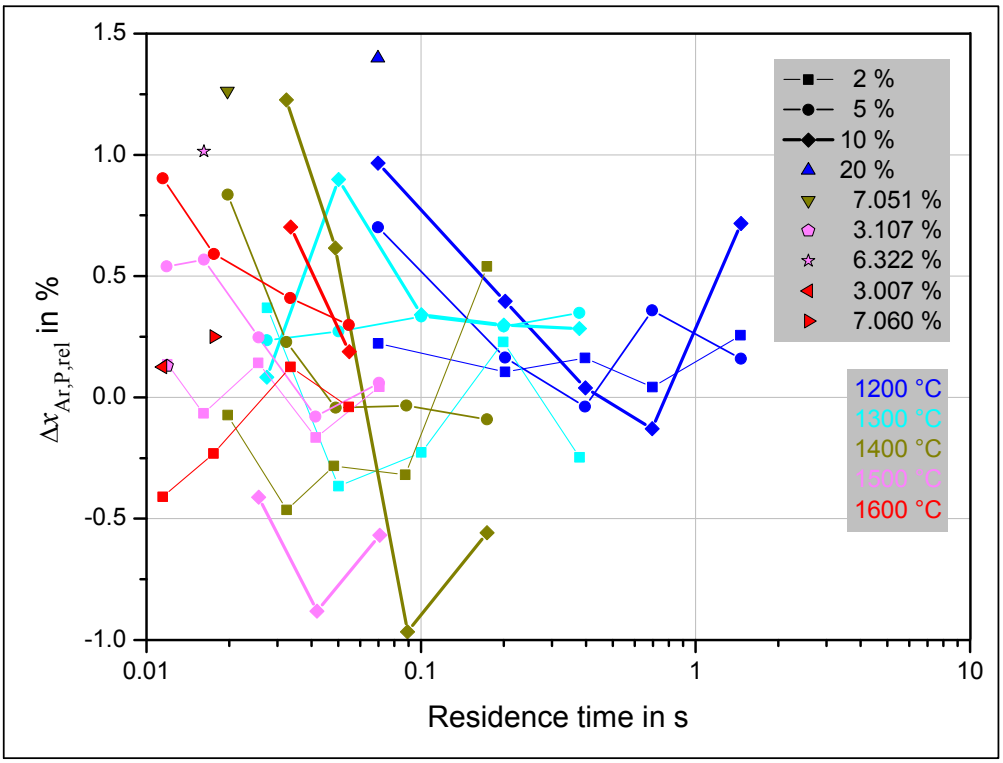

Figure 4-18: Relative difference between approximated (as 1 minus the sum of molar fractions of considered species except for argon) and measured molar fractions of argon in the product gas as a function of the residence time, the nominal furnace temperature and the initial molar fraction of methane.

A measure of cleanliness of the product flow is given by $Y_{C_2\text{-HC},H_2,rel}$, the yield of C_2-hydrocarbons $Y_{C_2\text{-HC}}$ related to the yield of hydrogen Y_{H_2}, following

$$Y_{C_2\text{-HC},H_2,rel} = \frac{Y_{C_2\text{-HC}}}{Y_{H_2}} \quad . \qquad \textbf{Equation 77}$$

The related yield decreases with residence time, nominal furnace temperature, and initial molar fraction of methane as can be extracted from Figure 4-19. As a result high temperatures, a high initial fraction of methane, and a sufficiently high residence time should be ensured in order to generate a product flow dominated by the desired products, hydrogen as well as carbon, and only marginally contaminated by intermediates.

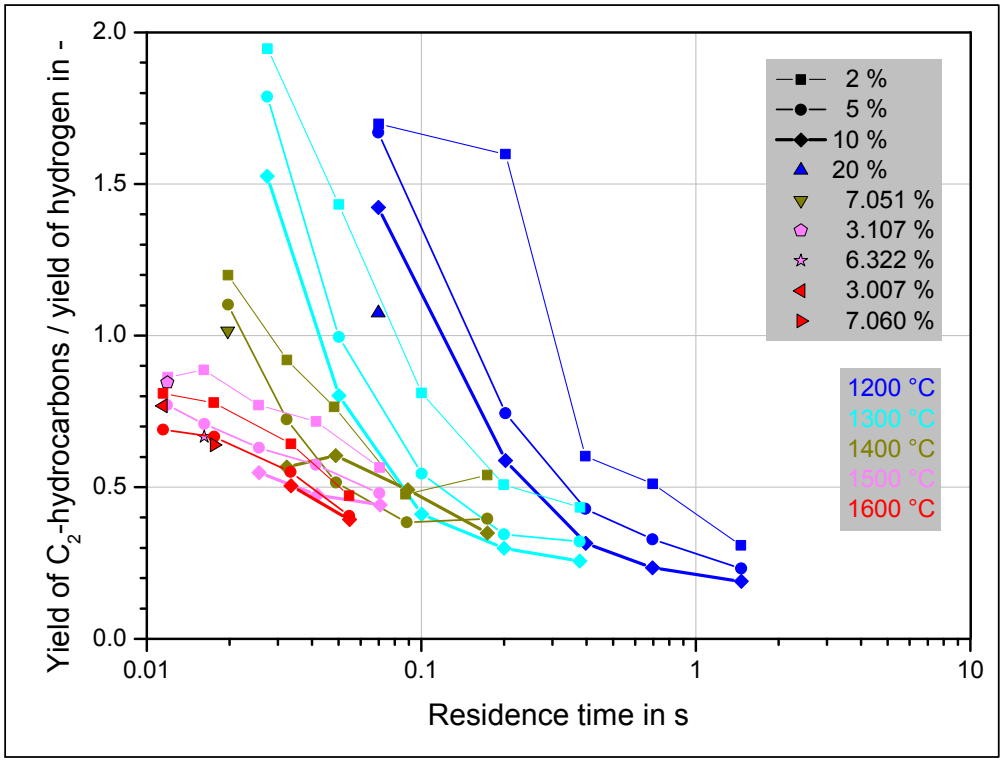

Figure 4-19: Yield of C_2-hydrocarbons related to the yield of hydrogen as a function of the residence time, the initial molar fraction of methane, and the nominal furnace temperature. Dilution gas: argon.

4.4.2 General results of experiments with helium as dilution gas

The measurement of the molar fraction of helium in the product gas was not possible, since helium was used as the GC's carrier gas. Presuming that neither argon nor helium undergo a reaction, but only influence the reaction conditions, the good agreement between $x_{\mathrm{Ar,P}}$ and $x_{\mathrm{Ar,P,approximated}}$ stated in Chapter 4.4.1 allows the conclusion that the molar fraction of helium in the product gas $x_{\mathrm{He,P}}$ can be estimated well according to

$$x_{\mathrm{He,P}} = x_{\mathrm{He,P,approximated}} \quad , \qquad \textbf{Equation 78}$$

with

$$x_{\mathrm{He,P,approximated}} = 1 - \sum_i x_{i,\mathrm{P}} \qquad i = \mathrm{CH_4}, \mathrm{H_2}, \mathrm{C_2H_6}, \mathrm{C_2H_4}, \mathrm{C_2H_2} \quad , \qquad \textbf{Equation 79}$$

and that the limits of $x_{\mathrm{He,P}}$ arise consistent with the maximum and minimum value of $\Delta x_{\mathrm{Ar,P,rel}}$ provided before. Onward calculations were carried out appropriate to argon experiments.

The conversion of methane and the yield of hydrogen calculated for experiments with helium as the dilution gas are shown in Figure 4-20 and Figure 4-21, respectively, as a function of the nominal furnace temperature, the initial molar fraction of methane, and the residence time. Similar to the results gained in experiments with argon, conversion and yield increase with rising residence time as well as with rising nominal furnace temperature and vary slightly depending on the initial fraction of methane. As a result of the better heat transfer characteristics of helium, the conversion of methane and the yield of hydrogen reach higher values for experiments with helium compared to experiments with argon regarding similar reaction conditions.

Analogous to experiments with argon, only low yields of ethane and ethene were achieved as can be extracted from Figure 4-22 and Figure 4-23, respectively. Generally the yields decrease with increasing nominal furnace temperature and residence time. The estimated yields of ethyne covering the range from 11.7 % to 62.5 % are presented in Figure 4-24. Clear dependencies on the temperature and the residence time can not be reported due to the low amount of available data. However, a maximum yield at moderate residence times comparable to the graphs determined for experiments with argon is possible. By trend, higher molar fractions of methane cause lower yields of all C_2-hydrocarbons.

The balance of hydrogen atoms was examined according to Equation 74. As can be seen in Figure 4-25 the balance of hydrogen atoms is reasonably satisfied also for experiments with helium as dilution gas.

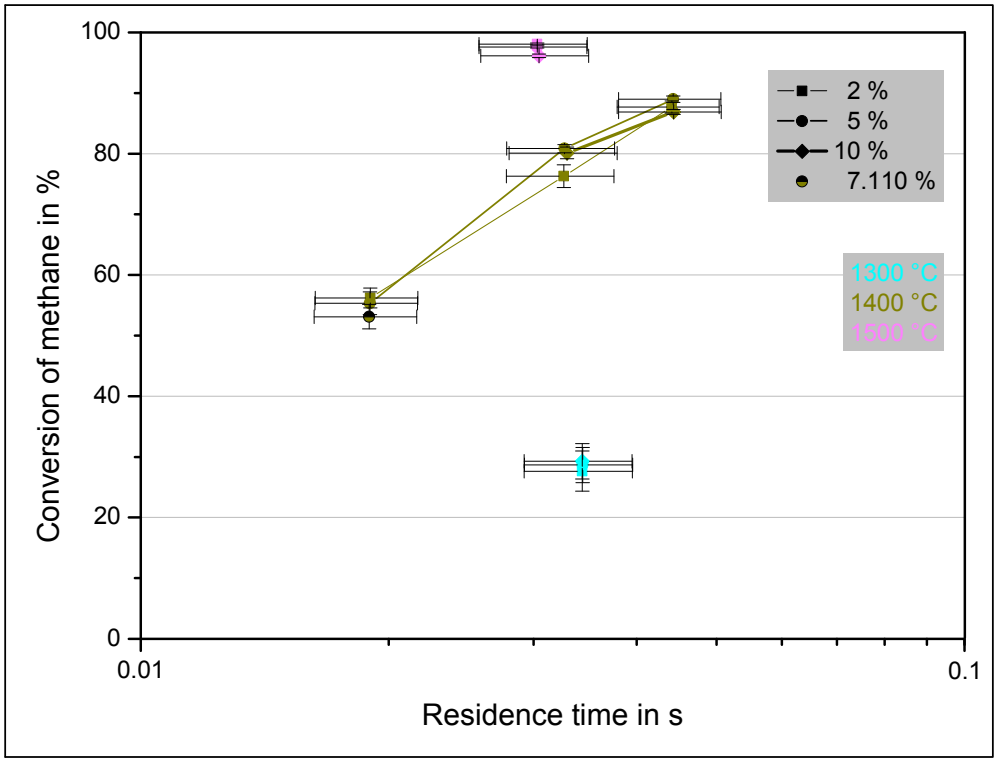

Figure 4-20: Conversion of methane as a function of the residence time, the nominal furnace temperature, and the initial molar fraction of methane. Dilution gas: helium. Indicators of uncertainty refer to maximum uncertainty for the residence time and to standard uncertainty for the conversion.

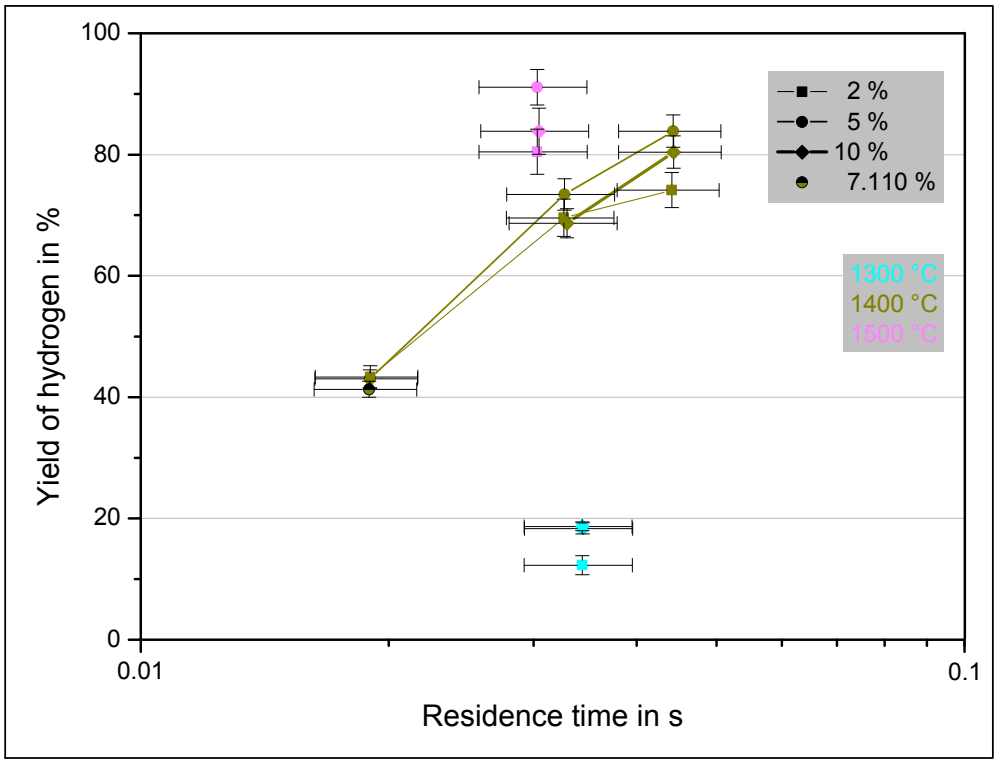

Figure 4-21: Yield of hydrogen as a function of the residence time, the nominal furnace temperature, and the initial molar fraction of methane. Dilution gas: helium. Indicators of uncertainty refer to maximum uncertainty for the residence time and to standard uncertainty for the yield.

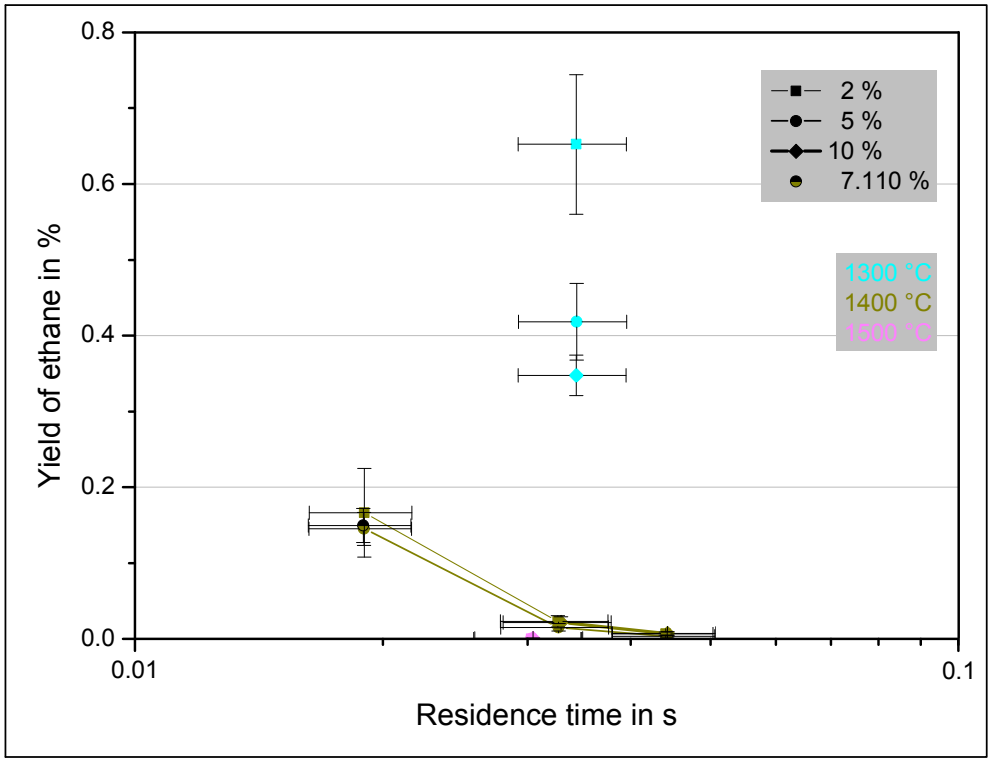

Figure 4-22: Yield of ethane as a function of the residence time, the nominal furnace temperature, and the initial molar fraction of methane. Dilution gas: helium. Indicators of uncertainty refer to maximum uncertainty for the residence time and to standard uncertainty for the yield.

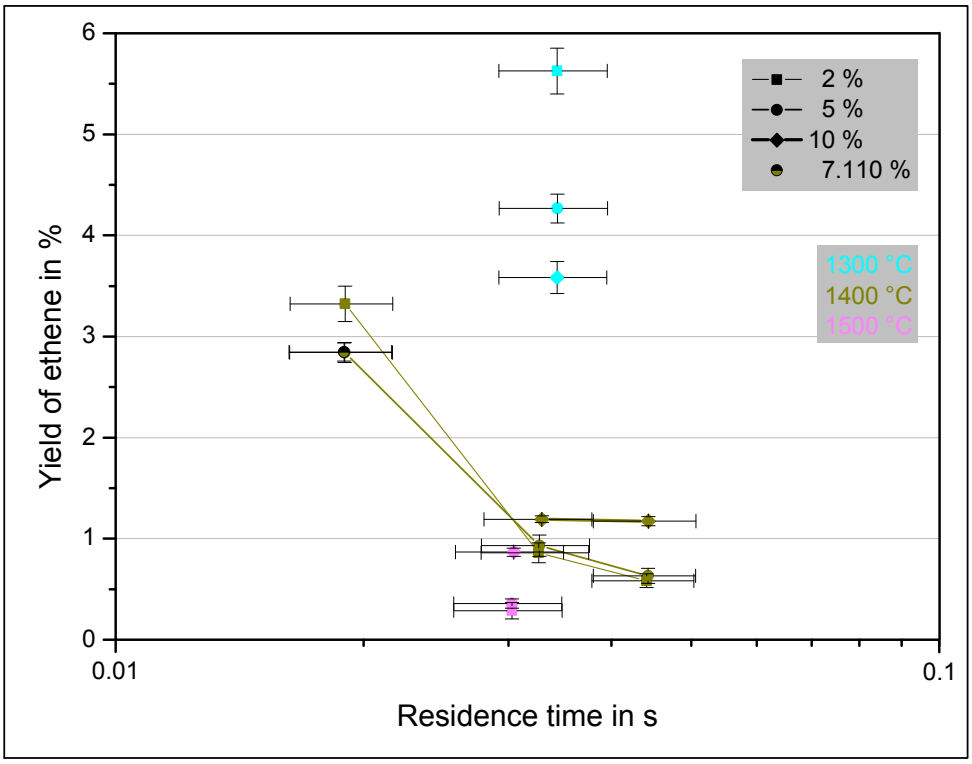

Figure 4-23: Yield of ethene as a function of the residence time, the nominal furnace temperature, and the initial molar fraction of methane. Dilution gas: helium. Indicators of uncertainty refer to maximum uncertainty for the residence time and to standard uncertainty for the yield.

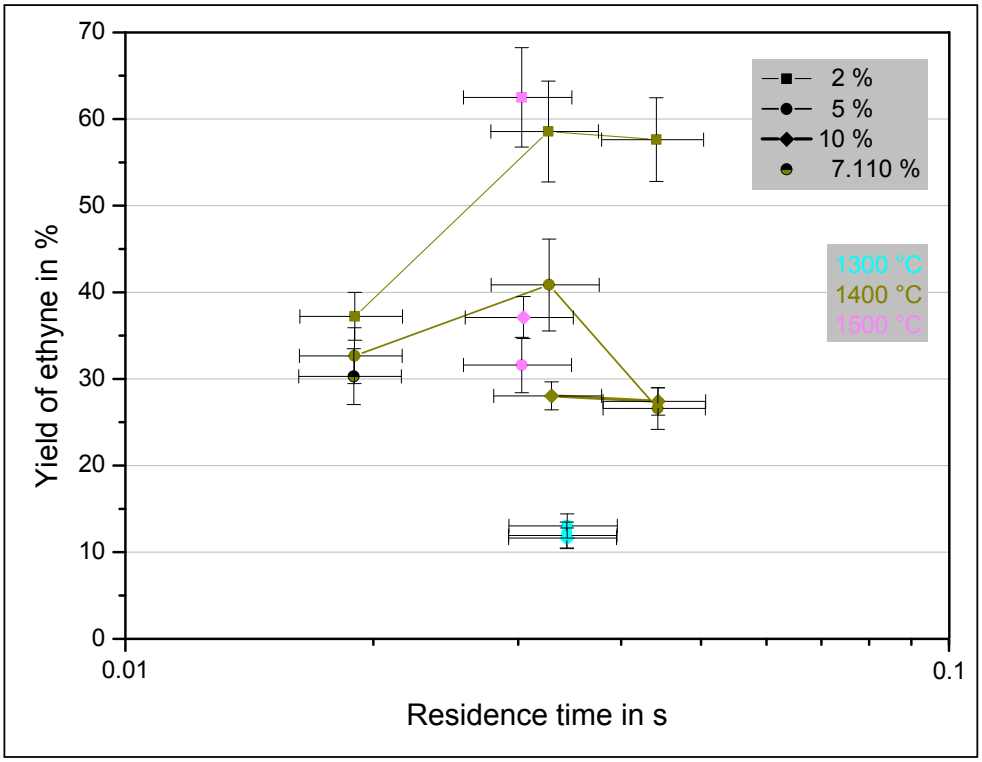

Figure 4-24: Yield of ethyne as a function of the residence time, the nominal furnace temperature, and the initial molar fraction of methane. Dilution gas: helium. Indicators of uncertainty refer to maximum uncertainty for the residence time and to standard uncertainty for the yield.

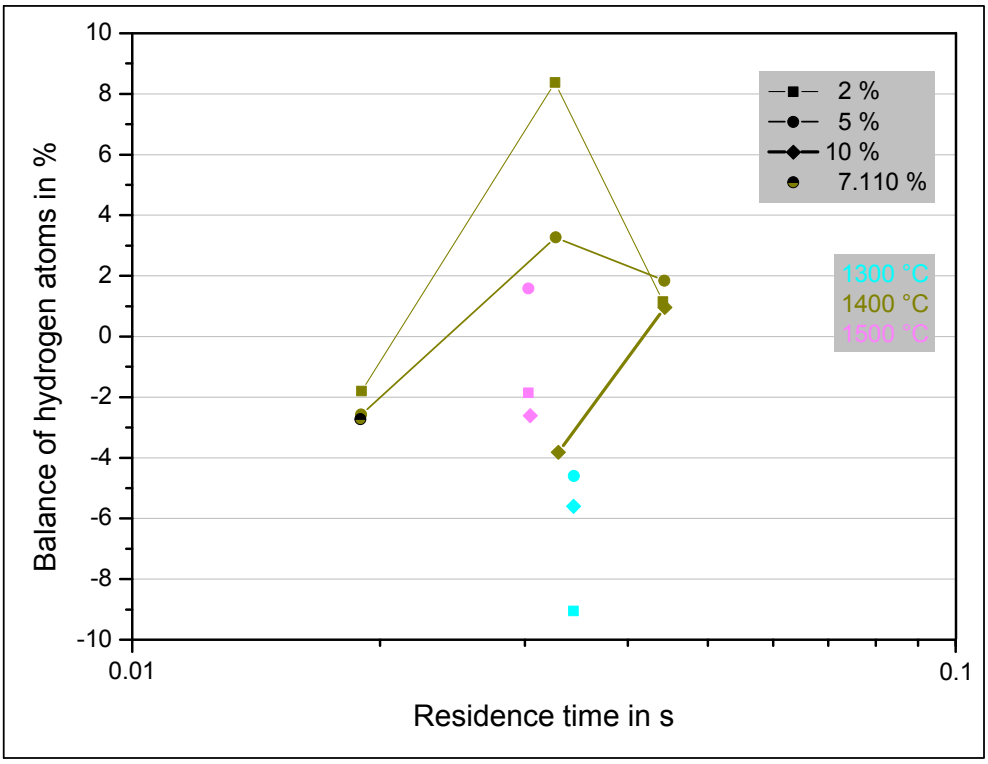

Figure 4-25: Balance of hydrogen atoms as a function of the residence time, the nominal furnace temperature, and the initial molar fraction of methane. Dilution gas: helium.

4.5 Measurement of temperature

A self-made thermocouple type S was used for the measurement of the temperature inside the reactor. It consists of two metal legs which are welded one-sided.[83] The voltage between the legs at the cold junction is finally a function of the temperature of the measuring junction. An alumina capillary tube was employed in order to avoid contact of the two metal legs. Furthermore, an aluminum oxide tube[84] closed at one side protects the thermocouple from reactive products of the decomposition of methane as well as from abrasive contact with the inner wall of the reactor and carbon particles. Figure 4-26 shows the assembly of the thermocouple.

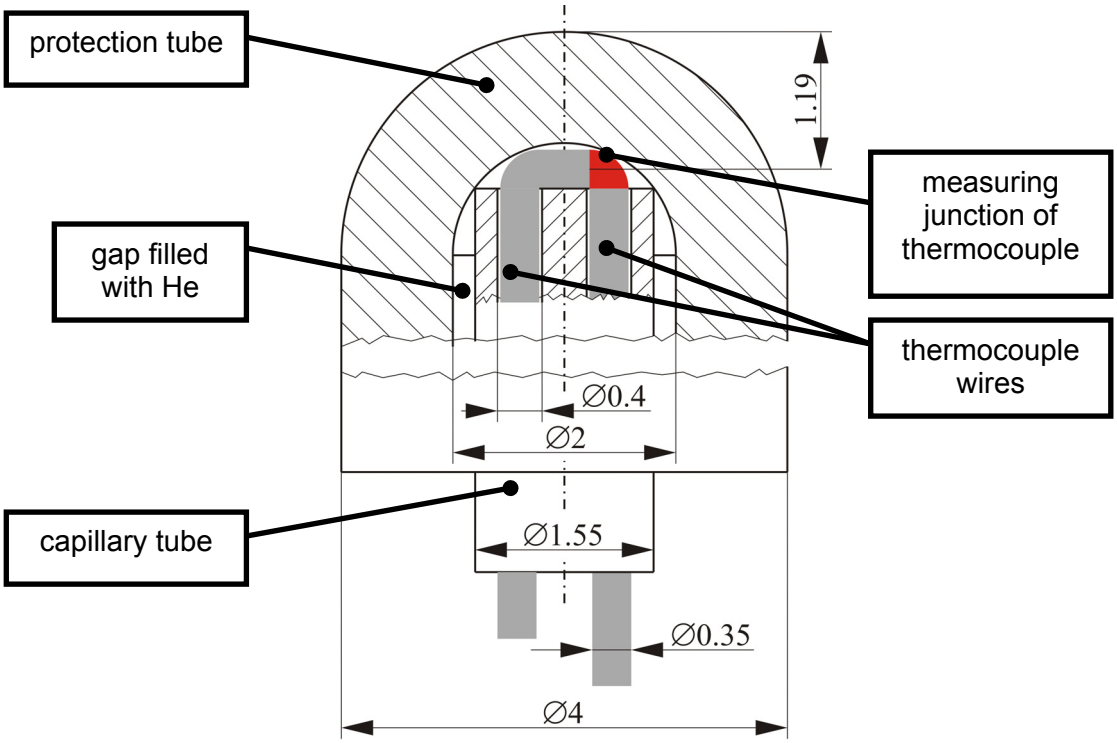

Figure 4-26: Assembly of the self-made thermocouple employed for temperature measurement inside the tube reactor (dimensions in mm)

Temperature profiles were determined for each set of nominal furnace temperature and residence time moving the thermocouple by steps of 20 mm through the reactor, which was passed by the dilution gas used in the particular cracking experiment, assuring that the total standard volume flow corresponds to the one of the respective experiment. The exclusive employment of the dilution gas instead of the particular gas mixture had several reasons:

[83] leg (+): 90 % Pt and 10 % Rh, leg (-): 100 % Pt; DIN EN 60584-2: 1994, class 1. Measuring junction welded by Janine Schneider (DLR WF-WP). Thermocouple calibrated by Claus-Jürgen Kröder (DLR WF-HF).
[84] Manufacturer: FRIATEC AG, Mannheim, Germany.

- The determination of temperature profiles often took more than two hours. Usually clogging would have occurred during that time.

- The deposition of generated carbon particles would have changed the optical properties of the thermocouple and finally influenced the temperature measurement.

- The temperature changes at position 320 mm after adding methane in a cracking experiment were moderate, suggesting that temperature profiles gained for the dilution gas flow are very similar to temperature profiles developed in the cracking experiments. This was confirmed by further observations at other positions in the reactor during reference experiments. Thus, the sole consideration of temperature profiles for a pure dilution gas flow offered a reasonable possibility of reduction of experimental time.

The measurement of temperature profiles started at position 320 mm and ended at the highest possible position of the thermocouple, which is position 0 mm, leading to temperature profiles with a length of 320 mm. All positions refer to the highest position of the inner wall of the protection tube, 1 mm (the wall-thickness of the protection tube) away from the tip of the thermocouple and approximately corresponding to the position of the measuring junction. By inclining the thermocouple, a maximum and a minimum temperature, which differ in part significantly, could be quantified at every axial position. An illustrating sketch is shown in Figure 4-27.

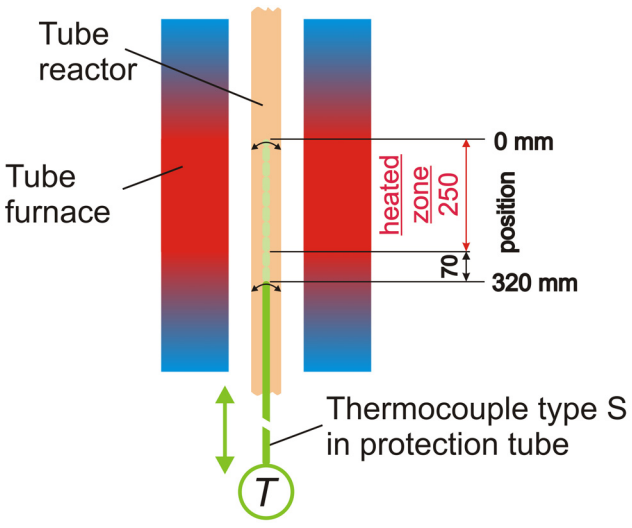

Figure 4-27: Start position, end position, and length of a measured temperature profile (dimensions in mm)

Additionally, the outer wall temperatures at the entrance of the reactor, matching the upper edge of the inlet water cooler, and at the outlet of the reactor, matching the lower edge of the outlet water cooler, were measured using a thermocouple type K. It is assumed that the temperatures inside the reactor are similar to those of the outer wall at the entrance and the

outlet of the reactor. The axial temperature drop at these positions was estimated using experimental experience and measurements. In order to approximate the temperature profile between the measured temperature profile mostly within the heated region of the reactor and the temperatures at the inlet and the outlet of the reactor, respectively, a 3rd order polynomial fit was used. Therefore 2 to 4 certain high temperatures nearest to the inlet or the outlet were employed beside the temperatures at the inlet and outlet. At very low flow rates the 3rd order polynomial fit might lead to higher temperatures for the profile of minimum temperatures compared to the profile of maximum temperatures at the entrance of the reactor. In these cases, however, the temperatures only differ not more than 3 K and an average value is used for both profiles. This procedure results in a quite reasonable shape for the overall temperature profile starting at the inlet and ending at the outlet of the reactor. In very few cases the temperature profiles were smoothed at certain positions by calculating plausible temperatures based on the collectivity of measured temperatures. Figure 4-28 gives an example of temperature profiles determined following the aforementioned procedure.

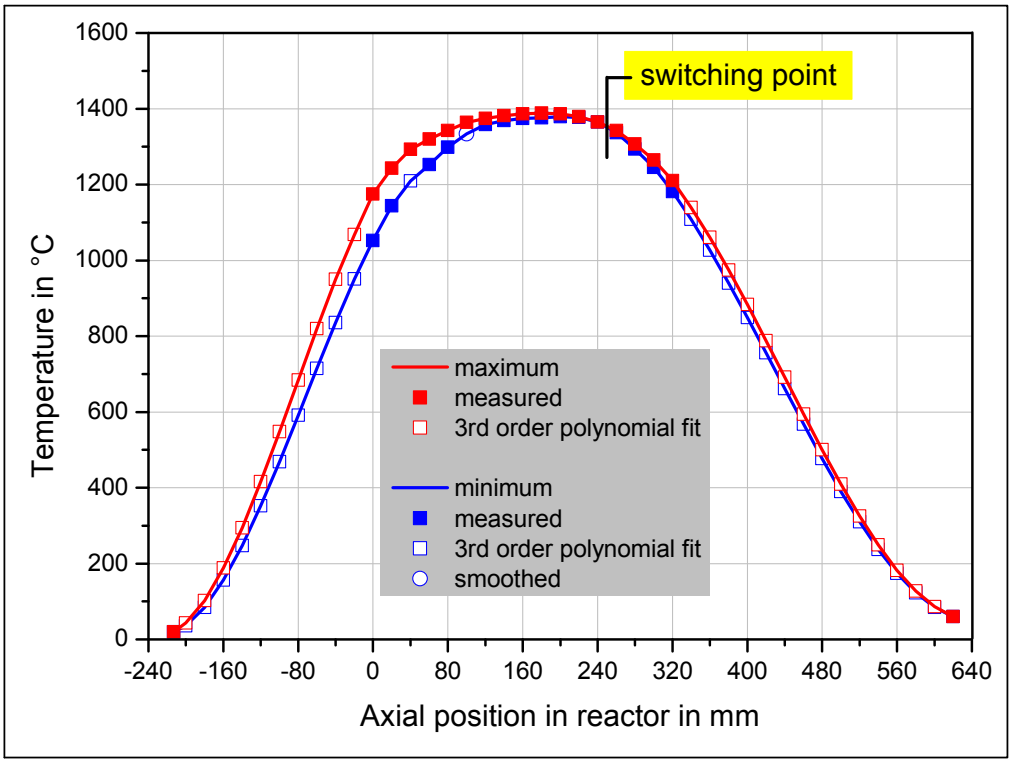

Figure 4-28: Profiles of minimum and maximum temperatures (1400 °C nominal furnace temperature and 2600 sccm nominal standard volume flow of Ar, average pressure at the reactor inlet: 1.031 bar, average pressure at the reactor outlet: 1.014 bar)

Considering the idea of a real externally heated tube reactor, one realizes that there is not only an axial temperature profile but also a radial temperature profile. Near the inlet of the reactor the wall of the reactor is hotter than the fluid passing it, whereas at the outlet of the reactor the situation is contradictory. At a certain axial position, at the here called switching point, the temperatures of wall and center of the reactor should be practically identically. Temperatures of

the maximum temperature profile are consequently assigned to the temperatures measured by the thermocouple in wall position and temperatures of the minimum temperature profile are assigned to the temperatures measured by the thermocouple in center position between the inlet of the reactor and the switching point. Downstream the switching point temperatures are allocated the other way round.

The measurement chain concerning the measurement of the temperature is shown in Figure 4-29. Similar to the measurement chain of the pressure, the output signal of the measuring device was interpreted by the data acquisition system. However, a transformation of the signal in the data acquisition system was not required.

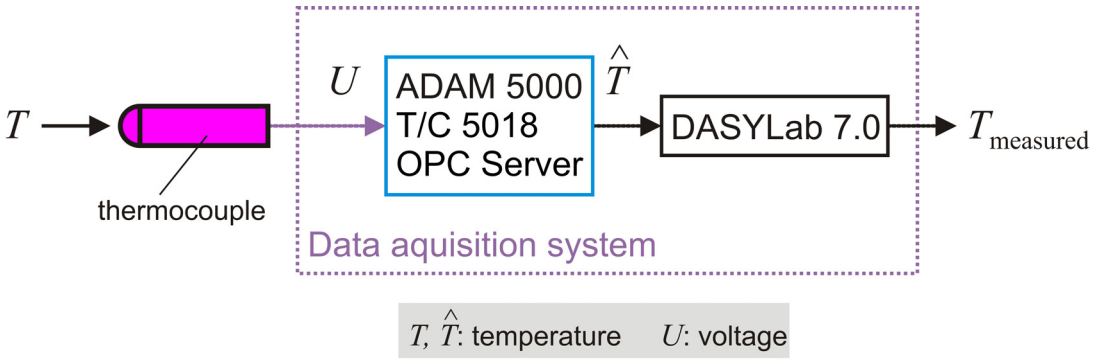

Figure 4-29: Measurement chain of the measurement of temperatures

The positioning of the thermocouple was done manually, resulting in a particular uncertainty regarding the axial position. Since the contact between wall and thermocouple guarantees a high level of accuracy concerning the positioning of the thermocouple in wall position, uncertainty of radial positioning only has to be considered for the center position. Moreover, the elements of the measurement chain contribute to the overall uncertainty. Respective information is summarized in Table 4-12.

Table 4-12: Information about thermocouples and the subsequent measurement chain

Position of thermocouple →	**Inside reactor**	**Inlet and Outlet of reactor**
Type / class of thermocouple according to DIN EN 60584-2: 1994	**S** / 1	**K** / 2
Accuracy[85]	0 °C – 1100 °C: +/- 1.0 K 1100 °C – 1600 °C: +/- [1 + (T/°C - 1100) * 0.003] K	- 40 °C – 333 °C: +/- 2.5 K 333 °C – 1200 °C: +/- 0.0075 * T/°C K
ADAM 5000 module	T/C 5018	
Temperature range	500 °C … 1750 °C	0 °C … 1370 °C
Accuracy[86]	+/- 0.1 % of range: +/- 1.25 K	+/- 0.1 % of range: +/- 1.37 K
Uncertainty due to rounding	+/- 0.5 K	
Uncertainty due to axial positioning	+/- 1 mm (estimated)	
Uncertainty due to radial positioning	+/- 0.5 mm (estimated, center position only)	no (contact with outer wall)

The maximum uncertainty of the temperature measurement in center position $u_{\max}(T_{\mathrm{TC-CP}})$ can be calculated by

$$u_{\max}(T_{\mathrm{TC-CP}}) = u_{\mathrm{TC,max}}(T_{\mathrm{TC-CP}}) + u_{\mathrm{ADAM,max}}(T_{\mathrm{TC-CP}}) + u_{\mathrm{axial,max}}(T_{\mathrm{TC-CP}}) + u_{\mathrm{radial,max}}(T_{\mathrm{TC-CP}}) + u_{\mathrm{round,max}}(T_{\mathrm{TC-CP}}),$$

Equation 80

with the maximum uncertainty resulting from the thermocouple itself $u_{\mathrm{TC,max}}$ and from the data acquisition system $u_{\mathrm{ADAM,max}}$ as well as from rounding $u_{\mathrm{round,max}}$ according to Table 4-12. Maximum uncertainty caused by imprecise axial positioning $u_{\mathrm{axial,max}}$ was estimated following

[85] cp. [TC, 2006], p. 7
[86] cp. [Advantech, 2007], p. 22

$$u_{\text{axial,max}}(T_{\text{TC–CP}}) = \begin{cases} \left|\dfrac{T_{\text{TC–CP}}(z+20\text{ mm}) - T_{\text{TC–CP}}(z)}{20\text{ mm}}\right| \cdot 1\text{ mm} \\ \text{if } \left|T_{\text{TC–CP}}(z+20\text{ mm}) - T_{\text{TC–CP}}(z)\right| \geq \left|T_{\text{TC–CP}}(z) - T_{\text{TC–CP}}(z-20\text{ mm})\right| \\ \left|\dfrac{T_{\text{TC–CP}}(z) - T_{\text{TC–CP}}(z-20\text{ mm})}{20\text{ mm}}\right| \cdot 1\text{ mm} \\ \text{if } \left|T_{\text{TC–CP}}(z+20\text{ mm}) - T_{\text{TC–CP}}(z)\right| < \left|T_{\text{TC–CP}}(z) - T_{\text{TC–CP}}(z-20\text{ mm})\right| \end{cases}, \quad \textbf{Equation 81}$$

whereas maximum uncertainty caused by imprecise radial positioning $u_{\text{radial,max}}$ was calculated by

$$u_{\text{radial,max}}(T_{\text{TC–CP}}) = \frac{\left|T_{\text{TC–CP}} - T_{\text{TC–WP}}\right|}{2\text{ mm}} \cdot 0.5\text{ mm} \quad . \qquad \textbf{Equation 82}$$

It only contributes to uncertainty in negative direction as long as $T_{\text{TC–WP}} \geq T_{\text{TC–CP}}$ and vice versa.

The maximum uncertainty of the temperature measurement in wall position $u_{\text{max}}(T_{\text{TC–WP}})$ was assessed similarly employing Equation 80 and Equation 81 rejecting $u_{\text{radial,max}}(T_{\text{TC–WP}})$, the maximum uncertainty caused by imprecise radial positioning, as stated above.

Figure 4-30 represents an example for temperature profiles determined for the temperatures measured by the thermocouple in wall position and in center position together with the position of the switching point. The maximum uncertainty of the temperatures measured by the thermocouple for this particular case is usually in the range of 6 K. Serious uncertainties may be found for the center position near the inlet of the reactor mainly due to a distinct radial temperature gradient.

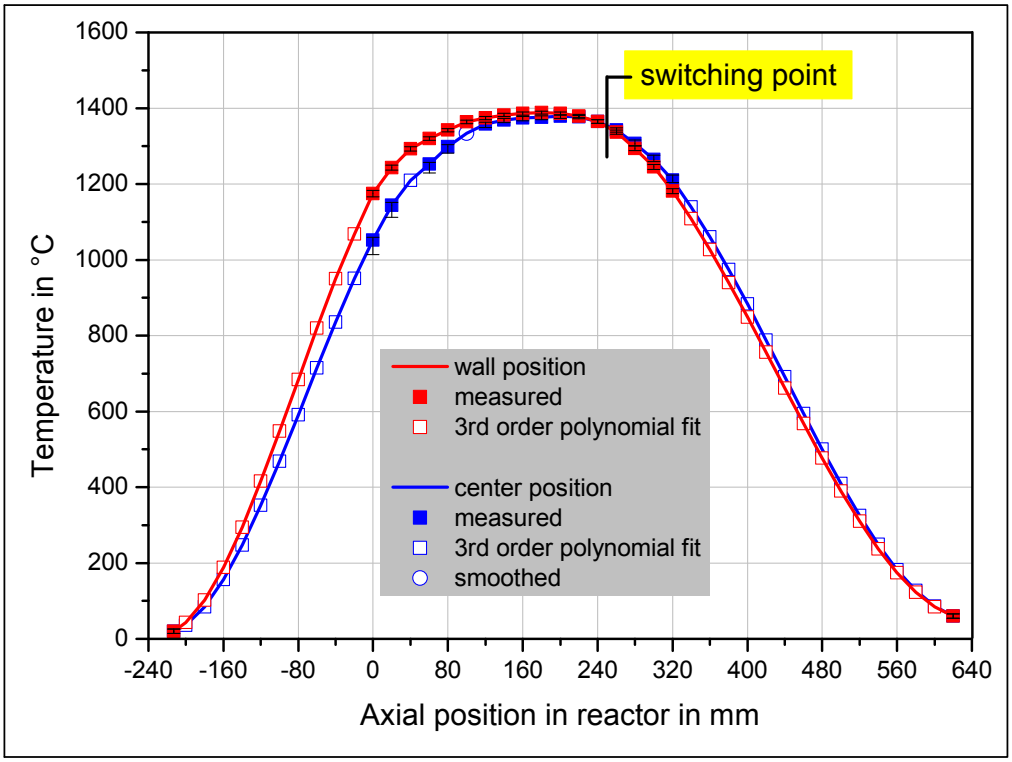

Figure 4-30: Determined temperature profiles for the thermocouple in wall position (WP) and in center position (CP) (1400 °C nominal furnace temperature and 2600 sccm nominal standard volume flow of Ar, average pressure at reactor inlet: 1.031 bar, average pressure at reactor outlet: 1.014 bar, indicators of uncertainty refer to maximum uncertainty)

An example for temperature profiles at conditions with higher nominal furnace temperature and standard volume flow is shown in Figure 4-31. A maximum temperature of 1424 °C was measured, which differs significantly from the nominal furnace temperature of 1600 °C. Either the flow was high enough to cool the wall down to temperatures dramatically lower than the furnace temperature or due to the geometrical situation and the high radial temperature gradient it was not possible to measure adequate temperatures near the wall. Remarkable radial temperature differences are also the reason for comparatively high uncertainty of the temperature measured in the center position. The switching point is not reached in the region where temperatures were determined but downstream the lowest position of the thermocouple.

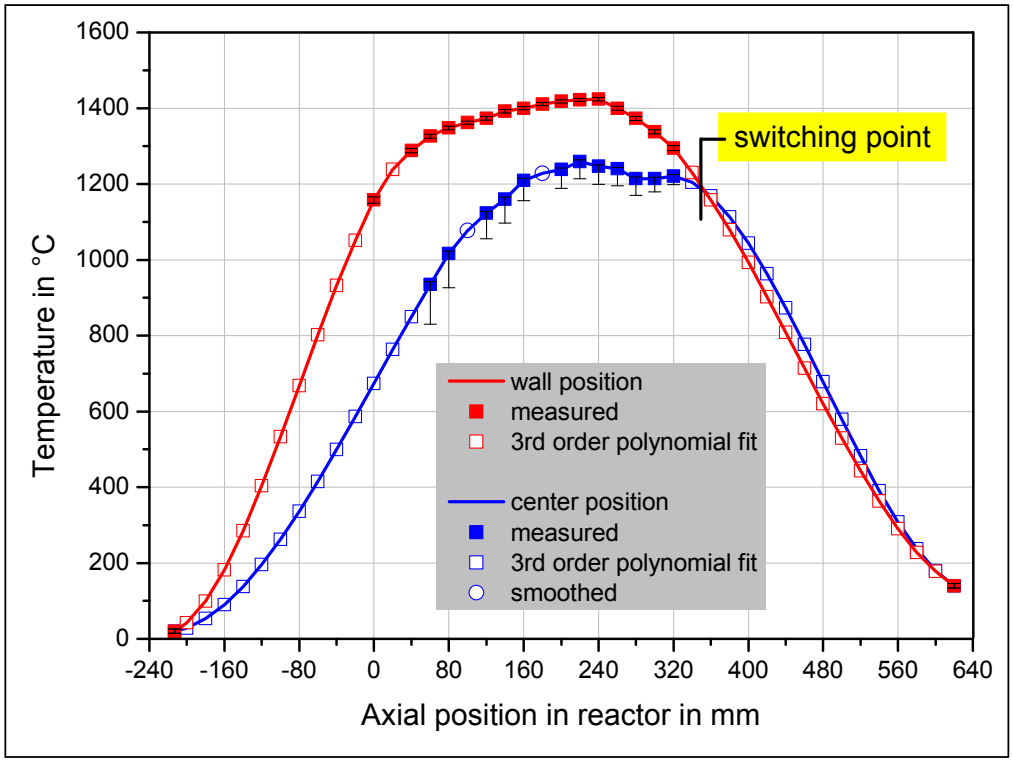

Figure 4-31: Profiles of determined temperature profiles for the thermocouple in wall position (WP) and in center position (CP) (1600 °C nominal furnace temperature and 9800 sccm nominal standard volume flow of Ar, average pressure in above reactor: 1.039 bar, average pressure below reactor: 1.006 bar, indicators of uncertainty refer to maximum uncertainty)

All determined temperature profiles related to the thermocouple in wall position and in center position for argon as well as for helium as the dilution gas can be found in Appendix C.

4.6 Additional experiments

Additional experiments were carried out in order to learn about the reliability of experimental results and to gain further information about the situation inside the reactor. Therefore selected reaction conditions were considered again in a second experimental campaign.[87] A second filter featuring a PTFE filter element with a nominal pore diameter of 2 µm was implemented in parallel position to the original one. By adjusting a three way cock with 90°-bore connected downstream to both filters and a pipe toward the flue, it was possible to chose the path of the particle laden product flow. As before, a pure flow of dilution gas with the same total standard volume flow than the mixture of dilution gas and methane considered later on was fed to the reactor until temperatures at position 320 mm inside the reactor reached constant levels. Then methane was introduced to the system, while the standard volume flow of the dilution gas was reduced simultaneously. A sample of product gas was extracted by vacuum pump of the GC as soon as the temperature at position 320 mm did not change any more. When the sample extraction was finished the abovementioned three way cock was switched over in order to lead to product flow through the second filter (sample filter). This way it could be guaranteed that no

[87] The second experimental campaign forms part of a student research paper, see [Maibauer, 2010].

particles formed during the first minutes after methane addition reached the second filter. Particles formed in this phase, in which temperatures in the reactor still approach a situation of thermal equilibrium, likely differ from particles formed later under more or less constant conditions. In order to allow the analysis of hydrocarbons higher than the C_2-hydrocarbons, the GC was not stopped after ethyne was detected but was in operation for an extended period of time of 45 min. Targeting constant reaction conditions the experiment was stopped as soon as the pressure rose more than 10 mbar compared to the initial conditions or the temperature rose for more that 1 % of the initial temperature at position 320 mm in K. When neither the pressure related nor the temperature related stop criterion was fulfilled, the experiment was brought to an end after about 60 min. Then the particles present in the sample filter were removed. Carbon deposition between the outlet of the reactor and the filter were negligible. However, a significant amount of carbonaceous material could be removed from the inside of the reactor during the cleaning procedure employing a metal wire, which was moved through the reactor with utmost care. The wire was introduced in the gap between the thermocouple and the TC elbow after removing respective sealing nuts, when the temperature of the tube furnace reached values below 700 °C. Both, the carbon sample from the filter and from the reactor were prepared for a further analysis, namely the determination of the BET specific surface. An overview about reaction conditions covered in the second campaign with argon and helium as dilution gas is provided in Table 4-13 and Table 4-14, respectively.

Table 4-13: Conditions covered in the second experimental campaign with argon as dilution gas

T_{furnace} in °C	$\dot{V}_{\text{N,tot,0}}$ in sccm	$x_{\text{CH}_4,0}$ in %	**Corresponding T_{furnace}/τ -set**
1200	200	5	2
	685	5	4
1300	650	5	7
	1300	5	8
	2600	5	9
1400	1400	5	12
	2600	2, 5, 10	13
	3800	5	14
1500	1600	5	16
	2800	5	17
1600	2000	5	21
	3350	5	22

Table 4-14: Conditions covered in the second experimental campaign with helium as dilution gas

T_{furnace} in °C	$\dot{V}_{\text{N,tot,0}}$ in sccm	$x_{\text{CH}_4,0}$ in %	**Corresponding** T_{furnace}/τ **-set**
1300	3800	5	25
1400	2800	5	26
	3800	2, 5, 10	27
	6500	5	28
1500	3800	5	29

The results of the second experimental campaign concerning the repeatability of results gained before (see Chapter 4.4), the location and the character of generated carbon as well as balances of H- and C-atoms are presented in the following chapters.

4.6.1 Repeatability of results

In order to access the repeatability of results concerning the conversion of methane, $\Delta X_{\text{CH}_4,2-1,\text{rel},u}$ was defined according to

$$\Delta X_{\text{CH}_4,2-1,\text{rel},u} = \frac{X_{\text{CH}_4,\text{campaign}2} - \overline{X}_{\text{CH}_4,2-1}}{u(X_{\text{CH}_4,\text{campaign}1})} \qquad \textbf{Equation 83}$$

relating the difference of the conversion determined in the second campaign $X_{\text{CH}_4,\text{campaign}2}$ and the average conversion to the standard uncertainty estimated for the conversion determined in the first campaign $u(X_{\text{CH}_4,\text{campaign}1})$. The average conversion of methane respecting the first and second experimental campaign $\overline{X}_{\text{CH}_4,2-1}$ arises from

$$\overline{X}_{\text{CH}_4,2-1} = 0.5 \cdot \left(X_{\text{CH}_4,\text{campaign}2} + X_{\text{CH}_4,\text{campaign}1}\right) \quad . \qquad \textbf{Equation 84}$$

Similarly $\Delta Y_{\text{H}_2,2-1,\text{rel},u}$, $\Delta Y_{\text{C}_2\text{H}_6,2-1,\text{rel},u}$, $\Delta Y_{\text{C}_2\text{H}_4,2-1,\text{rel},u}$, and $\Delta Y_{\text{C}_2\text{H}_2,2-1,\text{rel},u}$ were calculated based on the yield of hydrogen, ethane, ethene, and ethyne as well as on respective standard uncertainties. As presented in Table 4-15, for experiments with argon as dilution gas calculated values vary from - 5.69 to 3.42; however, absolute values mostly lie in the range between 0.5 and 1.5.

Table 4-15: Differences between values for the conversion of methane as well as the yields of hydrogen, ethane, ethene, and ethyne gained in the second campaign and average values regarding the first and second campaign with argon as dilution gas related to respective standard uncertainties determined in the first campaign. (Reaction condition: nominal furnace temperature in °C - nominal total standard volume flow in sccm - nominal initial molar fraction of methane in %)

Reaction condition	$\Delta X_{CH_4,2-1,rel,\mu}$ in -	$\Delta Y_{H_2,2-1,rel,\mu}$ in -	$\Delta Y_{C_2H_6,2-1,rel,\mu}$ in -	$\Delta Y_{C_2H_4,2-1,rel,\mu}$ in -	$\Delta Y_{C_2H_2,2-1,rel,\mu}$ in -
1200 - 200 - 5	-0.20	2.70	-0.36	-1.77	-0.47
1200 - 685 - 5	1.23	2.80	-1.02	-1.73	-0.03
1300 - 650 - 5	0.68	1.06	-0.56	-0.26	-0.61
1300 - 1300 - 5	0.19	0.87	-0.13	-3.57	-0.73
1300 - 2600 - 5	0.32	1.97	-0.04	-5.69	-0.66
1400 - 1400 - 5	-0.07	-0.34	-1.34	1.13	0.93
1400 - 2600 - 2	0.43	0.37	-1.14	-0.62	-0.39
1400 - 2600 - 5	0.16	0.04	-0.29	0.35	0.15
1400 - 2600 - 10	0.85	0.69	0.08	-0.26	-2.14
1400 - 3800 - 5	0.40	2.06	-0.29	-1.50	-0.47
1500 - 1600 - 5	0.76	0.36	0 / 0	-0.20	-0.76
1500 - 2800 - 5	0.98	0.81	0 / 0	-0.65	-1.30
1600 - 2000 - 5	3.12	0.21	0 / 0	-1.26	-1.85
1600 - 3350 - 5	3.42	1.45	0 / 0	-1.50	-2.30

Somewhat lower differences related to the estimated standard uncertainty were calculated for experiments with helium as dilution gas as can be seen in Table 4-16. Values range from - 1.01 to 2.49, whereas absolute values mostly lie between 0.4 and 0.7.

Table 4-16: Differences of values for the conversion of methane as well as the yields of hydrogen, ethane, ethene, and ethyne gained in the first and second experimental campaign with helium as dilution gas related to respective standard uncertainties. (Reaction condition: nominal furnace temperature in °C - nominal total standard volume flow in sccm - nominal initial molar fraction of methane in %)

Reaction condition	$\Delta X_{CH_4,2-1,rel,\mu}$ in -	$\Delta Y_{H_2,2-1,rel,\mu}$ in -	$\Delta Y_{C_2H_6,2-1,rel,\mu}$ in -	$\Delta Y_{C_2H_4,2-1,rel,\mu}$ in -	$\Delta Y_{C_2H_2,2-1,rel,\mu}$ in -
1300 - 3800 - 5	0.32	2.49	-0.51	-0.14	0.74
1400 - 2800 - 5	0.21	0.29	0.54	0.43	0.43
1400 - 3800 - 2	1.72	0.26	0.49	-0.67	-0.48
1400 - 3800 - 5	1.03	0.49	0.63	-0.20	-0.67
1400 - 3800 - 10	0.01	-0.01	0.03	0.00	-0.39
1400 - 6500 - 5	0.36	0.85	-0.08	-1.01	-0.21
1500 - 3800 - 5	0.13	0.15	0 / 0	0.69	-0.76

Since the difference between values gained in the two campaigns and the average value usually lies in range of the standard uncertainty, a quite good repeatability of results can be

deduced – in particular when taking into account that a simplified method of evaluation based on a two point calibration of the GC with respect to hydrogen and methane was adopted for the second campaign and that the second campaign was managed only with a pre-experimental calibration of the GC with respect to hydrogen, methane, and argon.

4.6.2 Location and character of generated carbon

As stated before, carbon deposit was not only found in the sample filter but also in the reactor. The weight of samples varied between 1 mg and 378 mg depending on the location of deposition, the reaction conditions, and the duration of the experiment. The samples from the filter showed a more or less uniform constitution, which could differ in general structure, macroscopic size of agglomerates, density, color, and odor depending on the reaction conditions. Respective examples are provided in Figure 4-32.

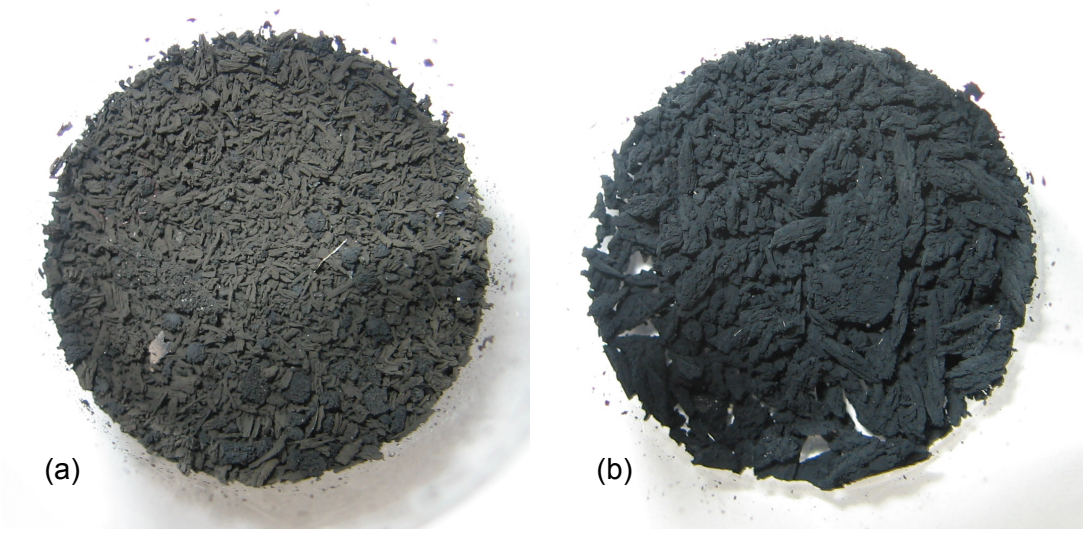

Figure 4-32: Examples for samples from the filter gained in experiments with argon as dilution gas: 1400 - 2600 - 10 (a) and 1300 - 650 - 5 (b) (Reaction condition: nominal furnace temperature in °C - nominal total standard volume flow in sccm - nominal initial molar fraction of methane in %)

As can be seen in Figure 4-32 (a), the samples may show a slightly brownish color indicating the presence of high molecular hydrocarbons. Mostly the samples from the reactor contained beside the particulate fraction a fraction of pyrocarbon which is a graphitic silvery deposition. The shape of the pyrocarbon fragments suggests its formation and deposition on the inner wall of the reactor. Some examples for carbon samples from the reactor are shown in Figure 4-33. Pyrocarbon volume fractions up to 100 % could be determined for samples from the reactor. However, an obvious dependency of the volume fraction of pyrocarbon in the samples from the reactor on the reaction conditions could not be found.

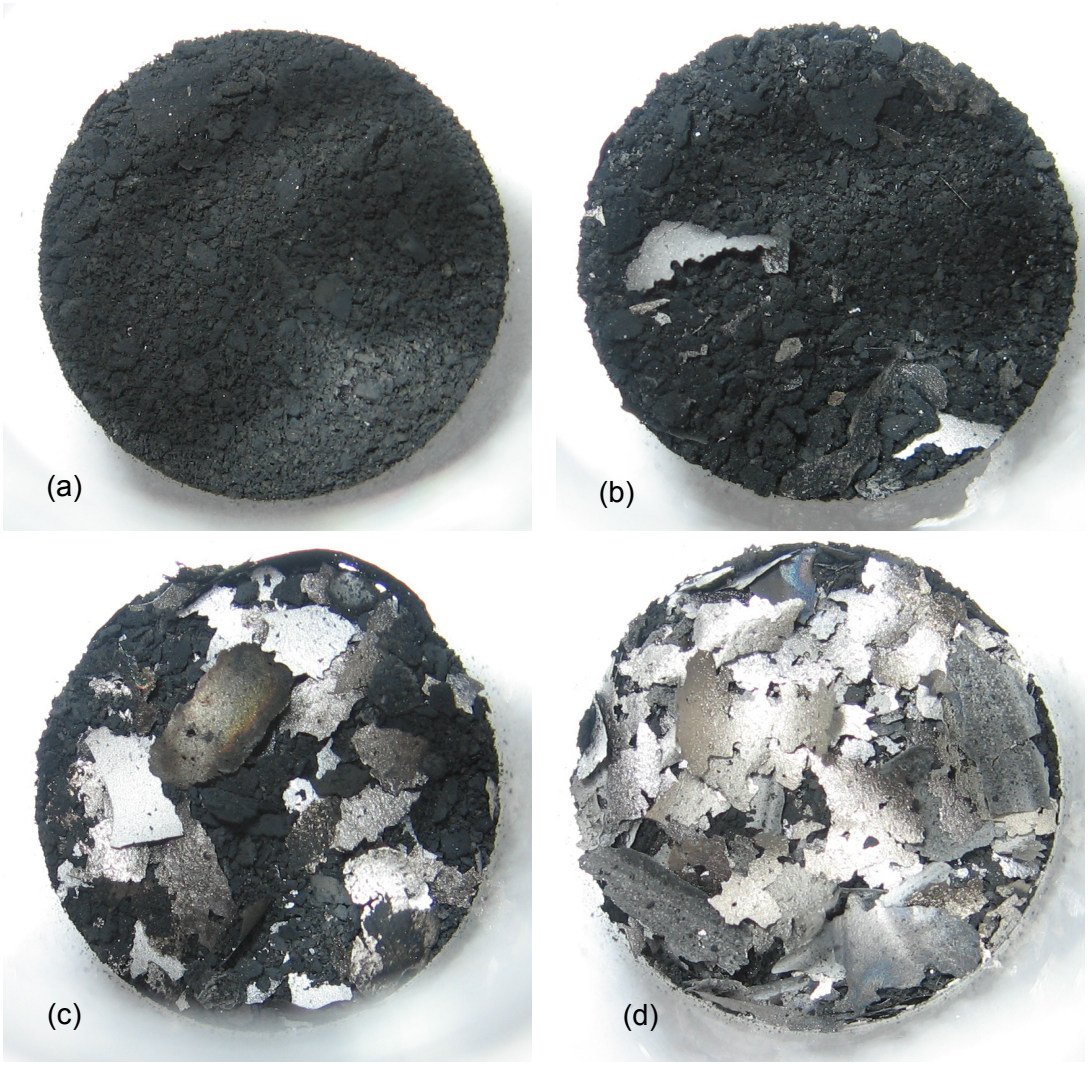

Figure 4-33: Examples for samples from the reactor gained in experiments with argon as dilution gas: 1400 - 2600 - 5 (a), 1600 - 2000 - 5 (b), 1500 - 2800 - 5 (c), and 1300 - 1300 - 5 (d) (Reaction condition: nominal furnace temperature in °C - nominal total standard volume flow in sccm - nominal initial molar fraction of methane in %)

The BET specific surfaces of the particulate fraction of every sample providing the required mass of about 20 mg were determined with a maximum uncertainty in the range of 0.5 m^2/g.[88] As can be seen in Figure 4-34, the values for the BET specific surface of samples from the reactor vary between 6.9 m^2/g and 56.4 m^2/g concerning experiments with argon as dilution gas and between 42.6 m^2/g and 94.7 m^2/g concerning experiments with helium as dilution gas. Most values can be found in the range from little less than 40 m^2/g to 60 m^2/g. Although great effort was made to entirely separate the pyrocarbon fraction from the particulate fraction, analyzed particulate sample may still have been contaminated with pyrocarbon to a certain extend, which is especially likely for measured BET values below 20 m^2/g. Contrariwise, samples from the filter are characterized by somewhat higher BET specific surfaces in the range from 22.3 m^2/g

[88] Measurements carried out by Dr. Eusebiu Grivei, TIMCAL, Willebroek, Belgium. 10 min preheating at 200 °C in nitrogen atmosphere.

and 139.1 m^2/g for experiments with argon as dilution gas and from 56.2 m^2/g to 66.4 m^2/g for experiments with helium as dilution gas, as can be extracted from Figure 4-35.

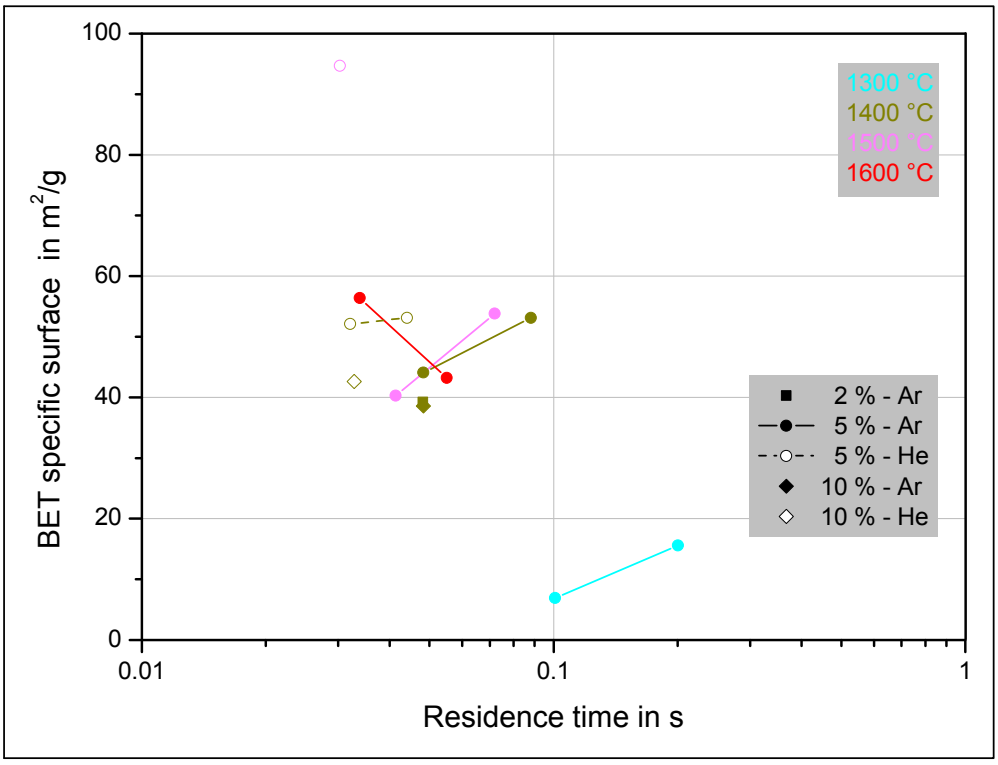

Figure 4-34: Specific surface area of carbon samples collected from the reactor

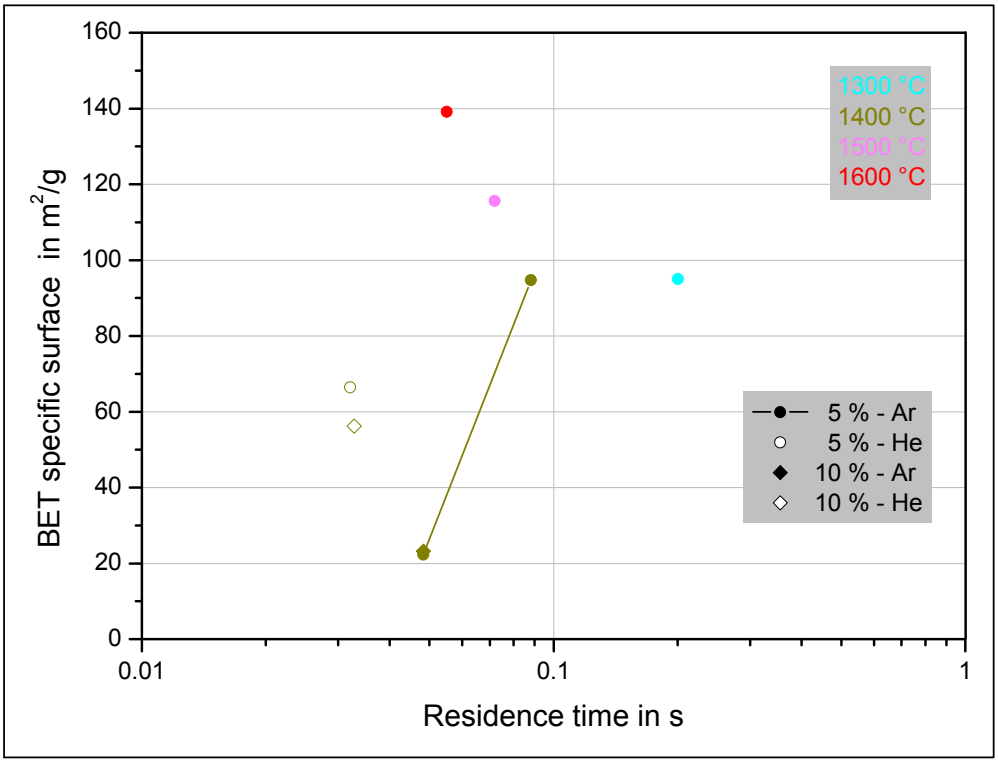

Figure 4-35: Specific surface area of carbon samples collected from the filter

The BET specific surface of samples from the filter are mostly higher compared to those from the reactor, probably due to the fact that smaller particles – corresponding to high specific surfaces – are more likely able to pass the reactor and finally to reach the filter. The present extend of data does not allow a comprehensive analysis of the dependencies of the BET specific surface on the reaction conditions. However, it becomes clear that the BET specific surfaces do not attain more or less constant values but differ in part significantly.

4.6.3 Balances of H- and C-atoms

As presented before, the balance of H-atoms based on the considered H-containing species, which are methane, hydrogen, ethane, ethene, and ethyne, is practically satisfied for the whole range of experimental conditions. With the knowledge about the mass of carbon deposition in the experimental system, specifically in the reactor itself and the filter, formed during particular experiments, it was possible to assess the balance of C-atoms as well. The calculative fraction of H-atoms in component i of the product gas $\hat{x}_{\mathrm{H\,in}\,i,\mathrm{P}}$ arises from

$$\hat{x}_{\mathrm{H\,in}\,i,\mathrm{P}} = \frac{f_{\mathrm{H\,in}\,i} \cdot \dot{n}_{i,\mathrm{P}}}{4 \cdot \dot{n}_{\mathrm{CH_4},0}} \qquad i = \mathrm{CH_4}, \mathrm{H_2}, \mathrm{C_2H_6}, \mathrm{C_2H_4}, \mathrm{C_2H_2} \qquad \textbf{Equation 85}$$

with $f_{\mathrm{H\,in}\,i}$ giving information about the number of H-atoms in one molecule of species i. The calculative fraction of H-atoms situated in other (not considered) species $\hat{x}_{\mathrm{H\,in\,others,P}}$ was determined by

$$\hat{x}_{\mathrm{H\,in\,others,P}} = 100\,\% - \sum_i \hat{x}_{\mathrm{H\,in}\,i,\mathrm{P}} \qquad i = \mathrm{CH_4}, \mathrm{H_2}, \mathrm{C_2H_6}, \mathrm{C_2H_4}, \mathrm{C_2H_2} \quad . \qquad \textbf{Equation 86}$$

If $\hat{x}_{\mathrm{H\,in\,others,P}} < 0$, the fraction of H-atoms situated in other (not considered) species $x_{\mathrm{H\,in\,others,P}}$ was set to 0 and the fraction of H-atoms in component i of the product gas $x_{\mathrm{H\,in}\,i,\mathrm{P}}$ was calculated by

$$x_{\mathrm{H\,in}\,i,\mathrm{P}} = \hat{x}_{\mathrm{H\,in}\,i,\mathrm{P}} \cdot \frac{100\,\%}{\sum_i \hat{x}_{\mathrm{H\,in}\,i,\mathrm{P}}} \qquad i = \mathrm{CH_4}, \mathrm{H_2}, \mathrm{C_2H_6}, \mathrm{C_2H_4}, \mathrm{C_2H_2} \quad , \qquad \textbf{Equation 87}$$

else $x_{\mathrm{H\,in\,others,P}} = \hat{x}_{\mathrm{H\,in\,others,P}}$ and $x_{\mathrm{H\,in}\,i,\mathrm{P}} = \hat{x}_{\mathrm{H\,in}\,i,\mathrm{P}}$.

Similarly $x_{\mathrm{C\,in}\,i,\mathrm{P}}$, the fraction of C-atoms situated in component i of the product gas, was determined by

$$x_{\mathrm{C\,in}\,i,\mathrm{P}} = \frac{f_{\mathrm{C\,in}\,i} \cdot \dot{n}_{i,\mathrm{P}}}{1 \cdot \dot{n}_{\mathrm{CH_4},0}} \qquad i = \mathrm{CH_4}, \mathrm{C_2H_6}, \mathrm{C_2H_4}, \mathrm{C_2H_2} \qquad \textbf{Equation 88}$$

with $f_{\mathrm{C\,in}\,i}$ giving information about the number of C-atoms in one molecule of species i. Beside gaseous products also solid products carry C-atoms, namely the carbon deposit in the reactor as well as the carbon deposit in the sample filter. The average molar deposition flow in the reactor $\overline{\dot{n}}_{\mathrm{C\,in\,reactor}}$ was estimated by

$$\overline{\dot{n}}_{\mathrm{C\,in\,reactor}} = \frac{m_{\mathrm{C\,in\,reactor}}}{t_{\mathrm{CH_4,reactor}} \cdot M_{\mathrm{C}}} \qquad \textbf{Equation 89}$$

employing the mass of carbon deposition inside the reactor $m_{\mathrm{C\,in\,reactor}}$, the period between the initialization and the termination of the methane flow $t_{\mathrm{CH_4,reactor}}$, and the molecular weight of carbon M_{C}. Accordingly, the average molar deposition flow in the sample filter $\overline{\dot{n}}_{\mathrm{C\,in\,filter}}$ was calculated by

$$\overline{\dot{n}}_{\mathrm{C\,in\,filter}} = \frac{m_{\mathrm{C\,in\,filter}}}{t_{\mathrm{CH_4,filter}} \cdot M_{\mathrm{C}}} \qquad \textbf{Equation 90}$$

employing the mass of carbon deposition in the sample filter $m_{\mathrm{C\,in\,filter}}$ and the period between switching over of the three way cock to the sample filter and the termination of the methane flow $t_{\mathrm{CH_4,filter}}$.

With $\overline{\dot{n}}_{\text{C in reactor}}$ and $\overline{\dot{n}}_{\text{C in filter}}$ the fractions of C-atoms situated in the carbon deposition in the reactor $x_{\text{C in C in reactor,P}}$ and in the filter $x_{\text{C in C in filter,P}}$ could be calculated following

$$x_{\text{C in } i\text{,P}} = \frac{f_{\text{C in } i} \cdot \overline{\dot{n}}_i}{1 \cdot \dot{n}_{\text{CH}_4,0}} \qquad i = \text{C in reactor}, \text{C in filter} \quad . \qquad \textbf{Equation 91}$$

Since a deposition of pure carbon has been considered, $f_{\text{C in C in reactor}} = f_{\text{C in C in filter}} = 1$.

The fraction of C-atoms situated in other (not considered) species $x_{\text{C in others,P}}$ was determined by

$$x_{\text{C in others,P}} = 100\,\% - \sum_i x_{\text{C in } i\text{,P}} \qquad i = \text{CH}_4, \text{C}_2\text{H}_6, \text{C}_2\text{H}_4, \text{C}_2\text{H}_2, \text{C in reactor}, \text{C in filter} \quad . \qquad \textbf{Equation 92}$$

Figure 4-36 represents the fractions of H- and C-atoms in particular species respecting the experimental conditions listed in Table 4-13 and Table 4-14. In accordance with results presented in Chapter 4.4, the hydrogen balance is practically satisfied resulting in a marginal fraction of H-atoms in other (not considered) species. Contrariwise, remarkable amounts of C-atoms form part of other species leading to high fractions of C-atoms in other species up to 48.3 % and about 28.5 % on average. This indicates the presence of further C-rich species in the product flow. Small molar fractions of the C_3-hydrocarbons propene (C_3H_6), propyne (C_3H_4), and probably propadiene (C_3H_4) were detected but with a molar fraction far below an order of magnitude, which could possibly explain a high value of $x_{\text{C in others,P}}$, namely in the order of magnitude of ethane regarding propene and in the order of magnitude of ethene regarding propyne and propadiene. Low amounts of high molecular byproducts, in particular hydrocarbons with a high C/H-ratio, could better justify the practically perfect H-balance on the one hand and the significant disagreement of the C-balance on the other hand. Suggested by the partly colored appearance and strong-smelling characteristics of the samples, polycyclic aromatic hydrocarbons (PAH), such as naphthalene ($C_{10}H_8$)[89], could have been generated. The formation of PAHs involved in the thermal splitting of methane has already been reported.[90]

[89] identified by Albermann in former experiments, cp. [Albermann, 2007], and confirmed by [Muradov, 2010]
[90] cp. e. g. [Hu, 2003]

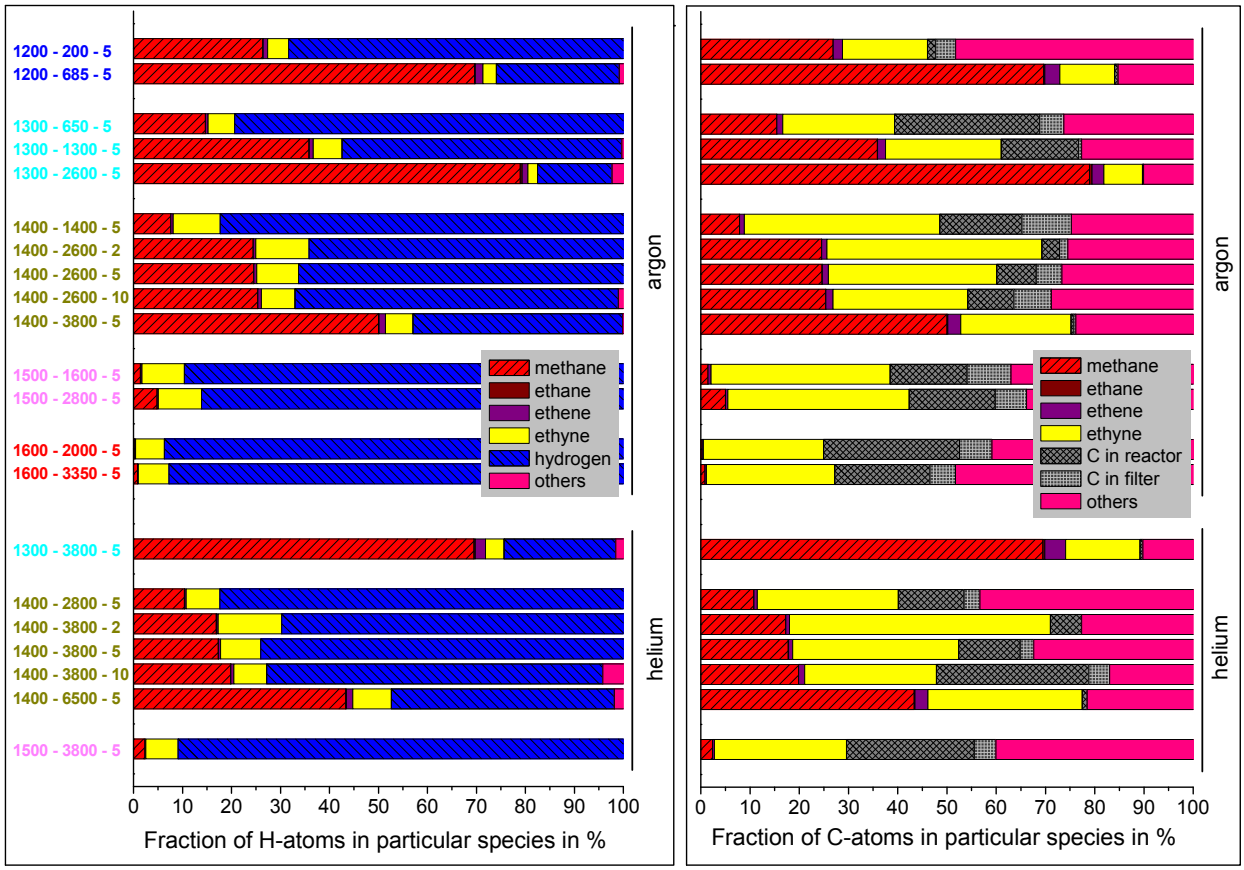

Figure 4-36: Fractions of H- and C-atoms situated in particular species as a function of the experimental conditions (nominal furnace temperature in °C - total standard volume flow in sccm - initial molar fraction of methane in %)

4.7 Experiments with added C-particles

In order to investigate heterogeneous effects caused by carbon particles, experiments were carried out employing an apparatus which allows seeding of the inlet gas.[91] An overview about the general configuration of the seeding apparatus is provided in Figure 4-37. It features a rotating dosing as well as a rotating dispersing element, which permits the continuous generation of gas/particle-flow made of the inlet substances argon and carbon particles.

Super P, a conductive carbon black with a typical BET specific surface of 62 m^2/g and a nominal particle size of 40 nm, was used as seeding material.[92] Depending on the number of revolution of the rotating dosing element different mass flows of particles were realized. The mass flow of the particles was determined employing the mass of particles found in a filter downstream the seeding apparatus and the respective duration of operation. It was found that a total standard volume flow of about 3610 sccm Ar allows almost complete discharge of dispersed particles

[91] Construction, design, qualification, optimization, and control of the apparatus forms part of a student research project and a diploma thesis, see [Förster, 2009].
[92] produced by TIMCAL, Willebroek, Belgium, cp. [TIMCAL, 2007]

from the seeding apparatus. The longer the operation time the higher the mass of particles in the filter. The prototype offers roughly linear characteristics a can be seen in Figure 4-38.

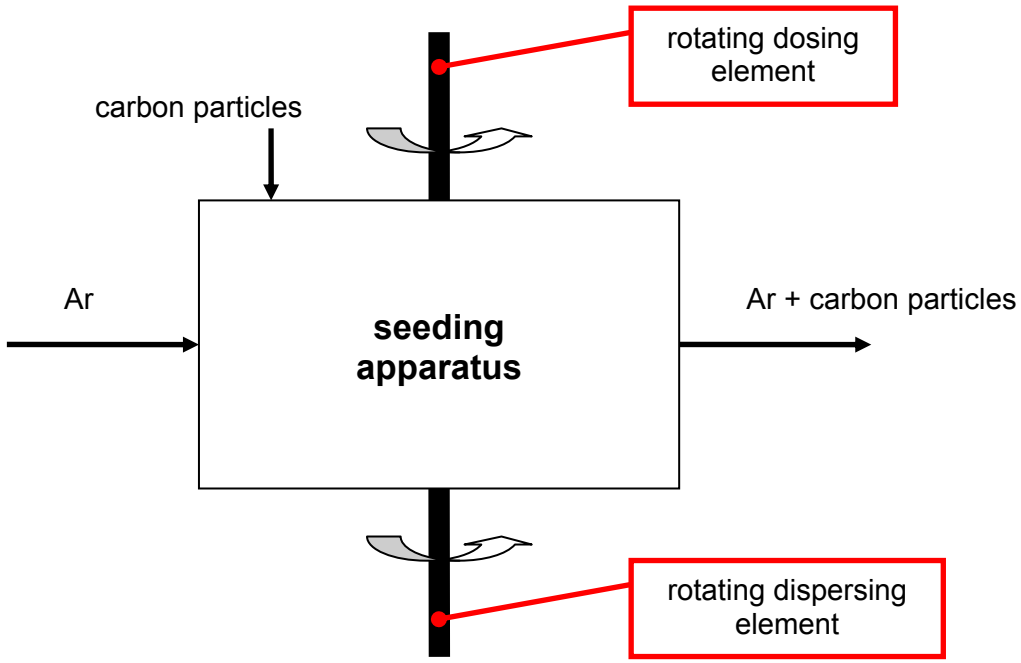

Figure 4-37: General configuration of the seeding apparatus

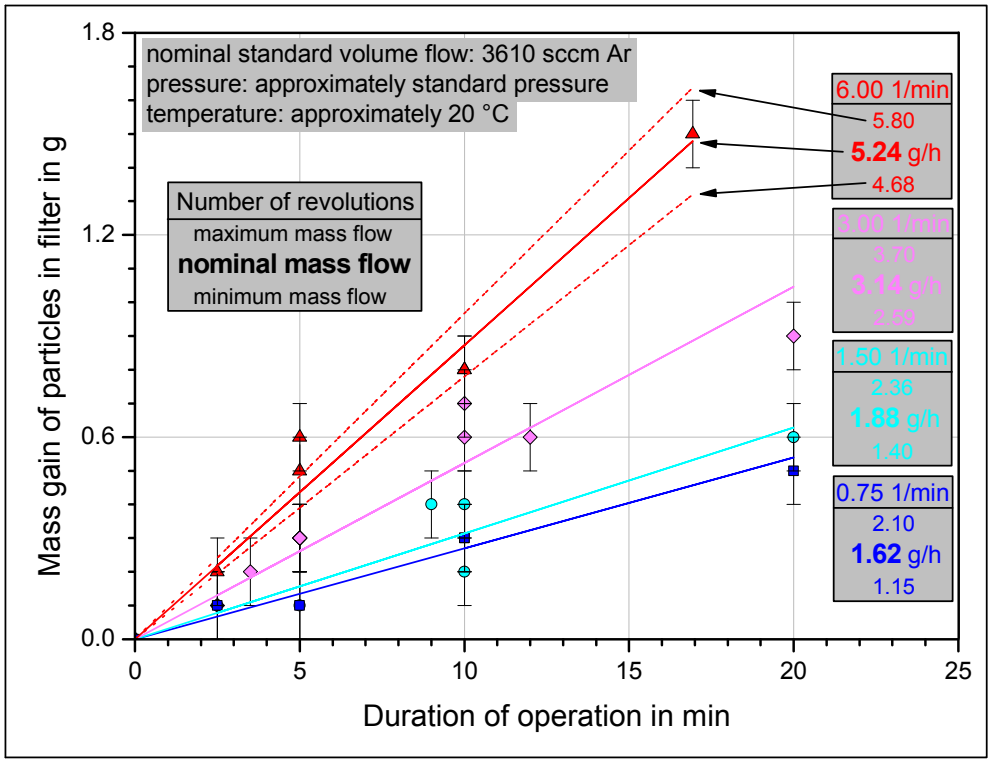

Figure 4-38: Calibration of the seeding apparatus and determination of maximum, nominal, and minimum mass flow of Super P depending on the number of revolutions of the dosing element

Resulting from the small amounts of the seeding material, the maximum uncertainty of the measurement of the particle mass inside the filter or rather the mass gain of the particles inside the filter is relatively high (approximately 0.1 g). However, general trends can be identified. The determined mass flow increases, when the number of revolution of the dosing element increases. Maximum, nominal, and minimum mass flows were determined employing a fitting line through the origin respecting maximum, nominal, and minimum values, respectively, as is illustrated in Figure 4-38, exemplarily for a number of revolutions of 6 1/min. Here the uncertainty of the duration of operation, which was not higher than 2 s, was neglected.

$T_{\mathrm{furnace}} / \tau$-set 14 with 5 % initial molar fraction of methane was chosen as the reference condition, because achieved conversion of methane and yield of hydrogen lie below 50 % and offer potential for enhancement. Although the corresponding total standard volume flow equals 3800 sccm, a standard volume flow of approximately 3610 sccm was applied to the seeding apparatus, because only argon entered the disperser and 190 sccm methane were added downstream in order to provide a mixture with 5 % molar fraction of methane in the gas phase at the inlet of the reactor. The addition of Super P results in a considerable increase of the conversion of methane and of the yield of hydrogen as can be extracted from Figure 4-39. More precisely, with the maximum mass flow of 5.24 g/h Super P through the reactor it was possible to increase the conversion of methane and the yield of hydrogen by 18 % and 33 %, respectively. Contrariwise, the yield of ethyne shows only a weak dependency on the mass flow of carbon particles, while the yields of the other C_2-hydrocarbons ethane and ethene decrease with rising mass flow of Super P – however, at comparatively low levels. Seeding obviously affects the cracking reactions, promoting the generation of the favored product hydrogen. The related yields of hydrogen and C_2-hydrocarbons rose from 1.38 to an averaged value of 1.81, when the particle mass flow reached its maximum. Thus, the addition of carbon black to the flow entering the reactor leads to a higher cleanliness of the product flow.

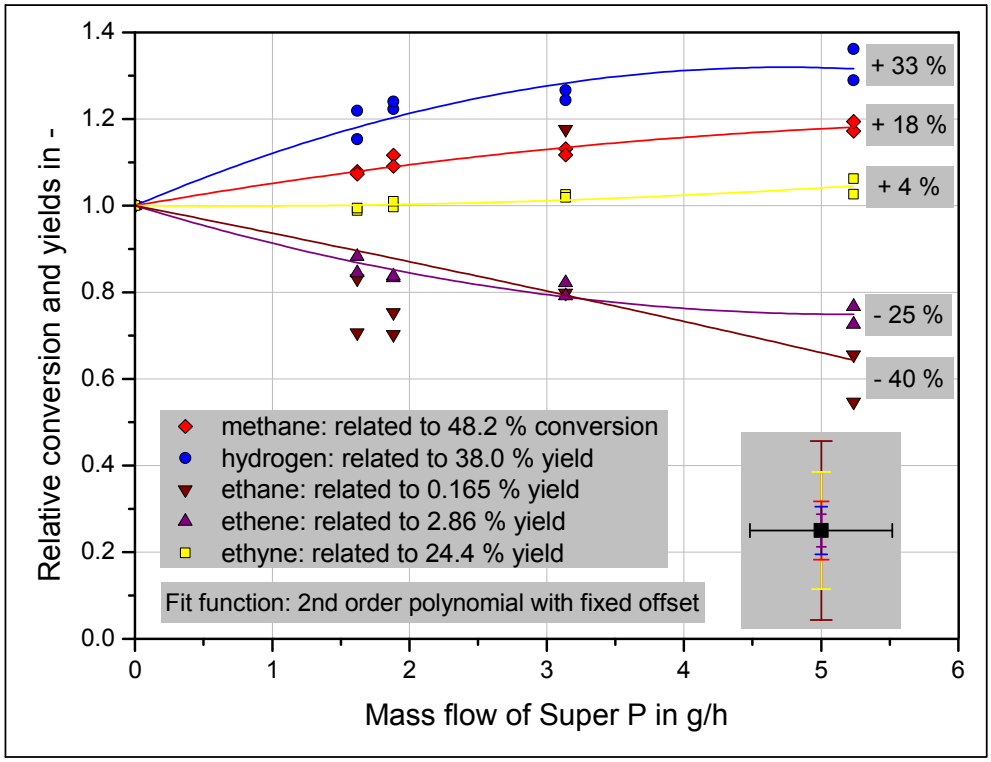

Figure 4-39: Conversion of methane and yield of hydrogen as well as of ethane, ethene, and ethyne as a function of the applied mass flow of Super P related to values determined without seeding. Indicators of uncertainty refer to the average maximum uncertainty concerning the mass flow and to typical standard uncertainty concerning relative conversion and yields. Nominal furnace temperature: 1400 °C, nominal total standard volume flow: 3800 sccm, nominal molar fraction of methane in argon: 5 %, pressure between 1.012 bar and 1.031 bar.

Seeding changes the reaction conditions inside the reactor in different ways. On the one hand the particles provide additional sites for heterogeneous reactions, whereas on the other hand the heat transfer between the reactor wall and the fluid is enhanced due to radiative effects. With the current configuration it was not possible to isolate these two effects, but it is admissible to state that the change of the conversion and yields is not only a result of a better heat transfer. This is because an unusual change of the temperature at the position 320 mm could not be detected after adding carbon particles, which could be expected for an extremely improved heat input in the fluid. An extinction of radiation in the visible regime by optical observation through the transparent glass tube at the outlet of the seeding apparatus with an inner diameter (corresponding to the maximum optical length) of 4 mm was not or only marginally noticeable although the absorption coefficient of carbon can be approximated by one. Since the inner diameter of the reactor equals 8 mm, the extinction in the reactor is higher than the extinction in the glass tube under the same circumstances. However, the consequences of a higher optical path are compensated by the increased volume flow in the reactor and the resulting lower concentration of carbon in the gas/particle-mixture, indicating that the extinction in the reactor should have the same order of magnitude than the extinction in the glass tube – also for radiation with other wavelengths, because the absorption coefficient does not exceed one.

The theoretical mass flow of generated carbon for the reference condition without seeding equals approximately 1.27 g/h. However, the examination of the carbon balance shows that the fraction of C-atoms in other (not considered) compounds of the product flow equals about 20 % resulting in a basically negligible mass flow of generated carbon. Consequently, the major part of carbon material inside the reactor originates from the seeding material and not from generated carbon. The surface provided by added particles in the heated region of the reactor $S_{\text{Super P,R}}$ can be roughly estimated following

$$S_{\text{Super P,R}} = s_{\text{BET,Super P}} \cdot \dot{m}_{\text{Super P}} \cdot \bar{\tau} \qquad \textbf{Equation 93}$$

employing the BET specific surface of Super P $s_{\text{BET,Super P}}$, the mass flow of Super P dispersed by the seeding apparatus $\dot{m}_{\text{Super P}}$, and the average residence time $\bar{\tau}$ according to Equation 55. Thus, with $s_{\text{BET,Super P}} = 62\ \text{m}^2/\text{g}$, $\bar{\tau} = 0.0329\ \text{s}$, and the maximum applied particle mass flow $\dot{m}_{\text{Super P,max}} = 5.24\ \text{g/h}$ the maximum particle based surface area in the reactor can be calculated to 0.0030 m^2. The geometrical inner surface of the heated region of the reactor nominally equals 0.0063 m^2 and therefore has the same order of magnitude. Therefore the reactor surface probably promotes heterogeneous reactions.

The BET specific surface of carbon deposit recovered from the reactor and the sample filter is usually comparable to (or even higher than) figures of Super P, suggesting that also generated particles represent favored reaction sites and support heterogeneous paths of the reactions.

5 Kinetic evaluation

For the kinetic evaluation of the experiments it was necessary to estimate realistic reactions conditions for all locations inside the reactor, in particular with respect to the reaction temperature, and to set up a suitable flow model as well as a kinetic model, which covers the dominating reactions.[93]

5.1 Interpretation of measured temperatures

The temperature on the surface of the protection tube of the thermocouple was a result of the convective heat transfer between the fluid and the protection tube as well as of the radiative heat transfer between reactor wall and the surface of the protection tube as is illustrated in Figure 5-1.

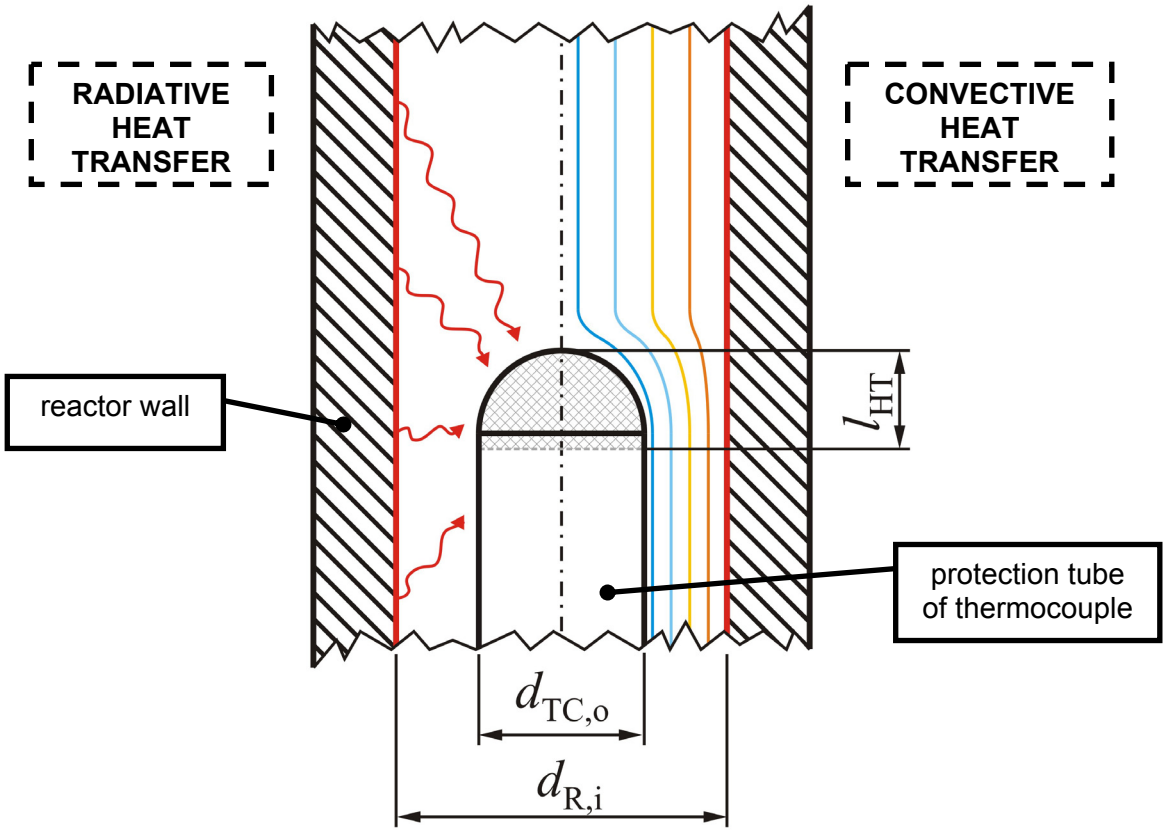

Figure 5-1: Illustration of heat transfers contributing to the temperature measured with the thermocouple

Respecting the diameters of the protection tube as well as of the inserted capillary tube and employing trigonometry, it can be shown that the distance between the contact line and the tip of the protection tube theoretically equals 1.368 mm. Thus, the distance between the center of the welded part of the thermocouple and the tip of the protection tube accounts for

[93] Some basic considerations can be found in [Wullenkord, 2010 b].

approximately 1.19 mm corresponding to the dimensions provided in Figure 4-26. It was postulated that l_{HT}, the length of the heat transfer region relevant for the measurement of the temperature, equals 2.38 mm, which is double of the aforementioned distance allowing a symmetric consideration of the heat transfer with respect to the center of the measuring junction.

Motivated by the low wall-thickness of the protection tube of the thermocouple (1 mm) and the helium filling, it was assumed that the upper part of the thermocouple corresponding to l_{HT} and including the measuring junction attained a uniform temperature. The thermal conductivity of FRIATEC's AL23, which is the material of the reactor and the protection tube of the thermocouple, lies in the range of 5 W/(m K) at 1000 °C. The material properties of AL23 provided by the manufacturer are content of Table 5-1.[94]

Table 5-1: Stated thermal conductivity and emissivity of AL23 produced by FRIATEC

T in °C	λ in $\frac{\mathrm{W}}{\mathrm{m\,K}}$	ε in –
100	30	-
1000	5	0.21

Since the amount of known data is very rare, but material properties had to be applied for subsequent calculation within a wide range of temperatures, other sources had to be used in order to estimate reasonable dependencies of the material properties on the temperature. The following chapter deals with material properties. Then the convective and radiative heat transfers are examined in detail before consequences are derived.

5.1.1 Material properties of AL23 and used gases

The software EES provides a database for the thermal conductivity of alumina (polycrystalline) in the temperature range between 300 K and 1000 K.[95] Additional data for corundum, containing 99 % alumina, can be found in [VDI, 2006][96] regarding the temperature range between 400 °C and 1200 °C. The approximation of the temperature depending function of the thermal conductivity of AL23 according to Figure 5-2 comprises the following steps:

- determination of a fit function for the collective of values of the thermal conductivity comprising data from EES (for temperatures up to 726.85 °C corresponding to 1000 K) and [VDI, 2006] (for temperatures above 726.85 °C)

[94] see [FRIATEC, 2003]
[95] EES: Engineering Equation Solver V8.412-3D (2009). Database provides data from [Incropera, 1996] and [Touloukian, 1972].
[96] p. Deb 3

- calculation of the ratio between values given by [FRIATEC, 2003] and the fit function
- determination of ratios for other temperatures by linear interpolation employing the above mentioned ratios with the constraint, that the value should be higher than 1
- calculation of values of the thermal conductivity employing the fit function and the ratios evaluated for certain temperatures
- determination of a 3rd order polynomial fit function for the values

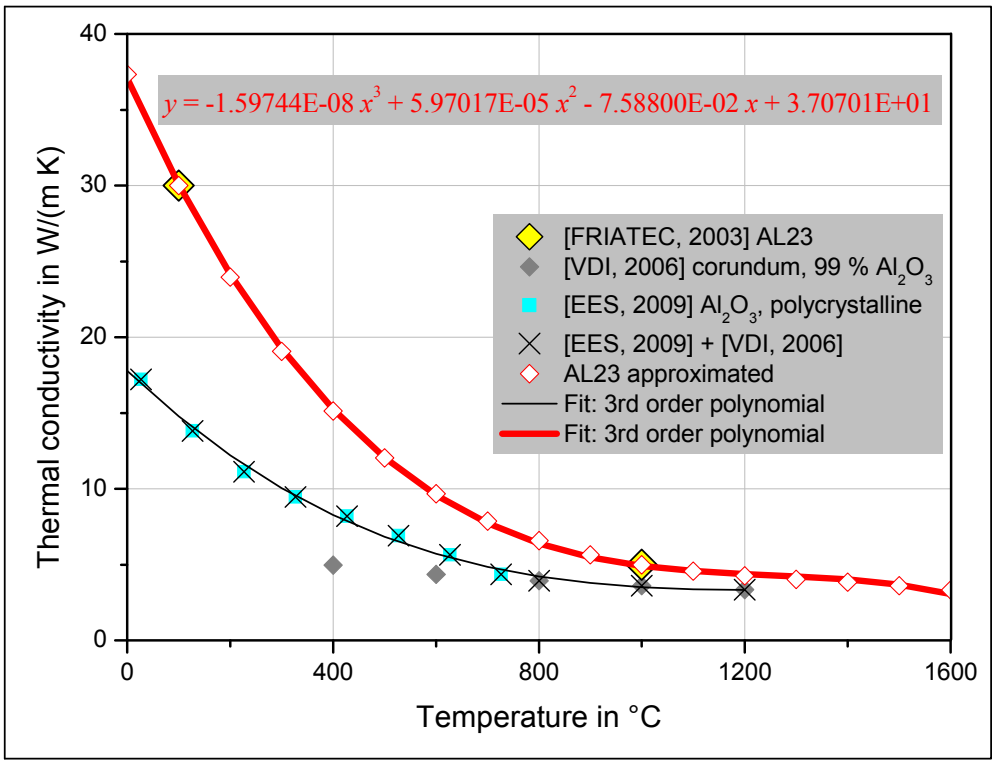

Figure 5-2: Approximation of the thermal conductivity of AL23 for temperatures between 0 °C and 1600 °C employing various information

The fit function for the thermal conductivity leads to a relative error of 0.21 % and - 1.65 % concerning the given values for 100 °C and 1000 °C, respectively. The values found in [EES, 2009] do not match those from [VDI, 2006] for low temperatures. However, the shapes of the curves suggest that latter values represent a limit at higher temperatures, which is also admissible for the first case.

Concerning the emissivity of AL23 the data sheet only provides one value, namely the emissivity for 1000 °C (see Table 5-1). Values found in [VDI, 2006][97] for the emissivity of alumina indicate a linear decrease with the temperature. Applying a linear fit function, a potential value for 1000 °C equals 0.533, what is about 2.54 times higher than the given value from the data sheet. Assuming that a linear decrease is admissible for AL23 and that the above

[97] p. Ka 5

mentioned discrepancy factor is also valid for other temperatures, the emissivity of AL23 was approximated for a wider temperature range consistent with Figure 5-3.

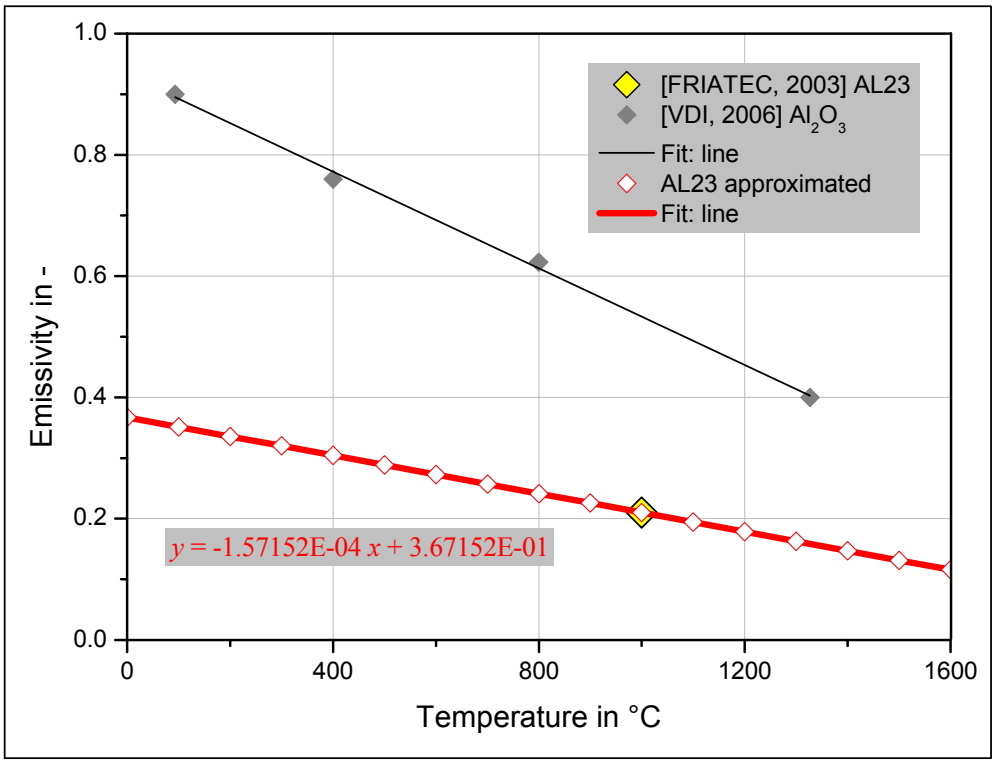

Figure 5-3: Approximation of the emissivity of AL23 for temperatures between 0 °C and 1600 °C employing various information

Material properties of used gases, specifically material properties of argon and helium, were mostly extracted from [VDI, 2006] and are summarized in Appendix D.

5.1.2 Convective heat transfer

A convective heat transfer took place between the protection tube of the thermocouple and the fluid passing it. The heat flux density on the wall of the thermocouple due to convection $\dot{q}_{\mathrm{TC,conv}}$ can be calculated by

$$\dot{q}_{\mathrm{TC,conv}} = \alpha_{\mathrm{conv}} \cdot \left(T_{\mathrm{TC,wall}} - T_{\mathrm{fluid}} \right) \quad , \qquad \textbf{Equation 94}$$

where α_{conv} is the local convective heat transfer coefficient, $T_{\mathrm{TC,wall}}$ represents the temperature of the wall of the protection tube of the thermocouple and considering an internal flow T_{fluid} stands for the adiabatic mixing temperature of the fluid at the respective axial position.[98]

[98] cp. [Baehr, 2006], p. 11 et seqq.

Assuming a constant heat capacity of the fluid in the range of considered temperatures, T_{fluid} is defined as

$$T_{\mathrm{fluid}} = \frac{2\pi}{\dot{m}_{\mathrm{fluid}}} \cdot \int_{R_{\mathrm{TC,o}}}^{R_{\mathrm{R,i}}} \rho \cdot v \cdot T \cdot r \cdot \mathrm{d}r \qquad \textbf{Equation 95}$$

for a flow through an annulus described by the inner radius of the reactor $R_{\mathrm{R,i}}$ and the outer radius of the thermocouple protection tube $R_{\mathrm{TC,o}}$. Employing Equation 1 and the relation between the amount of substance n and the corresponding mass m, following

$$m = M \cdot n \quad , \qquad \textbf{Equation 96}$$

where M represents the molecular weight, the density ρ of an ideal gas can be calculated by

$$\rho = \frac{M \cdot p}{\Re \cdot T} \qquad \textbf{Equation 97}$$

and leads to

$$T_{\mathrm{fluid}} = \frac{2\pi}{\dot{m}_{\mathrm{fluid}}} \cdot \int_{R_{\mathrm{TC,o}}}^{R_{\mathrm{R,i}}} \frac{M \cdot p}{\Re} \cdot v \cdot r \cdot \mathrm{d}r \quad . \qquad \textbf{Equation 98}$$

The convective heat transfer coefficient can be estimated using Nusselt correlations. Employing the hydraulic diameter d_{h} and the average thermal conductivity of the fluid $\overline{\lambda}_{\mathrm{fluid}}$ the Nusselt number Nu is defined as

$$\mathrm{Nu} = \frac{\alpha_{\mathrm{conv}} \cdot d_{\mathrm{h}}}{\overline{\lambda}_{\mathrm{fluid}}} \quad . \qquad \textbf{Equation 99}$$

The thermal conductivity should be evaluated for an average temperature of the fluid regarding the temperatures at the inlet and at the outlet of the considered part of the reactor.[99]

To estimate the order of magnitude of α_{conv}, the convective heat transfer in a concentric annular gap had to be examined. Ways to handle the problem can be found in [VDI, 2006][100]; however, the provided equations are based on further constraints. Firstly only a constant wall temperature is considered. The part of interest of the thermocouple's protection tube is its tip featuring a short length. It is admissible to consider this part to be isothermal. Secondly one has to decide, which of the following cases matches best to the considered problem:

- heat transfer at inner pipe, outer pipe isolated
- heat transfer at outer pipe, inner pipe isolated
- heat transfer at inner and outer pipe, wall temperatures identical

Since predominantly the heat transfer at the inner pipe affects the temperature measurement, the first situation was chosen for further calculations. Furthermore, in absence of additional knowledge about the velocity profile in an annulus featuring complex heat transfer processes properties of the fluid at a certain axial position were determined for

$$\overline{T}_{\mathrm{fluid}} = 0.5 \cdot \left(T_{\mathrm{R,wall}} + T_{\mathrm{TC,wall}} \right) \quad , \qquad \textbf{Equation 100}$$

the arithmetic mean of the wall temperatures of the reactor and the thermocouple.

Generally a flow can be characterized by the Reynolds number Re, which is defined as

[99] cp. [VDI, 2006], p. Gb 1
[100] p. Gb 1 et seqq.

$$\mathrm{Re} = \frac{\rho \cdot d_\mathrm{h} \cdot \bar{v}}{\eta} \quad , \qquad \textbf{Equation 101}$$

where ρ is the density, $\bar{v}$ is the average velocity of the flow, η stands for the dynamic viscosity, and d_h for the hydraulic diameter.

The average velocity $\bar{v}$ arises from

$$\bar{v} = \frac{\dot{V}}{A} \quad , \qquad \textbf{Equation 102}$$

based on the volume flow $\dot{V}$ and the cross sectional area A, through which $\dot{V}$ passes.

Following [VDI, 2006][101] the hydraulic diameter d_h can be calculated with the above mentioned cross sectional area A and the wetted perimeter of the cross section P_w:

$$d_\mathrm{h} = \frac{4 \cdot A}{P_\mathrm{w}} \quad . \qquad \textbf{Equation 103}$$

For an annular gap, in the present case defined by the outer diameter of the protection tube of the thermocouple $d_{\mathrm{TC,o}}$ and the inner diameter of the reactor $d_{\mathrm{R,i}}$, it can be shown that

$$d_\mathrm{h} = d_{\mathrm{R,i}} - d_{\mathrm{TC,o}} \quad . \qquad \textbf{Equation 104}$$

The Reynolds number never exceeds a value of 2300, which represents the reference value for the transition from laminar to turbulent flow. Flows characterized by Reynolds numbers below 2300 are certainly laminar flows.[102] Regarding a laminar flow in a region where temperature and velocity profiles develop coevally, the average Nusselt number Nu_ave can be estimated by

[101] p. LAB 4
[102] cp. [VDI, 2006], p. Ga 1

$$\mathrm{Nu}_{\mathrm{ave}} = \sqrt[3]{\mathrm{Nu}_1^3 + \mathrm{Nu}_2^3 + \mathrm{Nu}_3^3} \quad , \qquad \textbf{Equation 105}$$

where Nu_1 refers to the Nusselt number regarding a fully developed flow, concerning both, temperature and velocity, and arises from

$$\mathrm{Nu}_1 = 3.66 + 1.2 \cdot \left(\frac{d_{\mathrm{TC,o}}}{d_{\mathrm{R,i}}} \right)^{-0.8} \quad , \qquad \textbf{Equation 106}$$

where Nu_2 refers to the Nusselt number characterizing a thermally undeveloped flow with fully developed velocity profile and arises from

$$\mathrm{Nu}_2 = 1.615 \cdot \left[1 + 0.14 \cdot \left(\frac{d_{\mathrm{TC,o}}}{d_{\mathrm{R,i}}} \right)^{-0.5} \right] \cdot \left(\mathrm{Re} \cdot \mathrm{Pr} \cdot \frac{d_{\mathrm{h}}}{l_{\mathrm{HT}}} \right)^{\frac{1}{3}} \quad , \qquad \textbf{Equation 107}$$

and where Nu_3 arises from

$$\mathrm{Nu}_3 = \left(\frac{2}{1 + 22 \cdot \mathrm{Pr}} \right)^{\frac{1}{6}} \cdot \left(\mathrm{Re} \cdot \mathrm{Pr} \cdot \frac{d_{\mathrm{h}}}{l_{\mathrm{HT}}} \right)^{\frac{1}{2}} \quad .^{103} \qquad \textbf{Equation 108}$$

Nu_1 and Nu_2 are functions of the ratio of the outer diameter of the protection tube of the thermocouple $d_{\mathrm{TC,o}}$ and the inner diameter of the reactor $d_{\mathrm{R,i}}$. Further dependencies exist on the Reynolds number Re, the Prandtl number Pr, and the considered length of the heat transfer region l_{HT}. The Prandtl number is a function of properties of the fluid, namely the dynamic viscosity η, the thermal conductivity λ, and the specific heat capacity at constant pressure c_{p}, following

[103] cp. [VDI, 2006], p. Gb 1 et seqq. Information from [Stephan, 1962] and [Martin, 1990] is provided.

$$\mathrm{Pr} = \frac{\eta \cdot c_\mathrm{p}}{\lambda} \quad . \qquad \textbf{Equation 109}$$

The standard volume flow was varied in the range from 95 sccm to 9800 sccm, when argon was used as dilution gas, and in the range from 2800 sccm and 6500 sccm, when helium was used as dilution gas. For the subsequent calculations the pressure was approximated by the standard pressure p_N, since the aim of the calculations is just an estimation of the order of magnitude of the convective heat transfer coefficient.

Figure 5-4 shows the convective heat transfer coefficient corresponding to the average Nusselt number Nu_ave for different temperatures of the thermocouple and the reactor wall as well as for different standard volume flows of argon. Properties of the fluid, which are respected for the calculation of Nusselt numbers, were determined for an average temperature regarding the temperature of the thermocouple and the reactor wall.

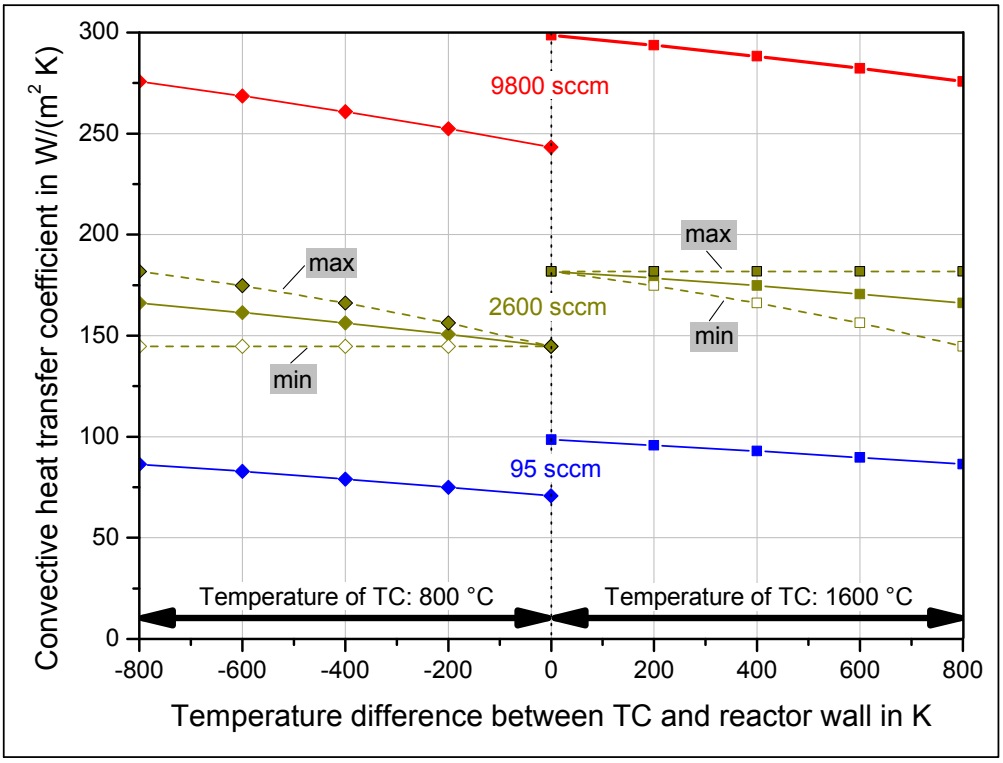

Figure 5-4: Convective heat transfer coefficients for two temperatures of the tip of the thermocouple (800 °C and 1600 °C) as a function of the temperature difference between the thermocouple and the reactor wall as well as of the standard volume flow of argon. Material properties of argon were calculated for the arithmetic mean of the temperature of the thermocouple and the reactor wall and exemplarily for the maximum (max) and minimum (min) temperature of considered combinations. Standard pressure.

Slightly different values can be found if not the average, but respective maximum or minimum temperatures are employed as also shown in the figure. However, values of the heat transfer

coefficient calculated for extreme temperatures do not extend the range of values calculated for average temperatures. The convective heat transfer coefficient strongly depends on the standard volume flow, whereas the influence of temperatures is moderate. Maximum heat transfer coefficients concerning the experiments with argon as the diluent can be found at a level of 300 W/(m^2 K).

Due to the high thermal conductivity of helium, the convective heat transfer coefficient is characterized by higher values compared to calculations with argon as can be seen in Figure 5-5. Here values up to 1100 W/(m^2 K) can be expected.

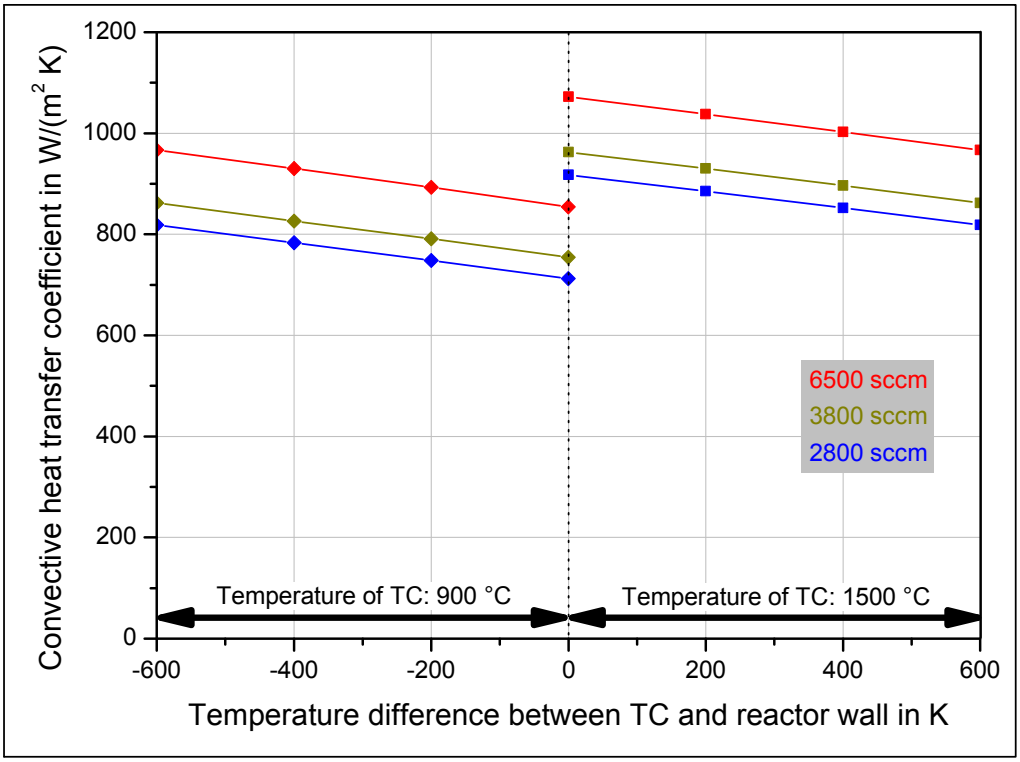

Figure 5-5: Convective heat transfer coefficients for two temperatures of the tip of the thermocouple (900 °C and 1500 °C) as a function of the temperature difference between the thermocouple and the reactor wall as well as of the standard volume flow of helium. Material properties of helium were calculated for the arithmetic mean of the temperature of the thermocouple and the reactor wall. Standard pressure.

5.1.3 Radiative heat transfer

A radiative heat transfer occurred between the wall of the thermocouple and the inner wall of the reactor. The heat flux density on the wall of the thermocouple due to radiation $\dot{q}_{\mathrm{TC,rad}}$, corresponding to the net radiative exchange between the surfaces of the thermocouple and the wall of the reactor, can be calculated by

$$\dot{q}_{\mathrm{TC,rad}} = \alpha_{\mathrm{rad}} \cdot \left(T_{\mathrm{TC,wall}} - T_{\mathrm{R,wall}}\right) \quad , \qquad \textbf{Equation 110}$$

where α_{rad} is the radiative heat transfer coefficient, $T_{\mathrm{TC,wall}}$ represents the temperature of the wall of the protection tube of the thermocouple and $T_{\mathrm{R,wall}}$ stands for the temperature of the inner wall of the reactor.

The radiative heat transfer coefficient arises from

$$\alpha_{\mathrm{rad}} = \frac{C_{\mathrm{TC,R}} \cdot \left(T_{\mathrm{TC,wall}}^4 - T_{\mathrm{R,wall}}^4\right)}{\left(T_{\mathrm{TC,wall}} - T_{\mathrm{R,wall}}\right)} \quad , \qquad \textbf{Equation 111}$$

employing $C_{\mathrm{TC,R}}$, a function comprising the optical and geometrical figures following

$$C_{\mathrm{TC,R}} = \frac{\sigma \cdot \varepsilon_{\mathrm{TC}} \cdot \varepsilon_{\mathrm{R}} \cdot \varphi_{\mathrm{TC,R}}}{1 - \left(1 - \varepsilon_{\mathrm{TC}}\right) \cdot \left(1 - \varepsilon_{\mathrm{R}}\right) \cdot \varphi_{\mathrm{TC,R}} \cdot \varphi_{\mathrm{R,TC}}} \quad , \qquad \textbf{Equation 112}$$

with the Stefan-Boltzmann constant σ, the emissivity of the thermocouple $\varepsilon_{\mathrm{TC}}$, the emissivity of the reactor ε_{R} as well as the view factors $\varphi_{\mathrm{TC,R}}$ and $\varphi_{\mathrm{R,TC}}$.[104]

The view factor $\varphi_{1,2}$ is defined as the fraction of radiation emitted by surface 1 which is captured by surface 2.[105] Since the surface of the reactor wall is much larger than the surface at the tip of the thermocouple and $\varphi_{\mathrm{TC,R}} \approx 1$, which means that approximately all radiation leaving the tip of the thermocouple is intercepted by the surface of the reactor wall, the reciprocity relation for view factors leads to $\varphi_{\mathrm{R,TC}} \approx 0$. Consequently, Equation 112 can be simplified and

[104] cp. [VDI, 2006], p. A 6, p. Ka 7
[105] cp. [Incropera, 2002], p. 790

$$C_{TC,R} \approx \sigma \cdot \varepsilon_{TC} \cdot \varepsilon_{R} \quad . \qquad \textbf{Equation 113}$$

Radiative heat transfer coefficients calculated for two temperatures of the thermocouple and arising from the temperature difference for various temperatures of the reactor wall are presented in Figure 5-6 based on an emissivity function according to Figure 5-3. As can be extracted from the diagram, the radiative heat transfer coefficient lies in the range between 16 W/(m^2 K) and 23 W/(m^2 K).

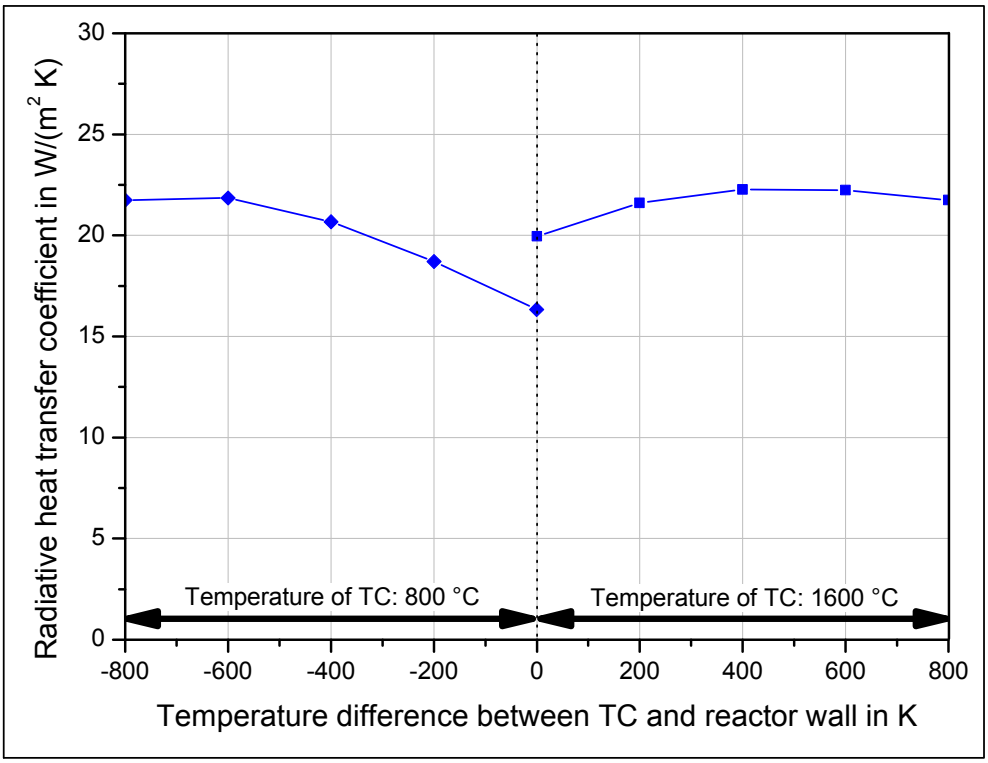

Figure 5-6: Radiative heat transfer coefficients for two temperatures of the tip of the thermocouple (800 °C and 1600 °C) as a function of the temperature difference between the thermocouple and the reactor

5.1.4 Comparison of heat transfer coefficients and consequences

The convective heat transfer coefficient reaches – partly an order of magnitude – higher values than the radiative heat transfer coefficient for all considered combinations as can be seen in Figure 5-7, where the ratio of convective to radiative heat transfer coefficient is depicted. A minimum ratio of about 4, determined for 95 sccm Ar, shows that the heat transfer between the reactor wall as well as the fluid to the thermocouple is dominated by convection. Thus, the measured temperature is predominantly a result of the convective heat transfer between the thermocouple and the surrounding fluid.

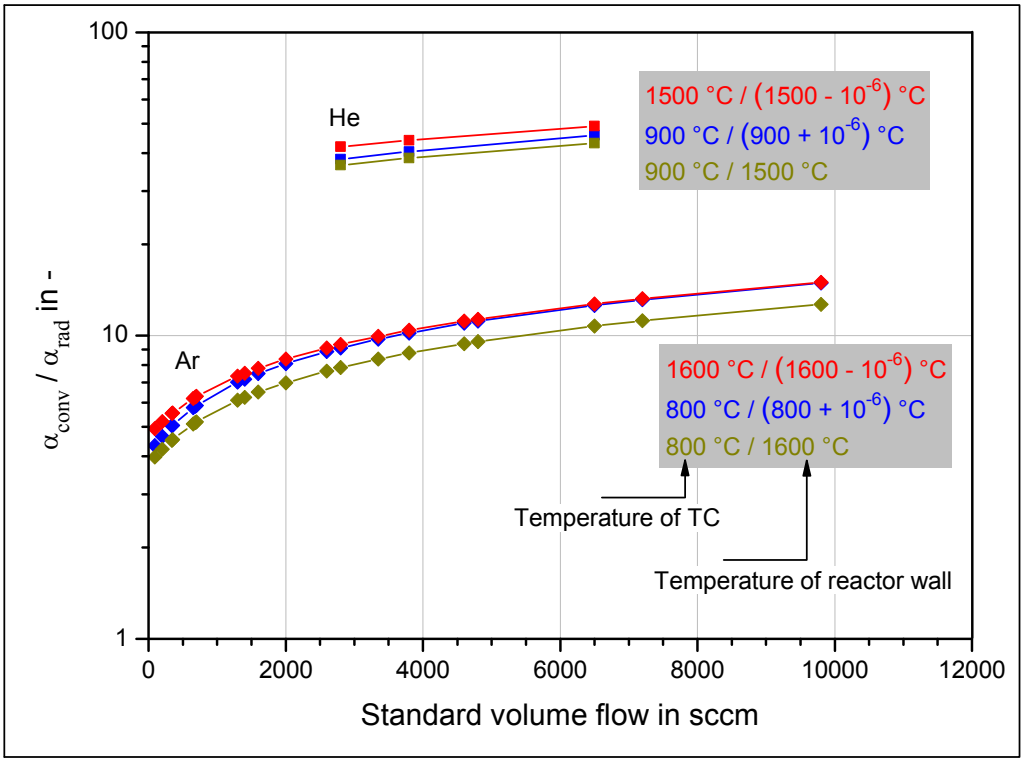

Figure 5-7: Ratio of convective heat transfer coefficient to radiative heat transfer coefficient for different combinations of temperature of the thermocouple (TC) and temperature of the reactor wall as a function of the standard volume flow of argon or helium. Material properties of argon and helium were calculated for the arithmetic mean of the temperature of the thermocouple and the reactor wall. Standard pressure.

However, with the current configuration it was not possible to measure the temperature at a certain point inside the reactor, since the thermocouple covered around 25 % of the cross sectional area of the reactor and consequently the tip of the thermocouple attained a somehow averaged temperature of the fluid in contact. The geometrical situation is illustrated in Figure 5-8.

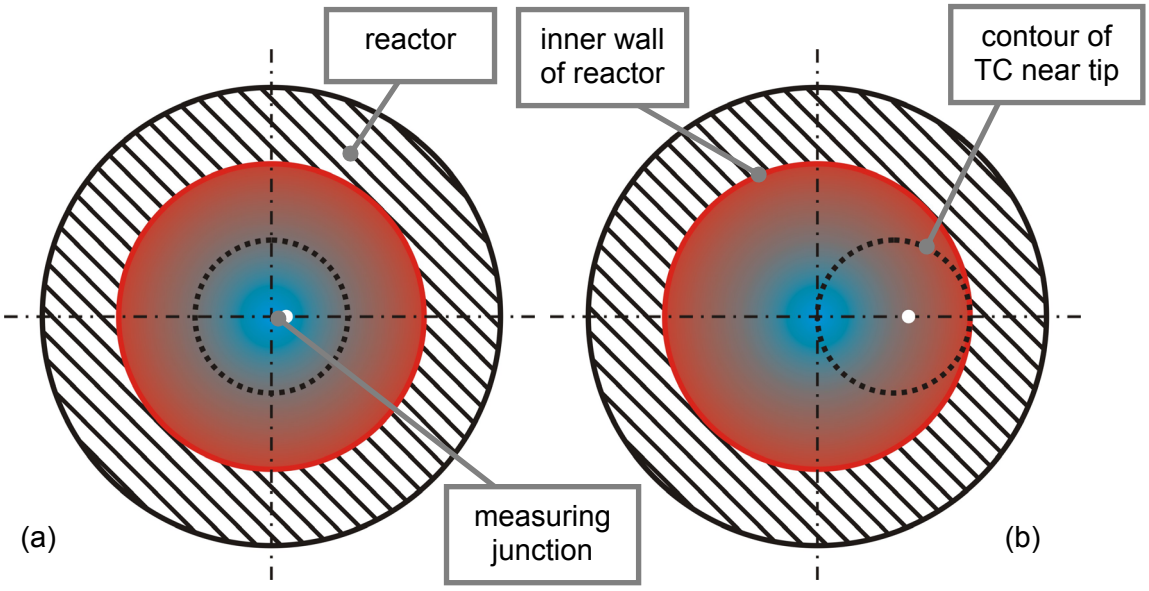

Figure 5-8: Geometrical situation of the thermocouple in center position (a) and in wall position (b) inside the reactor (sectional view). The color illustrates the temperature distribution in front of the thermocouple near the inlet of the reactor (red = hot, blue = cold).

As a result, only reaction conditions characterized by a moderate radial temperature gradient in the relevant region of the reactor should be considered for the kinetic evaluation, meaning the determination of kinetic parameters. A moderate radial temperature gradient assures that the temperatures of the fluid near the thermocouple, which could influence the temperature measurement, do not differ considerably. Consequently, at axial position z the temperature in the center of the reactor, where the radial position accounts for 0, $T_{\mathrm{C}}(z)$ can be well approximated by the temperature of the thermocouple in center position $T_{\mathrm{TC-CP}}(z)$:

$$T_{\mathrm{C}}(z) = T(z, r = 0) \approx T_{\mathrm{TC-CP}}(z) \quad . \qquad \textbf{Equation 114}$$

Moreover, the temperature of the thermocouple in wall position $T_{\mathrm{TC-WP}}(z)$ is a good estimation of the temperature of the wall of the reactor, where the radial position accounts for the inner radius of the reactor $R_{\mathrm{R,i}}$, $T_{\mathrm{W}}(z)$ and the temperature of the fluid next to it:

$$T_{\mathrm{W}}(z) = T(z, r = R_{\mathrm{R,i}}) \approx T_{\mathrm{TC-WP}}(z) \quad . \qquad \textbf{Equation 115}$$

The latter supposition is fortified by the fact that radiative heat transport supported the measurement of the wall temperature. Furthermore, contact between the reactor wall and the tip of the thermocouple in wall position allowed a certain conductive heat transfer.

It is assumed that a moderate radial temperature gradient at position z is fulfilled, when

$$\left| T_{\mathrm{TC-WP}}(z) - T_{\mathrm{TC-CP}}(z) \right| / \mathrm{K} \leq 0.05 \cdot \frac{T_{\mathrm{TC-WP}}(z)/\mathrm{K} + T_{\mathrm{TC-CP}}(z)/\mathrm{K}}{2} \quad . \qquad \textbf{Equation 116}$$

The region of the reactor between $z = 0$, corresponding to the upper edge of the heated region of the tube furnace, and $z = 320\,\mathrm{mm}$, corresponding to the position of the tip of the thermocouple during the cracking experiments, was covered by temperature measurement. Maximum temperatures and by far most of temperatures higher than 75 % of the maximum temperature of the considered temperature profile on a K-scale can be found within the aforementioned limits. This region was considered as the relevant region. It comprises 17 positions, since a step size of 20 mm was chosen for the temperature measurement. The temperature profiles determined with the thermocouple for different sets of nominal furnace

temperature and residence time were examined with respect to the radial temperature gradients. Table 5-2 gives an overview about the percentage of positions with moderate radial temperature gradients inside the relevant region according to the abovementioned definition regarding temperature profiles gained with argon. It was assumed that a percentage higher than 75 % is acceptable and that respective sets of $T_{\text{furnace}} / \tau$ could be employed for the kinetic evaluation, whereas other conditions – eight respecting argon – should be rejected for the evaluation step, due to an increased uncertainty of temperatures resulting from the lower percentage of valid positions.

Table 5-2: Review of temperature profiles gained with argon regarding the existence of moderate radial temperature gradients in the relevant region of reactor

$T_{\text{furnace}} / \tau$ **-set**	T_{furnace} in °C	**Level of** $\dot{V}_{\text{N,Ar}}$ in sccm	**Percentage of positions with moderate radial temperature gradients inside relevant region in %**
1	1200	95	**100** (17 / 17)
2		200	**100** (17 / 17)
3		350	**100** (17 / 17)
4		685	**100** (17 / 17)
5		2000	**88.2** (15 / 17)
6	1300	340	**100** (17 / 17)
7		650	**100** (17 / 17)
8		1300	**100** (17 / 17)
9		2600	**76.5** (13 / 17)
10		4800	**64.7** (11 / 17)
11	1400	700	**100** (17 / 17)
12		1400	**100** (17 / 17)
13		2600	**82.4** (14 / 17)
14		3800	**64.7** (11 / 17)
15		6500	**29.4** (5 / 17)
16	1500	1600	**100** (17 / 17)
17		2800	**82.4** (14 / 17)
18		4600	**58.8** (10 / 17)
19		7200	**29.4** (5 / 17)
20		9800	**0** (0 / 17)
21	1600	2000	**100** (17 / 17)
22		3350	**76.5** (13 / 17)
23		6500	**47.1** (8 / 17)
24		9800	**5.9** (1 / 17)
< 75 %	**75 % – 99.9 %**	**100 %**	

As can be gathered from Table 5-3, regarding helium all sets of nominal furnace temperature and residence time meet the requirements defined above and could be employed for the kinetic evaluation.

Table 5-3: Review of temperature profiles gained with helium regarding the existence of moderate radial temperature gradients in relevant region of reactor

$T_{\text{furnace}} / \tau$ **-set**	T_{furnace} in °C	**Level of** $\dot{V}_{\text{N,He}}$ in sccm	**Percentage of positions with moderate radial temperature gradients inside relevant region in %**
25	1300	3800	**100** (17 / 17)
26	1400	2800	**100** (17 / 17)
27		3800	**100** (17 / 17)
28		6500	**94.1** (16 / 17)
29	1500	3800	**100** (17 / 17)
< 75 %	**75 % – 99.9 %**	**100 %**	

Considering a laminar flow through the reactor a parabolic temperature profile at the axial position z following

$$T(z,r) = T_{\text{W}}(z) + \left(T_{\text{C}}(z) - T_{\text{W}}(z)\right) \cdot \left[1 - \left(\frac{r}{R_{\text{R,i}}}\right)^2\right] \qquad \textbf{Equation 117}$$

is a reasonable approach for the radial temperature distribution $T(z,r)$ inside the tube reactor at the axial position z, employing respective temperatures of the wall and the center of the reactor $T_{\text{W}}(z)$ and $T_{\text{C}}(z)$.[106]

5.2 Diffusion

Diffusion inside the reactor could occur in axial (z) and radial (r) direction. The considered gas mixture only contained methane and argon or helium at the inlet of the reactor. However, while the reactions proceed other substances come into play. The diffusive mass flux density of gas component i in a gas mixture containing N_{species} species $\boldsymbol{j}_i^*$ can be expressed as

[106] cp. [Adunka, 2004], p. 6-34

$$\boldsymbol{j}_i^* = \rho_{\mathrm{mix}} \cdot \sum_{\substack{k=1 \\ k \neq i}}^{N_{\mathrm{species}}} \frac{M_i \cdot M_k}{M_{\mathrm{mix}}^2} \cdot \hat{D}_{i,k} \cdot \nabla x_k \quad , \qquad \textbf{Equation 118}$$

if the average velocity of the mass of a volume element is chosen as the reference. Employed are the density of the gas mixture ρ_{mix}, the molecular weight of the considered component i M_i, of other components k M_k, and of the gas mixture M_{mix} as well as the gradient of the molar fraction of component k ∇x_k. In contrast to the simple formulation of the equation, the diffusion coefficients $\hat{D}_{i,k}$ for gas mixtures comprising more than two species are often unknown.[107]

5.2.1 Axial diffusion

Figure 5-9 represents the Péclet number Pe, calculable by

$$\mathrm{Pe} = \mathrm{Re} \cdot \mathrm{Pr} \quad , \qquad \textbf{Equation 119}$$

as a function of the standard volume flow and the nominal furnace temperature evaluated for standard pressure being a good approximation of pressures observed during the experiments. Axial diffusion is negligible for most reaction conditions, since the Péclet numbers usually exceed a value of 10, which is a reasonable limit for the exclusion of any influences of downstream conditions on the conditions at a certain axial position.[108] However, reaction conditions based on the two lowest standard volume flows of argon at 1200 °C nominal furnace temperature (95 sccm and 200 sccm) undercut the limit of 10, suggesting the disregard of concerned reaction conditions in subsequent kinetic calculations.

[107] cp. [Baehr, 2006], p. 79 (information from [Sherwood, 1975]), p. 248 et seqq. and [VDI, 2006], p. Da 29
[108] cp. [Patankar, 1980], p. 102

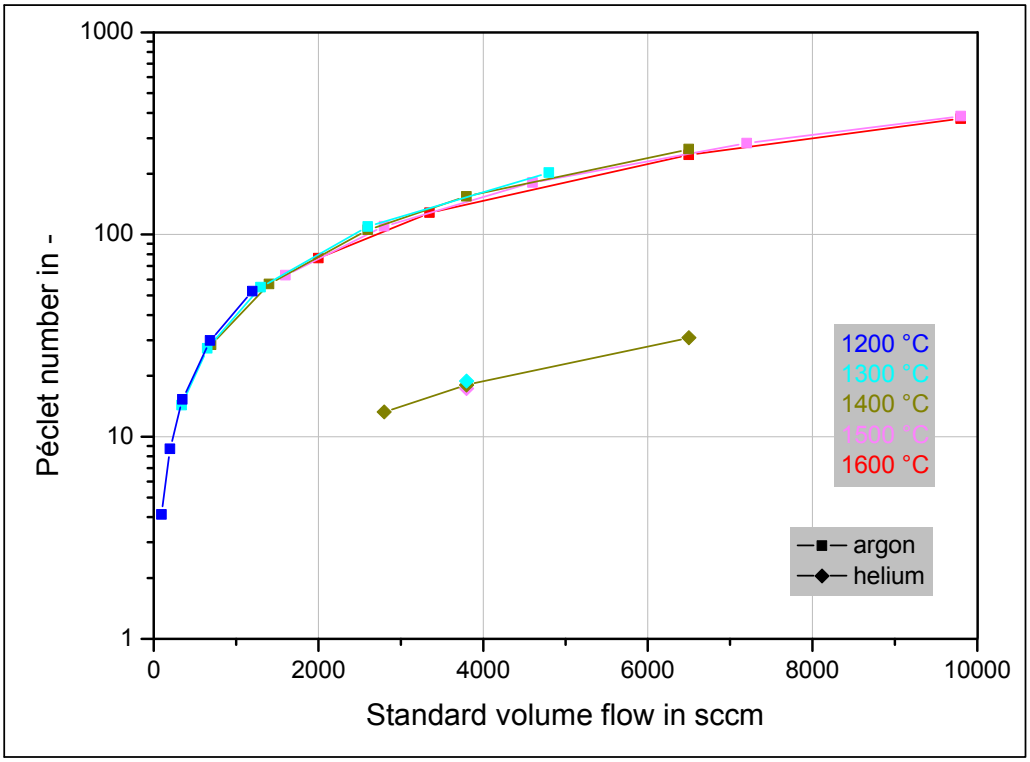

Figure 5-9: Péclet number for different standard volume flows of argon and helium through the tube reactor based on the nominal furnace temperature and standard pressure

5.2.2 Radial diffusion

Diffusive radial molar flows were calculated for each considered product component i, rejecting all other components of the gas mixture except for the dilution gas (DG), in order to assess the relevance of radial diffusive effects. Although strictly speaking these values are only valid for respective binary mixtures, they should lead to a reliable estimation of the order of magnitude of diffusive flows, because in any case the dilution gas forms by far the main fraction of considered gas mixtures. Molar fractions of argon below 80 % were only observed in one case, at reaction conditions based on 20 % initial molar fraction of methane. Corresponding to Fick's Law of Diffusion $j_{i,\mathrm{radial}}$, the diffusive molar flux density in radial direction concerning component i in a binary gas mixture containing component i and the dilution gas (DG) relative to the average radial molar velocity (≈ 0 for laminar flow) can be calculated by

$$j_{i,\mathrm{radial}} = -c \cdot D_{i,\mathrm{DG}} \cdot \frac{\mathrm{d}x_i}{\mathrm{d}r} \quad , \qquad \textbf{Equation 120}$$

where c represents the concentration and $D_{i,\mathrm{DG}}$ the binary diffusion coefficient.[109] According to the ideal gas law[110], the concentration c arises from

$$c = \frac{p}{\Re \cdot T} \quad , \qquad \textbf{Equation 121}$$

with the absolute pressure p, the universal gas constant $\Re$, and the temperature T. Binary diffusion coefficients $D_{i,k}$ also depend on the temperature T as well as on the pressure p and can be approximated by

$$D_{i,k} = \frac{0.00143 \cdot \left(\frac{T}{\mathrm{K}}\right)^{1.75} \cdot \sqrt{\left(\frac{M_i}{\mathrm{g/mol}}\right)^{-1} + \left(\frac{M_k}{\mathrm{g/mol}}\right)^{-1}}}{\frac{p}{\mathrm{bar}} \cdot \sqrt{2} \cdot \left(V_{\mathrm{d},i}^{1/3} + V_{\mathrm{d},k}^{1/3}\right)^2} \cdot 10^{-4} \cdot \frac{\mathrm{m}^2}{\mathrm{s}} \qquad \textbf{Equation 122}$$

for low pressures employing the diffusion volume V_{d} (method of Fuller).[111] The diffusion volume for different species is provided explicitly for simple molecules like helium, argon, and hydrogen, whereas values for more complex molecules like methane and the C_2-hydrocarbons have to be calculated from contributions of different atoms forming the molecule. Respective values are provided in Table 5-4.

Resulting from Equation 121 and Equation 122 $c \cdot D_{i,\mathrm{DG}}$ is independent from the pressure and proportional to $T^{0.75}$. The diffusive flux density reaches its maximum at the highest temperature, which can be approximated by the nominal furnace temperature T_{furnace}.

[109] cp. [Baehr, 2006], p. 79 and [Incropera, 2002], p. 862 et seq.
[110] see Equation 1
[111] cp. [VDI, 2006], p. Da 27 et seq.

Table 5-4: Diffusion volume of various species used for the method of Fuller

Species	V_d in –
argon	16.2
helium	2.67
hydrogen	6.12
methane	25.14 (= 1 * 15.9 + 4 * 2.31)
ethane	45.66 (= 2 * 15.9 + 6 * 2.31)
ethene	41.04 (= 2 * 15.9 + 4 * 2.31)
ethyne	36.42 (= 2 * 15.9 + 2 * 2.31)

A general measure of the relevance of radial diffusive effects may be the here introduced diffusive quotient $Q_{\mathrm{D,radial},i}$, representing the ratio of the molar flux of component i penetrating the cross section of the reactor $\dot{n}_i(z)$ to the estimated characteristic radial molar diffusive flux of component i through a certain diffusion face A_D evaluated at the axial position z $\dot{n}_{\mathrm{D},i}(z)$:

$$Q_{\mathrm{D,radial},i} = \frac{\dot{n}_i(z)}{\dot{n}_{\mathrm{D},i}(z)} = \frac{\dot{n}_i(z)}{j_{i,\mathrm{radial}} \cdot A_\mathrm{D}} \quad . \qquad \textbf{Equation 123}$$

A characteristic diffusion face A_D was defined by $R_\mathrm{D} = 0.002\,\mathrm{m}$, which is half of the inner radius of the reactor ($R_{\mathrm{R,i}} = 0.004\,\mathrm{m}$), and $\Delta z = 0.001\,\mathrm{m}$, being a reasonable increment for kinetic calculations as described later in Chapter 5.5. A respective illustration can be found in Figure 5-10.

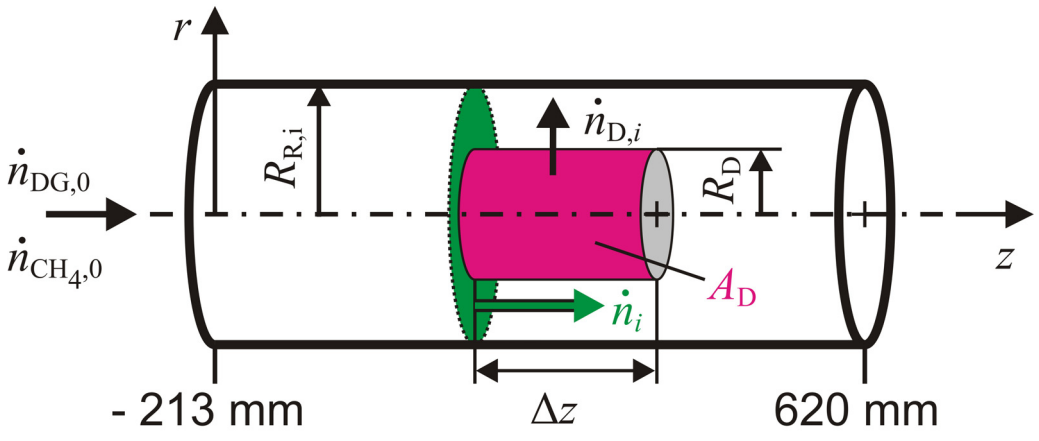

Figure 5-10: Geometric situation in the context of radial diffusion

Since

$$\dot{n}_i(z) = \bar{x}_i(z) \cdot \sum_j \dot{n}_j(z) = \bar{x}_i(z) \cdot \dot{n}_{\mathrm{tot,g}}(z) \quad , \qquad \textbf{Equation 124}$$

employing the average molar fraction of component i at the axial position z $\bar{x}_i(z)$, and

$$\dot{n}_{\mathrm{DG},0} + \dot{n}_{\mathrm{CH_4},0} \leq \dot{n}_{\mathrm{tot,g}} \leq \dot{n}_{\mathrm{DG},0} + 2 \cdot \dot{n}_{\mathrm{CH_4},0} \quad , \qquad \textbf{Equation 125}$$

because a maximum molar flow in the gas phase is achieved for total conversion of methane to hydrogen and carbon, $\dot{n}_{\mathrm{tot,g}}(z)$ can be approximated by

$$\dot{n}_{\mathrm{tot,g}}(z) \approx \dot{n}_{\mathrm{DG},0} + \dot{n}_{\mathrm{CH_4},0} \quad , \qquad \textbf{Equation 126}$$

with a maximum uncertainty of

$$\frac{\dot{n}_{\mathrm{DG},0} + 2 \cdot \dot{n}_{\mathrm{CH_4},0} - \left(\dot{n}_{\mathrm{DG},0} + \dot{n}_{\mathrm{CH_4},0}\right)}{\dot{n}_{\mathrm{DG},0} + \dot{n}_{\mathrm{CH_4},0}} = \frac{\dot{n}_{\mathrm{CH_4},0}}{\dot{n}_{\mathrm{DG},0} + \dot{n}_{\mathrm{CH_4},0}} = x_{\mathrm{CH_4},0} \quad . \qquad \textbf{Equation 127}$$

Thus, the maximum uncertainty implied by the aforementioned approximation of $\dot{n}_{\mathrm{tot,g}}(z)$ is usually below 10 %.

Applying Equation 120, Equation 124 as well as Equation 126 in Equation 123 and substituting finite differences for the derivative of x_i with respect to r, $Q_{\mathrm{D,radial},i}$ can be assessed via

$$Q_{\mathrm{D,radial},i} \approx \frac{\bar{x}_i \cdot \left(\dot{n}_{\mathrm{DG},0} + \dot{n}_{\mathrm{CH_4},0}\right)}{-c \cdot D_{i,\mathrm{DG}} \cdot \frac{\Delta x_i}{\Delta r} \cdot A_{\mathrm{D}}} \quad .$$

Equation 128

It is assumed that the consideration of $\Delta r = R_{\mathrm{R,i}}$ and $\Delta x_i = x_i(r = R_{\mathrm{R,i}}) - x_i(r = 0) = -\bar{x}_i$ lead to reasonable and roughly characteristic values for $Q_{\mathrm{D,radial},i}$, whose calculation then could be simplified to

$$Q_{\mathrm{D,radial},i} \approx \frac{\dot{n}_{\mathrm{DG},0} + \dot{n}_{\mathrm{CH_4},0}}{c \cdot D_{i,\mathrm{DG}} \cdot \frac{A_{\mathrm{D}}}{R_{\mathrm{R,i}}}} \quad ,$$

Equation 129

evaluating $c \cdot D_{i,\mathrm{DG}}$ for the nominal furnace temperature T_{furnace} and the pressure at the inlet of the reactor. $Q_{\mathrm{D,radial,CH_4}}$ is depicted in Figure 5-11 as a function of the residence time, the nominal furnace temperature, the initial molar fraction of methane, and the dilution gas.

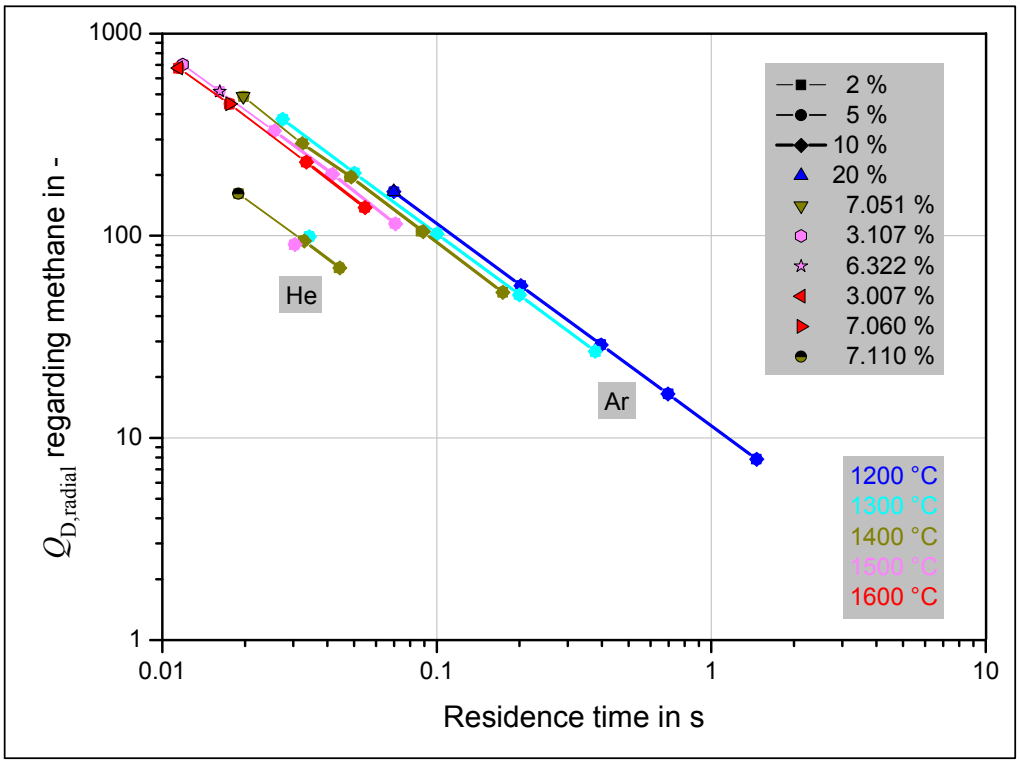

Figure 5-11: Diffusive quotient regarding methane as a function of the residence time, the nominal furnace temperature, the initial molar fraction of methane, and the dilution gas

Since $\dot{n}_{DG,0} + \dot{n}_{CH_4,0}$ is practically constant for a $T_{furnace} / \tau$-set, $Q_{D,radial,CH_4}$ (like all $Q_{D,radial,i}$) is independent from $x_{CH_4,0}$. $Q_{D,radial,CH_4}$ decreases with residence time and temperature. Somewhat lower values for $Q_{D,radial,CH_4}$ are achieved for helium as the dilution gas due to greater values of diffusion coefficients. The graphs indicate that radial diffusive effects may play a role, especially at higher residence times. Similar trends obtain for $Q_{D,radial,H_2}$ as can be seen in Figure 5-12 as well as for $Q_{D,radial,C_2H_6}$, $Q_{D,radial,C_2H_4}$, and $Q_{D,radial,C_2H_2}$ (see Appendix D). While diffusive quotients for C_2-hydrocarbons reach higher values than $Q_{D,radial,CH_4}$, $Q_{D,radial,H_2}$ attains clearly lower values compared to $Q_{D,radial,CH_4}$ resulting from the high diffusivity of hydrogen. This suggests that radial diffusive effects concerning hydrogen could already play a role at lower residence times.

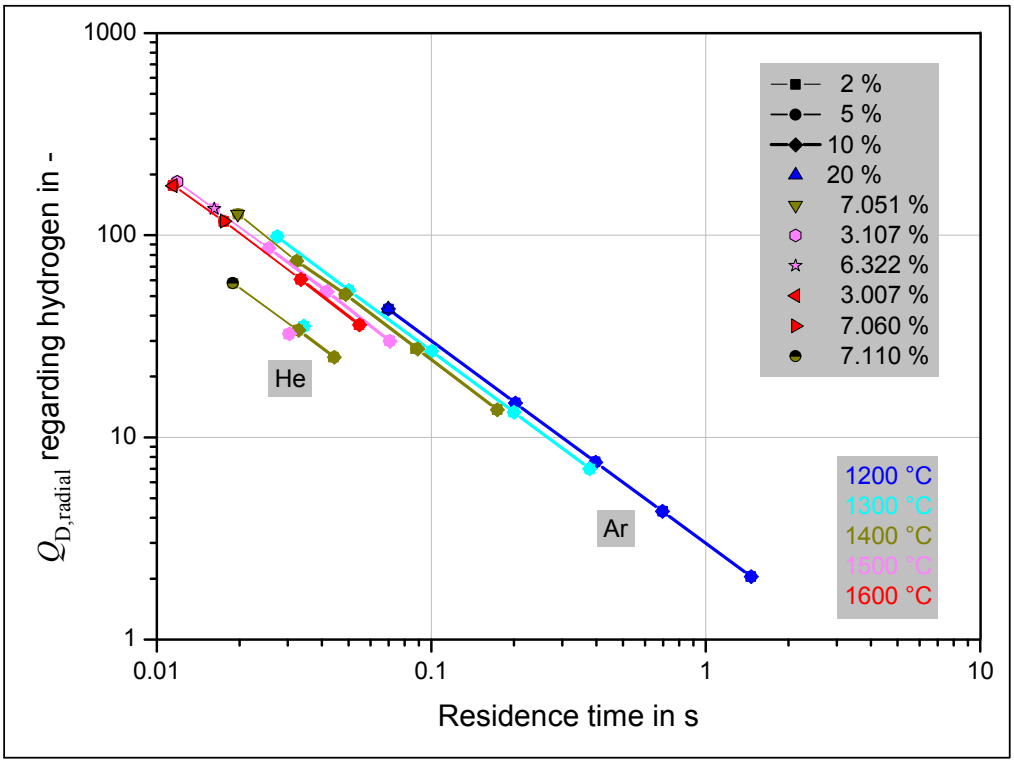

Figure 5-12: Diffusive quotient regarding hydrogen as a function of the residence time, the nominal furnace temperature, the initial molar fraction of methane, and the dilution gas

The present information signifies that radial diffusive effects are mostly of minor importance. However, it has to be kept in mind, that diffusive fluxes were calculated based on a characteristic diffusion face with a length of 1 mm. Consequently, even for lower values of $Q_{D,radial,i}$ diffusive fluxes could accumulate over several step sizes through the reactor. Moreover, the evolution of x_i in the reactor has to be evaluated later in order to verify abovementioned presumptions.

5.3 Flow model

In order to investigate the character of the flow inside the reactor, simulations were carried out employing ANSYS[112] for the unheated entrance region upstream the inlet of the reactor and COMSOL Multiphysics[113] for the reactor itself. According to the measurement of temperature profiles, only the dilution gases were considered in the gas phase. Employed material property functions form part of Appendix D.

5.3.1 Flow conditions at the inlet of the reactor

Figure 5-13 represents the geometry upstream the inlet of the reactor, which was named the entrance region of the reactor. All parts of the entrance region have an inner diameter of 0.008 m.

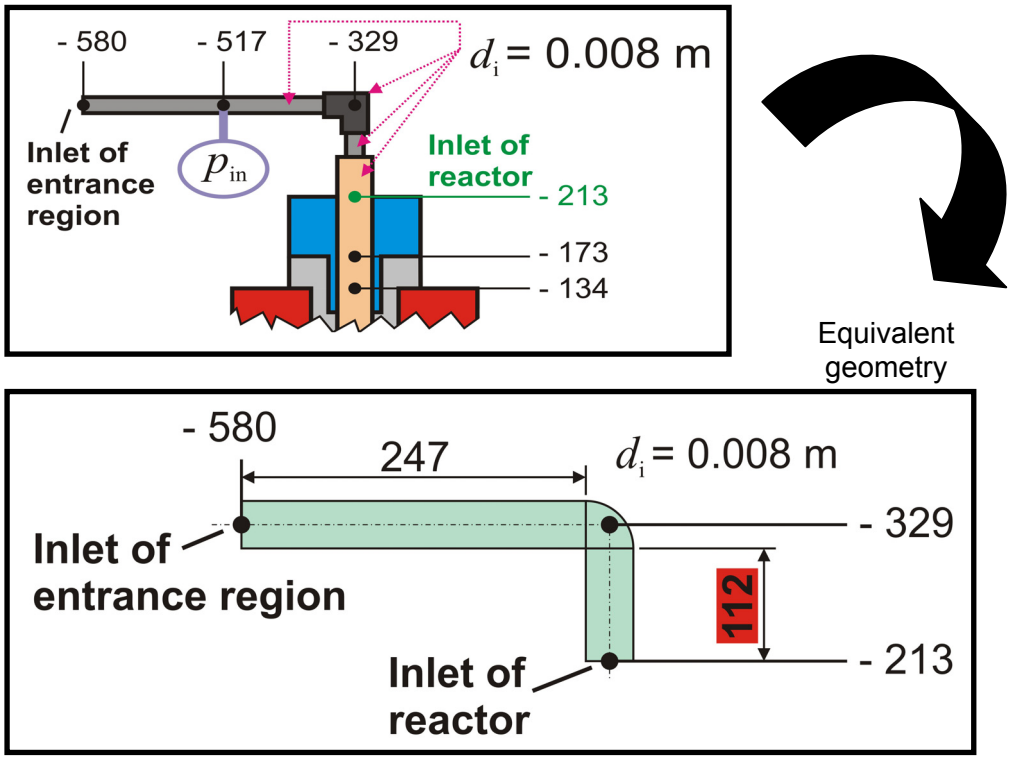

Figure 5-13: Geometry upstream the inlet of the reactor (entrance region). Dimensions and axial positions in mm unless otherwise stated.

As stated before, the Reynolds number, which is amongst others a function of the hydraulic diameter d_h, provides information about the general character of a flow. For round tubes with an inner diameter d_i, it can be shown that

[112] ANSYS 12.0.1
[113] COMSOL Multiphysics 3.4.0.248

$$d_h = d_i \quad .$$ **Equation 130**

Reynolds numbers calculated for the conditions in the entrance region are lower than 2300 and denote that a laminar flow has to be considered in the entrance region (like also in the reactor).[114] The entry length l_e complies with the length of the region downstream an elbow or a vessel outlet, where the velocity profile of a flow has not developed entirely yet and can be estimated by

$$l_e = b_{lam} \cdot \mathrm{Re} \cdot d_i \quad ,$$ **Equation 131**

with $b_{lam} = 0.06$.[115] Table 5-5 provides information about the Reynolds number in the entrance region and at the inlet of the reactor as well as the corresponding entry length regarding argon. The entry length lies in the range between 0.0097 m and 0.9983 m.

Respective information about the entry lengths to be taken into account for helium is given in Table 5-6. It can be seen that a significantly shorter distance is necessary in order to achieve a developed flow. Values for the entry length are clearly below 0.08 m.

[114] cp. Chapter 5.1.2
[115] cp. [Munson, 2002], p. 448 and [Schröder, 2000], p. 148. Other value: 0.056, cp. [Baehr, 2006], p. 374.

Table 5-5: Reynolds numbers at the inlet of the reactor and corresponding entry lengths for argon

T_{furnace} / τ **-set**	T_{furnace} in °C	$\dot{V}_{\text{N,tot,0}}$ in sccm	Re	l_e in m
1	1200	95	20	0.0097
2		200	42	0.0204
3		350	69	0.0333
4		685	145	0.0697
5		2000	424	0.2036
6	1300	340	71	0.0343
7		650	138	0.0661
8		1300	276	0.1324
9		2600	531	0.2548
10		4800	937	0.4496
11	1400	700	136	0.0654
12		1400	297	0.1424
13		2600	552	0.2649
14		3800	805	0.3862
15		6500	1378	0.6616
16	1500	1600	318	0.1529
17		2800	560	0.2689
18		4600	929	0.4460
19		7200	1462	0.7016
20		9800	1997	0.9587
21	1600	2000	393	0.1888
22		3350	710	0.3408
23		6500	1377	0.6608
24		9800	2080	0.9983

Table 5-6: Reynolds numbers at the inlet of the reactor and corresponding entry lengths for helium

T_{furnace} / τ **-set**	T_{furnace} in °C	$\dot{V}_{\text{N,tot,0}}$ in sccm	Re	l_e in m
25	1300	3800	88	0.0422
26	1400	2800	64	0.0310
27		3800	89	0.0428
28		6500	153	0.0734
29	1500	3800	88	0.0422

As can be seen in Figure 5-13, the length of the straight part of constant inner diameter above the inlet of the reactor equals 112 mm. As a consequence, a fully developed laminar velocity profile cannot be guaranteed for all experimental conditions leading to an entry length longer than 112 mm. Consulting Table 5-5, it becomes clear that applied experimental conditions

based on argon standard volume flows above 700 sccm lead to an entry length longer than the provided vertical way within the entrance region. Contrariwise, 112 mm are long enough to ensure a fully developed velocity profile for all applied experimental conditions regarding helium, due to the low Reynolds numbers. An ideal, fully developed laminar velocity profile $v(r)$ follows

$$v(r) = 2 \cdot \bar{v} \cdot \left[1 - \left(\frac{r}{R_\mathrm{i}} \right)^2 \right] \quad ,^{116}$$ **Equation 132**

with the inner radius of the considered tubular part R_i and the average velocity according to Equation 102 evaluated for the conditions at the inlet of the reactor defined by the temperature $T_\mathrm{R,inlet}$ and the pressure $p_\mathrm{R,inlet}$.

In order to provide appropriate information about the flow conditions at the inlet of the reactor for argon standard volume flows above 700 sccm and to know how much the actual velocity profile differs from the ideal one, the flow through the entrance region was simulated with ANSYS. Information about the geometry of the ANSYS model of the entrance region as well as about the mesh of the reactor inlet face is provided in Figure 5-14. Velocities along two lines on the reactor inlet face perpendicular to the axis of the reactor and to each other, namely Line X and Line Z, were evaluated. Both lines have a length of 8 mm corresponding to the diameter of the reactor. A position on Line X and Line Z relative to the center position is indicated by ΔX_Line and ΔZ_Line, respectively. Further information about the configuration of the ANSYS models can be found in Appendix E.

[116] cp. [Baehr, 2006], p. 376

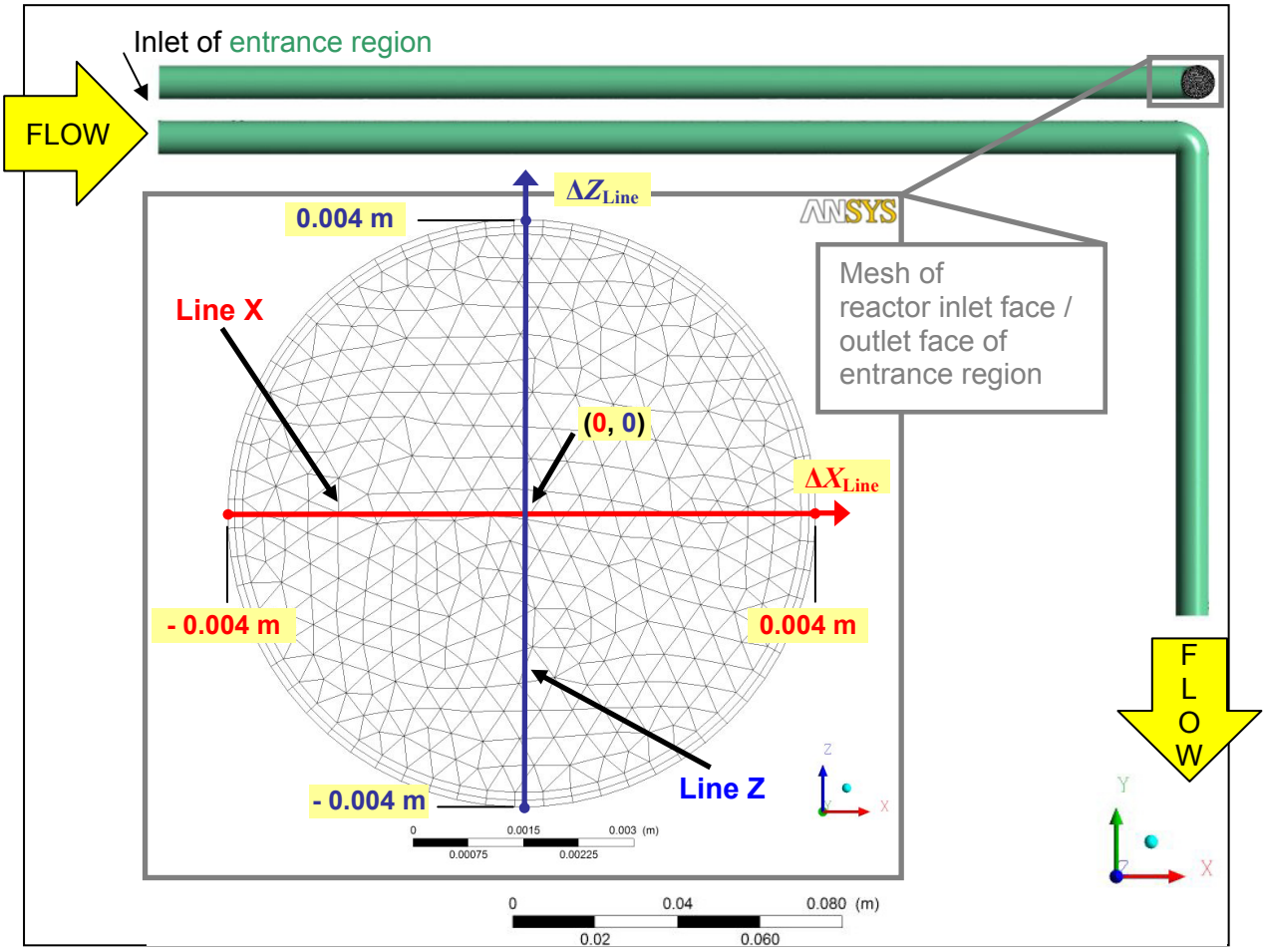

Figure 5-14: Basics concerning the ANSYS 12 model of the entrance region as well as positions of Line X and Line Z on the reactor inlet face

Figure 5-15 shows the result of the flow simulation with ANSYS 12 concerning the velocity component v in Y-direction, which is the direction normal to the reactor inlet face, for T_{furnace}/τ-set 11 based on a standard volume flow of 700 sccm Ar. Velocities u and w at the reactor inlet in X- and Z-direction, respectively, are usually significantly lower than the velocity in Y-direction and are not considered in the following.

The velocity v (multiplied by - 1 in order to provide positive values) along Line X and Line Z is represented in Figure 5-16 together with the fully developed laminar velocity profile for T_{furnace}/τ-set 11 (700 sccm Ar). As indicated by Equation 131, the length between the elbow of the entrance region and the inlet of the reactor is adequately long resulting in an almost completely mature velocity profile. Velocities along Line X and Line Z are practically equal to each other and velocities in Y-direction for an ideally laminar profile.

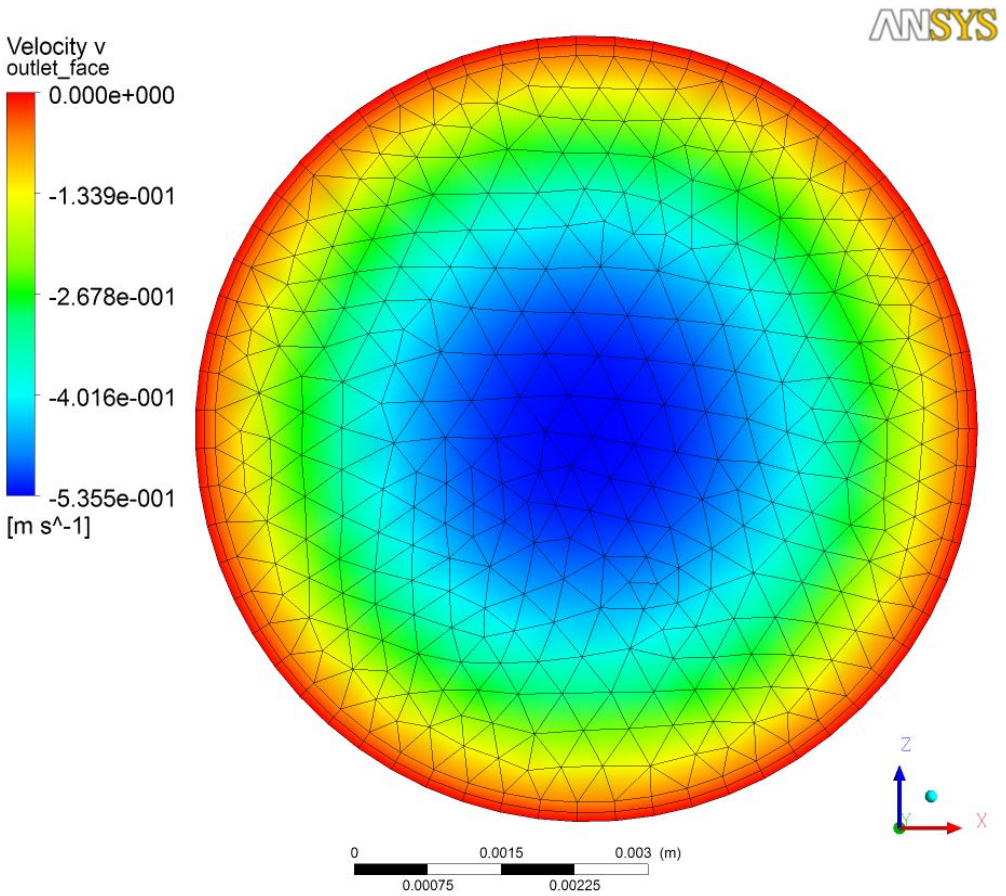

Figure 5-15: Results of flow simulations with ANSYS 12 – Velocity in Y-direction (normal to face) at the reactor inlet for a standard volume flow of 700 sccm Ar

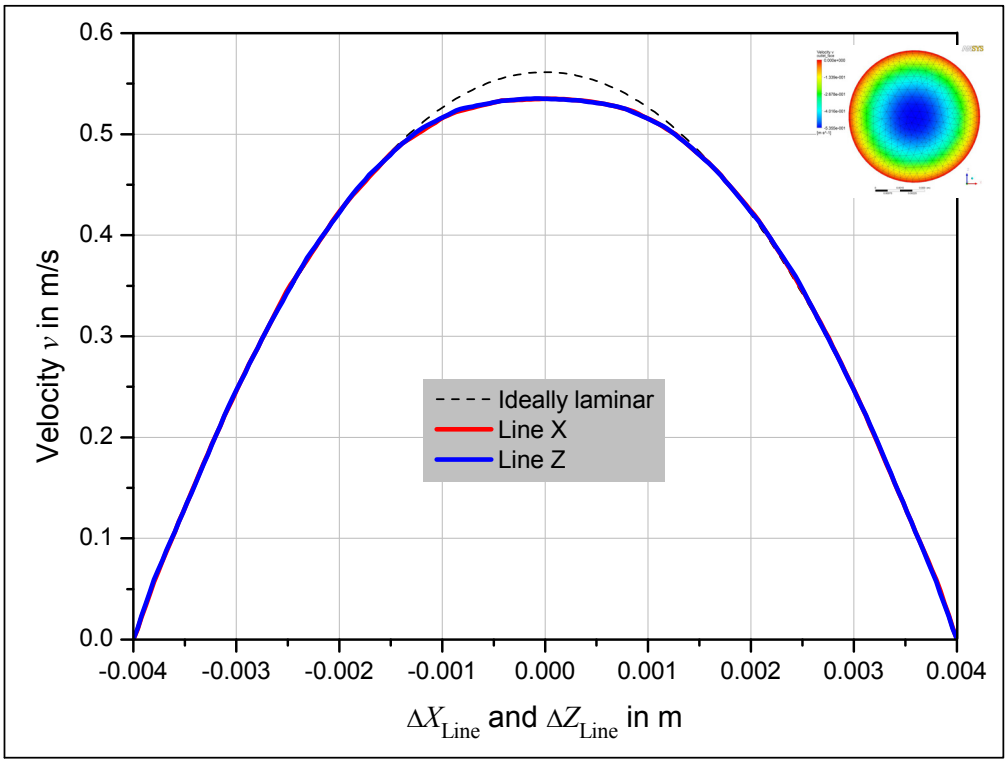

Figure 5-16: Results of ANSYS 12 calculations for the velocity in Y-direction (normal to face) along Line X and Line Z at the reactor inlet compared to an ideally laminar velocity profile. Corresponding conditions: 700 sccm Ar and 1400 °C nominal furnace temperature.

As expected, a higher volume flow in the entrance region causes a worse congruence of the ideally laminar profile and the of velocity profiles along Line X and Line Z. Figure 5-17 expresses the simulation output for $T_{\text{furnace}} / \tau$-set 13 (1400 °C, 2600 sccm Ar).

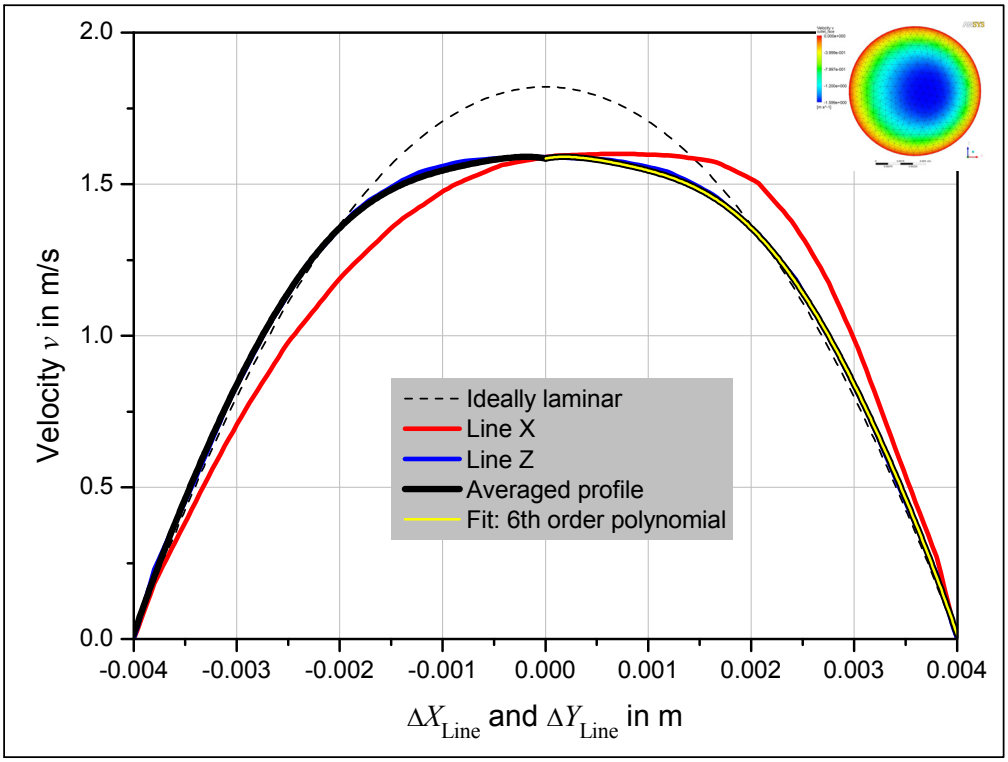

Figure 5-17: Results of ANSYS 12 calculations for the velocity in Y-direction (normal to face) along Line X and Line Z at the reactor inlet compared to an ideally laminar velocity profile. Corresponding conditions: 2600 sccm Ar and 1400 °C nominal furnace temperature.

In order to provide plausible information about the velocity distribution at the inlet of the reactor for subsequent 2D-simulations with COMSOL Multiphysics, velocity profiles determined by ANSYS had to be transformed into a reasonably averaged velocity profile. This was attempted by firstly computing an average value for every distance from the center point on Line X and Line Z following

$$\bar{v}_{\text{Line X}}(\Delta X_{\text{Line}}) = \bar{v}_{\text{Line X}}(-\Delta X_{\text{Line}}) = 0.5 \cdot \left[v(\Delta X_{\text{Line}}) + v(-\Delta X_{\text{Line}}) \right] \qquad \textbf{Equation 133}$$

as well as

$$\bar{v}_{\text{Line Z}}(\Delta Z_{\text{Line}}) = \bar{v}_{\text{Line Z}}(-\Delta Z_{\text{Line}}) = 0.5 \cdot \left[v(\Delta Z_{\text{Line}}) + v(-\Delta Z_{\text{Line}}) \right] \quad , \qquad \textbf{Equation 134}$$

and secondly by averaging the so determined velocity profiles by

$$\bar{v}_{\text{Line X+Z}}(\Delta X_{\text{Line}}) = \bar{v}_{\text{Line X+Z}}(-\Delta X_{\text{Line}}) = \bar{v}_{\text{Line X+Z}}(\Delta Z_{\text{Line}}) = \bar{v}_{\text{Line X+Z}}(-\Delta Z_{\text{Line}})$$
$$= 0.5 \cdot \left[\bar{v}_{\text{Line X}}(\Delta X_{\text{Line}}) + \bar{v}_{\text{Line Z}}(\Delta Z_{\text{Line}})\right] \quad \text{, with } \left|\Delta X_{\text{Line}}\right| = \left|\Delta Z_{\text{Line}}\right| \qquad \text{Equation 135}$$

Velocity profiles calculated for $T_{\text{furnace}} / \tau$-set 24 (1600 °C, 9800 sccm Ar), which show the greatest discrepancy compared to the ideal case, are depicted in Figure 5-18.

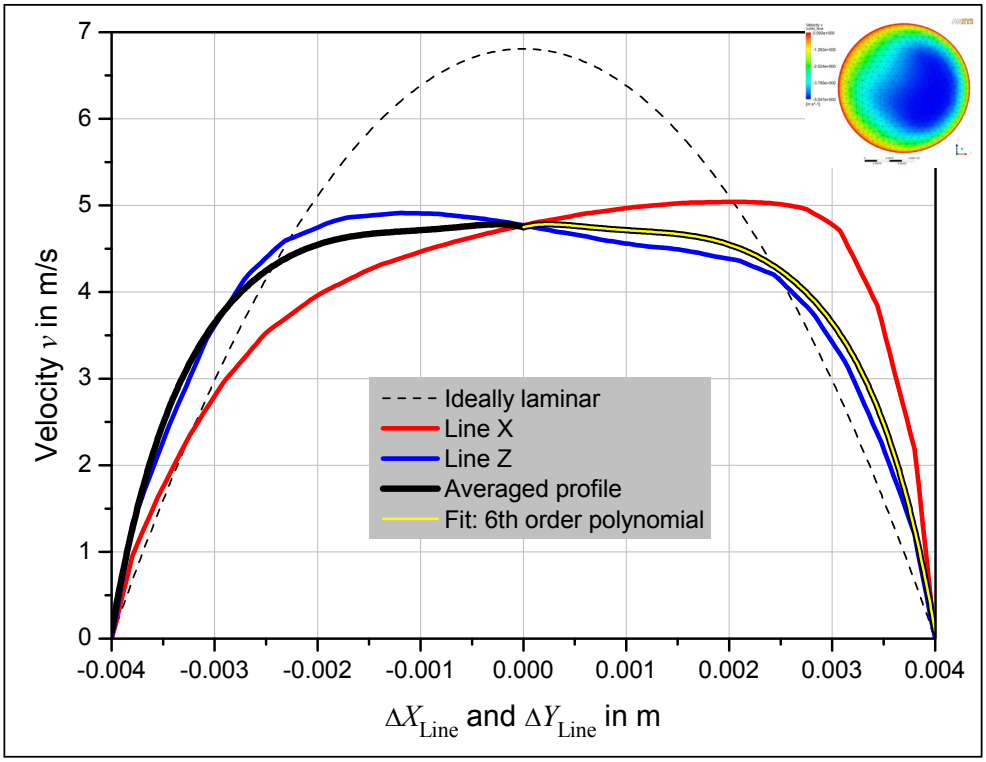

Figure 5-18: Results of ANSYS 12 calculations for the velocity in Y-direction (normal to face) along Line X and Line Z at the reactor inlet compared to an ideally laminar velocity profile. Corresponding conditions: 9800 sccm Ar and 1600 °C nominal furnace temperature.

With the intention of providing values for the velocity in Y-direction, normal to the reactor inlet face, at the reactor inlet as a function of the radial position r, 6th order polynomial fit functions were applied to the averaged velocity profiles $\bar{v}_{\text{Line X+Z}}$ according to

$$\bar{v}_{\text{Line X+Z,fitted}}(r) = k_6 \cdot r^6 + k_5 \cdot r^5 + k_4 \cdot r^4 + k_3 \cdot r^3 + k_2 \cdot r^2 + k_1 \cdot r + k_0 \qquad r \geq 0 \qquad \text{Equation 136}$$

as can be seen in Figure 5-17 and Figure 5-18. The coefficients k_6, k_5, k_4, k_3, k_2, k_1, and k_0 for sets of nominal furnace temperature and standard volume flow, with an calculated entry length longer than the provided distance of 112 mm are provided in Appendix E along with further ANSYS results concerning the components of velocity in X-, Y-, and Z-direction on the

reactor inlet face. The conformance of $\bar{v}_{\text{Line X+Z}}$ and $\bar{v}_{\text{Line X+Z,fitted}}$ satisfies at least 99.2 % and typically around 99.6 % for the respected conditions. Additional calculations considering not only argon but a mixture of argon and methane with 10 % molar fraction of the latter species led to the conclusion that differences between $\bar{v}_{\text{Line X+Z,fitted}}$ for the pure argon flow and the gas mixture are negligible.

5.3.2 Flow conditions inside the reactor

The fit functions for the averaged velocity profiles at the inlet of the reactor resulting from ANSYS calculations were employed in subsequent simulations with COMSOL Multiphysics 3.4. The usage of COMSOL Multiphysics targeted a better impression about probable conditions inside the reactor. An overview about the geometry and basic settings of the defined 2D reactor model is provided in Figure 5-19. The inlet of the reactor model used in COMSOL Multiphysics corresponds to the axial position $z = 0$, whereas the outlet of the reactor can be found at position $z = 0.833\,\text{m}$. The thermocouple was implemented as a solid and uniform body in order to reduce the complexity of the model. The wall thickness of the reactor was virtually decreased to 1 mm. However, an influence on the results of the simulation is not expected, due to the fact that the temperature of the inner wall of the reactor was provided anyway.

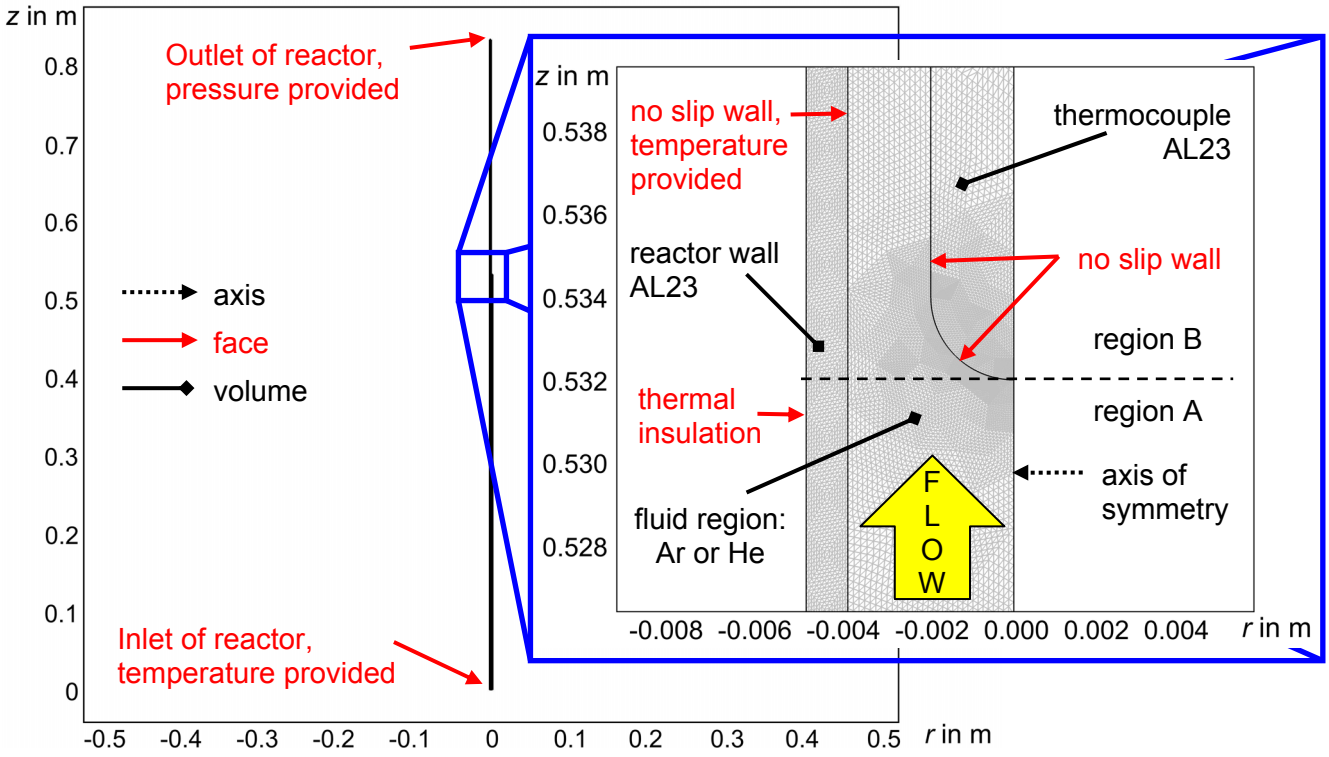

Figure 5-19: Geometry of the reactor model in COMSOL Multiphysics with the reactor wall, the fluid region, and the thermocouple (TC) along with basic settings. Level of mesh refinement: 3.

The conditions in the reactor were simulated based on the weakly compressible Navier-Stokes mode concerning the flow as well as on convection and conduction concerning the heat transfer. The weakly compressible Navier-Stokes mode comprises the fully compressible composition of the equation of continuity as well as the equations of momentum and is applicable for Mach numbers below 0.3. The Mach number is defined as

$$\mathrm{Ma} = \frac{v}{v_{\mathrm{sound}}} \quad , \qquad \textbf{Equation 137}$$

with the velocity v and the velocity of sound v_{sound}, which for an ideal gas arises from

$$v_{\mathrm{sound}} = \sqrt{R \cdot T \cdot \kappa} \quad , \qquad \textbf{Equation 138}$$

employing the specific gas constant R, the temperature T, and the specific heat ratio κ.[117] The specific gas constant R is connected to the universal gas constant $\Re$ by

$$R = \frac{\Re}{M} \quad , \qquad \textbf{Equation 139}$$

where M represents the molecular weight of the considered gas, while the specific heat ratio κ is defined as

$$\kappa = \frac{c_{\mathrm{p}}}{c_{\mathrm{v}}} \quad .^{118} \qquad \textbf{Equation 140}$$

Furthermore, the difference between the specific heat capacity at constant pressure c_{p} and the specific heat capacity at constant volume c_{v} results in the specific gas constant R:

[117] cp. [Munson, 2002], p. 686 et seqq.
[118] cp. [Munson, 2002], p. 680 et seqq.

$$c_p - c_v = R \quad . \qquad \textbf{Equation 141}$$

It can be shown, that a maximum Mach number around 0.03 for experiments with argon can be expected, whereas lower Mach numbers in the range of 0.006 represent the upper limit for experiments with helium. Consequently, the weakly compressible Navier-Stokes mode is applicable.

In absence of definite information about the wall temperatures of the reactor, especially in the part above the heated region of the reactor, simplified temperature profiles for the wall were applied for the calculations with COMSOL Multiphysics. These simplified wall temperature profiles were defined by

- the nominal furnace temperature within the heated length of the reactor ($0.213\,\mathrm{m} \le z \le 0.463\,\mathrm{m}$, corresponding to position 0 mm… 250 mm),
- the measured temperature at the inlet of the reactor ($z = 0$, corresponding to position - 213 mm),
- the measured temperature at the outlet of the reactor ($z = 0.833\,\mathrm{m}$, corresponding to position 620 mm), and
- linear interpolation for positions in between.

Preliminary calculations employing the established equations for the pressure drop in a laminar pipe flow indicated that the difference between the pressure at the inlet of the reactor and the outlet of the reactor should be marginal for the considered conditions.[119] Higher measured pressure differences might have been a result of carbon deposit in region B as explained in Chapter 5.3.2.3. Therefore it is admissible to state that the pressure measured at the inlet of the reactor is relevant for the major part of the reactor. Thus, the pressure at the outlet of the reactor was set to the pressure measured at the reactor inlet.

The mesh was refined until the output of the simulations was independent from the level of refinement. The independence was achieved for level 3 of mesh refinement corresponding to 187189 nodes and 366912 elements. The reactor wall and the thermocouple were modeled according to material properties presented in Chapter 5.1.1. However, the significance of AL23 properties on the results of the calculation is marginal. Although high temperatures – existent in

[119] Respective equations can e. g. be found in [VDI, 2006], p. Lab 1 et seqq.

the cracking reactor – suggest the consideration of radiative heat transfer, simulations without are valid for the greatest part of the reactor, since the inert gases argon and helium represent transparent phases. The implementation of radiative heat transfer only influences the temperature distribution downstream the tip of the thermocouple, where radiative exchange occurs between the inner wall of the reactor and the surface of the thermocouple. Keeping the approximate character of the calculations in mind, the implementation of radiation was rejected in favor of a better time efficiency of the simulations. Further details characterizing the model designed with COMSOL Multiphysics can be found in Appendix F.

5.3.2.1 Temperature distribution

Depending on the standard volume flow through the reactor and the provided temperature of the inner wall of the reactor, the fluid region (as well as the thermocouple) attains particular temperature distributions as illustrated in Figure 5-20 showing views not true to scale.

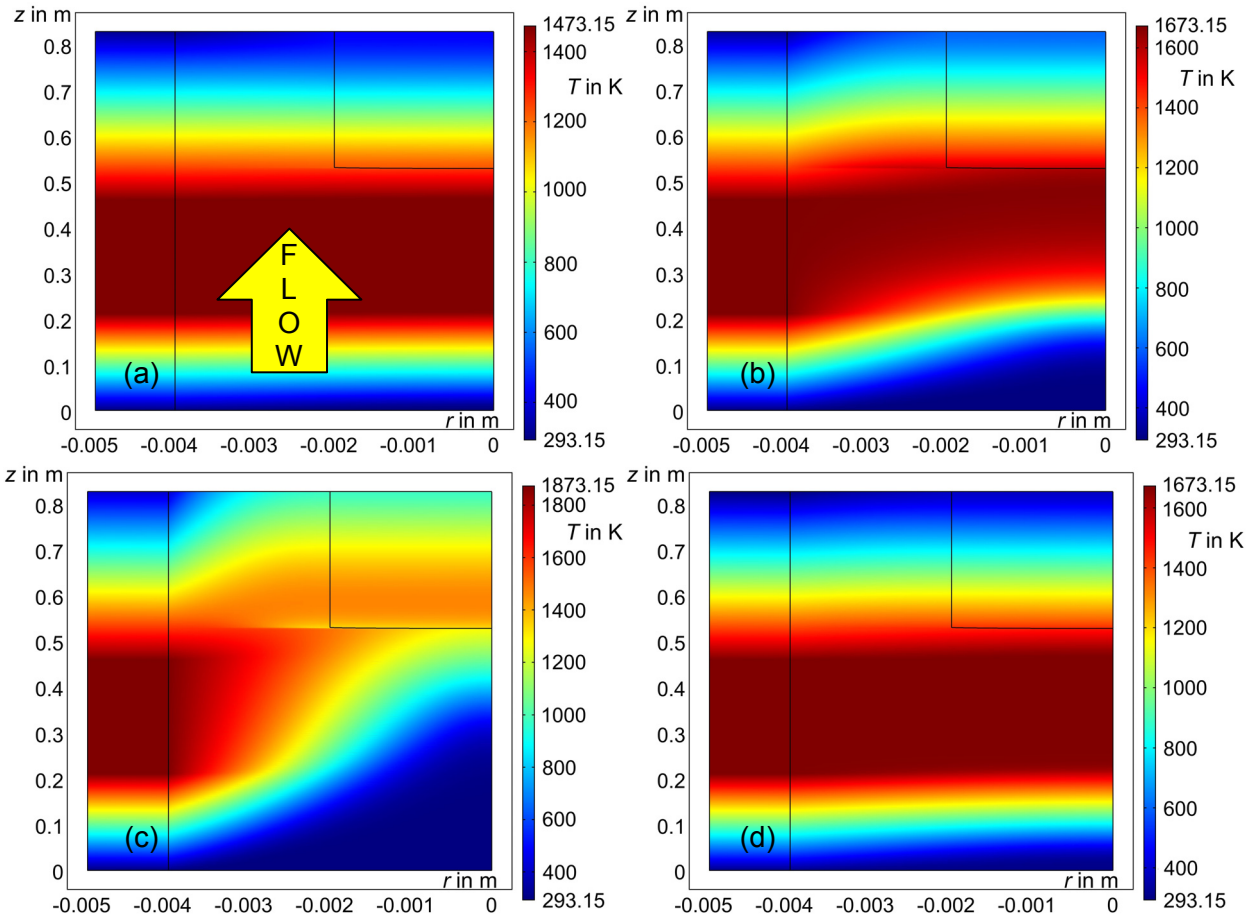

Figure 5-20: Results of COMSOL Multiphysics calculations based on a simplified temperature profile for the wall of the reactor concerning the temperature distribution in the reactor, in the wall of the reactor as well as in the thermocouple for different sets of nominal furnace temperature and standard volume flow: 1200 °C - 95 sccm Ar (a), 1400 °C - 2600 sccm Ar (b), 1600 °C - 9800 sccm Ar (c), and 1400 °C - 3800 sccm He (d)

The higher the standard volume flow the greater are the radial differences in temperature. Due to better thermal conductivity characteristics, radial temperature profiles for helium are more

even than for argon. Figure 5-21 shows the results of COMSOL Multiphysics calculations concerning the center temperature ($r = 0$) in region A as well as the temperature along the wall of the thermocouple ($r = 0.002\ \mathrm{m}$) in region B compared to the temperature profiles determined by thermocouple measurements for selected sets of nominal furnace temperature and standard volume flow. Corresponding to Figure 5-20 the difference between the temperature in the center of the reactor and the applied temperature of the wall increases when the standard volume flow increases.

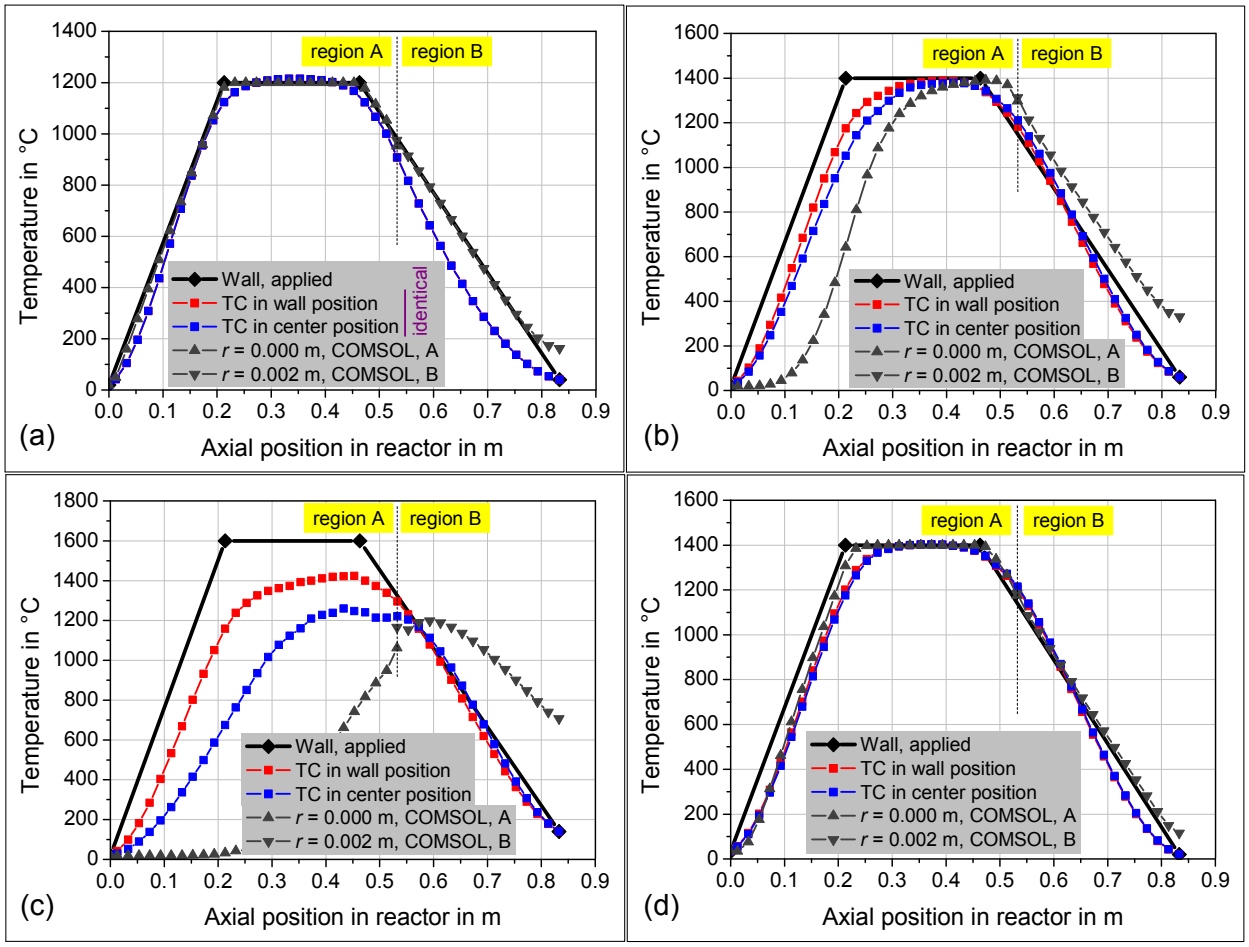

Figure 5-21: Results of COMSOL Multiphysics calculations based on a simplified temperature profile for the wall of the reactor concerning the temperature evaluation in the center of region A and along the wall of the thermocouple in region B compared to measurement with a thermocouple in wall and center position for different sets of nominal furnace temperature and standard volume flow: 1200 °C - 95 sccm Ar (a), 1400 °C - 2600 sccm Ar (b), 1600 °C - 9800 sccm Ar (c), and 1400 °C - 3800 sccm He (d)

Although calculated and real values of temperature in the center of the reactor may differ in detail, for instance due to the simplified applied wall temperature, the shape of the graphs suggests that it is applicable to interpret the measured temperatures of the thermocouple in wall and center position as a somehow averaged temperature of the fluid in contact.[120]

[120] cp. Chapter 5.1.4

Consequently, basic characteristics of the results of the flow simulations should be transferable to the real situation.

5.3.2.2 Flow lines and nested tube reactors

In every case, flow lines show a certain kind of order more or less matching the ideal laminar flow conditions, which would be represented by flow lines parallel to the rotation axis of the reactor characterized by $r = 0$. The flow lines for helium and for low standard volume flows of argon show good parallelism. However, the higher the standard volume flow the worse is the congruence with the ideally laminar situation. Further figures of flow lines can be found in Appendix F.

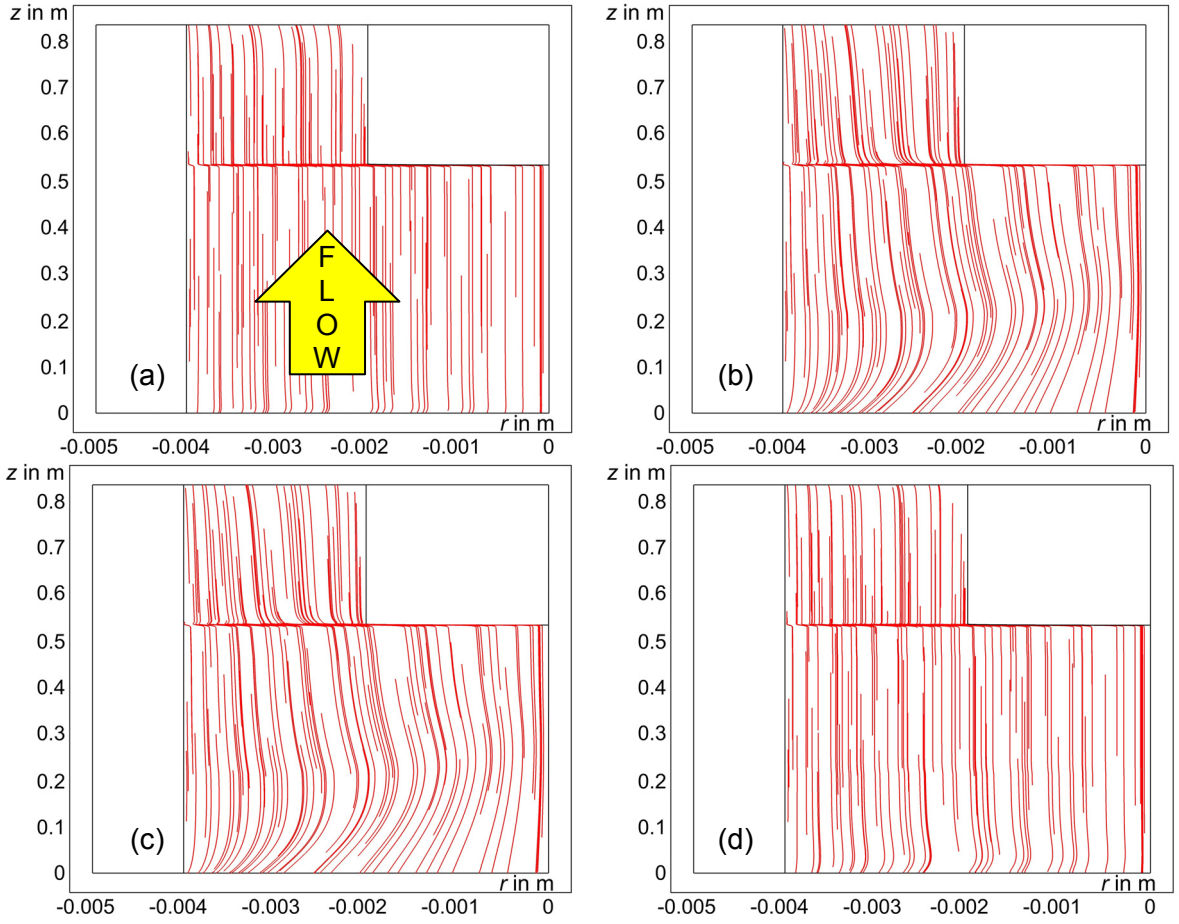

Figure 5-22: Results of COMSOL Multiphysics calculations based on a simplified temperature profile for the wall of the reactor concerning flow lines for different sets of nominal furnace temperature and standard volume flow: 1200 °C - 95 sccm Ar (a), 1400 °C - 2600 sccm Ar (b), 1600 °C - 9800 sccm Ar (c), and 1400 °C - 3800 sccm He (d)

A plug flow reactor model considers a turbulent flow and consequently an equal residence time of every volume element entering the reactor. Contrariwise, a laminar flow features different residence times depending on the radial position. The radial position of a volume element being part of an ideally laminar flow keeps constant on its way through the reactor. In order to reflect

different residence times of volume elements, the reactor was virtually divided into nested tube reactors (NTR) as presented in Figure 5-23.[121]

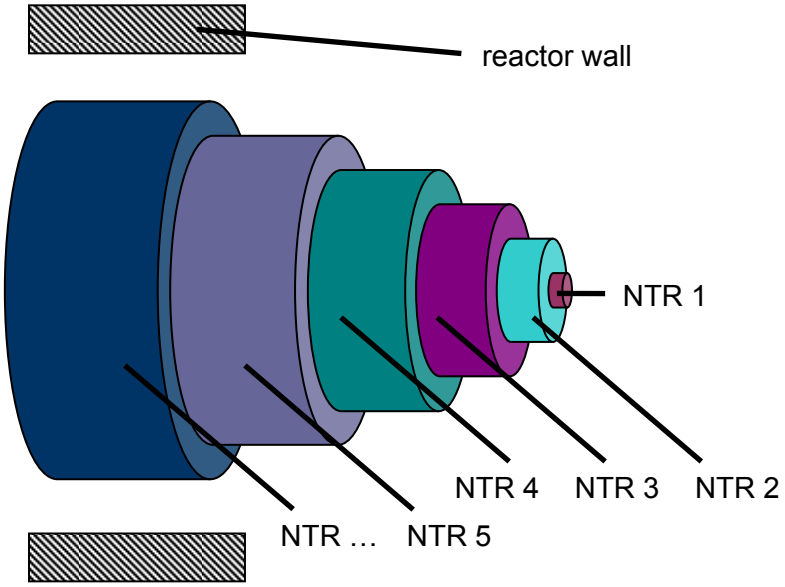

Figure 5-23: Illustration of the reactor divided into nested tube reactors (NTR)

Since the flow lines are not perfectly parallel with respect to the vertical axis of symmetry, it is not advisable to apply an enormous number of nested units because a significant fraction of flow lines would leave the unit in which they started. Respecting extreme conditions, defined by 1600 °C nominal furnace temperature and 9800 sccm Ar, a maximum number of five NTRs in region A and four NTRs in region B is rational as demonstrated in Figure 5-24. A reasonable number of NTRs in region A regarding the flow conditions not rejected for kinetic evaluations resulting from considerations explained before, predominantly in Chapter 5.1.4, is higher and lies in the range from five to ten. Here ten or less NTRs guarantee that most of flow lines stay in the same unit or at least enter it again after dropping out.

After leaving region A the flow of amount of substance has to be distributed to the nested tube reactors of region B. Near the tip of the thermocouple the velocity of flow elements shows considerable components in radial direction. At axial position $z = 0.537\ \mathrm{m}$, 5 mm downstream the tip of the thermocouple, radial velocities reach negligible levels again. Figure 5-25 (a) and (b) show the fraction of the total molar flow present in nested tube reactor 1 - 4 at position $z = 0.537\ \mathrm{m}$ of region B, respectively as a function of the molar flow of argon and helium at the inlet of the reactor. It can be extracted that the concerning fraction is obviously independent from other factors like the temperature, since practically identical values are achieved for differing reaction conditions as long as the molar flow at the reactor inlet is comparable. Hence

[121] cp. [Missen, 1999], p. 394

the aforementioned neglect of radiative heat transfer, which essentially influences the temperatures at the thermocouple, can be justified.

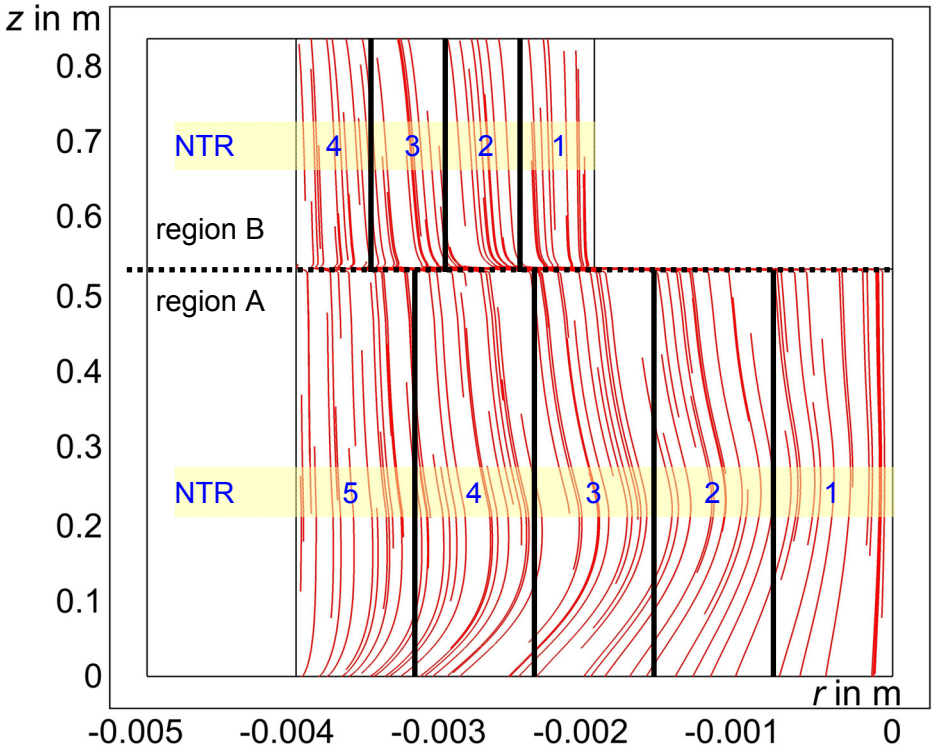

Figure 5-24: Results of COMSOL Multiphysics calculations based on a simplified temperature profile for the wall of the reactor concerning flow lines for 1600 °C nominal furnace temperature and 9800 sccm argon with indication of virtual nested tube reactors (NTR)

Resulting from the high dilution, the total molar flow through the reactor varies only slightly, namely at most by $x_{CH_4,0} \cdot \left(\dot{n}_{DG,0} + \dot{n}_{CH_4,0}\right)$ as already stated in Chapter 5.2.2, with the progress of the reaction and, consequently, with the axial position in the reactor. Accordingly, the molar flow passing from region A to region B roughly matches the molar flow at the reactor inlet. Thus, it is admissible to distribute the total molar flow at the border between region A and region B to the particular virtual nested tube reactors of region B consistent with the polynomial fit functions introduced in Figure 5-25. Respective values for the coefficients k_3, k_2, k_1, and k_0 of the fit functions can be found in Appendix F.

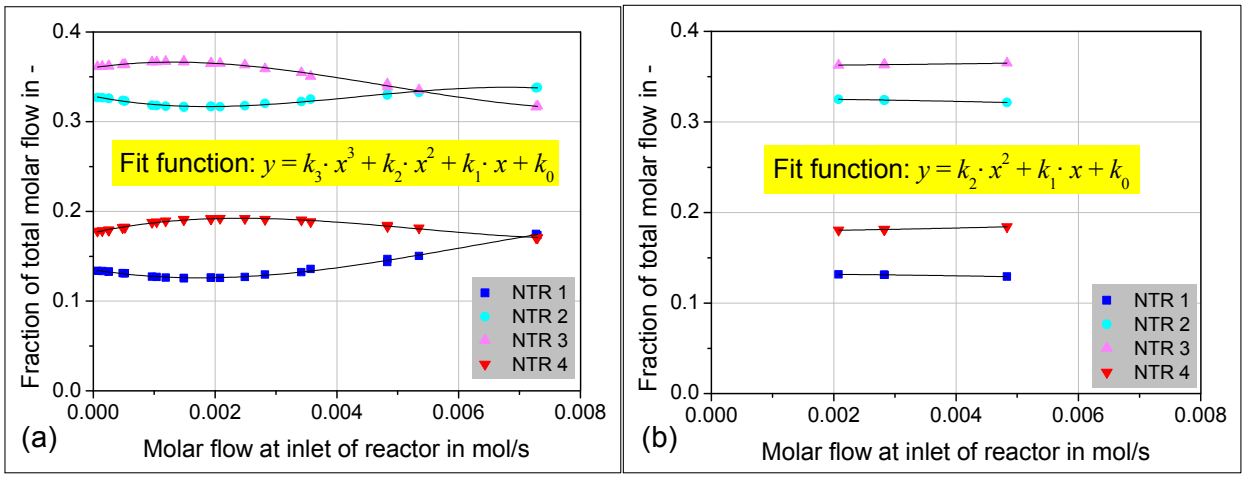

Figure 5-25: Results of COMSOL Multiphysics calculations based on a simplified temperature profile for the wall of the reactor concerning the fraction of the molar flow at the inlet of the reactor in particular nested tube reactors in region B 5 mm downstream the tip of the thermocouple as a function of the molar flow of argon (a) and helium (b) at the reactor inlet

5.3.2.3 Pressure distribution

Figure 5-26 gives information about the pressure distribution inside the reactor for different sets of nominal furnace temperature and standard volume flow. As one could have expected, radial pressure differences are negligible. Contrariwise, a moderate pressure drop in axial direction has to be reported.

The development of the pressure along lines of constant radius in region A ($r = 0.002\,\mathrm{m}$) and region B ($r = 0.003\,\mathrm{m}$) extracted from information provided in Figure 5-26 is represented in Figure 5-27. The COMSOL Multiphysics calculations show that the main pressure drop occurs in region B, where part of the cross section of the reactor is blocked by the thermocouple, and thereby confirm results of preliminary calculations referred to before.[122] However, in most cases experimentally determined pressure drops are somewhat higher than the calculated ones as can be seen in Figure 5-27 exemplarily for the considered sets of nominal furnace temperature and standard volume flow. This is probably due to the deposit of generated carbon in the gap between thermocouple and reactor wall at locations where temperatures are not high enough to remove carbon deposit by burning.

[122] see beginning of Chapter 5.3.2

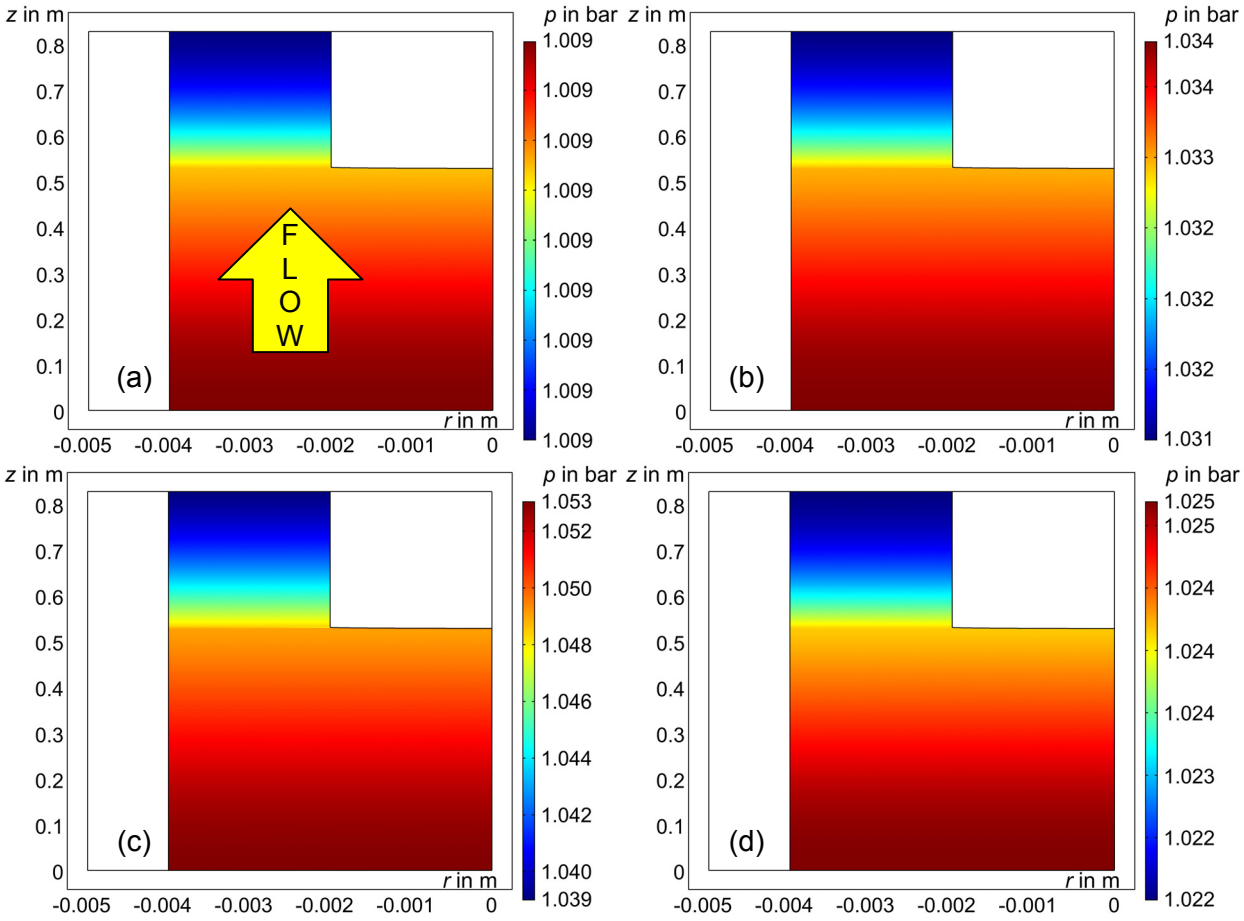

Figure 5-26: Results of COMSOL Multiphysics calculations based on a simplified temperature profile for the wall of the reactor concerning pressure distribution inside the reactor for different sets of nominal furnace temperature and standard volume flow: 1200 °C - 95 sccm Ar (a), 1400 °C - 2600 sccm Ar (b), 1600 °C - 9800 sccm Ar (c), and 1400 °C - 3800 sccm He (d)

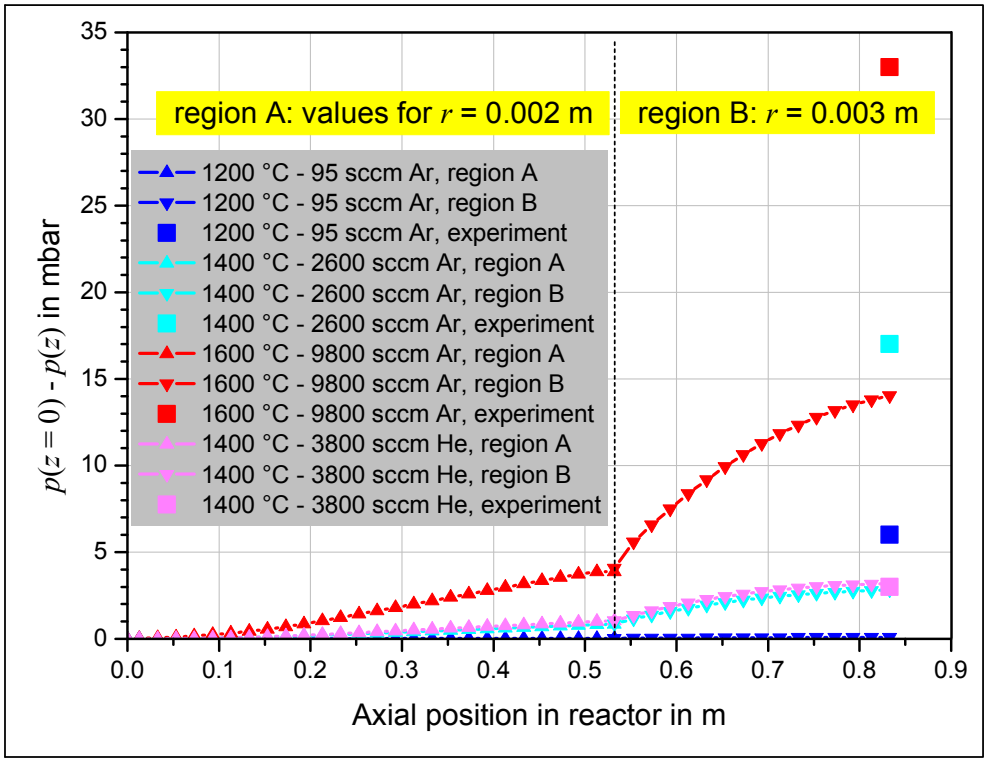

Figure 5-27: Results of COMSOL Multiphysics calculations based on a simplified temperature profile for the wall of the reactor concerning the pressure evaluation along average radii in region A and region B compared to experimental pressure differences between the inlet and the outlet of the reactor for different sets of nominal furnace temperature and standard volume flow

Employing the present information, it is applicable to consider the pressure above the thermocouple as a constant, whereas a linear pressure drop is assumed for region B, where the thermocouple blocks the center of the reactor. Taking relevant axial locations into account, the pressure p can be formulated as a function of the axial position z according to

$$p(z) = \begin{cases} \overline{p}_{\mathrm{R,inlet}} & \text{if } z < z_{\mathrm{TC}} - 1\,\mathrm{mm} \\ \overline{p}_{\mathrm{R,inlet}} + \dfrac{\overline{p}_{\mathrm{R,outlet}} - \overline{p}_{\mathrm{R,inlet}}}{728\,\mathrm{mm} - \left(z_{\mathrm{TC}} - 1\,\mathrm{mm}\right)} \cdot \left[z - \left(z_{\mathrm{TC}} - 1\,\mathrm{mm}\right)\right] & \\ & \text{if } z_{\mathrm{TC}} - 1\,\mathrm{mm} \le z \le 728\,\mathrm{mm} \end{cases}, \qquad \textbf{Equation 142}$$

with $z_{\mathrm{TC}} = 320\,\mathrm{mm}$.

5.4 Kinetic model

As stated above, the predominant species involved in the thermal dissociation of methane are – beside methane and the desired products hydrogen and carbon – the C_2-hydrocarbons ethane,

ethene, and ethyne. Consequently, the applied kinetic model comprises the dehydrogenation reactions starting with methane, forming the C_2-intermediates, and finally generating hydrogen and carbon:

- $2\ CH_4\ (g) \rightarrow C_2H_6\ (g) + H_2\ (g)$ {1}
- $C_2H_6\ (g) \rightarrow C_2H_4\ (g) + H_2\ (g)$ {2}
- $C_2H_4\ (g) \rightarrow C_2H_2\ (g) + H_2\ (g)$ {3}
- $C_2H_2\ (g) \rightarrow 2\ \text{“C”}\ (s) + H_2\ (g)$ {4}

Numerous other species are involved in the cracking reactions; however, since the balance of hydrogen atoms is generally more or less satisfied, only low amounts of other (not considered) species could be found in the product flow. The partly remarkable disagreement concerning the balance of carbon atoms suggests that low fractions of further species with high C/H-ratio were implicated. Without the consideration of further species, the amount of substance of formed carbon is considerably overestimated.[123] The reactions involved in the thermal dissociation of methane proceed in the gaseous phase (homogeneous character) and presumably on the surface of generated particles as well as on the wall of the reactor (heterogeneous character).[124] The extent of present experimental data prohibits a kinetic approach, which differentiates between homogeneous and heterogeneous reactions, because

- the amount of generated carbon is not exactly predictable due to the presence of not considered C-rich species.
- two types of generated carbon have to be distinguished: pyrocarbon and particulate carbon, whose functional dependencies of formation on the reaction conditions are not clear.
- knowledge about functional dependencies of the BET surface of generated particulate carbon on the reaction conditions remains incomplete.
- understanding of the fraction of generated carbon which does not pass the reactor but forms deposit inside is fragmentary.
- information about favored locations of carbon deposit in the reactor is not concrete.

[123] cp. Chapter 4.4 and Chapter 4.6.3
[124] cp. Chapter 4.7

Hence a certain reaction rate is interpreted as a combined result of homogeneous and heterogeneous effects. The reaction rate r_q of every considered reaction q is a function of the reaction conditions, in particular of the temperature T and the respective concentration of the reactant of reaction q $c_{\text{reactant},q}$. It is defined in accordance with Equation 19, Equation 20, and Equation 21 by

$$r_q = k_{0,q} \cdot e^{-\frac{E_{\text{a},q}}{\Re \cdot T}} \cdot c_{\text{reactant},q}^{m_q} \quad , \qquad \textbf{Equation 143}$$

employing – respectively for reaction q – the activation energy E_{a}, the reaction order m, and the pre-exponential factor k_0.

5.5 Procedure

Different reactor models have been applied for the kinetic evaluation. In accordance with the findings concerning the flow conditions inside the reactor, a model based on nested tube reactors (NTR) was introduced.[125] Since the relevance of radial diffusion could not be estimated sufficiently, two contrary cases were considered.[126] On the one hand respective effects were entirely neglected, whereas on the other hand ideal radial diffusion (D) was presumed. Furthermore, a plug flow model (PFR) was applied as a reference model.

For any model the volume of the reactor had to be divided into volume elements. Figure 5-28 shows an illustration of one of these volume elements ΔV_{R} along with entering and leaving molar flows.

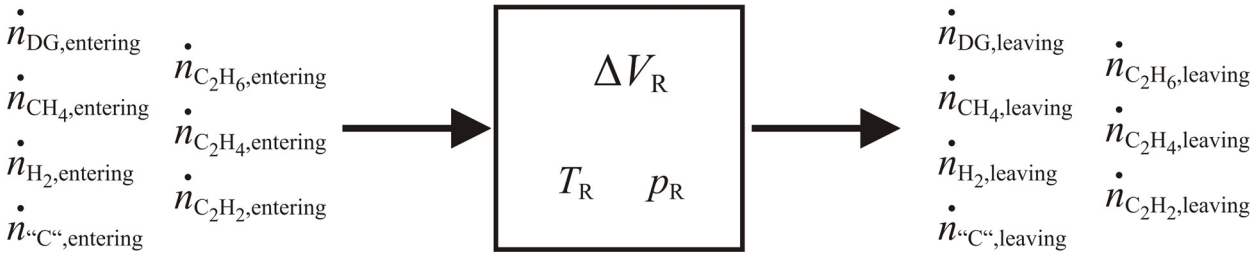

Figure 5-28: General configuration of a volume element of the reactor with ingoing and outgoing molar flows

[125] cp. Chapter 5.3
[126] cp. Chapter 5.2.2

Depending on the reaction conditions, dominated by the reaction temperature T_R and pressure p_R, as well as on the kinetic parameters, the reaction rates of the considered reactions r_1, r_2, r_3, and r_4 can be calculated employing Equation 143. In conformity with Equation 16 and the reaction scheme presented above, the molar flows leaving the particular volume element ΔV_R arise from

$$\dot{n}_{CH_4,leaving} = \dot{n}_{CH_4,entering} + r_1 \cdot \nu_{CH_4,1} \cdot \Delta V_R \qquad \textbf{Equation 144}$$

for methane, from

$$\dot{n}_{C_2H_6,leaving} = \dot{n}_{C_2H_6,entering} + r_1 \cdot \nu_{C_2H_6,1} \cdot \Delta V_R + r_2 \cdot \nu_{C_2H_6,2} \cdot \Delta V_R \qquad \textbf{Equation 145}$$

for ethane, from

$$\dot{n}_{C_2H_4,leaving} = \dot{n}_{C_2H_4,entering} + r_2 \cdot \nu_{C_2H_4,2} \cdot \Delta V_R + r_3 \cdot \nu_{C_2H_4,3} \cdot \Delta V_R \qquad \textbf{Equation 146}$$

for ethene, from

$$\dot{n}_{C_2H_2,leaving} = \dot{n}_{C_2H_2,entering} + r_3 \cdot \nu_{C_2H_2,3} \cdot \Delta V_R + r_4 \cdot \nu_{C_2H_2,4} \cdot \Delta V_R \qquad \textbf{Equation 147}$$

for ethyne, from

$$\dot{n}_{H_2,leaving} = \dot{n}_{H_2,entering} + r_1 \cdot \nu_{H_2,1} \cdot \Delta V_R + r_2 \cdot \nu_{H_2,2} \cdot \Delta V_R + r_3 \cdot \nu_{H_2,3} \cdot \Delta V_R + r_4 \cdot \nu_{H_2,4} \cdot \Delta V_R \qquad \textbf{Equation 148}$$

for hydrogen, and from

$$\dot{n}_{\text{"C",leaving}} = \dot{n}_{\text{"C",entering}} + r_4 \cdot \nu_{\text{"C",4}} \cdot \Delta V_{\text{R}} \qquad \textbf{Equation 149}$$

for carbon occupying $\nu_{i,q}$ the stoichiometric coefficient of species i concerning reaction q. The molar flow of the dilution gas keeps constant, since the inert dilution gas refuses to undergo any reaction.

The concentration of species i c_i, input factor for the calculation of the reaction rate, was calculated following Equation 15, respecting the molar flows of gaseous species for the estimation of the volume flow according to the ideal gas law following

$$c_i = \frac{\dot{n}_i}{\dot{V}} = \frac{\dot{n}_i}{\frac{\Re \cdot T_{\text{R}}}{p_{\text{R}}} \cdot \sum_j \dot{n}_{j,\text{entering}}} \qquad j = \text{DG}, \text{CH}_4, \text{H}_2, \text{C}_2\text{H}_6, \text{C}_2\text{H}_4, \text{C}_2\text{H}_2 \quad , \qquad \textbf{Equation 150}$$

where the pressure was calculated depending on the considered axial position.[127] A limitation of the sink terms guaranteed that the sink term of species i (corresponding to the source term of species j formed by the reaction, which consumes species i) never exceeded the actual entering flow of species i. The molar flows leaving a particular volume element serve as the entering flows of the subsequent volume element. Finally, the calculated molar flows at the outlet of the reactor $\dot{n}_{\text{CH}_4,\text{P,calculated}}$, $\dot{n}_{\text{H}_2,\text{P,calculated}}$, $\dot{n}_{\text{C}_2\text{H}_6,\text{P,calculated}}$, $\dot{n}_{\text{C}_2\text{H}_4,\text{P,calculated}}$, and $\dot{n}_{\text{C}_2\text{H}_2,\text{P,calculated}}$ are employed in order to estimate the calculated conversion of methane and the calculated yields of hydrogen, ethane, ethene, and ethyne based on the respective initial molar flow of methane $\dot{n}_{\text{CH}_4,0}$.

An optimization tool was used to find kinetic parameters, which allow best agreement between calculated values and experimental results.[128] Following Chi-Square fitting the model error $E^2_{\Sigma,\text{tot}}$, which is the quantity to be minimized, was defined as

[127] cp. Chapter 5.3.2.3, particularly Equation 142

[128] Optimization tool: Optimization Toolbox 4.0 embedded in MATLAB Version 7.6.0.324 (R2008a), Solver: “lsnonlin“ (Nonlinear least squares), algorithm based on the interior-reflective Newton method. For further information see Appendix G.

$$E^2_{\Sigma,\mathrm{tot}} = E^2_{\Sigma,\mathrm{CH_4}} + E^2_{\Sigma,\mathrm{H_2}} + E^2_{\Sigma,\mathrm{C_2H_6}} + E^2_{\Sigma,\mathrm{C_2H_4}} + E^2_{\Sigma,\mathrm{C_2H_2}} \qquad \textbf{Equation 151}$$

featuring

$$E^2_{\Sigma,\mathrm{CH_4}} = \sum_{k=1}^{N_{\mathrm{experiments}}} E^2_{\mathrm{CH_4},k} = \sum_{k=1}^{N_{\mathrm{experiments}}} \left(\frac{X_{\mathrm{CH_4},k,\mathrm{calculated}} - X_{\mathrm{CH_4},k}}{u(X_{\mathrm{CH_4},k})} \right)^2 \qquad \textbf{Equation 152}$$

and

$$E^2_{\Sigma,j} = \sum_{k=1}^{N_{\mathrm{experiments}}} E^2_{j,k} = \sum_{k=1}^{N_{\mathrm{experiments}}} \left(\frac{Y_{j,k,\mathrm{calculated}} - Y_{j,k}}{u(Y_{j,k})} \right)^2 \qquad j = \mathrm{H_2}, \mathrm{C_2H_6}, \mathrm{C_2H_4}, \mathrm{C_2H_2} \qquad \textbf{Equation 153}$$

based on $N_{\mathrm{experiments}}$ experimental conditions considered for the kinetic evaluation.[129] The equations show that the difference between the calculated and measured conversion or yields for experimental condition k was related to the estimated standard uncertainty of respective experimental results. The yield of ethane and ethyne partly attained quite low values. In order not to overvalue the respective contributions to $E^2_{\Sigma,j}$, a limit of marginal extend Y_{LME} was introduced and set to 0.001, for both ethane and ethyne. If the experimental value of the yield lies below this limit, two cases were distinguished:

$$Y_{j,k} < Y_{\mathrm{LME},j} \quad (= 0.001) \qquad j = \mathrm{C_2H_6}, \mathrm{C_2H_2}$$

$$\begin{aligned} &\mathrm{Case\,1:} \quad Y_{j,k,\mathrm{calculated}} < Y_{\mathrm{LME},j} \quad \Rightarrow \quad E_{j,k} = 0 \\ &\mathrm{Case\,2:} \quad Y_{j,k,\mathrm{calculated}} \geq Y_{\mathrm{LME},j} \quad \Rightarrow \quad E_{j,k} = \frac{Y_{j,k,\mathrm{calculated}} - Y_{\mathrm{LME},j}}{u(Y_{\mathrm{LME},j})} \end{aligned} \quad , \qquad \textbf{Equation 154}$$

where the standard uncertainties $u(Y_{\mathrm{LME},j})$ were estimated taking appropriate data into account. It was found that $u(Y_{\mathrm{LME,C_2H_6}})$ and $u(Y_{\mathrm{LME,C_2H_2}})$ can be approximated by 0.00027 and 0.0045, respectively, considering the relevant range close to Y_{LME}. The total number of reaction

[129] cp. [Press, 2007], p. 778 et seqq. and Chapter 2.4

conditions experimentally covered accounts for 88 (73 with Ar and 15 with He)[130]; however, due to the constrictions related to axial diffusion and the radial temperature gradient the number of experimental conditions employed for the kinetic evaluation was reduced to 57 (42 with Ar and 15 with He).[131]

Independent from the reactor model the axial step size through the reactor Δz was set to 1 mm, which features a reasonable compromise between accuracy and speed of computation. Reference calculations with an axial step size of 0.1 mm indicated that only marginal variations of $E_{\Sigma,\mathrm{tot}}^2$ should be expected, if step sizes smaller than 1 mm were applied. Different initial parameter sets (IPSs) covering a wide range of potential values have been applied in order to increase the probability of the identification of the global minimum instead of a local one. Respective initial parameters are summarized in Table 5-7.

Table 5-7: Initial parameter sets for the optimization process along with lower bounds (LB) and upper bounds (UB) of the parameters

Parameter	Initial Parameter Set (IPS)												LB	UB
	1	2	3	4	5	6	7	8	9	10	11	12		
$E_{\mathrm{a},1}$	381.0	381.0	381.0	381.0	571.5	190.5	571.5	190.5	571.5	190.5	571.5	190.5	0	700
$\log(k_{0,1})$	13.65	13.65	13.65	13.65	20.48	6.825	20.48	6.825	6.825	20.48	6.825	20.48	0.5	25
m_1	1	1	1	1	1.5	0.5	1.5	0.5	1	1	1	1	0.25	3
$E_{\mathrm{a},2}$	334.9	289.0	334.9	289.0	502.4	167.5	433.5	144.5	502.4	167.5	433.5	144.5	0	700
$\log(k_{0,2})$	16.65	14.00	16.65	14.00	24.98	8.325	21.00	7.000	8.325	24.98	7.000	21.00	0.5	25
m_2	1	1	1	1	1.5	0.5	1.5	0.5	1	1	1	1	0.25	3
$E_{\mathrm{a},3}$	167.0	167.0	167.0	167.0	250.5	83.50	250.5	83.50	250.5	83.50	250.5	83.50	0	700
$\log(k_{0,3})$	8.410	8.410	8.410	8.410	12.62	4.205	12.62	4.205	4.205	12.62	4.205	12.62	0.5	25
m_3	1	1	1	1	1.5	0.5	1.5	0.5	1	1	1	1	0.25	3
$E_{\mathrm{a},4}$	167.5	167.5	125.6	125.6	251.3	83.75	188.4	62.80	251.3	83.75	188.4	62.80	0	700
$\log(k_{0,4})$	10.33	10.33	6.23	6.23	15.50	5.165	9.345	3.115	5.165	15.50	3.115	9.345	0.5	25
m_4	2	2	1	1	3	1	1.5	0.5	2	2	1	1	0.25	3
E_{a} in $\frac{\mathrm{kJ}}{\mathrm{mol}}$, k_0 in $\frac{1}{\mathrm{s}} \cdot \left(\frac{\mathrm{mol}}{\mathrm{m}^3}\right)^{(1-m)}$, m in –														
IPSs 1-4 feature values on the basis of [Kozlov, 1962] IPS 1 combines maximum values, IPS 4 combines minimum values IPS 5 = IPS 1 * 1.5, IPS 6 = IPS 1 * 0.5, IPS 7 = IPS 4 * 1.5, IPS 8 = IPS 4 * 0.5 IPSs 9-12 are based on crosswise multiplication of E_{a} and $\log(k_0)$ of IPSs 1 and 4 by 1.5 and 0.5														

[130] cp. Chapter 4.2
[131] cp. Chapter 5.1.4 and Chapter 5.2.1

The common logarithm of the pre-exponential factor was altered by the optimization tool instead of the pre-exponential factor itself with the purpose of dealing with values, which have a somehow comparable order of magnitude.

Temperatures of the wall and the center of the reactor at axial position z, $T_W(z)$ and $T_C(z)$, respectively, were determined by linear interpolation employing the sets of measured temperatures. The following chapters provide further details about the applied reactor models.

5.5.1 Reactor model: Plug flow reactor

A common plug flow model (PFR) served as a reference model considering only an axial division of the reactor into volume elements as is illustrated in Figure 5-29.

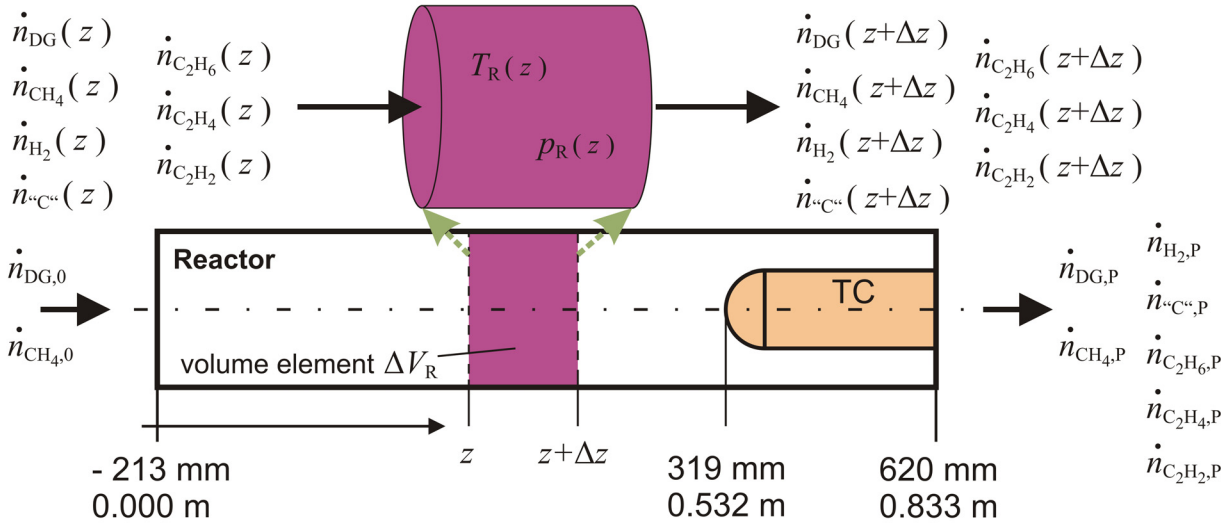

Figure 5-29: Illustration of a plug flow model applied to the tube reactor with thermocouple (TC)

The relevant reaction temperature at axial position z $T_R(z)$ was estimated by area-related averaging of a parabolic temperature profile[132] defined by the temperature of the center of the reactor $T_C(z)$ and the temperature at the wall of the reactor $T_W(z)$ leading to

$$T_R(z) = T_C(z) + 0.5 \cdot \left(T_W(z) - T_C(z)\right) \quad . \qquad \textbf{Equation 155}$$

In region B, starting at position 319 mm, the size of the axial volume element is reduced due to the presence of the thermocouple.

[132] see Equation 117

5.5.2 Reactor model: Nested tube reactors

In order to approximate the laminar flow conditions inside the reactor and to consider radial temperature differences, a more complex reactor model based on nested tube reactors (NTR) was suggested above.[133] Thereby the reactor with inner radius $R_{\mathrm{R,i}}$ was divided into N_{NTR} nested tube reactors with uniform thickness Δr arising from

$$\Delta r = \frac{R_{\mathrm{R,i}}}{N_{\mathrm{NTR}}} \quad . \qquad \textbf{Equation 156}$$

The outer radius $r_{j,\mathrm{o}}$ and inner radius $r_{j,\mathrm{i}}$ of NTR j meet

$$\Delta r = \Delta r_j = r_{j,\mathrm{o}} - r_{j,\mathrm{i}} \qquad \textbf{Equation 157}$$

and can consequently be calculated respecting $r_{1,\mathrm{i}} = 0$. An illustration of the reactor model is provided in Figure 5-30.

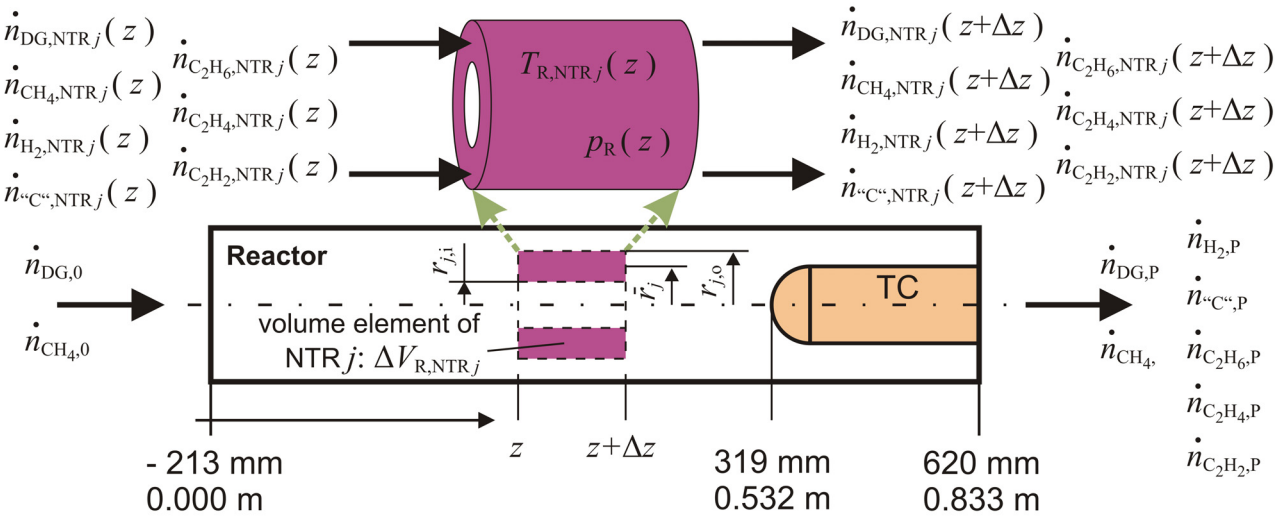

Figure 5-30: Illustration of a nested tube reactor model applied to the tube reactor with thermocouple (TC)

[133] see Chapter 5.3.2.2

At the inlet of the reactor the total volume flow had to be distributed to N_{NTR} nested tube reactors. $\dot{V}_{j,0}$, the volume flow entering nested tube reactor j with the inner radius $r_{j,\mathrm{i}}$ and the outer radius $r_{j,\mathrm{o}}$, was determined by

$$\dot{V}_{j,0} = \int_{A} v \cdot \mathrm{d}A = \int_{r_{j,\mathrm{i}}}^{r_{j,\mathrm{o}}} v(\hat{r}) \cdot 2 \cdot \pi \cdot \hat{r} \cdot \mathrm{d}\hat{r} \quad , \qquad \textbf{Equation 158}$$

employing the velocity profile $v(r)$ according to Equation 132 if a fully developed laminar velocity profile can be expected or according to Equation 136 if not. Since the conditions for the ANSYS simulations and the real conditions for the cracking experiment differ slightly, a correction factor was used being multiplied with each $\dot{V}_{j,0}$ assuring that the sum of all $\dot{V}_{j,0}$ equals the total volume flow at the inlet of the reactor for the particular experiment. Respective molar flows of dilution gas and methane at the inlet of nested tube reactor j, $\dot{n}_{\mathrm{DG},j}$ and $\dot{n}_{\mathrm{CH_4},j}$, were obtained using the ideal gas law and the initial molar fraction of methane.[134] The nested units were regarded separately meaning that no interaction takes place between each other and molecules either present at the inlet of the reactor or formed by reactions in a particular NTR stay inside. $T_{\mathrm{R,NTR}\,j}(z)$, the temperature in NTR j at the axial position z, was approximated by evaluating the presumed parabolic temperature profile at the mean radius $\bar{r}_j$ arising from

$$\bar{r}_j = 0.5 \cdot \left(r_{j,\mathrm{o}} + r_{j,\mathrm{i}}\right) \qquad \textbf{Equation 159}$$

employing the respective outer radius $r_{j,\mathrm{o}}$ and inner radius $r_{j,\mathrm{i}}$.

The calculated total molar flow at position 319 mm, which corresponds to the tip of the thermocouple, was distributed to the four nested tube reactors downstream, that is region B, in accordance with respective COMSOL Multiphysics simulation results presented before.[135] In region B $T_{\mathrm{R,NTR}\,j}(z)$, the relevant temperature in NTR j at axial position z, was approximated by linear interpolation following

[134] see Equation 2 and Equation 5
[135] cp. Chapter 5.3.2.2

$$T_{\mathrm{R,NTR}\,j}(z) = T_{\mathrm{C}}(z) + \frac{T_{\mathrm{W}}(z) - T_{\mathrm{C}}(z)}{R_{\mathrm{R,i}} - R_{\mathrm{TC,o}}} \cdot \left(\bar{r}_j - R_{\mathrm{TC,o}}\right)$$

Equation 160

with the outer radius of the thermocouple $R_{\mathrm{TC,o}}$. In region B $r_{1,\mathrm{i}} = R_{\mathrm{TC,o}} = 0.002\ \mathrm{m}$.

Two different numbers of NTR in region A were considered consistent with reasonable limits stated in Chapter 5.3.2.2, namely $N_{\mathrm{NTR}} = 5$ (5 NTR) and $N_{\mathrm{NTR}} = 10$ (10 NTR).

5.5.3 Reactor model: Nested tube reactors with ideal radial diffusion

The reactor model based on nested tube reactors with ideal radial diffusion comprises all features of the NTR model. However, an ideal radial diffusion step was attached to every reaction step as illustrated in Figure 5-31. Following Equation 120, ideal radial diffusion means that radial differences of molar fractions degrade attaining a value of 0.

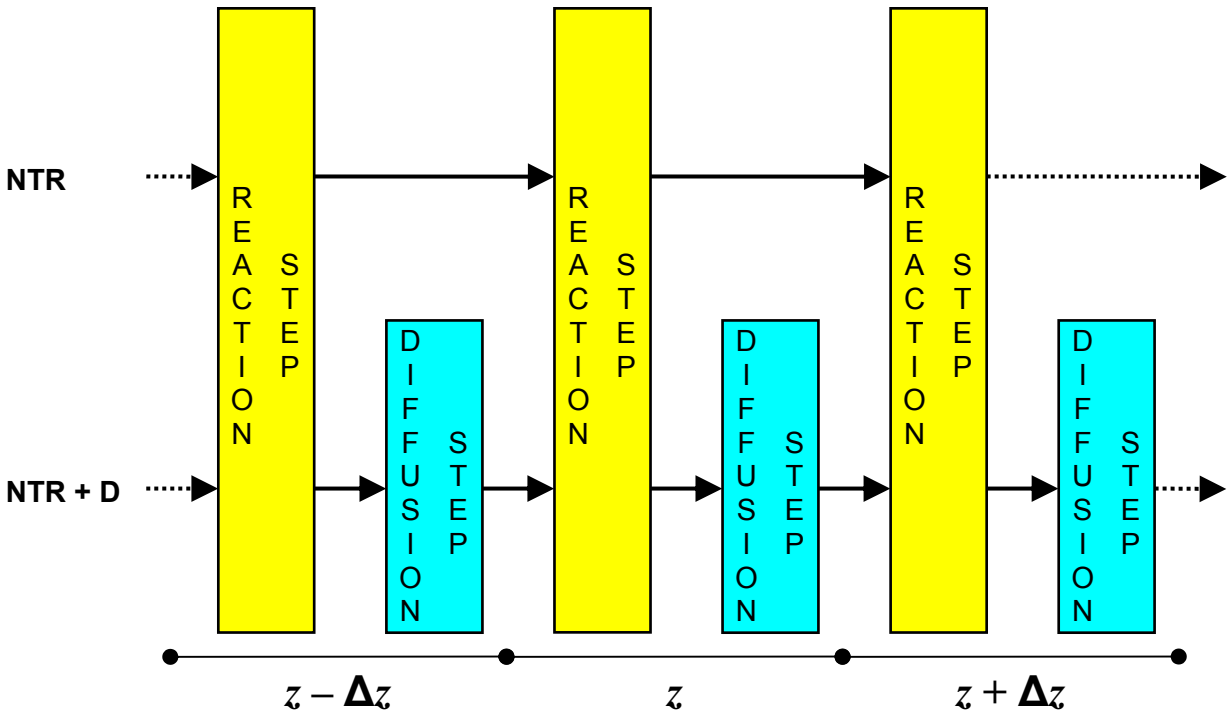

Figure 5-31: Illustration of reaction steps and diffusion steps for reactor models based on nested tube reactors with (NTR + D) and without ideal radial diffusion (NTR)

Hence the average molar fractions of all components i of the flow after the reaction step was calculated from

$$\bar{x}_{i,\text{after reaction}}(z) = \frac{\sum_{j=1}^{N_{\text{NTR}}} \dot{n}_{i,j,\text{after reaction}}(z)}{\sum_{k}\sum_{j=1}^{N_{\text{NTR}}} \dot{n}_{k,j,\text{after reaction}}(z)} \qquad k = \text{DG}, \text{CH}_4, \text{H}_2, \text{C}_2\text{H}_6, \text{C}_2\text{H}_4, \text{C}_2\text{H}_2 \,. \quad \textbf{Equation 161}$$

The molar flows after diffusion were determined under the assumption that the total molar flow of gaseous components in the considered NTRs do not change as a result of the diffusion step. Consequently, $\dot{n}_{i,j}(z+\Delta z)$, the molar flow of component i in NTR j entering a volume element at axial position $z+\Delta z$, arises from

$$\dot{n}_{i,j}(z+\Delta z) = \dot{n}_{i,j,\text{after diffusion}}(z) = \bar{x}_{i,\text{after reaction}}(z) \cdot \sum_{k} \dot{n}_{k,j,\text{after reaction}}(z) \qquad k = \text{DG}, \text{CH}_4, \text{H}_2, \text{C}_2\text{H}_6, \text{C}_2\text{H}_4, \text{C}_2\text{H}_2 \,. \quad \textbf{Equation 162}$$

5.6 Kinetic parameters and further results

Best fit kinetic parameters determined by the optimization tool are presented for the applied reactor models in Table 5-8 along with the respective values for $E^2_{\Sigma,\text{tot}}$, the quantity, which was minimized, as well as its constituents E^2_{Σ,CH_4}, E^2_{Σ,H_2}, $E^2_{\Sigma,\text{C}_2\text{H}_6}$, $E^2_{\Sigma,\text{C}_2\text{H}_4}$, and $E^2_{\Sigma,\text{C}_2\text{H}_2}$. As can be seen, the reactor model based on five nested tube reactors (5 NTR) lead to best agreement between experimental results and simulation resulting in $E^2_{\Sigma,\text{tot}} = 17809$. However, the optimization tool was capable of identifying best fit kinetic parameters, which lead to comparable $E^2_{\Sigma,\text{tot}}$ for all models. The results for five nested tube reactors with ideal radial diffusion (5 NTR + D) are very similar to those of the plug flow model (PFR) concerning both, the kinetic parameters and the achieved error of the model. The extension of the number of NTR from five to ten (10 NTR and 10 NTR + D) leads to almost identical results compared to the models based on five nested tube reactors. In the following, model 5 NTR which achieved the lowest value for $E^2_{\Sigma,\text{tot}}$ is analyzed more in detail.

Table 5-8: Comparison of best fit kinetic parameters and achieved agreement between experiments and optimization procedure for different reactor models: plug flow reactor (PFR), 5 nested tube reactors (5 NTR), 5 nested tube reactors with ideal radial diffusion (5 NTR + D), 10 nested tube reactors (10 NTR), and 10 nested tube reactors with ideal radial diffusion (10 NTR + D)

Reactor model →		PFR	5 NTR	5 NTR + D	10 NTR	10 NTR + D
Best fit kinetic parameters of reaction {1}	$E_{a,1}$	499.4	510.1	499.5	510.3	499.5
	$\log(k_{0,1})$	17.37	17.77	17.37	17.79	17.37
	m_1	1.331	1.283	1.329	1.286	1.328
Best fit kinetic parameters of reaction {2}	$E_{a,2}$	418.2	433.9	418.2	433.3	418.8
	$\log(k_{0,2})$	17.12	17.75	17.13	17.74	17.15
	m_2	1.044	1.049	1.046	1.050	1.044
Best fit kinetic parameters of reaction {3}	$E_{a,3}$	343.1	374.7	343.9	373.8	344.1
	$\log(k_{0,3})$	14.29	15.36	14.31	15.34	14.31
	m_3	1.333	1.301	1.328	1.303	1.327
Best fit kinetic parameters of reaction {4}	$E_{a,4}$	13.25	29.01	13.10	29.04	13.08
	$\log(k_{0,4})$	2.282	2.657	2.273	2.704	2.272
	m_4	1.966	1.599	1.965	1.638	1.964
Selection of experiments for kinetic evaluation: 42 x Ar and 15 x He	E^2_{Σ,CH_4}	7470	7700	7508	7689	7509
	E^2_{Σ,H_2}	1706	1688	1719	1752	1717
	E^2_{Σ,C_2H_6}	323	306	309	310	300
	E^2_{Σ,C_2H_4}	7570	6618	7550	6661	7577
	E^2_{Σ,C_2H_2}	1239	1498	1245	1426	1247
	$E^2_{\Sigma,tot}$ quantity to be minimized	18308	17809	18331	17838	18349
$E_a \text{ in } \frac{\text{kJ}}{\text{mol}}$, $k_0 \text{ in } \frac{1}{\text{s}} \cdot \left(\frac{\text{mol}}{\text{m}^3}\right)^{(1-m)}$, m in –						

The number of degrees of freedom of a model $N_{\text{degrees of freedom}}$ arises from the difference of the number of data points $N_{\text{data points}}$ and the number of adjustable parameters $N_{\text{parameters}}$ according to

$$N_{\text{degrees of freedom}} = N_{\text{data points}} - N_{\text{parameters}} \quad . \qquad \textbf{Equation 163}$$

Since 57 reaction conditions were employed for the kinetic evaluation and each reaction condition provides a result concerning X_{CH_4}, Y_{H_2}, $Y_{C_2H_6}$, $Y_{C_2H_4}$, and $Y_{C_2H_2}$, the number of data

points finally adds up to 285. On the other hand there are three kinetic parameters for each of the four considered reactions. Consequently, $N_{\text{parameters}} = 12$ and $N_{\text{degrees of freedom}} = 273$. A fairly good fit is typically characterized by $E^2_{\Sigma,\text{tot}} \approx N_{\text{degrees of freedom}}$. Contrariwise, the best present model features $E^2_{\Sigma,\text{tot}} = 17809 >> N_{\text{degrees of freedom}}$, indicating either an improper estimation of standard uncertainties or a weakness of the model itself.[136] This issue will be discussed later.

Table 5-9 gives information about the differences between calculated (reactor model 5 NTR with best fit kinetic parameters leading to $E^2_{\Sigma,\text{tot}} = 17809$) and experimentally determined values for X_{CH_4}, Y_{H_2}, $Y_{C_2H_6}$, $Y_{C_2H_4}$, and $Y_{C_2H_2}$. On average the absolute differences here equal 0.0657 and 0.0602 regarding the conversion of methane and the yield of hydrogen, respectively, corresponding to an average relative difference of about 14.5 %. Higher relative differences have to be reported pertaining to the yields of C_2-hydrocarbons. However, the yields of ethane and ethene, calculated and measured, are mostly much lower than the other considered quantities. Generally about two thirds of the derived differences are smaller than the relevant average value.

Table 5-9: Information about differences between quantities calculated with reactor model 5 NTR employing best fit kinetic parameters and experimentally determined quantities

Quantity	Absolute differences		Absolute differences relative to experimental results (data not used if experimental result = 0)	
	Average in -	Fraction of values smaller than average in %	Average in -	Fraction of values smaller than average in %
X_{CH_4}	0.0657	70.2	0.143	71.9
Y_{H_2}	0.0602	66.7	0.146	71.9
$Y_{C_2H_6}$	0.000664	64.9	2.86	78.9
$Y_{C_2H_4}$	0.00575	61.4	0.538	52.6
$Y_{C_2H_2}$	0.0806	59.6	0.473	70.2

[136] cp. [Press, 2007], p. 778 et seqq.

The uncertainty of molar flows at the inlet and the outlet of the reactor were respected by the estimation of the uncertainty of the conversion of methane and the yields of hydrogen as well as of the C_2-hydrocarbons, which form part of the error of the model and thus of the quantity, which was minimized by the optimization tool. Beside the mentioned figures also temperatures and pressures inside the reactor, being input information of the kinetic evaluation, are affected by uncertainty. In order to assess the relevance of these uncertainties, two further sets of temperature and pressure were investigated for the best model 5 NTR. The first extreme of conditions inside the reactor was determined by combination of minimum temperatures and pressures ($T_{\min}$, $p_{\min}$), calculated by means of maximum negative uncertainty. Minimum temperatures and pressures generally cause a decrease of reaction rates. Contrariwise, the second extreme is related to maximum reaction rates based on maximum temperatures and pressures ($T_{\max}$, $p_{\max}$) arising from respective maximum positive uncertainty. As can be seen in Table 5-10, good agreement between the results determined for nominal and extreme conditions concerning temperature and pressure inside the reactor has to be reported. Found best fit kinetic parameters and model errors for the extreme conditions practically conform to figures for nominal conditions. A somehow lower $E^2_{\Sigma,\mathrm{tot}}$ was achieved for the set of minimum temperatures and pressures. The good agreement indicates that the uncertainty of measured temperatures and pressures is low enough for a definite determination of kinetic parameters.

Different IPSs usually resulted in practically identical best fit kinetic parameter values and consequently to practically identical model errors indicating that global minima were found. However, in some cases IPS 9, 10, 11, or 12, which are based on opposed modification of the activation energies and the common logarithms of the pre-exponential factors,[137] led to local minima featuring clearly higher values of $E^2_{\Sigma,\mathrm{tot}}$ compared to the best fit situation: IPS 9 for PFR, IPSs 10-12 for 5 NTR, 5 NTR + D, 10 NTR, IPSs 9 and 11 for 10 NTR + D, IPSs 10 and 12 for 5 NTR employing minimum temperatures and pressures, and IPS 11 for 5 NTR employing maximum temperatures and pressures.

[137] cp. Table 5-7

Table 5-10: Comparison of best fit kinetic parameters and achieved agreement between experiments and optimization procedure for the reactor model based on 5 nested tube reactors (5 NTR) considering sets of nominal, minimum, and maximum temperatures and pressures

Reactor model →		**5 NTR**	**5 NTR** ($T_{\min}$, $p_{\min}$)	**5 NTR** ($T_{\max}$, $p_{\max}$)
Best fit kinetic parameters of reaction {1}	$E_{a,1}$	510.1	508.0	511.1
	$\log(k_{0,1})$	17.77	17.77	17.76
	m_1	1.283	1.304	1.280
Best fit kinetic parameters of reaction {2}	$E_{a,2}$	433.9	431.8	435.3
	$\log(k_{0,2})$	17.75	17.75	17.75
	m_2	1.049	1.055	1.048
Best fit kinetic parameters of reaction {3}	$E_{a,3}$	374.7	371.9	375.6
	$\log(k_{0,3})$	15.36	15.34	15.35
	m_3	1.301	1.316	1.299
Best fit kinetic parameters of reaction {4}	$E_{a,4}$	29.01	29.63	29.22
	$\log(k_{0,4})$	2.657	2.687	2.650
	m_4	1.599	1.593	1.596
Selection of experiments for kinetic evaluation: 42 x Ar and 15 x He	E^2_{Σ,CH_4}	7700	7442	7635
	E^2_{Σ,H_2}	1688	1638	1684
	E^2_{Σ,C_2H_6}	306	300	320
	E^2_{Σ,C_2H_4}	6618	6654	6681
	E^2_{Σ,C_2H_2}	1498	1501	1537
	$E^2_{\Sigma,tot}$ quantity to be minimized	17809	17534	17857
E_a in $\frac{kJ}{mol}$, k_0 in $\frac{1}{s}\cdot\left(\frac{mol}{m^3}\right)^{(1-m)}$, m in –				

Figure 5-32 gives information about the relative change of the model error of 5 NTR, when a particular kinetic parameter was varied keeping the other kinetic parameters constant. Within the considered limits of variation the model error increases most with the change of activation energies and common logarithms of reaction {1}, reaction {2}, and reaction {3}, whereas the kinetic parameters of reaction {4} and the reaction orders of all reactions influence the model error only marginally. The clear dependence of the model error $E^2_{\Sigma,tot}$ on E_a and $\log(k_0)$ can be explained by exponential expressions. By trend, kinetic parameters of the first reactions show greater influence than the ones of subsequent reactions, because the latter reactions are affected by products of the first reactions.

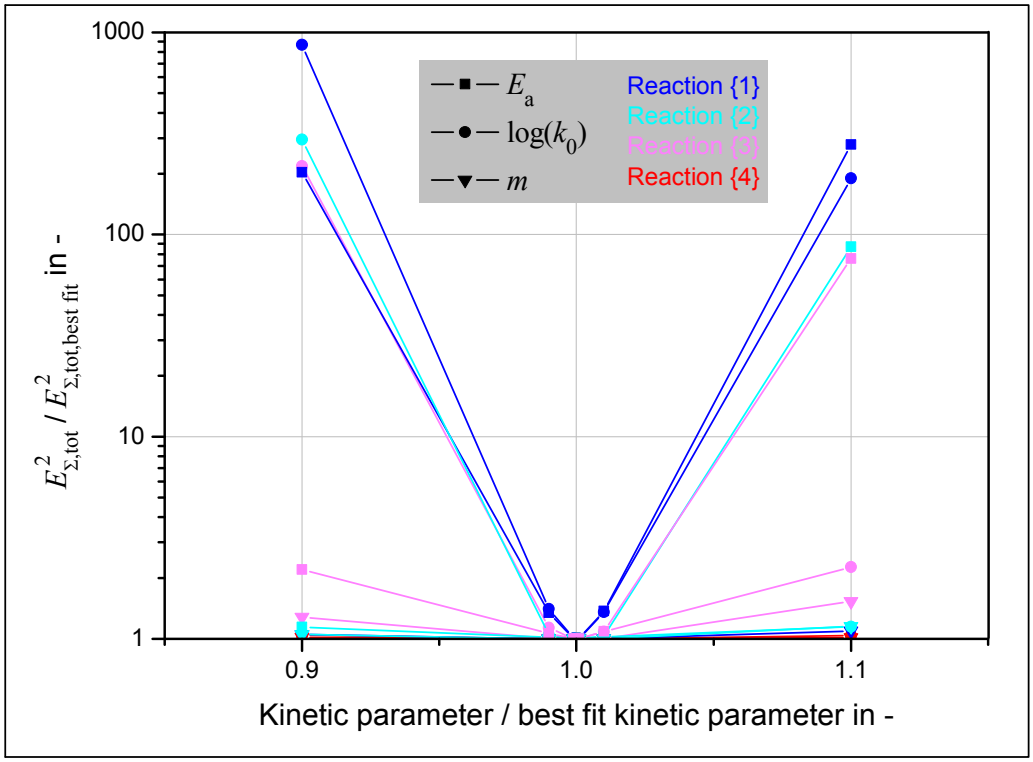

Figure 5-32: Model error related to the model error for best fit kinetic parameters as a function of kinetic parameters related to the best fit kinetic parameters (reactor model 5 NTR)

An analysis of molar fractions in the considered nested tube reactors at a function of the axial position calculated employing the reactor model 5 NTR and respective best fit kinetic parameters indicates that the assumption $\Delta x_i(z) \approx -\bar{x}_i(z)$ – made in Chapter 5.2.2 in order to assess radial diffusive effects – is in fact a realistic one, at least regarding the order of magnitude. Confirming values for the maximum radial difference of molar fractions related to the mean, averaged for the heated region of the reactor and for all experiments used for the kinetic evaluation, are provided in Table 5-11 along with standard deviation of values resulting from the particular reaction conditions. The greatest averaged value was calculated for ethyne and approaches 2.6.

Table 5-11: Averaged maximum radial differences of molar fractions in the heated region of the reactor for results associated with reactor model 5 NTR and respective best fit kinetic parameters

Species i	$\left.\frac{x_{i,\max} - x_{i,\min}}{\bar{x}_i}\right\|_z$ in – averaged for the heated region of the reactor averaged for all experiments used for the kinetic evaluation	Standard deviation concerning the experiments in -
methane	0.93	0.70
hydrogen	1.86	1.20
ethane	1.22	0.72
ethene	1.90	1.10
ethyne	2.59	1.76

Subsequently conversions and yields associated with results gained with reactor model 5 NTR and respective best fit kinetic parameters are exemplarily compared to experimental findings expanding the general information given in Table 5-9. Beside reaction conditions characterized by 5 % methane (molar fraction) in argon, all reaction conditions dealing with helium as dilution gas are considered. Further comparative diagrams can be found in Appendix G.

Figure 5-33, Figure 5-34, Figure 5-35, Figure 5-36, and Figure 5-37 represent corresponding graphs concerning the conversion of methane, the yield of hydrogen, the yield of ethane, the yield of ethene, and the yield of ethyne, respectively, considering argon as dilution gas. According to the achieved model error ($E^2_{\Sigma,\mathrm{tot}} = 17809$) and Table 5-9, more or less clear disagreement of experimentally determined and calculated values has to be reported. However, the graphs often show qualitative consistence and calculated values mostly lie within or at least close to the range, which is defined by maximum experimental uncertainty. This observation applies to both, reaction conditions used and not used for the kinetic evaluation.

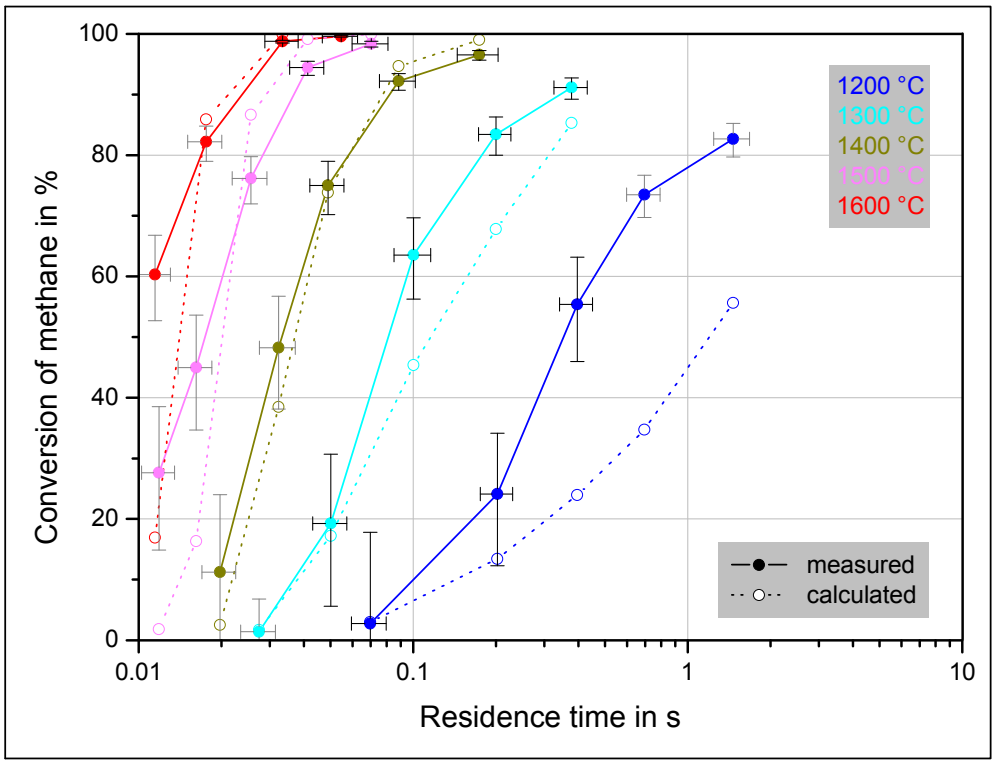

Figure 5-33: Comparison of experimentally determined conversion of methane (as a function of the residence time and the nominal furnace temperature) with calculated values employing reactor model 5 NTR and respective best fit kinetic parameters. 5 % initial molar fraction of methane in argon. Indicators of uncertainty refer to maximum uncertainty (black: used for kinetic evaluation, gray: not used for kinetic evaluation).

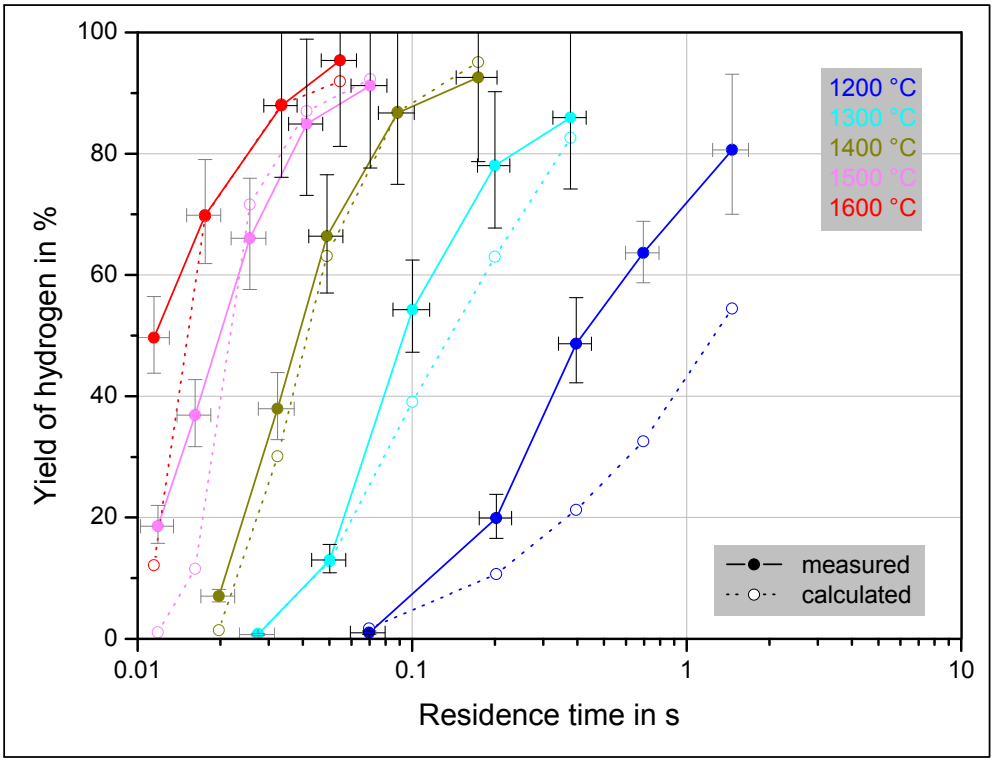

Figure 5-34: Comparison of experimentally determined yield of hydrogen (as a function of the residence time and the nominal furnace temperature) with calculated values employing reactor model 5 NTR and respective best fit kinetic parameters. 5 % initial molar fraction of methane in argon. Indicators of uncertainty refer to maximum uncertainty (black: used for kinetic evaluation, gray: not used for kinetic evaluation).

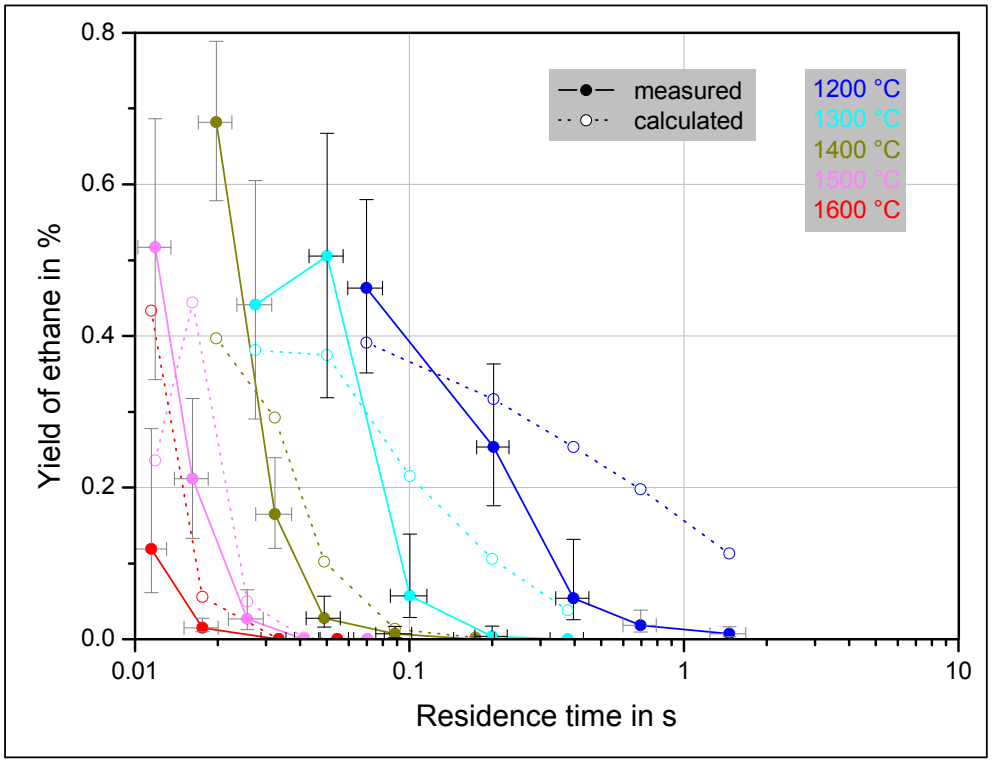

Figure 5-35: Comparison of experimentally determined yield of ethane (as a function of the residence time and the nominal furnace temperature) with calculated values employing reactor model 5 NTR and respective best fit kinetic parameters. 5 % initial molar fraction of methane in argon. Indicators of uncertainty refer to maximum uncertainty (black: used for kinetic evaluation, gray: not used for kinetic evaluation).

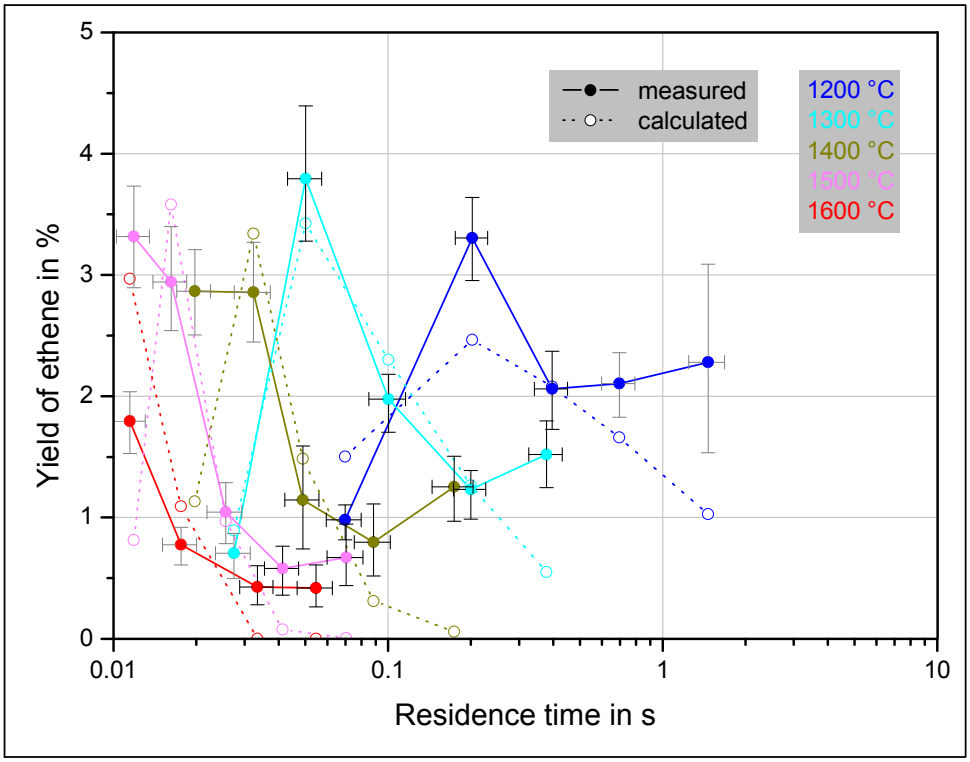

Figure 5-36: Comparison of experimentally determined yield of ethene (as a function of the residence time and the nominal furnace temperature) with calculated values employing reactor model 5 NTR and respective best fit kinetic parameters. 5 % initial molar fraction of methane in argon. Indicators of uncertainty refer to maximum uncertainty (black: used for kinetic evaluation, gray: not used for kinetic evaluation).

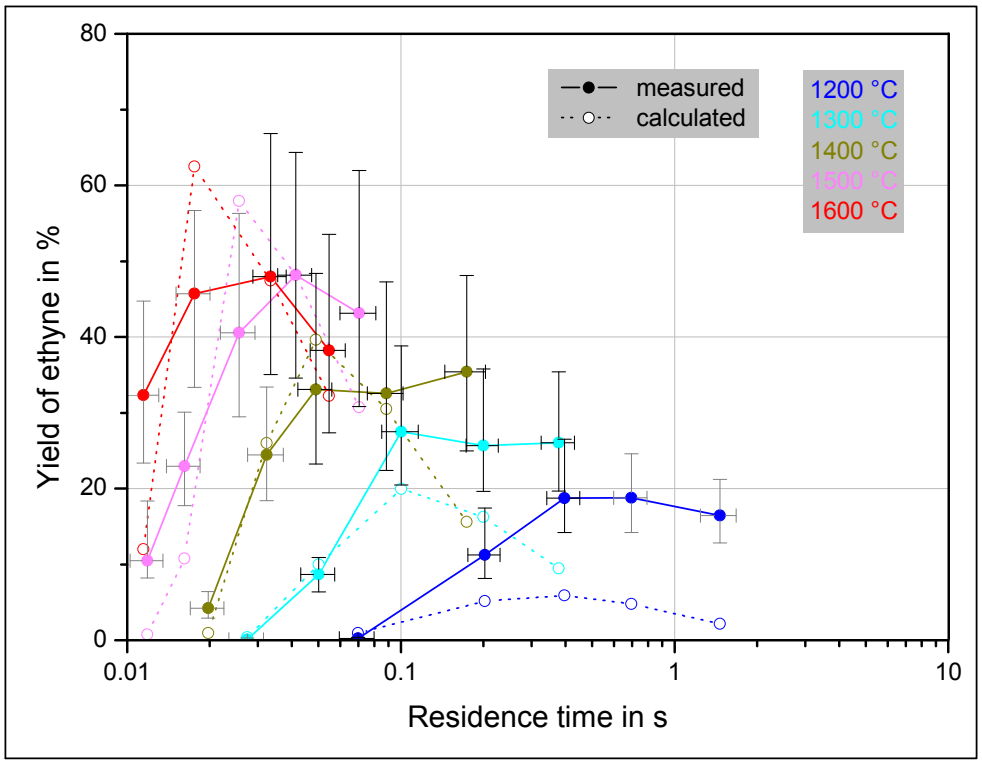

Figure 5-37: Comparison of experimentally determined yield of ethyne (as a function of the residence time and the nominal furnace temperature) with calculated values employing reactor model 5 NTR and respective best fit kinetic parameters. 5 % initial molar fraction of methane in argon. Indicators of uncertainty refer to maximum uncertainty (black: used for kinetic evaluation, gray: not used for kinetic evaluation).

Results gained in experiments with helium as dilution gas are compared to results from the kinetic evaluation concerning the conversion of methane, the yield of hydrogen, the yield of ethane, the yield of ethene, and the yield of ethyne, in Figure 5-38, Figure 5-39, Figure 5-40, Figure 5-41, and Figure 5-42, respectively. The agreement between calculated and measured values is definitely better than the agreement achieved for argon as the dilution gas. Measured values could regularly be reproduced by calculation within the limits of maximum uncertainty.

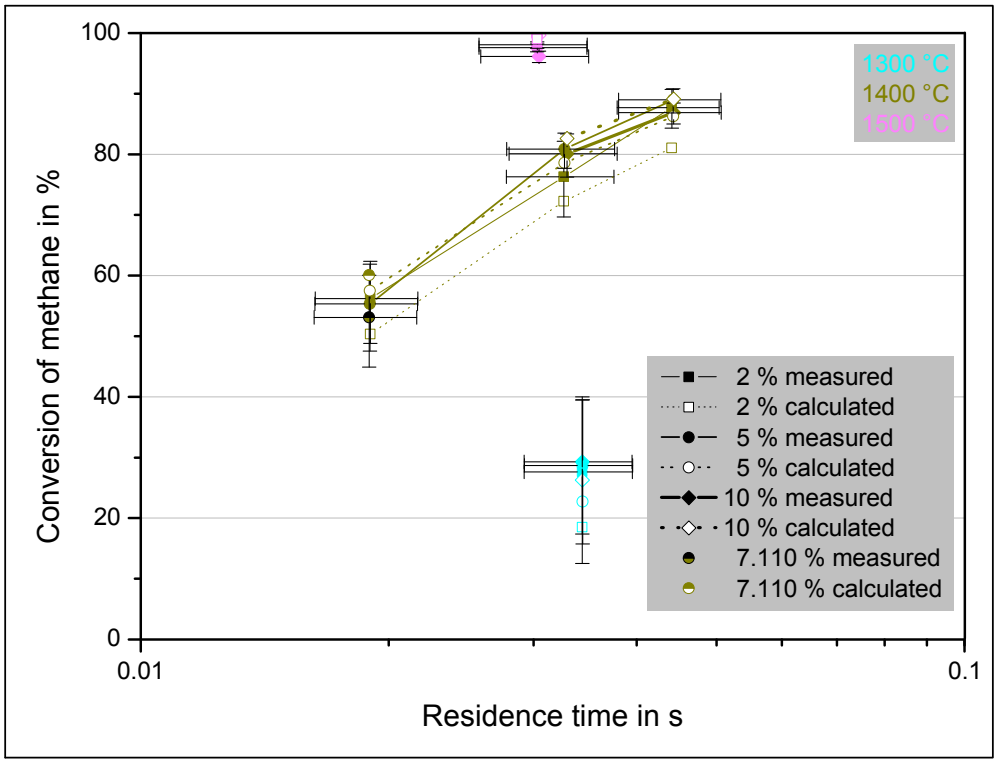

Figure 5-38: Comparison of experimentally determined conversion of methane (as a function of the residence time, the nominal furnace temperature, and the initial molar fraction of methane) with calculated values employing reactor model 5 NTR and respective best fit kinetic parameters. Dilution gas: helium. Indicators of uncertainty refer to maximum uncertainty.

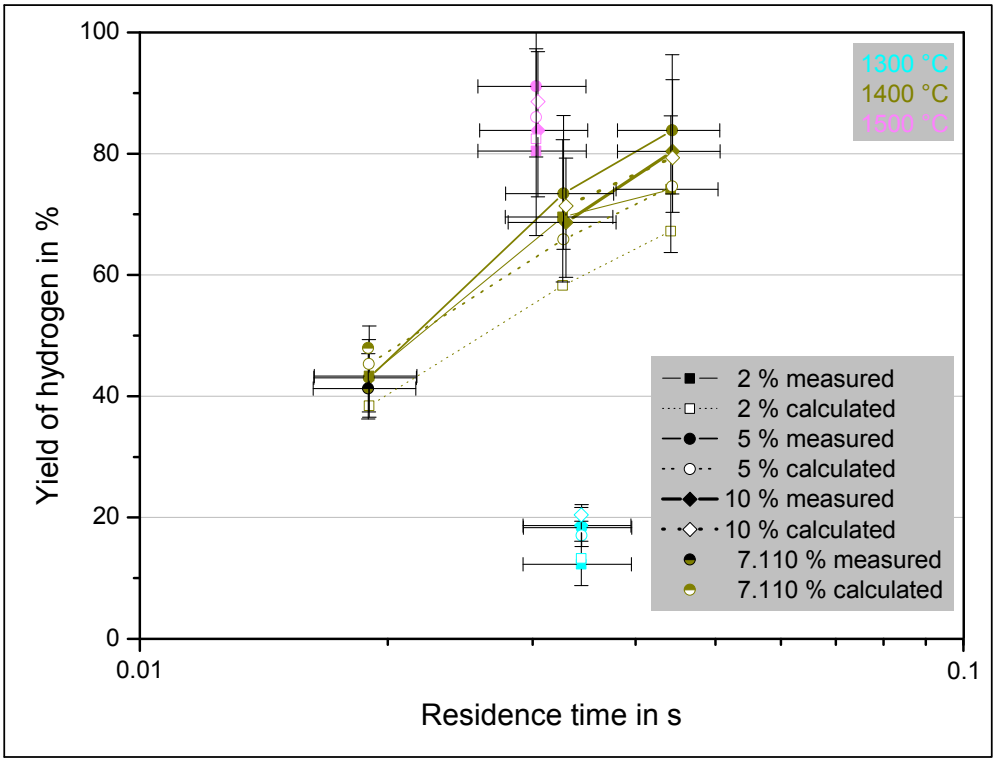

Figure 5-39: Comparison of experimentally determined yield of hydrogen (as a function of the residence time, the nominal furnace temperature, and the initial molar fraction of methane) with calculated values employing reactor model 5 NTR and respective best fit kinetic parameters. Dilution gas: helium. Indicators of uncertainty refer to maximum uncertainty.

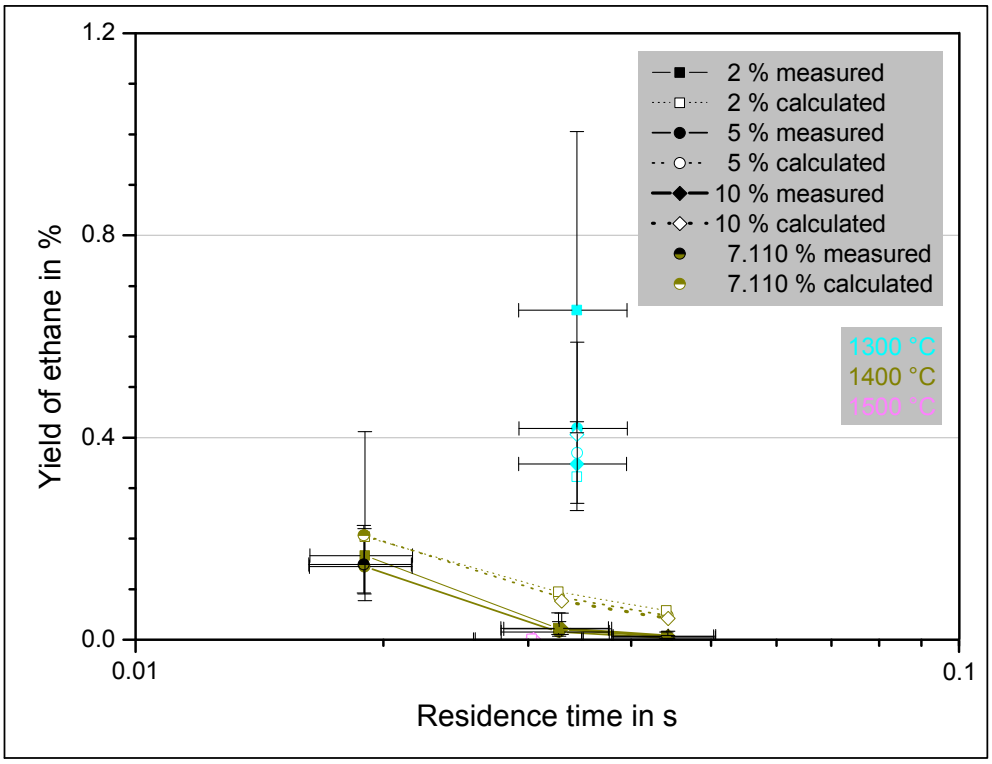

Figure 5-40: Comparison of experimentally determined yield of ethane (as a function of the residence time, the nominal furnace temperature, and the initial molar fraction of methane) with calculated values employing reactor model 5 NTR and respective best fit kinetic parameters. Dilution gas: helium. Indicators of uncertainty refer to maximum uncertainty.

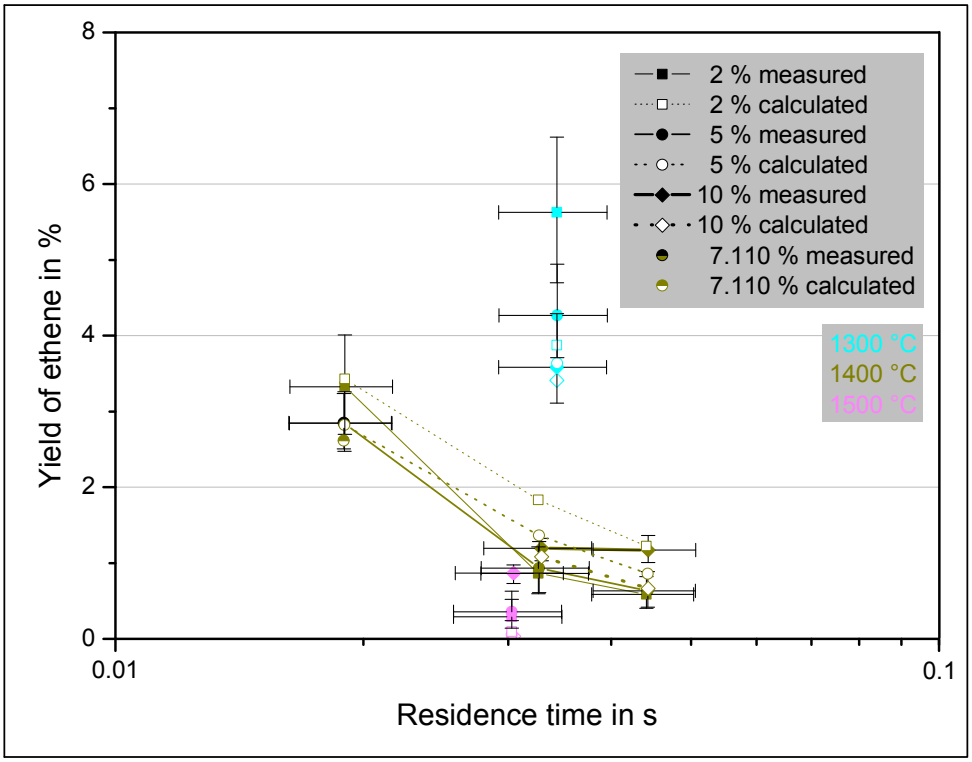

Figure 5-41: Comparison of experimentally determined yield of ethene (as a function of the residence time, the nominal furnace temperature, and the initial molar fraction of methane) with calculated values employing reactor model 5 NTR and respective best fit kinetic parameters. Dilution gas: helium. Indicators of uncertainty refer to maximum uncertainty.

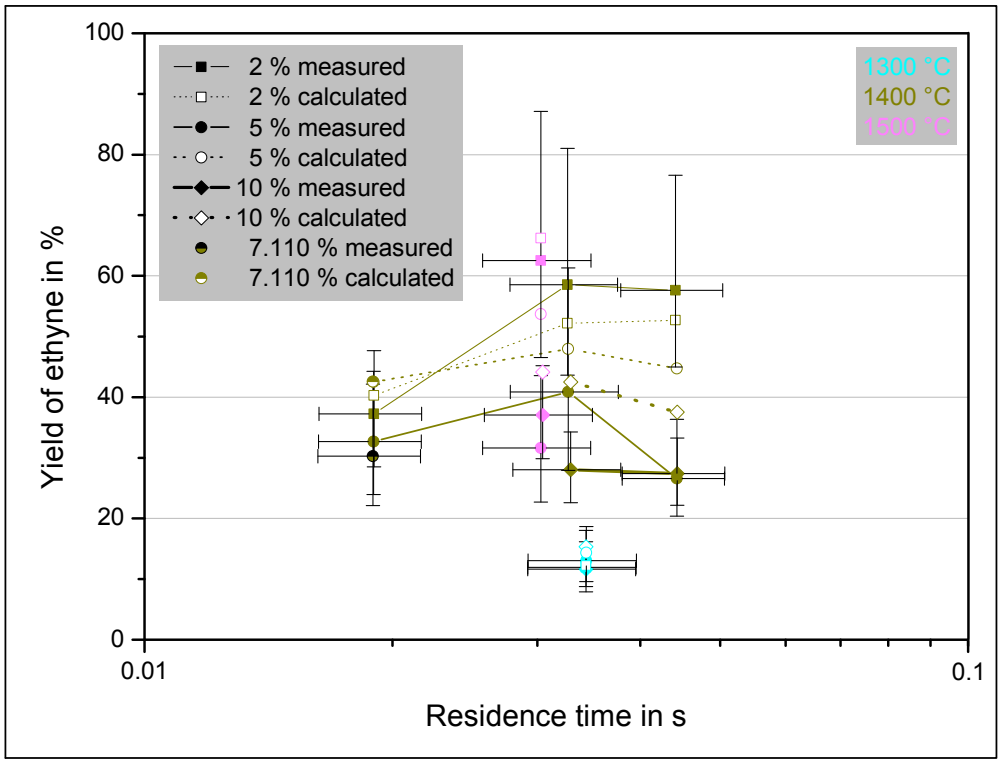

Figure 5-42: Comparison of experimentally determined yield of ethyne (as a function of the residence time, the nominal furnace temperature, and the initial molar fraction of methane) with calculated values employing reactor model 5 NTR and respective best fit kinetic parameters. Dilution gas: helium. Indicators of uncertainty refer to maximum uncertainty.

The standard uncertainties of estimated best fit parameters for the reactor model 5 NTR, which were calculated following the procedure explained in Chapter 2.4, are presented in Table 5-12, whereas the calculated covariance matrix $Cov(\boldsymbol{\psi})$ can be found in Appendix G. As can be seen in the table, the standard uncertainties of measured conversions and yields, which contribute to $E^2_{\Sigma,\mathrm{tot}}$, and the model itself allow the determination of best fit kinetic parameters with remarkably low standard uncertainty, mainly below 2.5 % relative to the estimated parameter value. Somewhat higher uncertainties have to be reported for the kinetic parameters of reaction {4} which describes the decay of ethyne. That corresponds to their comparatively low influence on the model error as depicted before in Figure 5-32.

Table 5-12: Standard uncertainties of best fit kinetic parameters for model 5 NTR

Kinetic parameters $\boldsymbol{\psi}$	Best fit value	Absolute standard uncertainty	Relative standard uncertainty in %
$E_{\mathrm{a},1}$	510.1	1.82	0.36
$\log(k_{0,1})$	17.77	0.0634	0.36
m_1	1.283	0.00710	0.55
$E_{\mathrm{a},2}$	433.9	9.38	2.16
$\log(k_{0,2})$	17.75	0.349	1.97
m_2	1.049	0.0251	2.39
$E_{\mathrm{a},3}$	374.7	3.14	0.84
$\log(k_{0,3})$	15.36	0.114	0.74
m_3	1.301	0.0127	0.97
$E_{\mathrm{a},4}$	29.01	3.73	12.86
$\log(k_{0,4})$	2.657	0.133	5.00
m_4	1.599	0.0335	2.10
$E_\mathrm{a}\ \mathrm{in}\ \frac{\mathrm{kJ}}{\mathrm{mol}},\ k_0\ \mathrm{in}\ \frac{1}{\mathrm{s}}\cdot\left(\frac{\mathrm{mol}}{\mathrm{m}^3}\right)^{(1-m)},\ m\ \mathrm{in}\ -$			

The matrix of correlation coefficients for the kinetic parameters $\boldsymbol{\psi}$ $Corr(\boldsymbol{\psi})$ derived from the covariance matrix is provided in Table 5-13. Except for the correlation of parameters bound to the same reaction, values do generally not exceed 0.25 and are mostly clearly below this limit. However, for all reactions a high correlation between the activation energy and the common logarithm of the pre-exponential factor is evident featuring correlation coefficients between 0.97 and 1. Suggested by the high correlation, these parameters can be varied simultaneously that way that the change of the model error is moderate. The combined standard uncertainty of

quantities derived from parameters with high correlation increases due to the fact that covariances have to be taken into account.[138]

Table 5-13: Matrix of correlation coefficients calculated based on the best fit kinetic parameters for model 5 NTR. Blocks colored in orange indicate the correlation of kinetic parameters describing the same reaction.

$Corr(\psi)$	1	2	3	4	5	6	7	8	9	10	11	12	Related to
1	1.00	1.00	0.63	0.01	0.02	0.08	0.10	0.14	0.24	-0.02	0.00	0.09	$E_{a,1}$
2	1.00	1.00	0.68	0.01	0.02	0.09	0.08	0.12	0.25	-0.02	0.00	0.09	$\log(k_{0,1})$
3	0.63	0.68	1.00	-0.01	0.01	0.12	-0.10	-0.04	0.25	-0.01	-0.01	0.01	m_1
4	0.01	0.01	-0.01	1.00	0.98	0.07	0.01	-0.02	-0.06	0.00	0.00	0.01	$E_{a,2}$
5	0.02	0.02	0.01	0.98	1.00	0.28	0.01	-0.03	-0.06	0.00	0.00	0.01	$\log(k_{0,2})$
6	0.08	0.09	0.12	0.07	0.28	1.00	-0.03	-0.03	0.01	0.00	0.00	0.00	m_2
7	0.10	0.08	-0.10	0.01	0.01	-0.03	1.00	0.97	0.09	0.00	0.02	0.09	$E_{a,3}$
8	0.14	0.12	-0.04	-0.02	-0.03	-0.03	0.97	1.00	0.34	0.00	0.02	0.09	$\log(k_{0,3})$
9	0.24	0.25	0.25	-0.06	-0.06	0.01	0.09	0.34	1.00	-0.01	0.00	0.03	m_3
10	-0.02	-0.02	-0.01	0.00	0.00	0.00	0.00	0.00	-0.01	1.00	0.97	-0.29	$E_{a,4}$
11	0.00	0.00	-0.01	0.00	0.00	0.00	0.02	0.02	0.00	0.97	1.00	-0.06	$\log(k_{0,4})$
12	0.09	0.09	0.01	0.01	0.01	0.00	0.09	0.09	0.03	-0.29	-0.06	1.00	m_4
$E_a \text{ in } \frac{\text{kJ}}{\text{mol}}$, $k_0 \text{ in } \frac{1}{\text{s}} \cdot \left(\frac{\text{mol}}{\text{m}^3}\right)^{(1-m)}$, $m \text{ in } -$													

5.7 Discussion

Best fit values for the kinetic parameters were determined employing an optimization tool by minimizing the model error. Regarding the particular models seriously different applied initial parameter sets usually lead to practically identical best fit values for the kinetic parameters and consequently to same values of the minimum model error. Thus, a global character of the determined minimum model errors is indicated. The lowest value for the model error could be located for the reactor model based on five nested tube reactors without the consideration of radial diffusion (5 NTR). The corresponding model based on ten nested tube reactors features virtually equal agreement and best fit kinetic parameters suggesting that the laminar flow characteristics are respected sufficiently well by employing five nested tube reactors. The same conclusion can be drawn by comparing the reactor models involving ideal radial diffusion. For models respecting radial diffusion, minimum model errors only about 2.9 % higher than those of

[138] cp. [ISO, 2008], p. 21

the models disregarding radial diffusion could be achieved. Thus, it is indicated that the limiting conditions concerning radial diffusion are capable of reflecting the real conditions inside the reactor more or less comparably well, or in other words, that the real conditions can be found somewhere between the extreme effects. However, in spite of the principal difference of the models, there exists remarkable conformity of derived best fit values of the kinetic parameters. Except for parameters of reaction {4}, best fit values corresponding to models with ideal radial diffusion do not differ more than 8.2 % and mainly not more than 3.6 % from values corresponding to models without radial diffusion. This could signify a rudimentarily universal character of the determined parameter values. The gained best fit parameter values and the achieved model error as well as its components are practically identical for the plug flow model and for the models based on nested tube reactors featuring ideal radial diffusion. Obviously, the latter models basically approach plug flow conditions. This proposes that the approximation of laminar flow does not offer any advantage, when perfect radial diffusion is assumed, and that a more sophisticated consideration of radial diffusion is advisable. It is admissible to state that reaction temperatures were considered reasonably, since reaction conditions with doubtful temperature distribution were excluded from the kinetic evaluation. Taking the residual uncertainty of temperatures as well as the uncertainty of pressures inside the reactors into account, additional optimization runs were performed based on the best present model 5 NTR. The resulting best fit parameter values conform to values determined for the sets of nominal temperature and pressure. Thus, the accuracy of temperatures and pressures is high enough to definitely calculate best fit parameter values. Furthermore, a distinct finding concerning the determined parameter values is indicated by quite low standard uncertainties derived from the covariance matrix. Except for the correlation between the activation energy and the common logarithm of the pre-exponential factor related to the same reaction the correlation between the kinetic parameters is usually negligible. In spite of the relatively high model error, reactor model 5 NTR is capable of reflecting general tendencies and orders of magnitude of methane conversion as well as of yields of hydrogen, ethane, ethene, and ethyne. When maximum uncertainty is taken into account, calculated values are often in reach of results of both, experiments with argon and helium as dilution gas.

In literature the integers 1 and 2 are suggested as reaction orders of the thermal decomposition of methane as well as the thermal decomposition of C_2-hydrocarbons without presence of additional material as presented in Chapter 3.4. Contrariwise, parameter fitting to model 5 NTR led to values between 1 and 2, namely 1.283, 1.049, 1.301, and 1.599 for reaction {1}, {2}, {3}, and {4}, respectively. The fractional nature of derived parameters is not a general sign of poor quality but confirms the summarizing character of net reactions and possibly reveals limitations of a simplified kinetic approach considering a wide range of reaction conditions. The calculated activation energy of reaction {1} lies beyond the scope of activation energies reported in

literature. However, also the pre-exponential factor is somewhat higher and accounts for a partial compensation. The activation energies of the other decomposition reactions follow the vague trend depending on the number of H-atoms as indicated by literature values exposed in Chapter 3.4.3. Activation energies of the thermal decomposition of ethyne reported in literature are much higher than the determined value of 29.01 kJ/mol suggesting some principal differences of mechanisms relevant for the direct pyrolysis of ethyne on the one hand and for the decomposition of ethyne in presence of unconverted methane and other reaction products on the other hand. The best fit parameter set of reaction {4} is somehow similar to the parameters reported in [Schulz, 1985], where parameters were also fitted to data gained in experiments investigating the thermal decomposition of methane. When results of this work are compared to findings presented in literature, is has to be taken into account that reaction temperatures employed there for further calculations often have an approximate nature due to imprecise measurement techniques (e. g. pyrometer measurements concerning the outer wall, calculation from shock speed, thermocouple measurements at particular locations), which of course imply an uncertainty of stated parameter values. Furthermore, uncertainties may result from assumed ideal flow conditions, which could be doubtful as shown in this work.

Experiments under seeding conditions showed that carbon black, featuring a specific surface similar to the particle samples extracted from the reactor and the filter, has great potential to enhance heterogeneous reactions. Thus, a respective activity of generated particulate carbon is indicated. Consequently, the relatively high model error is probably partly attributed to the simplified kinetic model, which does not distinguish between homogeneous effects and heterogeneous effects. However, the assessment of surface area provided by generated particles is complicated by the presence of not considered species, which hold significant fractions of C-atoms, and by uncertainties related to the characteristics of formed carbon as well as the locations of carbon deposition.

6 Summary and Outlook

The kinetics of the thermal decomposition of methane was investigated using an alumina tubular reactor with an inner diameter of 8 mm heated by a vertical electric tube furnace. Experiments at absolute pressures around 1 bar were carried out using argon and helium as dilution gases. The initial molar fraction of methane was varied between 2 % and 10 %. Nominal furnace temperatures ranged from 1200 °C to 1600 °C. Initial total standard volume flows, varied from 95 sccm to 9800 sccm, led to residence times between 0.0115 s and 1.47 s. Depending on the reaction conditions, conversions of methane between 1.20 % and 99.8 % were achieved, whereas the yields of hydrogen lay in the range from 0.546 % to 95.4 %. Similarly to the yield of hydrogen, the conversion of methane increases with residence time and temperature, while the initial molar fraction of methane has minor influence. Beside hydrogen and carbon, the intermediates ethane, ethene, and ethyne could be found at the outlet of the reactor featuring maximum yields of 0.927 %, 5.63 %, and 62.5 %, respectively. The detected species form major part of the gaseous product flow and the hydrogen balance is practically satisfied for every reaction condition. Graphs confirm that ethane is the first formed C_2-hydrocarbon followed by ethene and ethyne. The yield of C_2-hydrocarbons related to the yield of hydrogen generally decreases when the temperature, the residence time, and / or the initial molar fraction of methane increase. In order to achieve product flows predominantly containing hydrogen and carbon, reaction conditions characterized by low dilution of methane, high reaction temperatures, and high residence times should be applied.

Additional experiments attested good repeatability of results. Furthermore, the collection of carbon samples from the reactor and the downstream filter allowed the assessment of the balance of carbon atoms, which showed disagreement up to 48.3 % and about 28.5 % on average. Low molar fractions of the C_3-hydrocarbons propene, propyne, and most likely propadiene were detected, but determined molar fractions lay far below an order of magnitude which could possibly account for the disagreement of the carbon balance, namely in the order of magnitude of ethane regarding propene and in the order of magnitude of ethene regarding propyne and propadiene. This leads to the conclusion that small amounts of not considered high molecular substances with a low H/C-ratio were probably present in the product flow.

Usually more carbon could be found in the reactor than in the filter. The BET specific surface of carbon samples from the reactor ranged from 6.9 m^2/g to 94.7 m^2/g, whereas BET specific surfaces of samples from the filter were somewhat higher and ranged from 22.3 m^2/g to 139.1 m^2/g. The samples from the reactor not only contained particulate carbon but also up to 100 % volume fraction of pyrocarbon formed at the inner wall of the reactor. A clear dependency of the sample constitution on the reaction conditions could not be extracted.

A novel apparatus was employed in order to add Super P, a carbon black with a typical BET specific surface of 62 m^2/g, to the gaseous flow at the inlet of the reactor and to examine the reactions under seeding conditions. By inserting a mass flow of 5.24 g/h Super P through the reactor, the conversion of methane and the yield of hydrogen could be increased by 18 % and 33 %, respectively, compared to the reference conditions without seeding defined by 1400 °C nominal furnace temperature, 3800 sccm total standard volume flow at the inlet of the reactor, and 5 % initial molar fraction of methane in argon. Simultaneously the yield of hydrogen related to the yield of C_2-hydrocarbons rose from 1.38 to an averaged value of 1.81, indicating that seeding offers the possibility to enhance reaction rates and to raise the cleanliness of the product flow as also reported in literature. Since the specific surface of Super P is similar to the specific surface of extracted particle samples, rate increasing influence of generated particles is suggested. The geometrical inner surface of the heated region of the reactor lay in the same order of magnitude as the surface provided by added particles. It could consequently have offered reaction sites as well and could thereby have enhanced heterogeneous reactions.

Temperature profiles inside the reactor were determined for every set of nominal furnace temperature and total standard volume flow with a self-made thermocouple type S shielded by an alumina protection tube. Instead of gas mixtures containing methane, pure flows of the respective dilution gas were employed. At every considered axial position a maximum and a minimum temperature could be measured by inclining the thermocouple. The higher the total standard volume flow the greater was the measured radial temperature difference reaching maximum levels of about 400 K. Helium caused clearly lower radial temperature differences than argon resulting from better heat transfer characteristics. The temperature measurement was influenced by convection and radiation. A comparison of respective heat transfer coefficients showed that the temperature measurement was dominated by the convective heat transfer. The geometrical situation disallowed a reasonable association of measured temperatures and temperatures of the fluid at the wall and in the center of the reactor for every case. Provided that a moderate radial temperature gradient could be expected, such an alignment was executed. Experimental results were respected in the kinetic evaluation, only if they were gained for conditions which ensure that at least 75 % of the considered positions in the relevant region of the reactor show a moderate radial temperature gradient.

Axial diffusion could generally be neglected as was shown by Péclet number considerations. Though two sets of nominal furnace temperature and residence time, which could involve significant axial diffusion, were excluded from the kinetic evaluation. Calculations concerning radial diffusion indicate that respective effects are mostly of minor importance. Nonetheless, radial diffusion may become more relevant the higher the residence time is – possibly reaching noteworthy levels especially regarding hydrogen.

The flow through the entrance region and the reactor was generally laminar. However, it was shown that a fully developed laminar velocity profile could not be expected at the inlet of the reactor for every considered reaction condition. Simulations with ANSYS allowed assessing the velocity profiles at the inlet of the reactor, which more or less differ from the ideal case predominantly depending on the applied volume flow. Subsequent simulations with COMSOL Multiphysics were carried out in order to develop a general idea of the flow characteristics inside the reactor providing simplified temperature profiles of the wall. Even though not perfectly parallel to each other and to the axis of symmetry of the reactor, in all cases flow lines clearly show a general order which reflects the laminar characteristics of the flow. It was confirmed that the main pressure drop occurred in the lower part of the reactor, where the center was occupied by the thermocouple.

The shape of flow lines calculated with COMSOL Multiphysics led to the establishment of a reactor model based on virtual nested tube reactors. Five different reactor models were applied. Based on five and ten nested tube reactors four different models were created by implementing ideal radial diffusion on the one hand and by entire disregard of radial diffusion on the other hand. Furthermore, a plug flow model served as a reference case. A simplified kinetic model comprising the net dehydrogenation reactions of methane and the intermediates ethane, ethene, and ethyne according to

- 2 CH_4 (g) → C_2H_6 (g) + H_2 (g) {1}
- C_2H_6 (g) → C_2H_4 (g) + H_2 (g) {2}
- C_2H_4 (g) → C_2H_2 (g) + H_2 (g) {3}
- C_2H_2 (g) → 2 “C” (s) + H_2 (g) {4}

with the rate of reaction $\{q\}$ defined as

$$r_q = k_{0,q} \cdot e^{-\frac{E_{a,q}}{\Re \cdot T}} \cdot c_{\text{reactant},q}^{m_q}$$

was considered. Resulting from the lack of information related to the formation and deposition of carbon it was refused to differentiate between homogeneous and heterogeneous reactions. Employing an optimization tool, best fit values for the kinetic parameters – the activation energy E_a, the common logarithm of the pre-exponential factor $\log(k_0)$, and the reaction order m – for all four reactions were determined by minimizing the model error following Chi-Square fitting.

The model error was a function of the differences between experimentally assessed and calculated conversions and yields as well as of estimated standard uncertainties of measured values. Best agreement between experimental results and calculations, respecting 42 reaction conditions with argon as diluent and 15 reaction conditions with helium as diluent, could be achieved with the reactor model based on five nested tube reactors when the radial diffusion was neglected. Respective values for kinetic parameters and standard uncertainties derived from the covariance matrix are:

$$E_{\mathrm{a},1} = 510.1 \pm 1.82 \,\frac{\mathrm{kJ}}{\mathrm{mol}}, \quad \log(k_{0,1}) = 17.77 \pm 0.0634 \log\left[\frac{1}{\mathrm{s}} \cdot \left(\frac{\mathrm{mol}}{\mathrm{m}^3}\right)^{(1-m_1)}\right], \quad m_1 = 1.283 \pm 0.00710$$

$$E_{\mathrm{a},2} = 433.9 \pm 9.38 \,\frac{\mathrm{kJ}}{\mathrm{mol}}, \quad \log(k_{0,2}) = 17.75 \pm 0.349 \log\left[\frac{1}{\mathrm{s}} \cdot \left(\frac{\mathrm{mol}}{\mathrm{m}^3}\right)^{(1-m_2)}\right], \quad m_2 = 1.049 \pm 0.0251$$

$$E_{\mathrm{a},3} = 374.7 \pm 3.14 \,\frac{\mathrm{kJ}}{\mathrm{mol}}, \quad \log(k_{0,3}) = 15.36 \pm 0.114 \log\left[\frac{1}{\mathrm{s}} \cdot \left(\frac{\mathrm{mol}}{\mathrm{m}^3}\right)^{(1-m_3)}\right], \quad m_3 = 1.301 \pm 0.0127$$

$$E_{\mathrm{a},4} = 29.01 \pm 3.73 \,\frac{\mathrm{kJ}}{\mathrm{mol}}, \quad \log(k_{0,4}) = 2.657 \pm 0.133 \log\left[\frac{1}{\mathrm{s}} \cdot \left(\frac{\mathrm{mol}}{\mathrm{m}^3}\right)^{(1-m_4)}\right], \quad m_4 = 1.599 \pm 0.0335$$

The correlation of parameters not associated with the same reaction is generally low. However, for all reactions a high correlation between the activation energy and the common logarithm of the pre-exponential factor was revealed featuring correlation coefficients close to 1. Therefore, also covariances have to be taken into account for the determination of uncertainty of quantities derived from the kinetic parameters. Very similar best fit kinetic parameters were found for extreme values of temperatures and pressures, which represent input data for the kinetic calculations. Moreover, best fit kinetic parameters for the other considered reactor models as well as resulting model errors are somehow comparable with the results for the reactor model based on five nested tube reactors without radial diffusion, indicating a rudimentarily universal character of the determined values of the kinetic parameters. This work provides a comprehensive and traceable analysis of uncertainty in all relevant fields of the kinetic evaluation. The uncertainty in measurement and its propagation were respected. Finally the standard uncertainty as well as the correlation of derived kinetic parameters was declared, what can be rarely found in respective literature.

The given values for the kinetic parameters lead to a minimum model error, but the model error remains relatively high. Great effort was made to estimate representative standard uncertainties

of experimental findings. Furthermore, only reaction conditions were considered which feature a reasonable assessment of the temperature distribution. Consequently, the model error is basically attributed to an imprecise model. On average the differences between calculated and experimentally determined values for the conversion of methane, the yield of hydrogen, the yield of ethane, the yield of ethene, and the yield of ethyne equal 0.0657, 0.0602, 0.000664, 0.00575, and 0.0806, respectively. Mean differences related to experimental results lie in the fair region of 14.5 % for the conversion of methane and the yield of hydrogen, but show clearly higher values regarding the yields of ethane, ethene, and ethyne: 286 %, 53.8 %, and 47.3 %. However, especially concerning ethane and ethene the latter differences appear to be less radical when the lower level of measured values is taken into account. Moreover, general trends are respected and calculated values for the conversion of methane as well as the yields of hydrogen and C_2-hydrocarbons are often in reach of maximum uncertainty of experimental results.

Two potentially problematic fields could be identified regarding the discrepancy of the models. The considered models either assume ideal radial diffusion or totally neglect respective effects. The real conditions might have featured diffusive characteristics, which cannot globally be described by these extreme cases. In principle, this problem may be solved with extensive work of implementation, which goes beyond the scope of this work. In addition, the kinetic model ignores any heterogeneous effects either on the wall of the reactor or on the surface of formed carbon. An appropriate assessment of provided surfaces is complicated in several respects. It was shown that a remarkable fraction of C-atoms formed part of not considered species. Consequently, the amount of generated carbon is overestimated as long as other relevant species are not respected. Important (intermediate) species could be benzene and particular PAHs. The formed carbon refuses uniform characteristics regarding the principal constitution (particulate carbon vs. pyrocarbon) and specific surfaces. In absence of suitable information, a possibility to practically include heterogeneous effects in a model could be a modification of the activation energy that way that this parameter is not constant but a function of an accessible dimension, such as the concentration of formed carbon. However, significant fraction of formed carbon does not keep a dispersed state in the flow but forms deposit on the wall and there alters surface related properties. Before heterogeneous reactions on the wall and on the surface of generated particles can be implemented accurately, further research has to be done in order to understand the dependencies of carbon formation and locations of deposition on the reaction conditions. As long as fundamental information about related mechanisms is not available, the transfer of kinetic laws to arbitrary specifications of reactors and reaction conditions implies an uncertainty difficult to assess.

7 References

[Abanades, 2005] S. Abanades and G. Flamant (2005). "Production of hydrogen by thermal methane splitting in a nozzle-type laboratory-scale reactor." International Journal of Hydrogen Energy **30**: 843-853.

[Abanades, 2006] S. Abanades and G. Flamant (2006). "Solar hydrogen production from the thermal splitting of methane in a high temperature solar chemical reactor." Solar Energy **80**(10): 1321-1332.

[Abanades, 2007] S. Abanades and G. Flamant (2007). "Experimental study and modeling of a high-temperature solar chemical reactor for hydrogen production from methane cracking." International Journal of Hydrogen Energy **32**: 1508-1515.

[Abanades, 2009] S. Abanades, S. Tescari, et al. (2009). "Natural gas pyrolysis in double-walled reactor tubes using thermal plasma or concentrated solar radiation as external heating source." Journal of Natural Gas Chemistry **18**(1): 1-8.

[Abbas, 2009] H. F. Abbas and W. M. A. Wan Daud (2009). "Thermocatalytic decomposition of methane using palm shell based activated carbon: Kinetic and deactivation studies." Fuel Processing Technology **90**(9): 1167-1174.

[Abbas, 2010 a] H. F. Abbas and W. M. A. Wan Daud (2010). "Hydrogen production by methane decomposition: A review." International Journal of Hydrogen Energy **35**(3): 1160-1190.

[Abbas, 2010 b] H. F. Abbas and W. M. A. W. Daud (2010). "Hydrogen production by thermocatalytic decomposition of methane using a fixed bed activated carbon in a pilot scale unit: Apparent kinetic, deactivation and diffusional limitation studies." International Journal of Hydrogen Energy **35**(22): 12268-12276.

[Adunka, 2004] F. Adunka (2004). Handbuch der Wärmeverbrauchsmessung. Grundlagen. Methoden. Probleme. Essen, Vulkan.

[Advantech, 2007] Advantech Co., Ltd. (2007). ADAM-5000 Series. I/O Module. User's Manual. 2.2 rd Edition. Milpitas, Advantech Co., Ltd.

[Albermann, 2007] E. Albermann (2007). Identifizierung und quantitative Analyse der bei der thermischen Dissoziation von Methan gebildeten Nebenprodukte. Köln, Universität zu Köln. (Diploma thesis at the DLR, Institute of

Technical Thermodynamics, Solar Research, Köln)

[ANALYT, 2006] ANALYT-MTC Messtechnik GmbH & Co. KG (2006). Bedienungsanleitung DC-Lite. Müllheim, ANALYT-MTC Messtechnik GmbH & Co. KG.

[Ashok, 2008] J. Ashok, S. N. Kumar, et al. (2008). "COx free hydrogen by methane decomposition over activated carbons." Catalysis Communications **9**(1): 164-169.

[Atkins, 2010] P. Atkins and J. de Paula (2010). Atkins' Physical Chemistry. 9. ed. Oxford, Oxford University Press.

[Ausubel, 2000] J. H. Ausubel (2000). "Where is energy going?" The Industrial Physicist **6**(1): 16-19.

[Back, 1983] M. H. Back and R. A. Back (1983). Thermal Decomposition and Reactions of Methane. In: Pyrolysis. Theory and Industrial Practice. L. F. Albright, B. L. Crynes, and W. H. Corcoran. New York, Academic Press, Inc.: 1-24.

[Baehr, 2006] H. D. Baehr and K. Stephan (2006). Wärme- und Stoffübertragung. 5. ed. Berlin, Springer.

[Bai, 2005] Z. Bai, H. Chen, et al. (2005). "Catalytic decomposition of methane over activated carbon." Journal of Analytical and Applied Pyrolysis **73**(2): 335-341.

[Bai, 2006] Z. Bai, H. Chen, et al. (2006). "Hydrogen production by methane decomposition over coal char." International Journal of Hydrogen Energy **31**: 899-905.

[Berthelot, 1866] M. Berthelot (1866). "Ueber die Einwirkung der Hitze auf einige Kohlenwasserstoffe." Justus Liebigs Annalen der Chemie **139**(3): 272-282.

[Billaud, 1989] F. Billaud, F. Baronnet, et al. (1989). "Thermal decomposition of methane. Bibliographic study and proposal of a mechanism." Revue de l'Institut français du pétrole **44**(6): 813-823.

[Billaud, 1992] F. Billaud, C. Gueret, et al. (1992). "Thermal decomposition of pure methane at 1263 K. Experiments and mechanistic modelling." Thermochimica Acta **211**: 303-322.

[Bios, 2006] Bios International Corporation (2006). DryCal DC-Lite Models. http://drycal.com/drycal/dc-lite-models.htm, accessed 17 February 2006.

[Bios, 2009] M. Aziz (02 April 2009). Personal e-mail to M. Wullenkord (DLR), Bios International Corporation, Butler.

[Chen, 1975] C.-J. Chen, M. H. Back, et al. (1975). "The Thermal Decomposition of Methane. I. Kinetics of the Primary Decomposition to $C_2H_6 + H_2$; Rate Constant for the Homogeneous Unimolecular Dissociation of Methane and its Pressure Dependence." Canadian Journal of Chemistry **53**: 3580-3590.

[Chorkendorff, 2003] I. Chorkendorff and J. W. Niemantsverdriet (2003). Concepts of Modern Catalysis and Kinetics. Weinheim, WILEY-VCH.

[Dahl, 2001] J. K. Dahl, J. Tamburini, et al. (2001). "Solar-Thermal Processing of Methane to Produce Hydrogen and Syngas." Energy & Fuels **15**: 1227-1232.

[Dahl, 2002] J. K. Dahl, K. J. Buechler, et al. (2002). Rapid Solar-thermal Dissociation of Natural Gas in an Aerosol Flow Reactor. 11th SolarPACES International Symposium on Concentrated Solar Power and Chemical Energy Technologies, Zurich.

[Dahl, 2004] J. K. Dahl, K. J. Buechler, et al. (2004). "Solar-thermal dissociation of methane in a fluid-wall aerosol flow reactor." International Journal of Hydrogen Energy **29**: 725-736.

[Dean, 1990] A. M. Dean (1990). "Detailed kinetic modeling of autocatalysis in methane pyrolysis." The Journal of Physical Chemistry **94**(4): 1432-1439.

[DLR, 2005] DLR, NERC, et al. (2005). MED-CSP. Concentrating Solar Power for the Mediterranean Region. Study commissioned by The Federal Ministry for the Environment, Nature Conservation and Nuclear Safety, Germany. http://www.dlr.de/tt/med-csp.

[Dunn, 2002] S. Dunn (2002). "Hydrogen futures: toward a sustainable energy system." International Journal of Hydrogen Energy **27**: 235-264.

[Ebbing, 2005] D. D. Ebbing and S. D. Gammon (2005). General Chemistry. 8. ed. New York, Houghton Mifflin.

[EES, 2009] EES Engineering Equation Solver 2009. V8.412-3D.

[Eisenberg, 1967] B. Eisenberg and H. Bliss (1967). "Kinetics of Methane Pyrolysis." Chemical Engineering Progress Symposium Series **63**(72): 3-17.

[Fincke, 2002] J. R. Fincke, R. P. Anderson, et al. (2002). "Plasma Pyrolysis of Methane to Hyrogen and Carbon Black." Industrial and Engineering Chemistry Research **41**(6): 1425-1435.

[Flamant, 2007] G. Flamant (2007). SOLHYCARB: Hydrogen and carbon nanomaterials from solar energy without CO_2 emission. The Parliament Magazine. **238:** 68.

[Fletcher, 2001] E. A. Fletcher (2001). "Solarthermal Processing: A Review." Journal of Solar Energy Engineering **123**: 63-74.

[Fluke, 2002] Fluke Corporation (2002). Model 187 & 189. True RMS Multimeter. Bedienungs-Handbuch. Rev. 2, Everett, Fluke Corporation.

[Förster, 2009] B. Förster (2009). Qualifizierung, Optimierung und Steuerung einer Baugruppe zum Dispergieren von Carbon Black in einem Gasstrom. Berlin, Beuth Hochschule für Technik. (Diploma thesis at the DLR, Institute of Technical Thermodynamics, Solar Research, Köln)

[FRIATEC, 2003] FRIATEC AG (2003). DEGUSSIT. Delivery Programme Oxide Ceramics: Tubes, rods, laboratory ware and insulating powders. Mannheim, FRIATEC AG. (Brochure 977a)

[Fulcheri, 2002] L. Fulcheri, N. Probst, et al. (2002). "Plasma processing: a step towards the production of new grades of carbon black." Carbon **40**: 169-176.

[Gardiner, 1975] W. C. Gardiner Jr., J. H. Owen, et al. (1975). "Rate and mechanism of methane pyrolysis from 2000° to 2700°K." Symposium (International) on Combustion **15**(1): 857-868.

[Geitmann, 2002] S. Geitmann (2002). Wasserstoff & Brennstoffzellen. Die Technik von morgen! Berlin, Hydrogeit.

[Gero, 2006] S. Becht (10 October 2006). Personal e-mail to M. Wullenkord (DLR), Gero Hochtemperaturöfen GmbH & Co. KG, Neuhausen.

[Glick, 1959] H. S. Glick (1959). "Shock tube studies of reaction kinetics of aliphatic hydrocarbons." Symposium (International) on Combustion **7**: 98-107.

[Gordon, 1948] A. S. Gordon (1948). "Pyrolysis of Methane Flowing Through a

Porcelain Tube in the Region 1000°." Journal of the American Chemical Society **70**: 395-401.

[Grenda, 2003] J. M. Grenda, I. P. Androulakis, et al. (2003). "Application of Computational Kinetic Mechanism Generation to Model the Autocatalytic Pyrolysis of Methane." Industrial & Engineering Chemistry Research **42**(5): 1000-1010.

[Guerét, 1994] C. Guerét and F. Billaud (1994). "Thermal coupling of methane: influence of hydrogen at 1330°C. Experimental and Simulated Results." Journal of Analytical and Applied Pyrolysis **29**: 183-205.

[Hagen, 2004] J. Hagen (2004). Chemiereaktoren. Auslegung und Simulation. Weinheim, WILEY-VCH.

[Happel, 1967] J. Happel and L. Kramer (1967). "Acetylene and hydrogen from the pyrolysis of methane." Journal of Industrial and Engineering Chemistry **59**(1): 39-50.

[Hartig, 1971] R. Hartig, J. Troe, et al. (1971). "Thermal decomposition of methane behind reflected shock waves." Symposium (International) on Combustion **13**(1): 147-154.

[Hefner, 2002] R. A. Hefner III (2002). "The age of energy gases." International Journal of Hydrogen Energy **27**(1): 1-9.

[Hidaka, 1985] Y. Hidaka, S. Shiba, et al. (1985). "Thermal decomposition of ethane in shock waves." International Journal of Chemical Kinetics **17**(4): 441-453.

[Hirsch, 2001] D. Hirsch, M. Epstein, et al. (2001). "The solar thermal decarbonization of natural gas." International Journal of Hydrogen Energy **26**: 1023-1033.

[Hirsch, 2004 a] D. Hirsch and A. Steinfeld (2004). "Solar hydrogen production by thermal decomposition of natural gas using a vortex-flow reactor." International Journal of Hydrogen Energy **29**: 47-55.

[Hirsch, 2004 b] D. Hirsch and A. Steinfeld (2004). "Radiative transfer in a solar chemical reactor for the co-production of hydrogen and carbon by thermal decomposition of methane." Chemical Engineering Science **59**: 5771-5778.

[Holmen, 1976] A. Holmen, O. A. Rokstad, et al. (1976). "High-Temperature Pyrolysis of Hydrocarbons. 1. Methane to Acetylene." Industrial & Engineering

Chemistry Process Design and Development **15**(3): 439-444.

[Holmen, 1995] A. Holmen, O. Olsvik, et al. (1995). "Pyrolysis of natural gas: chemistry and process concepts." Fuel Processing Technology **42**: 249-267.

[Hu, 2003] Z. J. Hu and K. J. Hüttinger (2003). "Influence of the surface area/volume ratio on the chemistry of carbon deposition from methane." Carbon **41**(8): 1501-1508.

[Incropera, 1996] F. P. Incropera and D. P. DeWitt (1996). Introduction To Heat Transfer. 3. ed. New York, John Wiley & Sons.

[Incropera, 2002] F. P. Incropera and D. P. DeWitt (2002). Fundamentals of Heat and Mass Transfer. 5. ed. New York, John Wiley & Sons.

[IPCC, 2007] IPCC (2007). Climate Change 2007: Mitigation. Contribution of Working Group III to the Fourth Assessment Report of the Intergovernmental Panel on Climate Change. B. Metz, O. R. Davidson, P. R. Bosch, R. Dave, and L. A. Meyer. Cambridge and New York, Cambridge University Press.

[ISO, 2008] ISO (2008). ISO/IEC Guide 98-3:2008(E). Uncertainty of measurement – Part 3: Guide to the expression of uncertainty in measurement (GUM:1995). Geneva, International Organization for Standardization.

[Jung, 2007] J. Jung, W. Nam, et al. (2007). "Hydrogen production by catalytic decomposition of methane over carbon catalysts in a fluidized bed." Korean Journal of Chemical Engineering **24**(4): 674-678.

[Kassel, 1932] L. S. Kassel (1932). "The thermal decomposition of methane." Journal of the American Chemical Society **54**: 3949-3962.

[Kevorkian, 1960] V. Kevorkian, C. E. Heath, et al. (1960). "The decompostion of methane in shock waves." The Journal of Physical Chemistry **64**(8): 964-968.

[Khan, 1970] M. S. Khan and B. L. Crynes (1970). "Survey of Recent Methane Pyrolysis Literature." Industrial and Engineering Chemistry **62**(10): 54-59.

[Kiefer, 1993] J. H. Kiefer and S. S. Kumaran (1993). "Rate of CH_4 Dissociation over 2800-4300 K: The Low-Pressure-Limit Rate Constant." The Journal of Physical Chemistry **97**(2): 414-420.

[Kim, 2004] M. H. Kim, E. K. Lee, et al. (2004). "Hydrogen production by catalytic decomposition of methane over activated carbons: kinetic study." International Journal of Hydrogen Energy **29**: 187-193.

[Kodama, 2003] T. Kodama (2003). "High-temperature solar chemistry for converting solar heat to chemical fuels." Progress in Energy and Combustion Science **29**(6): 567-597.

[Kogan, 2003] M. Kogan and A. Kogan (2003). "Production of hydrogen and carbon by solar thermal methane splitting. I. The unseeded reactor." International Journal of Hydrogen Energy **28**(11): 1187-1198.

[Kogan, 2004] A. Kogan, M. Kogan, et al. (2004). "Production of hydrogen and carbon by solar thermal methane splitting. II. Room temperature simulation tests of seeded solar reactor." International Journal of Hydrogen Energy **29**: 1227-1236.

[Kogan, 2005] A. Kogan, M. Kogan, et al. (2005). "Production of hydrogen and carbon by solar thermal methane splitting. III. Fluidization, entrainment and seeding powder particles into a volumetric solar receiver." International Journal of Hydrogen Energy **30**: 35-43.

[Kogan, 2007] A. Kogan, M. Israeli, et al. (2007). "Production of hydrogen and carbon by solar thermal methane splitting. IV. Preliminary simulation of a confined tornado flow configuration by computational fluid dynamics." International Journal of Hydrogen Energy **32**(18): 4800-4810.

[Koike, 2000] T. Koike, M. Kudo, et al. (2000). "Rate Constants of CH_4 + M=CH_3 + H + M and CH_3OH + M=CH_3 + OH + M over 1400-2500 K." International Journal of Chemical Kinetics **32**(1): 1-6.

[Kozlov, 1962] G. I. Kozlov and V. G. Knorre (1962). "Single-pulse Shock Tube Studies on the Kinetics of the Thermal Decomposition of Methane." Combust. Flame **6**: 253-263.

[Kreysa, 2008] G. Kreysa (2008). "Methan - Chance für eine klimaverträgliche Energieversorgung." Chemie Ingenieur Technik **80**(7): 901-908.

[Kreysa, 2009] G. Kreysa (2009). "Climate Protection by an Alternative Use of Methane–The Carbon Moratorium." ChemSusChem **2**(1): 49-55.

[Lee, 2004 a] K. K. Lee, G. Y. Han, et al. (2004). "Thermocatalytic hydrogen production from the methane in a fluidized bed with activated carbon catalyst." Catalysis Today **93-95**: 81-86.

[Lee, 2004 b] K. L. Lee, S. Y. Lee, et al. (2004). "Catalytic decomposition of methane over carbon blacks for CO_2-free hydrogen production." Carbon **42**: 2641-2648.

[Lee, 2008] S. Y. Lee, B. H. Ryu, et al. (2008). "Catalytic characteristics of specialty carbon blacks in decomposition of methane for hydrogen production." Carbon **46**(14): 1978-1986.

[Lucas, 1990] P. Lucas and A. Marchand (1990). "Pyrolytic carbon deposition from methane: An analytical approach to the chemical process." Carbon **28**(1): 207-219.

[Lucas, 2008] K. Lucas (2008). Thermodynamik. Die Grundgesetze der Energie- und Stoffumwandlungen. 7. ed. Berlin, Springer.

[Maag, 2009] G. Maag, G. Zanganeh, et al. (2009). "Solar thermal cracking of methane in a particle-flow reactor for the co-production of hydrogen and carbon." International Journal of Hydrogen Energy **34**(18): 7676-7685.

[Maibauer, 2010] T. Maibauer (2010). Vorbereitung, Durchführung und Auswertung von reaktionskinetischen Experimenten im Umfeld der solarthermischen Spaltung von Methan zur Wasserstofferzeugung. Aachen, RWTH Aachen. (Student research project at the DLR, Institute of Technical Thermodynamics, Solar Research, Köln)

[Marbán, 2007] G. Marbán and T. Valdés-Solís (2007). "Towards the hydrogen economy?" International Journal of Hydrogen Energy **32**(12): 1625-1637.

[Martin, 1990] H. Martin (1990). Vorlesung Wärmeübertragung II. Karlsruhe, Universität Karlsruhe (TU).

[Matheu, 2003] D. M. Matheu, A. M. Dean, et al. (2003). "Mechanism Generation with Integrated Pressure Dependence: A New Model for Methane Pyrolysis." The Journal of Physical Chemistry A **107**(41): 8552-8565.

[Missen, 1999] R. W. Missen, C. A. Mims, et al. (1999). Introduction to chemical reaction engineering and kinetics. New York, John Wiley & Sons.

[Mortimer, 1996] C. E. Mortimer (1996). Chemie. Das Basiswissen der Chemie. 6. ed. Stuttgart, Georg Thieme.

[Munson, 2002] B. R. Munson, D. F. Young, et al. (2002). Fundamentals of Fluid Mechanics. 4. ed. New York, John Wiley & Sons.

[Muradov, 2001 a] N. Z. Muradov (2001). "Catalysis of methane decomposition over elemental carbon." Catalysis Communications **2**: 89-94.

[Muradov, 2001 b] N. Z. Muradov (2001). "Hydrogen via methane decomposition: an application for decarbonization of fossil fuel." International Journal of Hydrogen Energy **26**: 1165-1175.

[Muradov, 2005 a] N. Z. Muradov and T. N. Veziroglu (2005). "From hydrocarbon to hydrogen-carbon to hydrogen economy." International Journal of Hydrogen Energy **30**: 225-237.

[Muradov, 2005 b] N. Z. Muradov, F. Smith, et al. (2005). "Catalytic activity of carbons for methane decomposition reaction." Catalysis Today **102-103**: 225-233.

[Muradov, 2008] N. Z. Muradov and T. N. Veziroglu (2008). ""Green" path from fossil-based to hydrogen economy: An overview of carbon-neutral technologies." International Journal of Hydrogen Energy **33**(23): 6804-6839.

[Muradov, 2010] N. Z. Muradov (19 May 2010). Comment at 18th World Hydrogen Energy Conference 2010 (WHEC 2010), Essen.

[Napier, 1972] D. H. Napier and N. Subrahmanyam (1972). "Pyrolysis of Methane in a Single Pulse Shock Tube." Journal of Applied Chemistry & Biotechnology **22**: 303-317.

[Olsvik, 1994] O. Olsvik and F. Billaud (1994). "Thermal coupling of methane. A comparison between kinetic model data and experimental data." Thermochimica Acta **232**: 155-169.

[Olsvik, 1995] O. Olsvik, O. A. Rokstad, et al. (1995). "Pyrolysis of Methane in the Presence of Hydrogen." Chemical Engineering & Technology **18**: 349-358.

[Ozalp, 2009] N. Ozalp, A. Kogan, et al. (2009). "Solar decomposition of fossil fuels as an option for sustainability." International Journal of Hydrogen Energy **34**: 710-720.

[Palmer, 1963] H. B. Palmer and T. J. Hirt (1963). "The activation energy for the pyrolysis of methane." Journal of Physical Chemistry **67**: 709-711.

[Palmer, 1968] H. B. Palmer, J. Lahaye, et al. (1968). "On the Kinetics and Mechanism of the Thermal Decomposition of Methane in a Flow System." The Journal of Physical Chemistry **72**: 348-353.

[Patankar, 1980] S. V. Patankar (1980). Numerical Heat Transfer and Fluid Flow. Washington, Hemisphere.

[Pilla, 2010] G. L. Pilla, D. F. Davidson, et al. "Shock tube/laser absorption measurements of ethylene time-histories during ethylene and n-heptane pyrolysis." Proceedings of the Combustion Institute *In Press, Corrected Proof*.

[Pinilla, 2008] J. L. Pinilla, I. Suelves, et al. (2008). "Kinetic study of the thermal decomposition of methane using carbonaceous catalysts." Chemical Engineering Journal **138**(1-3): 301-306.

[Pregger, 2009] T. Pregger, D. Graf, et al. (2009). "Prospects of solar thermal hydrogen production processes." International Journal of Hydrogen Energy **34**(10): 4256-4267.

[Press, 2007] W. H. Press, S. A. Teukolsky, et al. (2007). Numerical Recipes. The Art of Scientific Computing. 3. ed. Cambridge, Cambridge University Press.

[Rempel, 2009] H. Rempel, S. Schmidt, et al. (2009). Reserven, Ressourcen und Verfügbarkeit von Energierohstoffen - Kurzstudie 2009 -. Hannover, Bundesanstalt für Geowissenschaften und Rohstoffe.

[Richter, 2000] H. Richter and J. B. Howard (2000). "Formation of polycyclic aromatic hydrocarbons and their growth to soot–a review of chemical reaction pathways." Progress in Energy and Combustion Science **26**(4-6): 565-608.

[Rodat, 2009] S. Rodat, S. Abanades, et al. (2009). "Hydrogen production from solar thermal dissociation of natural gas: development of a 10 kW solar chemical reactor prototype." Solar Energy **83**(9): 1599-1610.

[Rodat, 2010 a] S. Rodat, S. Abanades, et al. (2010). "A pilot-scale solar reactor for the production of hydrogen and carbon black from methane splitting." International Journal of Hydrogen Energy **35**(15): 7748-7758.

[Rodat, 2010 b] S. Rodat, S. Abanades, et al. "Co-production of hydrogen and carbon black from solar thermal methane splitting in a tubular reactor prototype." Solar Energy *In Press, Corrected Proof*.

[Roscoe, 1985] J. M. Roscoe and M. J. Thompson (1985). "Thermal decomposition of methane: Autocatalysis." International Journal of Chemical Kinetics **17**(9): 967-990.

[Schröder, 2000] W. Schröder (2000). Fluidmechanik. 2. ed. Mainz, Wissenschaftsverlag.

[Schulz, 1985] G. Schulz, H.-D. Klotz, et al. (1985). "Reaktionsmodell zur Bruttokinetik der Pyrolyse von Methan im Stoßwellenrohr bei Temperaturen von 1800 K bis 2500 K." Zeitschrift für Chemie **25**(3): 88-92.

[Serban, 2003] M. Serban, M. A. Lewis, et al. (2003). "Hydrogen Production by Direct Contact Pyrolysis of Natural Gas." Energy & Fuels **17**(3): 705-713.

[Shantarovich, 1962] P. S. Shantarovich and B. V. Pavlov (1962). "Thermal cracking of methane." International Chemical Engineering **2**(3): 415-418.

[Sherwood, 1975] T. K. Sherwood, R. L. Pigford, et al. (1975). Mass Transfer. New York, McGraw-Hill.

[Skinner, 1959] G. B. Skinner and R. A. Ruehrwein (1959). "Shock tube studies on the pyrolysis and oxidation of methane." The Journal of Physical Chemistry **63**: 1736-1742.

[Spath, 2003] P. L. Spath and W. A. Amos (2003). "Using a Concentrating Solar Reactor to Produce Hydrogen and Carbon Black via Thermal Decomposition of Natural Gas: Feasibility and Ecomomics." Journal of Solar Energy Engineering **125**: 159-164.

[Steinberg, 1989] M. Steinberg and H. S. Cheng (1989). "Modern and prospective technologies for hydrogen production from fossil fuels." International Journal of Hydrogen Energy **14**(11): 797-820.

[Steinberg, 1998] M. Steinberg (1998). "Production of hydrogen and methanol from natural gas with reduced CO_2 emission." International Journal of Hydrogen Energy **26**(6): 419-425.

[Steinfeld, 1997] A. Steinfeld, V. Kirillov, et al. (1997). "Production of filamentous carbon and hydrogen by solarthermal catalytic cracking of methane." Chemical Engineeing Science **52**(20): 3599-3603.

[Steinfeld, 2001] A. Steinfeld and R. Palumbo (2001). Solar Thermochemical Process Technology. Encyclopedia of Physical Science and Technology. R. A. Meyers. New York, Academic Press. **15:** 237-256.

[Steinfeld, 2004] A. Steinfeld and A. Meier (2004). Solar Fuels and Materials. Encyclopedia of Energy. C. J. Cleveland. New York, Elsevier. **5:** 623-637.

[Steinfeld, 2005] A. Steinfeld (2005). "Solar thermochemical production of hydrogen–a review." Solar Energy **78**(5): 603-615.

[Stephan, 1962] K. Stephan (1962). "Wärmeübergang bei turbulenter und laminarer Strömung in Ringspalten." Chemie Ingenieur Technik **34**: 207-212.

[Stewart, 1989] P. H. Stewart, G. P. Smith, et al. (1989). "The pressure and temperature dependence of methane decomposition." International Journal of Chemical Kinetics **21**(10): 923-945.

[Stolten, 2010] D. Stolten, Ed. (2010). Hydrogen and Fuel Cells: Fundamentals, Technologies and Applications. Weinheim, WILEY-VCH.

[Stroppe, 2008] H. Stroppe (2008). Physik für Studierende der Natur- und Ingenieurwissenschaften. 14. ed. München, Hanser.

[Sundaram, 1977 a] K. M. Sundaram and G. F. Froment (1977). "Modeling of thermal cracking kinetics–I : Thermal cracking of ethane, propane and their mixtures." Chemical Engineering Science **32**(6): 601-608.

[Sundaram, 1977 b] K. M. Sundaram and G. F. Froment (1977). "Modeling of thermal cracking kinetics–II : Cracking of iso-butane, of n-butane and of mixtures ethane–propane–n-butane." Chemical Engineering Science **32**(6): 609-617.

[Sundaram, 1978] K. M. Sundaram and G. F. Froment (1978). "Modeling of Thermal Cracking Kinetics. 3. Radical Mechanisms for the Pyrolysis of Simple Paraffins, Olefins, and Their Mixtures." Industrial & Engineering Chemistry Fundamentals **17**(3): 174-182.

[Sutherland, 2001] J. W. Sutherland, M.-C. Su, et al. (2001). "Rate Constants for H + CH_4, CH_3 + H_2, and CH_4 Dissociation at High Temperature." International Journal of Chemical Kinetics **33**(11): 669-684.

[Tabayashi, 1979] K. Tabayashi and S. H. Bauer (1979). "The Early Stages of Pyrolysis and Oxidation of Methane." Combustion and Flame **34**: 63-83.

[Tanashev, 1998] Y. Y. Tanashev, V. I. Fedoseev, et al. (1998). "Methane processing under microwave radiation: Recent findings and problems." Catalysis Today **42**(3): 333-336.

[TC, 2006] TC Meß- und Regeltechnik GmbH (2006). Handbuch zur Temperaturmessung mit Thermoelementen und Widerstandsthermometern. Mönchengladbach, TC Meß- und Regeltechnik GmbH.

[TIMCAL, 2007] TIMCAL Ltd. (2007).Technical Data Sheet. Super P. Conductive Carbon Black. Version 03/07. Bodio, TIMCAL Ltd.

[Touloukian, 1972] Y. S. Touloukian and C. Y. Ho, Eds. (1972). Thermophysical Properties of Matter. Vol. 1-13. New York, Plenum Press.

[Trommer, 2004] D. Trommer, D. Hirsch, et al. (2004). "Kinetic investigation of the thermal decomposition of CH_4 by direct irradiation of a vortex-flow laden with carbon particles." International Journal of Hydrogen Energy **29**: 627-633.

[Tynnukov, 2002] Y. G. Tynnukov, M. V. Genkin, et al. (2002). "Modeling of Methane Pyrolysis Reactors." Petroleum Chemistry **42**(2): 85-92.

[VDI, 2006] VDI-Gesellschaft Verfahrenstechnik und Chemieingenieurwesen, Ed. (2006). VDI-Wärmeatlas. 10. ed. Berlin, Springer.

[Weimer, 2001] A. W. Weimer, J. K. Dahl, et al. (2001). Thermal dissociation of methane using a solar coupled aerosol flow reactor. 2001 U.S. DOE Hydrogen Program Review, Baltimore.

[Weingärtner, 2003] H. Weingärtner (2003). Chemische Thermodynamik. Einführung für Chemiker und Chemieingenieure. Stuttgart, Teubner.

[WIKA, 2005] WIKA Alexander Wiegand GmbH & Co. KG (2005). Universal-Drucktransmitter. UniTrans. Betriebsanleitung. Klingenberg, WIKA Alexander Wiegand GmbH & Co. KG.

[WIKA, 2006] WIKA Alexander Wiegand GmbH & Co. KG (2006). Elektronische Druckmesstechnik. Druckmessumformer für allgemeine Anwendungen. Typ S-10, Standardausführung. Typ S-11, frontbündige Membrane. Datenblatt PE 81.01. Klingenberg, WIKA Alexander Wiegand GmbH & Co. KG.

[Wu, 1987] C. H. Wu, H. J. Singh, et al. (1987). "Pyrolysis of acetylene behind reflected shock waves." International Journal of Chemical Kinetics **19**(11): 975-996.

[Wullenkord, 2008] M. Wullenkord, K.-H. Funken, et al. (2008). Wasserstofferzeugung durch die solarthermische Spaltung von Methan - Untersuchungen zur Reaktionskinetik. 11. Kölner Sonnenkolloquium. Solare Turmkraftwerke. Potential und Technologie, Köln, DLR.

[Wullenkord, 2009 a] M. Wullenkord, K.-H. Funken, et al. (2009). Reaktionskinetische Untersuchungen zur thermischen Spaltung von Methan. 12. Kölner

Sonnenkolloquium. Qualifizierung von Komponenten solarthermischer Kraftwerke, Köln, DLR.

[Wullenkord, 2009 b] M. Wullenkord, K.-H. Funken, et al. (2009). "Kinetische Untersuchungen zur thermischen Spaltung von Methan." Chemie Ingenieur Technik **81**(8): 1036.

[Wullenkord, 2010 a] M. Wullenkord, T. Maibauer, et al. (2010). Neue Untersuchungen zur thermischen Spaltung von Methan. 13. Kölner Sonnenkolloquium. Strom aus der Wüste, Köln, DLR.

[Wullenkord, 2010 b] M. Wullenkord, K.-H. Funken, et al. (2010). Hydrogen Production by Thermal Cracking of Methane – Investigation of Reaction Conditions. 18th World Hydrogen Energy Conference 2010 – WHEC 2010, Essen. [Schriften des Forschungszentrums Jülich, Energy & Environment **78**(3)]

[Younessi-Sinaki, 2009] M. Younessi-Sinaki, E. A. Matida, et al. (2009). "Kinetic model of homogeneous thermal decomposition of methane and ethane." International Journal of Hydrogen Energy **34**(9): 3710-3716.

[Zedtwitz, 2006] P. v. Zedtwitz, J. Petrasch, et al. (2006). "Hydrogen production via the solar thermal decarbonization of fossil fuels." Solar Energy **80**: 1333-1337.

8 Nomenclature

Formula symbols

$\boldsymbol{A}$	matrix consisting of partial derivatives	various
A	cross sectional area, face	m^2
A_{peak}	peak area of GC measurement	mV s
a	activity	-
a	half width of an interval	various
a^+	upper limit for a measured value	various
a^-	lower limit for a measured value	various
b	uncertainty factor	%
b_{lam}	factor for a laminar flow	-
$C_{TC,R}$	factor comprising emissivity and geometry of thermocouple and reactor	$W / (m^2 K^4)$
c	concentration	mol / m^3
c_p	specific heat capacity at constant pressure	J / (kg K)
c_v	specific heat capacity at constant volume	J / (kg K)
D	diffusion coefficient in a binary gas mixture	m^2 / s
$\hat{D}$	diffusion coefficient in a gas mixture with more than two species	m^2 / s
d	diameter	m
d_h	hydraulic diameter	m
E	error	-
E_a	activation energy	kJ / mol
F	factor, ratio of stoichiometric coefficients	-
f	factor regarding number of certain atoms in a molecule	-

G	Gibbs energy (free enthalpy)	J
I	electric current	A
$\boldsymbol{j}$	diffusive molar flux related to the average molar velocity	mol / (s m^2)
$\boldsymbol{j}^*$	diffusive mass flux related to the average mass velocity	kg / (s m^2)
k	coefficient of a polynomial fit function	various
k	rate constant	(mol / m^3)$^{(1-\Sigma m_i)}$ / s and others
k_p	coverage factor	-
k_0	pre-exponential factor	(mol / m^3)$^{(1-\Sigma m_i)}$ / s and others
l	length	m
l_e	entry length	m
M	molecular weight	g / mol
Ma	Mach number	-
m	mass	kg
m	reaction order	-
m_i	reaction order regarding component i	-
$\dot{m}$	mass flow	kg / s or g / h
N	total number (e. g. of runs, of species in a gas mixture)	-
Nu	Nusselt number	-
n	amount of substance	mol
$\dot{n}$	molar flow	mol / s
$\overline{\dot{n}}$	average molar flow	mol / s
Pe	Péclet number	-
Pr	Prandtl number	-
P_w	wetted perimeter	m
p	pressure	bar
$\overline{p}$	average pressure	bar

p_N	standard pressure (1.01325)	bar
Q_D	diffusive quotient	-
$\dot{q}$	heat flux density	W / m^2
$\Re$	universal gas constant (8.314472, see [Stroppe, 2008])	J / (mol K)
R	specific gas constant	J / (kg K)
R	radius	m
Re	Reynolds number	-
r	reaction rate (equivalent ~)	mol / (s m^3) or mol / (s m^2) or mol / (s kg)
r	radial position, radius	m or mm
$\hat{r}$	radial position, radius	m or mm
$\bar{r}$	mean radius	m or mm
S	surface	m^2
s	specific surface	m^2 / g
s_{rel}	relative standard deviation	%
$s_{rel,max}$	maximum relative deviation	%
T	temperature	K or °C
T_N	standard temperature (273.15)	K
t	time	min or s
U	voltage	V
$\hat{U}$	voltage	V
u	velocity component in X-direction (ANSYS)	m / s
u	standard uncertainty	various
u_{max}	maximum uncertainty	various
$\bar{u}_{max}$	average maximum uncertainty	various
V	volume	m^3
V_d	diffusion volume	-

$\dot{V}$	volume flow	m^3 / s
$\dot{V}_N$	standard volume flow (referring to T_N and p_N)	sccm
v	velocity / velocity component in Y-direction (ANSYS)	m / s
$\bar{v}$	average velocity	m / s
w	velocity component in Z-direction (ANSYS)	m / s
X	conversion	% or -
$\overline{X}$	average conversion	% or -
$\boldsymbol{x}_i$	vector of variables defining a condition i	various
x	molar fraction	% or -
x	measured value	various
$\hat{x}$	molar fraction	% or -
$\bar{x}$	average molar fraction	% or -
Y	yield	% or -
y	quantity, which is a function of other quantities	various
y_i	part of data point, observation related to condition i	various
$\tilde{y}_i$	discrepancy between observation and model related to condition i relative to the standard deviation of the observation	-
z	axial position	m or mm
$\boldsymbol{\alpha}$	matrix used to determine a covariance matrix	various
α	heat transfer coefficient	W / (m^2 K)
α_{kl}	component of matrix $\boldsymbol{\alpha}$ in row k and column l	various
χ^2	merit function to be minimized (Chi-Square fitting)	-
ΔG_R	free enthalpy of reaction	J
ΔH_R^0	standard reaction enthalpy	J
ΔX_{Line}	position on Line X relative to the center position	m
$\Delta X_{CH_4,2-1,rel,\mu}$	difference of conversions of methane related to	-

	standard uncertainty respecting experimental campaign 1 and 2	
$\Delta Y_{C_2H_2,2-1,rel,u}$	difference of yields of ethyne related to standard uncertainty respecting experimental campaign 1 and 2	-
$\Delta Y_{C_2H_4,2-1,rel,u}$	difference of yields of ethene related to standard uncertainty respecting experimental campaign 1 and 2	-
$\Delta Y_{C_2H_6,2-1,rel,u}$	difference of yields of ethane related to standard uncertainty respecting experimental campaign 1 and 2	-
$\Delta Y_{H_2,2-1,rel,u}$	difference of yields of hydrogen related to standard uncertainty respecting experimental campaign 1 and 2	-
ΔZ_{Line}	position on Line Z relative to the center position	m
ε	emissivity	-
φ	view factor	-
η	dynamic viscosity	N s / m^2
κ	specific heat ratio	-
λ	thermal conductivity	W / (m K)
$\overline{\lambda}$	average thermal conductivity	W / (m K)
μ	chemical potential	J / mol
ν	kinematic viscosity	m^2 / s
ν	stoichiometric coefficient	-
ρ	density	kg / m^3
σ	Stefan-Boltzmann constant (5.67040 10^{-8}, see [Baehr, 2006])	W / (m^2 K^4)
σ	standard deviation	various
τ	residence time	s
$\overline{\tau}$	average residence time	s
$\boldsymbol{\psi}$	vector of model parameters	various
ψ	model parameter	various
$Corr(\,)$	matrix of correlation coefficients	
$Cov(\,)$	covariance matrix	

f	general function
∇	nabla operator, gradient

Indices and subscripts

AL23	alumina, material manufactured by FRIATEC
Ar	argon
ave	average
C	carbon
CH_4	methane
CP	center position
C_2H_2	ethyne
C_2H_4	ethene
C_2H_6	ethane
C_2-HC	C_2-hydrocarbons
c	combined
cat	catalyst
cond	conductive
conv	convective
D	diffusive
DG	dilution gas
eq	equivalent
g	gaseous
H	hydrogen
He	helium
HT	heat transfer

H_2	hydrogen
h	hydrodynamic
het	heterogeneous
hom	homogeneous
i	inner
i	component i of a gas mixture
i	condition i
ig	ideal gas
j	run j of a collectivity of experimental runs
j	interval j of a collectivity of intervals defined by molar fractions
j	species j
j	nested tube reactor j
k	component k of a gas mixture
k	experiment k
k	row of a matrix
k	model parameter k
LME	limit of marginal extend
l	column of a matrix
l	model parameter l
MFC	mass flow controller
max	maximum
min	minimum
mix	mixture
N	at standard conditions (T_N, p_N)
N	total number
o	outer
P	product
PT	protection tube

q	reaction q
R	reaction
R	reactor
R	resistor
rad	radiative
rel	relative, related
s	solid
T	transpose (of matrix)
TC	thermocouple
tot	total
WP	wall position
0	initial conditions
0	at standard / reference condition
-1	inverse (of matrix)
$+$	positive
$-$	negative

Abbreviations and chemical nomenclature

AB	acetylene black
AC	activated carbon
Al_2O_3	alumina
Ar	argon
ave	average
BET	Brunauer, Emmett and Teller (specific surface)

"C"	particulate carbon
CB	carbon black
CC	coal char
CCS	carbon capture and storage
CH_2	methylene radical
CH_3	methyl radical
CH_4	methane
CO	carbon monoxide
CO_2	carbon dioxide
CSP	concentrating solar power
C_mH_n	hydrocarbons (not further specified)
C_2H_2	ethyne
C_2H_4	ethene
C_2H_6	ethane
C_2-HC	C_2-hydrocarbons
C_3H_4	propyne or propadiene
C_3H_6	propene
C_3H_8	propane
C_4H_3	unsaturated hydrocarbon radical featuring 4 C-atoms and 3 H-atoms
$C_{10}H_8$	naphthalene
c	combined
cat	catalyst
D	diffusion
DG	dilution gas
DLR	Deutsches Zentrum für Luft- und Raumfahrt e.V. (German Aerospace Center)

DWV	Deutscher Wasserstoff- und Brennstoffzellen-Verband e.V. (German Hydrogen and Fuel Cell Association)
EUMENA	Europe, Middle East, North Africa
e. g.	for example
et seq.	et sequens
et seqq.	et sequentes
FS	full scale
GC	gas chromatograph
GCF	gas correction factor
GUM	Guide to the expression of uncertainty in measurement
H	hydrogen atom
He	helium
HID	helium ionization detector
H_2	hydrogen
H_2O	water
IPCC	Intergovernmental Panel on Climate Change
IPS	initial parameter set
$i\text{-}C_4H_{10}$	isobutane
Kr	krypton
LB	lower bounds
M	collision partner
MFC	mass flow controller
MFR	mixed flow reactor
$MoSi_2$	molybdenum disilicide
MS	molecular sieve
max	maximum
min	minimum
Ne	neon

NTR	nested tube reactor(s)
Ni	nickel
N_2	nitrogen
n. s.	not specified
$n\text{-}C_4H_{10}$	unbranched butane
OM	order of magnitude
O_2	oxygen
P	product species
PAH	polycyclic aromatic hydrocarbon
PFR	plug flow reactor
PTFE	polytetrafluoroethylene
Pt	platinum
Rh	rhodium
SLM	standard liter per minute (referring to T_N and p_N)
SOLHYCARB	Hydrogen from solar thermal energy: high temperature solar chemical reactor for co-production of hydrogen and carbon black from natural gas cracking (European project)
sccm	standard cubic centimeters per minute (referring to T_N and p_N)
TCD	thermal conductivity detector
UB	upper bounds
X	direction of a Cartesian coordinate system
Y	direction of a Cartesian coordinate system
Z	direction of a Cartesian coordinate system

Appendix

List of Figures of Appendix

List of Tables of Appendix

Appendix A: Thermodynamics

Table of Appendix 1: Species considered for calculations of equilibrium compositions. Species in gray form significant part of composition at equilibrium.

Gaseous species:											
CH4(g)	C5H8(CPEg)	C6H10(3Hg)	C7H14(C12DMCPg)	C7H12(14DMCPg)	C8H16(T3E2Hg)	C8H16(C1E3MCPg)	C8H16(1E2MCPg)	C8H10(OXYg)	C20H12(BjAAg)
C2H6(g)	C5H8(C13Pg)	C6H10(33DM1Bg)	C7H14(5M1Hg)	C7H12(13DMCPg)	C8H16(T35DM2Hg)	C8H16(C14Dg)	C8H16(1E1MCPg)	C8H10(MXYg)	C22H14(DahBAg)
C2H4(g)	C5H8(3M12Bg)	C6H10(2Hg)	C7H14(44DM2Pg)	C7H12(12DMCPg)	C8H16(T34D3Mg)	C8H16(C13Dg)	C8H16(11DMCHg)	C8H10(EE1357OTg)	C22H14(DBAacg)
C2H2(g)	C5H8(31MBYg)	C6H10(24THDg)	C7H14(41MEXg)	C7H10(2NOBg)	C8H16(T34DM2Hg)	C8H16(C12DMCHg)	C8H16(112TMCPg)	C8H10(EBZg)	C22H12(BghiFg)
H2(g)	C5H8(2PYg)	C6H10(24HXDg)	C7H14(3THPg)	C7H10(13CHg)	C8H16(T344TM2Pg)	C8H16(6M1Hg)	C8H14(EX2MBC221Hg)	C8H9(4MPMg)	C22H12(DBdefmnoCg)
C3H8(PPEg)	C5H8(2M13Bg)	C6H10(23DMBg)	C7H14(3RS4DM1Pg)	C7H8(TLUg)	C8H16(T2Og)	C8H16(5RSM1Hg)	C8H14(E2MBC221Hg)	C8H9(4EPg)	C22H12(I123cdFg)
C3H6(PPYg)	C5H8(23Pg)	C6H10(1MCPg)	C7H14(3E2Pg)	C7H8(BC221H25Dg)	C8H16(T2M3Hg)	C8H16(55DM1Hg)	C8H14(CYEg)	C8H9(3MPMg)	C24H12(Cg)
C3H6(CPAg)	C5H8(1PYg)	C6H10(1HEg)	C7H14(33DM1Pg)	C7H8(135Cg)	C8H16(T25DM3Hg)	C8H16(4RSM1Hg)	C8H14(6M3Hg)	C8H9(35DMPg)	C26H14(BaAg)
C3H4(PPYg)	C5H8(14Pg)	C6H10(15HEXg)	C7H14(31MEXg)	C7H7(PMg)	C8H16(T23DM3Hg)	C8H16(4RS5DM1Hg)	C8H14(6M2Hg)	C8H9(34DMPg)	C26H14(BbAg)
C3H4(ALEg)	C5H8(12Pg)	C6H10(14HEXg)	C7H14(31ETPg)	C8H18(OCTg)	C8H16(T22DM3Hg)	C8H16(4E1Hg)	C8H14(6M1Hg)	C8H9(2PEg)	C26H14(BeAg)
C3H4(CPg)	C5H6(213MBYg)	C6H8(Z135Hg)	C7H14(2THPg)	C8H18(4MHg)	C8H16(T1E3MCPg)	C8H16(44DM1Hg)	C8H14(5RSM3Hg)	C8H9(2MPMg)	C26H14(DBaghiPg)
C4H10(NBAg)	C5H6(13PNYg)	C6H8(MECYg)	C7H14(2M2Hg)	C8H18(3RS4RSDMHg)	C8H16(T14Dg)	C8H16(3RSM1Hg)	C8H14(5RSM2Hg)	C8H9(25DMPg)	C26H14(DBbghiPg)
C4H10(2MPg)	C5H6(13CPg)	C6H8(EQ135Hg)	C7H14(2E3M1Pg)	C8H18(3MHg)	C8H16(T13Dg)	C8H16(3RSE4M1Pg)	C8H14(5RSM1Hg)	C8H9(24DMPg)	C26H14(DBcd,lmPg)
C4H8(T2Bg)	C6H14(HXAg)	C6H8(E135Hg)	C7H14(24DM2Pg)	C8H18(3EHg)	C8H16(T12Dg)	C8H16(3RSE1Hg)	C8H14(55DM2Hg)	C8H9(23DMPg)	C26H14(DBeghiPg)
C4H8(MCPg)	C6H14(3MPg)	C6H8(14CHg)	C7H14(24DM1Pg)	C8H18(3E3Mg)	C8H16(PCPg)	C8H16(3RS5DM1Hg)	C8H14(55DM1Hg)	C8H9(1PEg)	C26H14(N1234ghiPg)
C4H8(CBAg)	C6H14(2MPg)	C6H8(13CHg)	C7H14(23RSDM1Pg)	C8H18(3E2Mg)	C8H16(IPCg)	C8H16(3RS4RSDM1Hg)	C8H14(4RSM2Hg)	C8H8(STYg)	C26H14(N8i12bcdPg)
C4H8(C2Bg)	C6H14(23DMBg)	C6H6(BZEg)	C7H14(23DM2Pg)	C8H18(34Dg)	C8H16(ECHg)	C8H16(3RS44TM1Pg)	C8H14(4RSM1Hg)	C8H8(COTg)	C26H14(Rg)
C4H8(2MPg)	C6H14(22DMBg)	C7H16(HTAg)	C7H14(233T1Bg)	C8H18(33Dg)	C8H16(CYAg)	C8H16(3M2IP4Bg)	C8H14(4RS5DM2Hg)	C8H6(EYBg)	C28H16(HZg)
C4H8(1BTg)	C6H12(T4M2Pg)	C7H16(3MHg)	C7H14(21ETPg)	C8H18(2MHg)	C8H16(CT124TMCPg)	C8H16(3E3M1Pg)	C8H14(4RS5DM1Hg)	C8H2(1357OTg)	C30H16(Tg)
C4H6(MCPg)	C6H12(T2Hg)	C7H16(3EPg)	C7H14(1HEg)	C8H18(25Dg)	C8H16(CC124TMCPg)	C8H16(3E3Hg)	C8H14(4Og)	C9H8(INDg)	C32H14(Og)
C4H6(CBg)	C6H12(MCPg)	C7H16(33DMPg)	C7H14(13TDCg)	C8H18(24Dg)	C8H16(CC123TMCPg)	C8H16(3E2M2Pg)	C8H14(4E2Hg)	C10H8(NPHg)	C34H16(DBcdpqBAg)
C4H6(2BYg)	C6H12(CHAg)	C7H16(2MHg)	C7H14(13DMCIg)	C8H18(23Dg)	C8H16(C6M3Hg)	C8H16(3E2M1Pg)	C8H14(4E1Hg)	C11H10(1MNg)	C36H16(BaOg)
C4H6(1MCPg)	C6H12(C4M2Pg)	C7H16(24DMPg)	C7H14(11DMCPg)	C8H18(234Tg)	C8H16(C6M2Hg)	C8H16(33DM1Hg)	C8H14(44DM2Hg)	C11H10(2MNg)	C38H16(DBbcefOg)
C4H6(1BYg)	C6H12(C3M2Pg)	C7H16(23DMPg)	C7H12(CYPg)	C8H18(233Tg)	C8H16(C5RSM3Hg)	C8H16(334TM1Pg)	C8H14(44DM1Hg)	C12H10(BPHg)	C40H16(BbcN2187stuvOg)
C4H6(13Bg)	C6H12(C3Hg)	C7H16(22DMPg)	C7H12(BC221Hg)	C8H18(22Dg)	C8H16(C5RSM2Hg)	C8H16(2P1Pg)	C8H14(3RSM1Hg)	C12H10(ANg)	C40H16(C26Ag)
C4H6(12Bg)	C6H12(C2Hg)	C7H16(223TMBg)	C7H12(5M2Hg)	C8H18(224Tg)	C8H16(C55DM2Hg)	C8H16(2M3MHg)	C8H14(3RSE4M1Pg)	C12H8(ANPHg)	C40H16(C26PAg)
C4H4(1B3Yg)	C6H12(4M1Pg)	C7H14(T4RSM2Hg)	C7H12(5M1Hg)	C8H18(223Tg)	C8H16(C4RSM2Hg)	C8H16(2M2Hg)	C8H14(3RSE1Hg)	C13H10(Fg)	C42H16(CPg)
C4H4(13CBg)	C6H12(3THXg)	C7H14(T44DM2Pg)	C7H12(4RSM2Hg)	C8H18(2233TMBg)	C8H16(C4RS5DM2Hg)	C8H16(2M1Hg)	C8H14(3RS5DM1Hg)	C14H10(Ag)	C54H18(CCg)
C4H2(BDYg)	C6H12(33D1Bg)	C7H14(T3M3Hg)	C7H12(4RSM1Hg)	C8H16(c14DCHg)	C8H16(C4Og)	C8H16(2E4M1Pg)	C8H14(3RS4RSDM1Hg)	C14H10(PAg)	C66H20(CVg)
C5H12(PENg)	C6H12(32MTPg)	C7H14(T3M2Hg)	C7H12(44DM2Pg)	C8H16(TT124TMCPg)	C8H16(C4E2Hg)	C8H16(2E3RSM1Pg)	C8H14(3RS44TM1Pg)	C15H10(45MPHEg)	C80H22(2CPg)
C5H12(2MBg)	C6H12(32MPCg)	C7H14(T34DM2Pg)	C7H12(44DM1Pg)	C8H16(TT123TMCPg)	C8H16(C44DM2Hg)	C8H16(2E33DM1Bg)	C8H14(3Og)	C16H10(Pg)	C96H24(2CCg)
C5H12(22Dg)	C6H12(31MEPg)	C7H14(T2M3Hg)	C7H12(3RSM1Hg)	C8H16(T6M3Hg)	C8H16(C3Og)	C8H16(2E1Hg)	C8H14(3E3M1Pg)	C16H10(FLUg)	C(g)
C5H10(T2Pg)	C6H12(2M2Pg)	C7H14(T12DMCPg)	C7H12(3RS4DM1Pg)	C8H16(T6M2Hg)	C8H16(C3M3Hg)	C8H16(25D2M2Hg)	C8H14(33DM1Hg)	C17H12(17HCPaPHEg)	C2(g)
C5H10(CPAg)	C6H12(2M1Pg)	C7H14(MCHg)	C7H12(3Hg)	C8H16(T5RSM3Hg)	C8H16(C3M2Hg)	C8H16(25D1Mg)	C8H14(334TM1Pg)	C17H12(1HCPbAg)	C3(g)
C5H10(C2Pg)	C6H12(2E1Bg)	C7H14(ECPg)	C7H12(3E1Pg)	C8H16(T5RSM2Hg)	C8H16(C3E4M2Pg)	C8H16(24RSDM2Hg)	C8H14(2Og)	C17H12(1HCPIPHEg)	C4(g)
C5H10(3M1Bg)	C6H12(23D2Bg)	C7H14(CHAg)	C7H12(35ttDMCPg)	C8H16(T55DM2Hg)	C8H16(C3E2Hg)	C8H16(24RSDM1Hg)	C8H14(2M3Hg)	C18H12(Cg)	C5(g)
C5H10(2M2Bg)	C6H12(23D1Bg)	C7H14(C4RSM2Hg)	C7H12(35ccDMCPg)	C8H16(T4RSM2Hg)	C8H16(C35DM2Hg)	C8H16(244TM2Pg)	C8H14(25DM3Hg)	C18H12(BAg)	C60(g)
C5H10(2M1Bg)	C6H12(1HEg)	C7H14(C44DM2Pg)	C7H12(34ttDMCPg)	C8H16(T4RS5DM2Hg)	C8H16(C34RSDM2Hg)	C8H16(244T1Pg)	C8H14(22DM3Hg)	C18H10(BghiFg)	
C5H10(1PEg)	C6H10(MCPg)	C7H14(C3M3Hg)	C7H12(34ccDMCPg)	C8H16(T4Og)	C8H16(C34DM3Hg)	C8H16(23RSDM1Hg)	C8H14(1OCg)	C18H10(CPcdPYRg)	
C5H10(12DMCPtg)	C6H10(CHEg)	C7H14(C3M2Hg)	C7H12(33DMCPg)	C8H16(T4E2Hg)	C8H16(C344TM2Pg)	C8H16(23RS4TM1Pg)	C8H12(CC15COg)	C20H14(Cg)	
C5H10(12DMCPcg)	C6H10(4MCPg)	C7H14(C3Hg)	C7H12(33DM1Pg)	C8H16(T44DM2Hg)	C8H16(C2Og)	C8H16(23DM2Hg)	C8H12(CC13COg)	C20H14(Tg)	**Solid species:**
C5H10(11DMCPg)	C6H10(4M2Pg)	C7H14(C34DM2Pg)	C7H12(2M3Hg)	C8H16(T3Og)	C8H16(C2M3Hg)	C8H16(23DM1Hg)	C8H12(15COg)	C20H12(BaPg)	
C5H8(t13PDEg)	C6H10(4M1Pg)	C7H14(C2M3Hg)	C7H12(2Hg)	C8H16(T3M3Hg)	C8H16(C25DM3Hg)	C8H16(234TM2Pg)	C8H12(13COg)	C20H12(BePg)	
C5H8(SPEg)	C6H10(3RSM1Pg)	C7H14(C2Hg)	C7H12(1Hg)	C8H16(T3M2Hg)	C8H16(C23DM3Hg)	C8H16(233TM1Pg)	C8H10(ZZ1357OTg)	C20H12(BkFg)	C
C5H8(MCBg)	C6H10(3MCPg)	C7H14(C13DMCPg)	C7H12(15DMCPg)	C8H16(T3E4M2Pg)	C8H16(C22DM3Hg)	C8H16(1OCg)	C8H10(PXYg)	C20H12(Pg)	

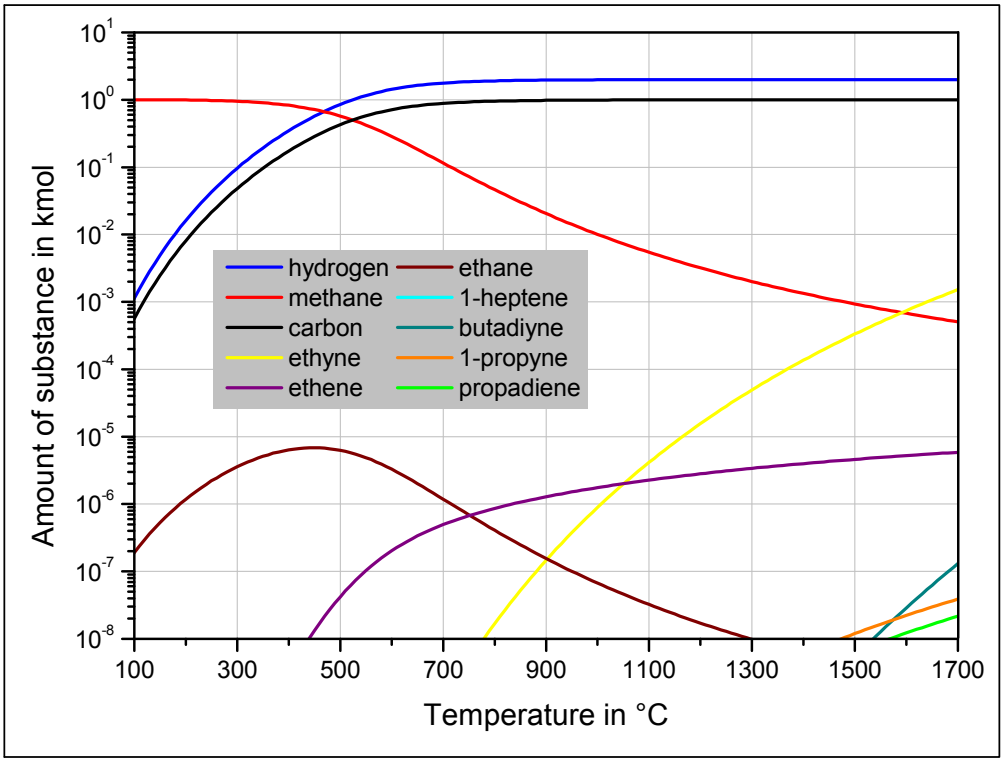

Figure of Appendix 1: Equilibrium compositions at 0.5 bar as a function of the temperature (based on an initial amount of 1 kmol methane)

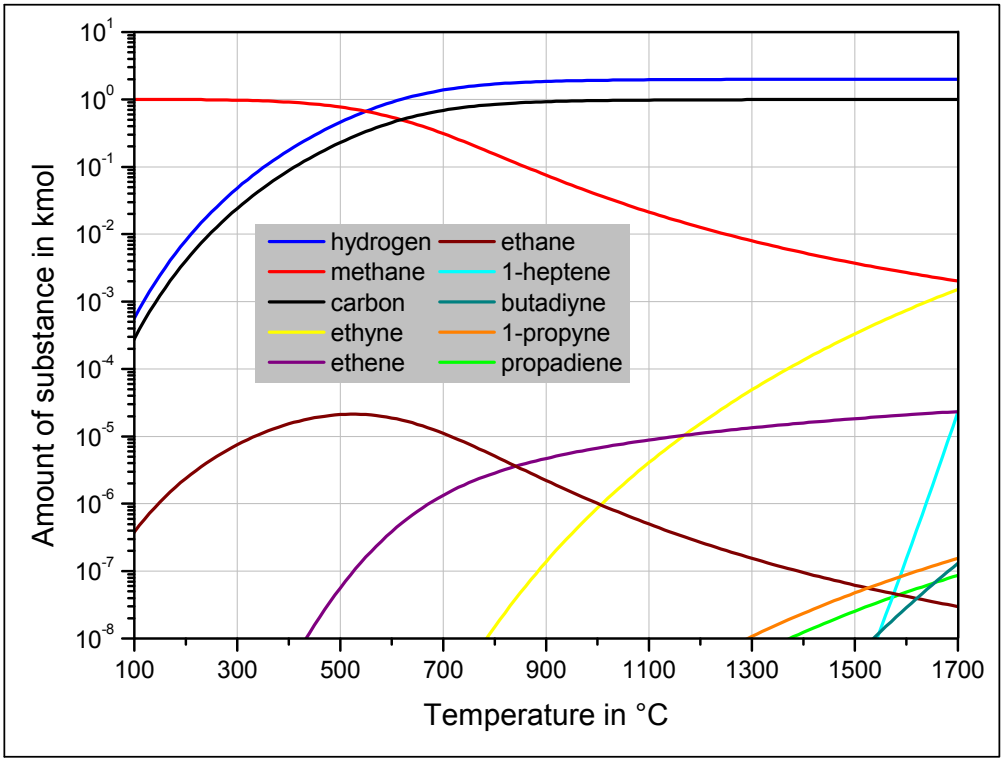

Figure of Appendix 2: Equilibrium compositions at 2 bar as a function of the temperature (based on an initial amount of 1 kmol methane)

Appendix B: Gas chromatograph

Table of Appendix 2: Parameters of gas chromatograph and their set points

Parameter	Set point	Actual
Pressure of Carrier #1	21 psi	21 psi
Pressure of Carrier #2	21 psi	21 psi
Pressure of HID make up gas	21 psi	20 psi
Ion Current of HID	120 mA	120 mA
Temperature of valve	60 °C	67 °C
Temperature of HID (labeled as Detector 1)	200 °C	205 °C
Temperature of TCD	251 °C	257 °C
Sensitivity of HID	medium gain	
Sensitivity of TCD	high gain	

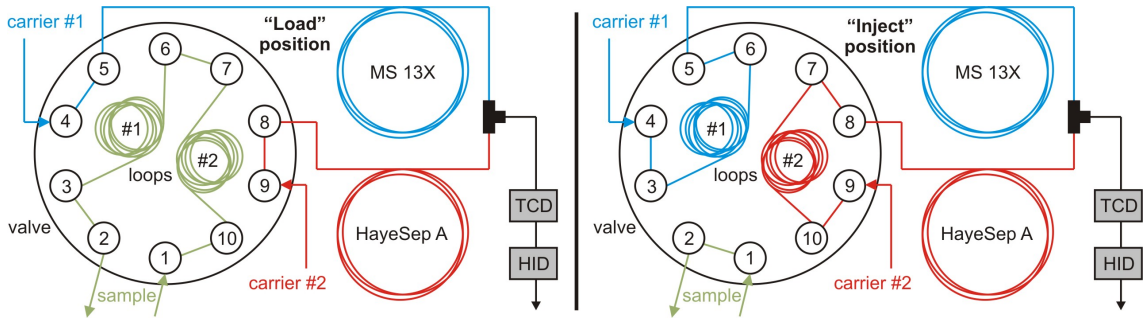

Figure of Appendix 3: Valve in "Load" position and "Inject" position

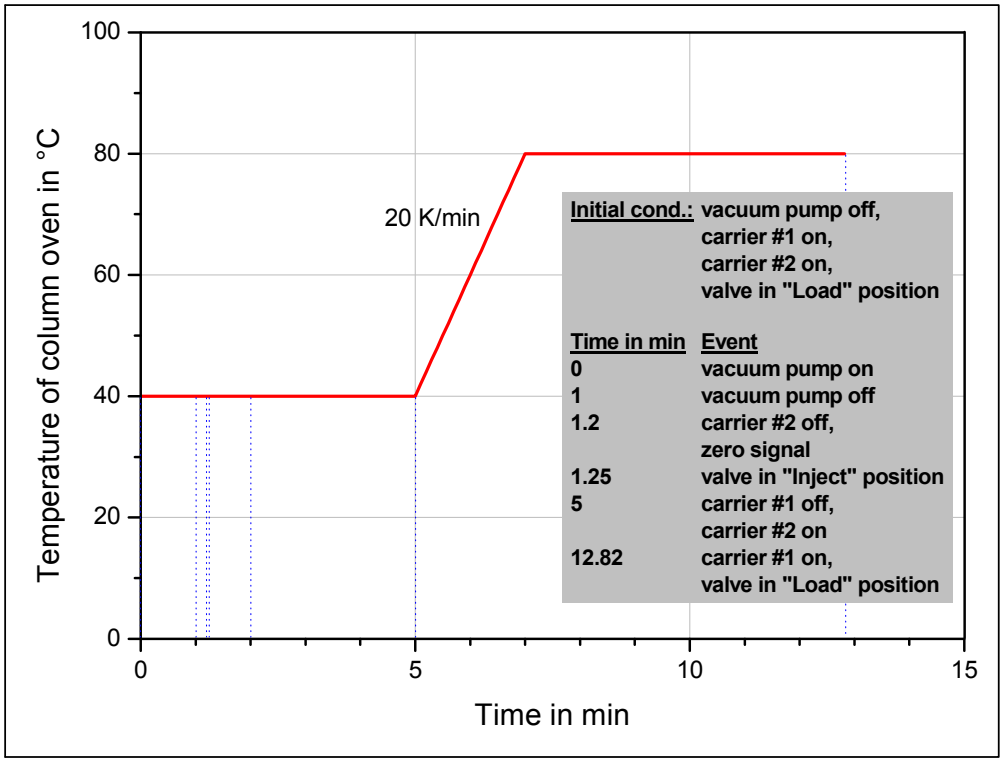

Figure of Appendix 4: Temperature program and event program for the measurement procedure

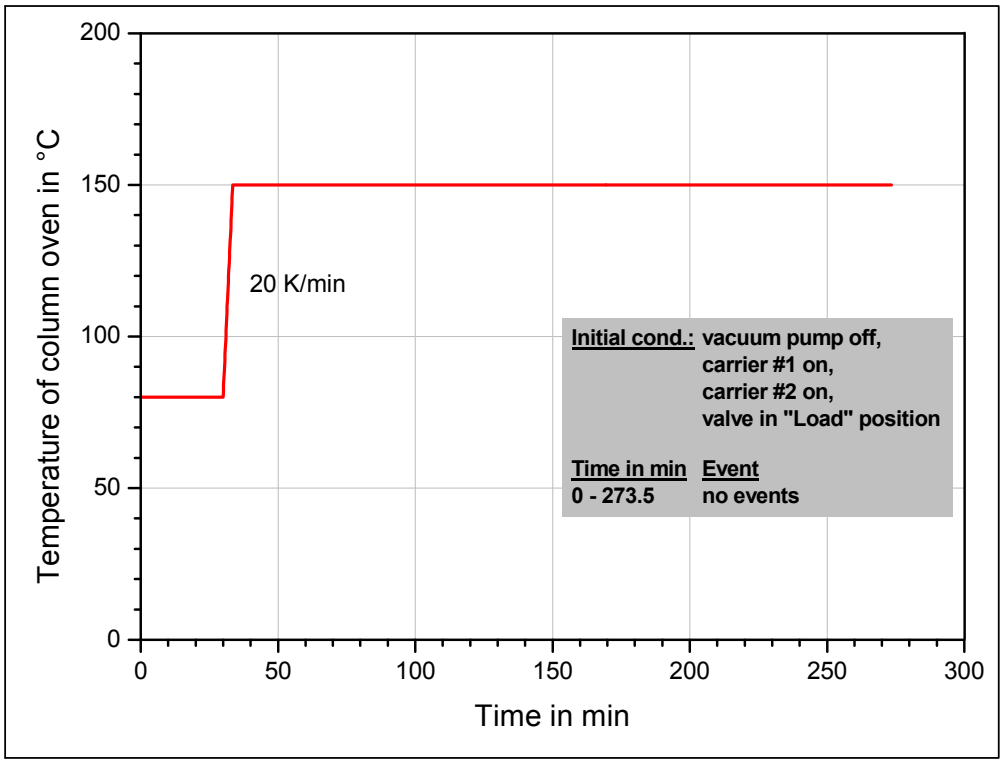

Figure of Appendix 5: Temperature program and event program for the column bake-out procedure

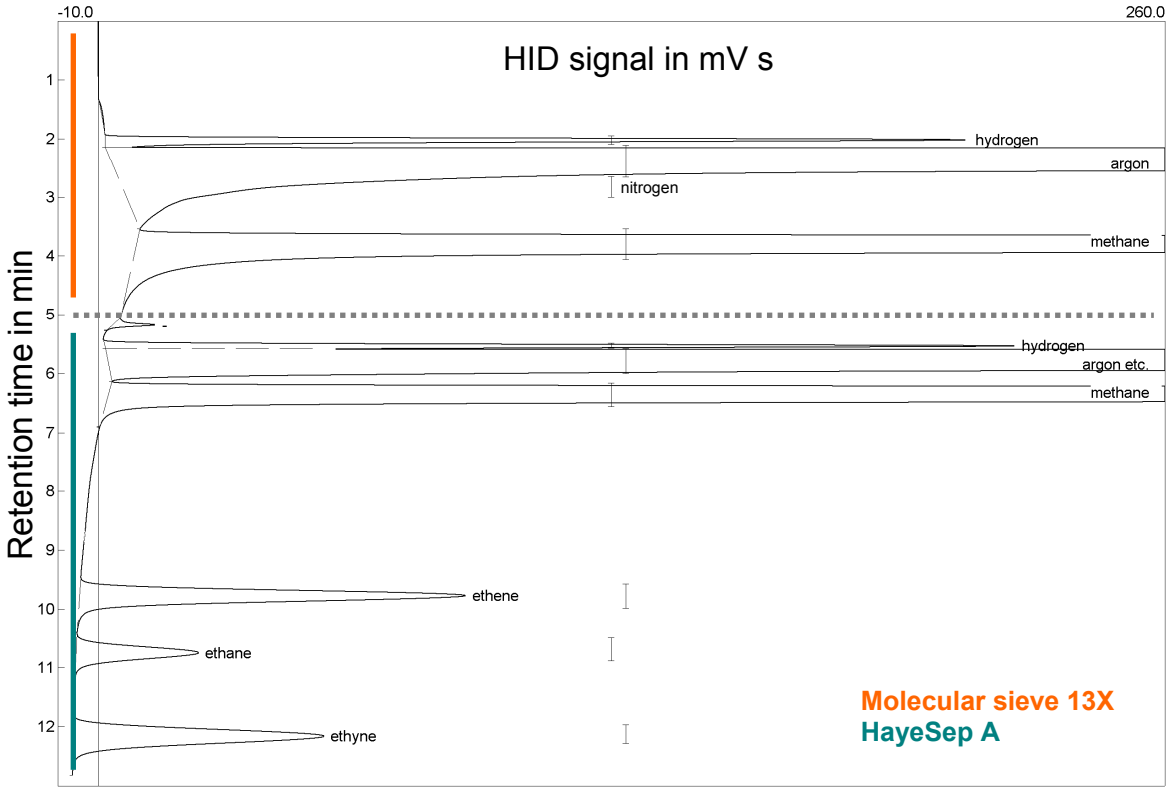

Figure of Appendix 6: Example for a chromatogram of the product gas respecting signals of the HID. Hydrocarbons with a molecular weight higher than the C_2-hydrocarbons were not considered.

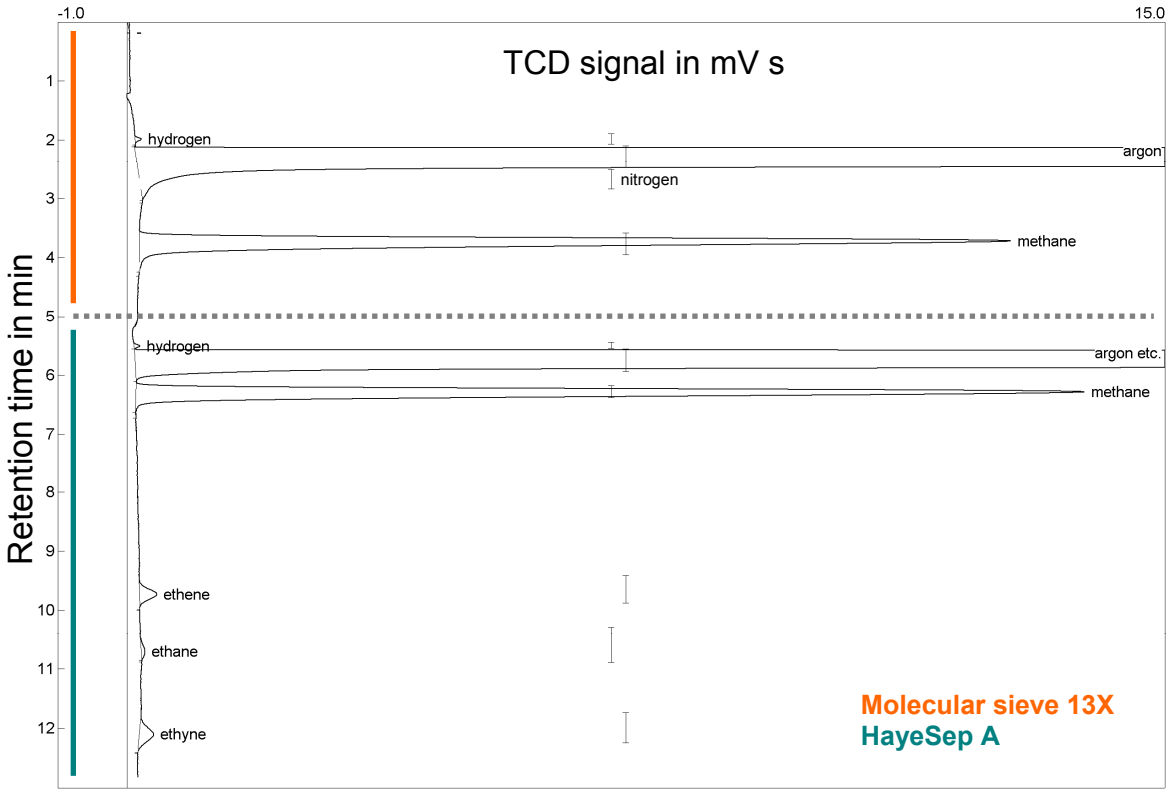

Figure of Appendix 7: Example for a chromatogram of the product gas respecting signals of the TCD. Hydrocarbons with a molecular weight higher than the C_2-hydrocarbons were not considered.

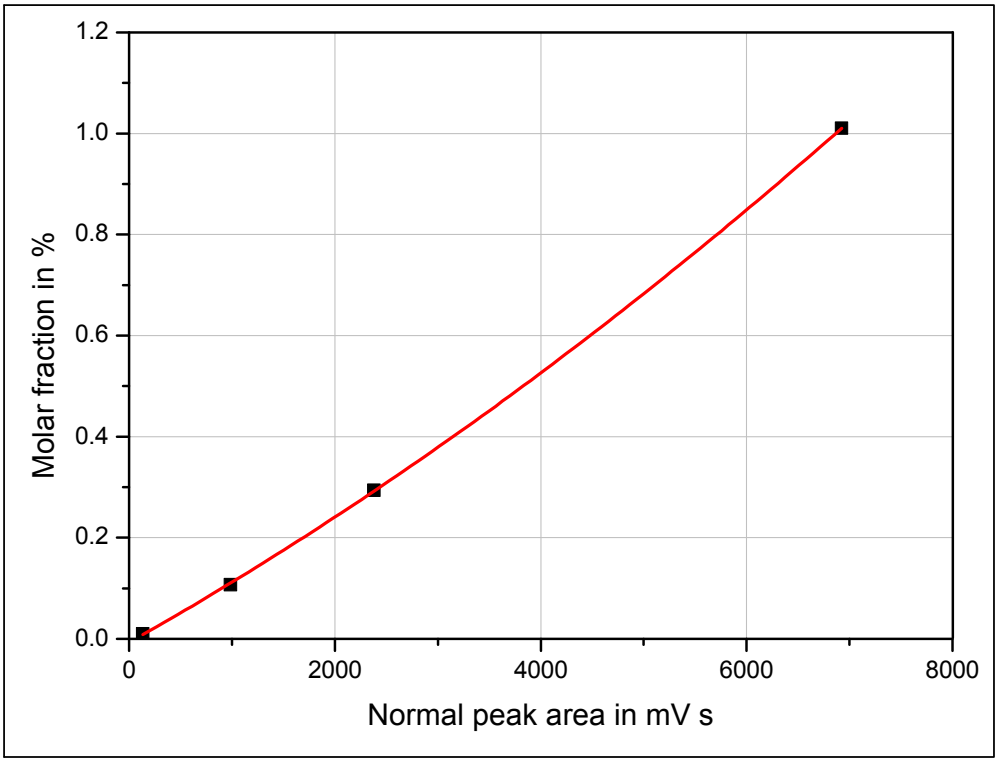

Figure of Appendix 8: Example for a GC calibration curve: methane detected by the HID (2nd order polynomial)

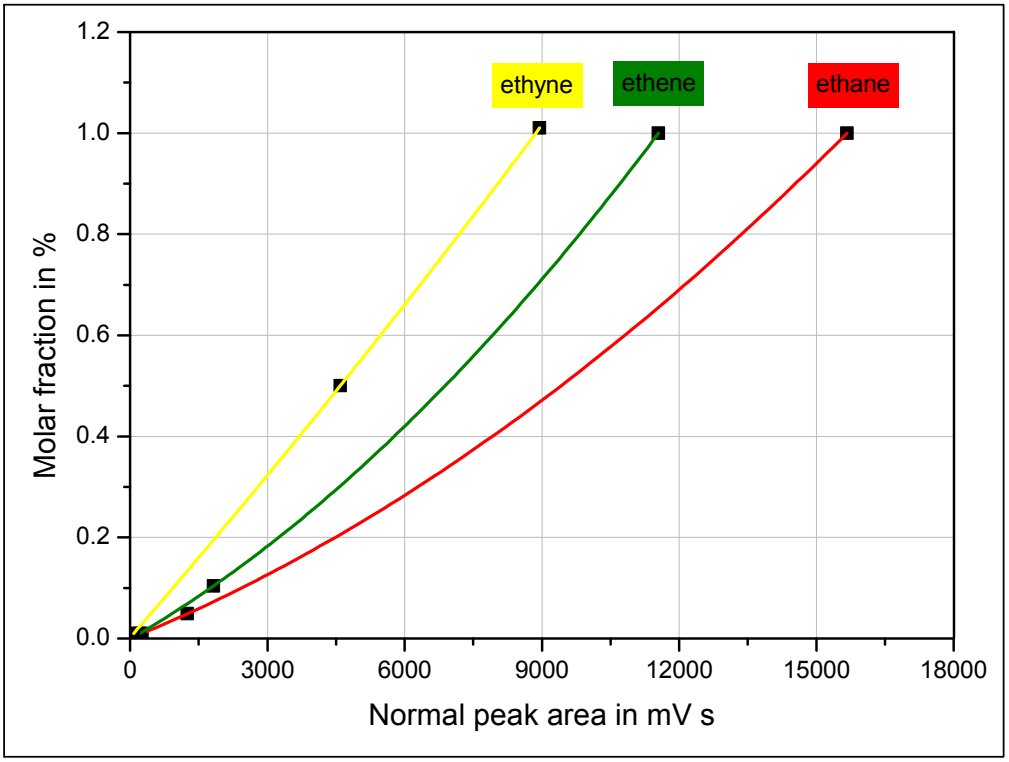

Figure of Appendix 9: Example for GC calibration curves: C_2-hydrocarbons detected by the HID (2nd order polynomial)

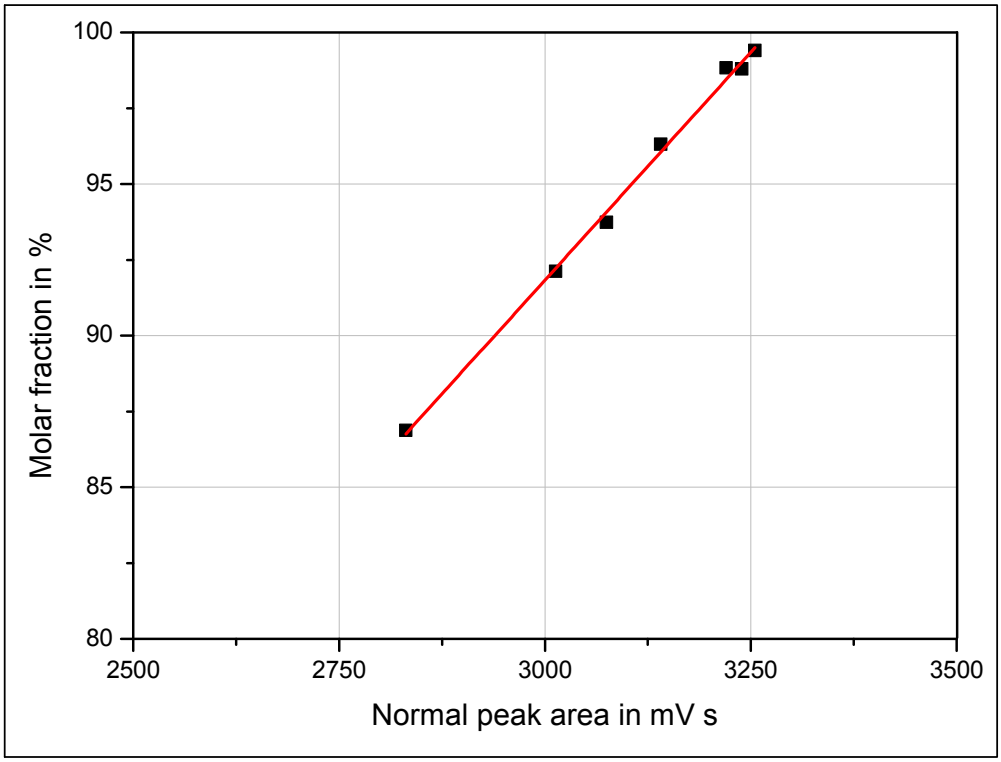

Figure of Appendix 10: Example a GC calibration curve: argon detected by the TCD (line)

Table of Appendix 3: Standard deviations, maximum positive deviations, and maximum negative deviations relative to mean peak areas determined in GC measurements (HID) for different molar fractions of hydrogen (extreme values in red)

Molar fraction	# Runs day 1 # Runs day 2 ...	s_{rel} in %	$s^{+}_{rel,max}$ in %	$s^{-}_{rel,max}$ in %
100 ppm	4 3 4	1.47 0.29 **7.29**	1.53 0.17 **7.09**	-2.00 -0.33 **-7.41**
1 %	6 48 48 9	**1.38** 1.05 0.61 0.82	1.48 **2.14** 1.39 1.63	-1.80 **-2.48** -1.29 -0.74
10 %	19	**0.39**	**0.62**	**-0.70**

Table of Appendix 4: Standard deviations, maximum positive deviations, and maximum negative deviations relative to mean peak areas determined in GC measurements (HID and TCD) for different molar fractions of methane (extreme values in red)

Detector	Molar fraction	# Runs day 1 # Runs day 2 ...	s_{rel} in %	$s^{+}_{rel,max}$ in %	$s^{-}_{rel,max}$ in %
HID	100 ppm	4	0.74	1.02	-0.75
		3	0.56	0.49	-0.62
		4	**3.06**	**2.35**	**-4.13**
	1 %	9	0.28	0.40	-0.51
		22	0.28	0.77	-0.34
		14	0.34	0.51	-0.63
		14	**1.07**	1.11	**-2.11**
		14	0.84	**1.58**	-1.15
		6	0.23	0.30	-0.29
TCD	1 %	9	**0.77**	**1.68**	-0.92
		22	0.53	0.85	**-1.21**
		14	0.62	1.05	-0.93
		14	0.67	0.99	-1.09
		5	0.68	0.90	-0.58

Table of Appendix 5: Standard deviations, maximum positive deviations, and maximum negative deviations relative to mean peak areas determined in GC measurements (TCD) for different molar fractions of argon (extreme values in red)

Molar fraction	# Runs day 1 # Runs day 2 ...	s_{rel} in %	$s^{+}_{rel,max}$ in %	$s^{-}_{rel,max}$ in %
98.8 %	8	0.25	0.29	-0.39
	5	0.39	0.34	-0.53
	5	0.59	0.73	-0.57
	5	0.45	0.61	-0.50
	5	**0.64**	**1.05**	**-0.68**
	5	0.43	0.75	-0.35

Table of Appendix 6: Standard deviations, maximum positive deviations, and maximum negative deviations relative to mean peak areas determined in GC measurements (HID) for different molar fractions of ethane (extreme values in red)

Molar fraction	# Runs day 1 # Runs day 2 ...	s_{rel} in %	$s^{+}_{rel,max}$ in %	$s^{-}_{rel,max}$ in %
100 ppm	4	**3.76**	**3.71**	**-3.75**
	3	1.63	1.45	-1.77
	4	0.39	0.48	-0.45
490 ppm	14	0.52	0.87	-1.21
	8	0.64	0.84	-0.59
	5	0.54	0.54	-0.60
	5	0.81	1.03	-0.69
	5	0.53	0.78	-0.50
	5	**1.20**	**1.28**	**-1.48**
	5	0.44	0.37	-0.62
1 %	5	**2.49**	**1.67**	**-4.31**
	4	0.44	0.57	-0.35
	9	0.56	0.74	-1.11

Table of Appendix 7: Standard deviations, maximum positive deviations, and maximum negative deviations relative to mean peak areas determined in GC measurements (HID) for different molar fractions of ethene (extreme values in red)

Molar fraction	# Runs day 1 # Runs day 2 ...	s_{rel} in %	$s^{+}_{rel,max}$ in %	$s^{-}_{rel,max}$ in %
100 ppm	4	**3.06**	**3.34**	**-3.00**
	3	1.35	1.53	-1.04
	4	1.38	1.03	-1.95
1040 ppm	14	1.04	**1.05**	-2.30
	8	0.44	0.53	-0.51
	5	0.65	0.70	-0.73
	5	0.77	0.91	-0.61
	5	0.53	0.73	-0.52
	5	**1.74**	1.02	**-3.10**
	5	0.41	0.41	-0.52
1 %	5	**2.44**	**1.57**	**-4.28**
	4	0.16	0.20	-0.20
	9	0.82	1.33	-1.39

Table of Appendix 8: Standard deviations, maximum positive deviations, and maximum negative deviations relative to mean peak areas determined in GC measurements (HID) for different molar fractions of ethyne (extreme values in red)

Molar fraction	# Runs day 1 # Runs day 2 ...	s_{rel} in %	$s^{+}_{rel,max}$ in %	$s^{-}_{rel,max}$ in %
100 ppm	4 3 4	4.86 1.87 **14.49**	5.27 2.09 **16.38**	-4.66 -1.52 **-13.59**
0.5 %	5 4 9	**4.89** 0.51 2.91	**3.19** 0.67 3.08	**-8.57** -0.49 -4.13
1.01 %	14 8 5 5 5 5 5	4.31 3.87 1.57 3.79 2.88 5.06 **5.78**	5.07 3.99 1.84 4.54 2.65 6.80 **8.33**	**-9.45** -7.80 -2.25 -5.93 -3.89 -5.11 -7.11

Table of Appendix 9: Maximum relative deviation of GC measurements for hydrogen (HID)

H_2 HID **Molar fraction in %**			**maximum relative deviation** **measured and extended (safety factor)** **estimated (assumed worst case factor)**	
basic / substituting additional	lower bound of interval	upper bound of interval	POSITIVE	NEGATIVE
0.001	0	0.00316	78.0 (10)	-81.5 (10)
0.01	0.00316	0.0316	7.09 7.80 (1.1)	-7.41 -8.15 (1.1)
0.1	0.0316	0.316	5.08	-5.44
1	0.316	3.16	2.14 2.35 (1.1)	-2.48 -2.73 (1.1)
10	3.16	31.6	0.622 0.684 (1.1)	-0.697 -0.767 (1.1)
minimum molar fraction applied or determined in experiments: 0.01 % maximum molar fraction applied or determined in experiments: 17.0 %				

Table of Appendix 10: Maximum relative deviation of GC measurements for methane (HID)

CH_4 HID **Molar fraction in %**			**maximum relative deviation** **measured and extended (safety factor)** **estimated (assumed worst case factor)**	
basic / substituting additional	lower bound of interval	upper bound of interval	POSITIVE	NEGATIVE
0.001	0	0.00316	25.9 (10)	-45.4 (10)
0.01	0.00316	0.0316	2.35 2.59 (1.1)	-4.13 -4.54 (1.1)
0.1	0.0316	0.316	2.16	-3.43
1	0.316	3.16	1.58 1.74 (1.1)	-2.11 -2.32 (1.1)
10	3.16	31.6	8.69 (5)	-11.6 (5)
minimum molar fraction applied or determined in experiments: 0.00152 % maximum molar fraction applied or determined in experiments: 3.37 % molar fractions > 1 % rarely employed				

Table of Appendix 11: Maximum relative deviation of GC measurements for methane (TCD)

CH_4 TCD **Molar fraction in %**			**maximum relative deviation** **measured and extended (safety factor)** **estimated (assumed worst case factor)**	
basic / substituting additional	lower bound of interval	upper bound of interval	POSITIVE	NEGATIVE
0.1	0.0316	0.316	9.24 (5)	-6.66 (5)
1	0.316	3.16	1.68 1.85 (1.1)	-1.21 -1.33 (1.1)
10	3.16	31.6	1.85 (1)	-1.33 (1)
minimum molar fraction applied or determined in experiments: 0.105 % maximum molar fraction applied or determined in experiments: 20.0 % molar fractions < 0.6 % rarely employed				

Table of Appendix 12: Maximum relative deviation of GC measurements for argon (TCD)

Ar TCD **Molar fraction in %**			**maximum relative deviation** **measured and extended (safety factor)** **estimated (assumed worst case factor)**	
basic / substituting additional	lower bound of interval	upper bound of interval	POSITIVE	NEGATIVE
98.8	31.4	100	1.05 1.16 (1.1)	-0.679 -0.747 (1.1)
minimum molar fraction applied or determined in experiments: 78.8 % maximum molar fraction applied or determined in experiments: 100 %				

Table of Appendix 13: Maximum relative deviation of GC measurements for ethane (HID)

C_2H_6 HID **Molar fraction in %**			**maximum relative deviation** **measured and extended (safety factor)** **estimated (assumed worst case factor)**	
basic / substituting additional	lower bound of interval	upper bound of interval	POSITIVE	NEGATIVE
0.001	0	0.00316	40.8 (10)	-41.3 (10)
0.01	0.00316	0.0221	3.71 4.08 (1.1)	-3.75 -4.13 (1.1)
0.049	0.0221	0.0700	1.28 1.41 (1.1)	-1.48 -1.63 (1.1)
0.1	0.0700	0.316	1.51	-2.36
1	0.316	3.16	1.67 1.84 (1.1)	-4.31 -4.74 (1.1)
minimum molar fraction applied or determined in experiments: 0.0000206 % maximum molar fraction applied or determined in experiments: 1 %				

Table of Appendix 14: Maximum relative deviation of GC measurements for ethene (HID)

C_2H_4 HID **Molar fraction in %**			**maximum relative deviation** **measured and extended (safety factor)** **estimated (assumed worst case factor)**	
basic / substituting additional	lower bound of interval	upper bound of interval	POSITIVE	NEGATIVE
0.001	0	0.00316	36.7 (10)	-33.0 (10)
0.01	0.00316	0.0322	3.34 3.67 (1.1)	-3.00 -3.30 (1.1)
0.104	0.0322	0.322	1.05 1.16 (1.1)	-3.10 -3.41 (1.1)
1	0.322	3.16	1.57 1.73 (1.1)	-4.28 -4.71 (1.1)
minimum molar fraction applied or determined in experiments: 0.00159 % maximum molar fraction applied or determined in experiments: 1.00 %				

Table of Appendix 15: Maximum relative deviation of GC measurements for ethyne (HID)

C_2H_2 HID **Molar fraction in %**			**maximum relative deviation** **measured and extended (safety factor)** **estimated (assumed worst case factor)**	
basic / substituting additional	lower bound of interval	upper bound of interval	POSITIVE	NEGATIVE
0.001	0	0.00316	180 (10)	-97.2 (6.5)
0.01	0.00316	0.0316	16.4 18.0 (1.1)	-13.6 -15.0 (1.1)
0.1	0.0316	0.224	9.49	-11.7
0.5	0.224	0.711	3.19 3.51 (1.1)	-8.57 -9.43 (1.1)
1.01	0.711	3.18	8.33 9.16 (1.1)	-9.45 -10.4 (1.1)
minimum molar fraction applied or determined in experiments: 0.000150 % maximum molar fraction applied or determined in experiments: 1.99 %				

Appendix C: Reaction conditions and experimental results

Table of Appendix 16: Various information about reaction conditions for with argon as dilution gas and nominal furnace temperatures of 1200 °C and 1300 °C (nominal furnace temperature in °C - nominal total standard volume flow in sccm - nominal initial molar fraction of methane in %) I

Set	$\dot{V}_{N,Ar,0}$ in sccm			$\dot{V}_{N,CH_4,0}$ in sccm			$\dot{V}_{N,tot,0}$ in sccm	$x_{CH_4,0}$ in %
1200 - 95 - 2	93.06	1.1	2.7	1.898	0.0	0.1	94.96	1.999
1200 - 95 - 5	90.10	1.1	2.6	4.735	0.1	0.1	94.84	4.993
1200 - 95 - 10	85.51	1.1	2.6	9.513	0.1	0.2	95.02	10.01
1200 - 200 - 2	195.5	1.8	4.1	4.027	0.1	0.1	199.5	2.018
1200 - 200 - 5	189.8	1.7	4.0	10.03	0.1	0.2	199.8	5.019
1200 - 200 - 10	179.9	1.7	3.9	19.95	0.4	0.9	199.9	9.982
1200 - 350 - 2	343.7	2.9	6.2	7.060	0.1	0.1	350.8	2.013
1200 - 350 - 5	333.3	2.8	6.0	17.54	0.4	0.8	350.8	4.999
1200 - 350 - 10	313.9	2.7	5.8	35.13	0.4	1.1	349.0	10.07
1200 - 685 - 2	671.2	5.5	10.8	13.50	0.3	0.8	684.7	1.972
1200 - 685 - 5	650.4	5.3	10.5	34.19	0.4	1.1	684.6	4.994
1200 - 685 - 10	616.4	5.0	10.0	69.09	0.6	1.5	685.5	10.08
1200 - 2000 - 2	1959	20.3	49.3	39.94	0.5	1.1	1999	1.998
1200 - 2000 - 5	1905	19.9	48.6	100.2	1.8	4.3	2005	4.997
1200 - 2000 - 10	1804	19.3	47.2	200.1	2.3	5.7	2004	9.985
1200 - 2000 - 20	1600	18.1	44.3	400.1	3.8	9.1	2000	20.00
1300 - 340 - 2	332.9	2.8	6.0	6.717	0.3	0.7	339.6	1.978
1300 - 340 - 5	323.1	2.7	5.9	16.98	0.4	0.8	340.1	4.993
1300 - 340 - 10	306.5	2.6	5.7	33.89	0.4	1.1	340.4	9.956
1300 - 650 - 2	637.0	5.2	10.3	12.91	0.3	0.8	649.9	1.986
1300 - 650 - 5	616.9	5.0	10.0	32.58	0.4	1.0	649.5	5.016
1300 - 650 - 10	584.3	4.8	9.6	64.91	0.6	1.5	649.2	10.00
1300 - 1300 - 2	1276	16.3	39.8	26.06	0.4	0.9	1302	2.001
1300 - 1300 - 5	1236	16.1	39.2	65.05	0.6	1.5	1301	5.000
1300 - 1300 - 10	1172	15.8	38.3	130.1	2.0	4.7	1302	9.992
1300 - 2600 - 2	2549	24.2	57.6	51.64	0.5	1.3	2601	1.986
1300 - 2600 - 5	2470	23.6	56.5	129.3	2.0	4.7	2599	4.974
1300 - 2600 - 10	2340	22.8	54.7	259.4	2.7	6.5	2599	9.979
1300 - 4800 - 2	4695	49.4	120.5	95.96	1.8	4.2	4791	2.003
1300 - 4800 - 5	4556	48.6	118.6	239.6	2.6	6.2	4796	4.996
1300 - 4800 - 10	4345	47.3	115.6	460.6	4.2	9.9	4806	9.585
standard uncertainty / maximum uncertainty								

Table of Appendix 17: Various information about reaction conditions for with argon as dilution gas and nominal furnace temperatures of 1400 °C, 1500 °C, and 1600 °C (nominal furnace temperature in °C - nominal total standard volume flow in sccm - nominal initial molar fraction of methane in %) I

Set	$\dot{V}_{N,Ar,0}$ in sccm			$\dot{V}_{N,CH_4,0}$ in sccm			$\dot{V}_{N,tot,0}$ in sccm	$x_{CH_4,0}$ in %
1400 - 700 - 2	686.0	13.8	31.5	14.02	0.4	0.8	700.0	2.003
1400 - 700 - 5	665.2	13.8	31.2	35.03	0.4	1.1	700.2	5.003
1400 - 700 - 10	629.5	13.6	30.7	69.95	0.7	1.6	699.5	10.00
1400 - 1400 - 2	1373	16.8	41.1	27.83	0.4	1.0	1401	1.987
1400 - 1400 - 5	1330	16.6	40.5	69.90	0.7	1.6	1400	4.993
1400 - 1400 - 10	1258	16.2	39.5	140.0	2.0	4.8	1398	10.01
1400 - 2600 - 2	2549	24.2	57.6	51.67	0.5	1.3	2601	1.987
1400 - 2600 - 5	2471	23.6	56.5	129.8	2.0	4.7	2601	4.991
1400 - 2600 - 10	2340	22.8	54.7	260.5	2.7	6.5	2601	10.02
1400 - 3800 - 2	3718	43.6	106.9	76.15	1.8	3.9	3794	2.007
1400 - 3800 - 5	3615	43.1	105.4	190.4	2.3	5.5	3805	5.003
1400 - 3800 - 10	3427	42.1	102.8	380.2	3.5	8.2	3807	9.986
1400 - 6500 - 2	6362	60.4	143.9	129.5	2.0	4.7	6492	1.995
1400 - 6500 - 5	6168	59.0	141.2	324.6	3.1	7.4	6493	5.000
1400 - 6500 - 7.1	6044	58.2	139.4	458.5	4.2	9.9	6503	7.051
1500 - 1600 - 2	1566	17.9	43.8	31.99	0.4	1.0	1598	2.002
1500 - 1600 - 5	1522	17.6	43.2	80.00	1.8	4.0	1602	4.994
1500 - 1600 - 10	1433	17.2	42.0	159.9	2.1	5.1	1593	10.04
1500 - 2800 - 2	2743	25.9	61.7	55.64	0.6	1.4	2799	1.988
1500 - 2800 - 5	2665	25.0	59.2	140.0	2.0	4.8	2805	4.991
1500 - 2800 - 10	2522	24.0	57.2	280.5	2.8	6.8	2803	10.01
1500 - 4600 - 2	4504	48.2	117.9	91.98	1.8	4.2	4596	2.001
1500 - 4600 - 5	4369	47.4	116.0	229.7	2.5	6.1	4599	4.995
1500 - 4600 - 10	4166	46.2	113.1	430.9	4.0	9.5	4597	9.374
1500 - 7200 - 2	7056	65.2	153.6	144.0	2.0	4.9	7200	2.000
1500 - 7200 - 5	6824	63.6	150.3	360.0	3.4	7.9	7184	5.011
1500 - 7200 - 6.3	6735	63.0	149.1	454.5	4.2	9.8	7190	6.322
1500 - 9800 - 2	9600	83.8	189.2	196.6	2.3	5.6	9797	2.007
1500 - 9800 - 3.1	9490	83.0	187.7	304.3	3.0	7.1	9794	3.107
1500 - 9800 - 5	9350	81.9	185.7	464.7	4.3	10.0	9815	4.735
1600 - 2000 - 2	1960	20.3	49.4	40.01	0.5	1.1	2000	2.000
1600 - 2000 - 5	1903	19.9	48.6	99.91	1.8	4.3	2003	4.988
1600 - 2000 - 10	1800	19.3	47.1	200.8	2.3	5.7	2001	10.04
1600 - 3350 - 2	3285	29.8	69.3	66.76	0.6	1.5	3352	1.992
1600 - 3350 - 5	3189	29.1	67.9	167.5	2.1	5.2	3357	4.990
1600 - 3350 - 10	3020	27.9	65.6	334.7	3.2	7.6	3355	9.977
1600 - 6500 - 2	6367	60.4	143.9	129.9	2.0	4.7	6497	1.999
1600 - 6500 - 5	6180	59.1	141.3	326.3	3.1	7.4	6506	5.015
1600 - 6500 - 7.1	6045	58.2	139.4	459.2	4.2	9.9	6504	7.060
1600 - 9800 - 2	9576	83.6	188.9	195.8	2.3	5.6	9772	2.004
1600 - 9800 - 3	9486	82.9	187.6	294.1	2.9	7.0	9780	3.007
1600 - 9800 - 5	9339	81.8	185.5	460.7	4.2	9.9	9800	4.701

standard uncertainty / maximum uncertainty

Table of Appendix 18: Various information about reaction conditions for with argon as dilution gas and nominal furnace temperatures of 1200 °C and 1300 °C (nominal furnace temperature in °C - nominal total standard volume flow in sccm - nominal initial molar fraction of methane in %) II

Set	$p_{R,inlet}$ in bar		$p_{R,outlet}$ in bar		τ in s		# Runs
	start	end	start	end			
1200 - 95 - 2	1.006	1.006	0.999	0.999	1.46	0.218	1
1200 - 95 - 5	1.005	1.005	0.998	0.997	1.46	0.218	1
1200 - 95 - 10	1.009	1.009	0.999	0.999	1.47	0.218	1
1200 - 200 - 2	1.008	1.008	1.009	1.009	0.697	0.0974	2
1200 - 200 - 5	1.008	1.008	1.009	1.009	0.696	0.0971	2
1200 - 200 - 10	1.008	1.008	1.009	1.009	0.696	0.0993	1
1200 - 350 - 2	1.006	1.006	1.008	1.008	0.396	0.0539	2
1200 - 350 - 5	1.006	1.006	1.008	1.008	0.396	0.0546	2
1200 - 350 - 10	1.006	1.006	1.007	1.007	0.398	0.0549	1
1200 - 685 - 2	1.006	1.007	1.006	1.007	0.203	0.0273	1
1200 - 685 - 5	1.006	1.007	1.006	1.007	0.203	0.0273	2
1200 - 685 - 10	1.006	1.007	1.006	1.007	0.203	0.0273	1
1200 - 2000 - 2	1.012	1.012	1.013	1.013	0.0699	0.0101	1
1200 - 2000 - 5	1.012	1.012	1.013	1.013	0.0696	0.0102	2
1200 - 2000 - 10	1.012	1.012	1.013	1.013	0.0697	0.0102	1
1200 - 2000 - 20	1.012	1.012	1.013	1.013	0.0698	0.0102	1
1300 - 340 - 2	0.995	0.995	0.996	0.996	0.379	0.0523	1
1300 - 340 - 5	0.994	0.994	0.996	0.996	0.378	0.0522	2
1300 - 340 - 10	0.994	0.994	0.996	0.996	0.377	0.0522	1
1300 - 650 - 2	1.004	1.005	1.004	1.005	0.200	0.0270	1
1300 - 650 - 5	1.005	1.005	1.005	1.005	0.200	0.0270	2
1300 - 650 - 10	1.005	1.005	1.005	1.005	0.200	0.0270	1
1300 - 1300 - 2	1.012	1.011	1.013	1.013	0.100	0.0152	1
1300 - 1300 - 5	1.011	1.011	1.012	1.013	0.100	0.0152	2
1300 - 1300 - 10	1.011	1.011	1.012	1.013	0.100	0.0154	1
1300 - 2600 - 2	1.009	1.009	1.007	1.007	0.0501	0.00709	1
1300 - 2600 - 5	1.009	1.009	1.008	1.008	0.0502	0.00715	2
1300 - 2600 - 10	1.009	1.009	1.008	1.008	0.0502	0.00715	2
1300 - 4800 - 2	1.020	1.020	1.019	1.019	0.0275	0.00400	2
1300 - 4800 - 5	1.020	1.020	1.018	1.019	0.0275	0.00399	2
1300 - 4800 - 10	1.020	1.020	1.018	1.019	0.0274	0.00399	1
maximum uncertainty							

Table of Appendix 19: Various information about reaction conditions for with argon as dilution gas and nominal furnace temperatures of 1400 °C, 1500 °C, and 1600 °C (nominal furnace temperature in °C - nominal total standard volume flow in sccm - nominal initial molar fraction of methane in %) II

Set	$p_{R,inlet}$ in bar		$p_{R,outlet}$ in bar		τ in s		# Runs
	start	end	start	end			
1400 - 700 - 2	1.003	1.003	1.005	1.005	0.174	0.0295	1
1400 - 700 - 5	1.003	1.003	1.005	1.005	0.174	0.0295	2
1400 - 700 - 10	1.003	1.003	1.005	1.005	0.174	0.0296	1
1400 - 1400 - 2	1.011	1.012	1.004	1.004	0.0877	0.0132	2
1400 - 1400 - 5	1.021	1.021	1.010	1.010	0.0886	0.0133	1
1400 - 1400 - 10	1.026	1.030	1.010	1.010	0.0893	0.0136	2
1400 - 2600 - 2	1.031	1.031	1.025	1.025	0.0482	0.00680	1
1400 - 2600 - 5	1.048	1.048	1.030	1.030	0.0490	0.00695	1
1400 - 2600 - 10	1.045	1.046	1.028	1.028	0.0488	0.00694	1
1400 - 3800 - 2	1.013	1.013	1.012	1.012	0.0324	0.00484	1
1400 - 3800 - 5	1.013	1.013	1.012	1.013	0.0323	0.00482	2
1400 - 3800 - 10	1.013	1.014	1.012	1.012	0.0323	0.00482	1
1400 - 6500 - 2	1.058	1.058	1.050	1.050	0.0198	0.00279	1
1400 - 6500 - 5	1.057	1.057	1.049	1.049	0.0198	0.00279	2
1400 - 6500 - 7.1	1.057	1.057	1.049	1.049	0.0197	0.00279	1
1500 - 1600 - 2	0.985	0.985	0.984	0.984	0.0707	0.0105	2
1500 - 1600 - 5	0.984	0.984	0.984	0.984	0.0704	0.0106	1
1500 - 1600 - 10	0.985	0.985	0.984	0.984	0.0709	0.0106	1
1500 - 2800 - 2	1.010	1.010	1.006	1.006	0.0414	0.00585	1
1500 - 2800 - 5	1.011	1.011	1.005	1.005	0.0413	0.00585	1
1500 - 2800 - 10	1.017	1.024	1.005	1.005	0.0417	0.00591	1
1500 - 4600 - 2	1.025	1.025	1.024	1.024	0.0256	0.00373	1
1500 - 4600 - 5	1.027	1.027	1.024	1.024	0.0256	0.00373	2
1500 - 4600 - 10	1.028	1.028	1.024	1.024	0.0256	0.00374	1
1500 - 7200 - 2	1.016	1.016	1.011	1.011	0.0162	0.00227	2
1500 - 7200 - 5	1.016	1.016	1.011	1.011	0.0162	0.00228	2
1500 - 7200 - 6.3	1.015	1.016	1.010	1.010	0.0162	0.00228	1
1500 - 9800 - 2	1.018	1.017	1.005	1.005	0.0119	0.00164	3
1500 - 9800 - 3.1	1.016	1.017	1.004	1.004	0.0119	0.00164	1
1500 - 9800 - 5	1.016	1.016	1.004	1.004	0.0119	0.00164	1
1600 - 2000 - 2	1.008	1.008	1.008	1.008	0.0547	0.00790	2
1600 - 2000 - 5	1.008	1.008	1.009	1.009	0.0546	0.00797	1
1600 - 2000 - 10	1.009	1.009	1.009	1.009	0.0547	0.00798	1
1600 - 3350 - 2	1.034	1.034	1.032	1.032	0.0335	0.00467	1
1600 - 3350 - 5	1.035	1.035	1.032	1.032	0.0335	0.00469	2
1600 - 3350 - 10	1.036	1.037	1.032	1.032	0.0335	0.00470	1
1600 - 6500 - 2	1.052	1.052	1.044	1.044	0.0176	0.00248	2
1600 - 6500 - 5	1.054	1.055	1.044	1.044	0.0176	0.00248	2
1600 - 6500 - 7.1	1.055	1.057	1.044	1.044	0.0176	0.00249	1
1600 - 9800 - 2	1.033	1.033	1.022	1.022	0.0115	0.00158	1
1600 - 9800 - 3	1.033	1.033	1.023	1.023	0.0115	0.00158	2
1600 - 9800 - 5	1.034	1.035	1.023	1.023	0.0115	0.00158	1
maximum uncertainty							

Table of Appendix 20: Conversion of methane as well as yields of hydrogen and ethyne along with respective maximum and standard uncertainties for experiments with argon as dilution gas and nominal furnace temperatures of 1200 °C and 1300 °C

Set	X_{CH_4} in %				Y_{H_2} in %				$Y_{C_2H_2}$ in %			
1200 - 95 - 2	81.81	0.9693	3.551	-4.467	82.05	3.381	15.84	-13.64	24.08	1.504	6.448	-5.455
1200 - 95 - 5	82.70	0.6514	2.574	-3.015	80.63	2.555	12.46	-10.61	16.44	1.159	4.774	-3.591
1200 - 95 - 10	82.74	0.6057	2.437	-2.842	80.21	2.887	13.60	-11.39	12.08	1.011	4.199	-2.802
1200 - 200 - 2	71.68	1.213	4.378	-5.287	58.16	2.089	9.496	-7.981	28.10	2.921	11.54	-7.476
1200 - 200 - 5	73.46	0.8297	3.217	-3.712	63.64	1.074	5.223	-4.912	18.78	1.596	5.807	-4.580
1200 - 200 - 10	73.92	0.9432	3.891	-4.682	69.72	2.659	13.06	-10.78	13.90	1.324	5.712	-3.632
1200 - 350 - 2	50.39	2.280	7.617	-8.927	41.55	1.738	6.938	-5.977	22.71	2.127	8.874	-4.607
1200 - 350 - 5	55.39	2.112	7.754	-9.445	48.66	1.584	7.599	-6.431	18.73	1.773	7.784	-4.535
1200 - 350 - 10	59.38	1.787	6.668	-7.980	52.67	1.699	8.302	-7.004	14.36	1.283	5.275	-3.513
1200 - 685 - 2	17.87	3.211	12.17	-14.76	9.316	1.572	5.332	-4.456	10.45	1.900	8.082	-3.907
1200 - 685 - 5	24.09	2.542	10.03	-11.82	19.88	0.9276	3.957	-3.284	11.22	1.468	6.223	-3.049
1200 - 685 - 10	29.15	2.451	9.403	-11.05	23.38	0.7941	3.550	-3.107	10.67	1.231	4.979	-2.818
1200 - 2000 - 2	7.044	4.379	15.94	-7.044	0.8381	0.06438	0.2514	-0.1993	0.09395	0.8529	4.671	-0.07012
1200 - 2000 - 5	2.734	3.728	15.07	-2.734	1.003	0.06605	0.2809	-0.2221	0.2320	0.03713	0.1448	-0.09034
1200 - 2000 - 10	2.523	3.544	14.39	-2.523	1.346	0.08716	0.3628	-0.2862	0.4195	0.08027	0.3248	-0.1652
1200 - 2000 - 20	3.577	3.414	14.05	-3.577	2.196	0.1345	0.5468	-0.4735	0.7550	0.1337	0.5645	-0.2660
1300 - 340 - 2	91.67	0.6194	1.977	-2.747	87.19	4.872	12.81	-15.07	37.08	3.729	16.71	-10.90
1300 - 340 - 5	91.18	0.4318	1.589	-1.956	85.95	2.896	14.05	-11.79	26.06	2.191	9.337	-6.405
1300 - 340 - 10	89.96	0.4264	1.617	-1.955	85.10	3.087	14.86	-12.29	19.47	1.847	7.032	-5.477
1300 - 650 - 2	83.54	1.366	4.468	-5.339	72.29	3.156	14.43	-11.69	36.06	4.889	21.63	-10.86
1300 - 650 - 5	83.45	0.8142	2.869	-3.446	78.05	2.581	12.18	-10.29	25.65	2.409	10.13	-6.009
1300 - 650 - 10	82.45	0.6171	2.400	-2.811	77.95	2.790	12.76	-10.69	21.39	1.812	6.120	-5.954
1300 - 1300 - 2	61.63	2.148	7.603	-9.561	48.18	1.897	9.194	-7.647	36.76	4.877	21.28	-10.88
1300 - 1300 - 5	63.55	1.639	6.125	-7.269	54.29	1.652	8.180	-7.035	27.50	2.731	11.31	-7.049
1300 - 1300 - 10	63.15	1.704	6.701	-8.193	58.03	2.119	10.88	-9.014	21.80	1.816	6.755	-6.473
1300 - 2600 - 2	19.05	2.603	10.40	-12.22	9.418	1.574	4.993	-4.378	8.064	0.7638	2.404	-2.544
1300 - 2600 - 5	19.23	2.803	11.45	-13.61	13.02	0.5577	2.539	-2.140	8.659	0.6402	2.259	-2.308
1300 - 2600 - 10	22.10	2.579	10.49	-12.28	14.54	0.4611	2.220	-1.906	8.219	0.5504	2.164	-1.787
1300 - 4800 - 2	1.196	2.680	8.978	-1.196	0.5461	0.03740	0.1575	-0.1218	0.01521	0.1667	0.9270	-0.01226
1300 - 4800 - 5	1.401	1.498	5.407	-1.401	0.6944	0.04302	0.1740	-0.1391	0.09628	0.03771	0.1913	-0.02746
1300 - 4800 - 10	1.744	1.287	4.565	-1.744	0.9496	0.06674	0.2667	-0.2065	0.1515	0.03804	0.1405	-0.08064

standard uncertainty / maximum uncertainty

Table of Appendix 21: Yields of ethane and ethene along with respective maximum and standard uncertainties for experiments with argon as dilution gas and nominal furnace temperatures of 1200 °C and 1300 °C

Set	$Y_{C_2H_6}$ in %				$Y_{C_2H_4}$ in %			
1200 - 95 - 2	0.002102	0.0006941	0.003017	-0.001157	1.222	0.1492	0.5782	-0.4325
1200 - 95 - 5	0.006905	0.002274	0.009456	-0.003721	2.281	0.2369	0.8061	-0.7474
1200 - 95 - 10	0.02731	0.008992	0.03733	-0.01469	3.069	0.2865	0.9783	-0.9334
1200 - 200 - 2	0.01790	0.005117	0.02112	-0.008536	1.560	0.1426	0.4105	-0.5190
1200 - 200 - 5	0.01827	0.005076	0.02026	-0.008685	2.105	0.06331	0.2542	-0.2770
1200 - 200 - 10	0.02368	0.008549	0.03774	-0.01276	2.419	0.09122	0.4579	-0.3639
1200 - 350 - 2	0.1020	0.02954	0.1196	-0.04710	2.222	0.1352	0.3693	-0.5364
1200 - 350 - 5	0.05376	0.01804	0.07809	-0.02796	2.060	0.07521	0.3117	-0.3339
1200 - 350 - 10	0.03947	0.01336	0.05695	-0.02050	2.189	0.07380	0.3591	-0.2974
1200 - 685 - 2	0.3922	0.05315	0.2108	-0.1366	4.055	0.1635	0.6166	-0.7274
1200 - 685 - 5	0.2533	0.02931	0.1097	-0.07694	3.304	0.07226	0.3335	-0.3494
1200 - 685 - 10	0.1931	0.02316	0.08048	-0.06375	2.891	0.1159	0.5553	-0.3774
1200 - 2000 - 2	0.5438	0.03971	0.1564	-0.1249	0.7854	0.05362	0.2134	-0.1728
1200 - 2000 - 5	0.4634	0.03022	0.1165	-0.1122	0.9795	0.03192	0.1246	-0.1642
1200 - 2000 - 10	0.4296	0.01781	0.07483	-0.07524	1.066	0.02777	0.1275	-0.1410
1200 - 2000 - 20	0.3994	0.01089	0.05423	-0.05097	1.206	0.04511	0.2273	-0.1727
1300 - 340 - 2	0.02406	0.008360	0.03936	-0.01342	0.7001	0.09583	0.4001	-0.2694
1300 - 340 - 5	0	0	0	0	1.518	0.06559	0.2795	-0.2722
1300 - 340 - 10	0.008609	0.002954	0.01265	-0.004528	2.313	0.07861	0.3856	-0.3194
1300 - 650 - 2	0	0	0	0	0.6750	0.08840	0.3428	-0.2395
1300 - 650 - 5	0.003538	0.003132	0.01382	-0.003538	1.231	0.04978	0.1560	-0.2437
1300 - 650 - 10	0.009792	0.003335	0.01415	-0.004961	1.895	0.05800	0.2642	-0.2449
1300 - 1300 - 2	0.07641	0.02603	0.1141	-0.03947	2.203	0.1377	0.4511	-0.5913
1300 - 1300 - 5	0.05719	0.01900	0.08162	-0.02881	1.976	0.05010	0.2059	-0.2708
1300 - 1300 - 10	0.05004	0.01705	0.07590	-0.02606	1.976	0.06930	0.3527	-0.3042
1300 - 2600 - 2	0.7084	0.09525	0.3338	-0.2536	4.711	0.1945	0.8124	-0.7475
1300 - 2600 - 5	0.5056	0.05334	0.1619	-0.1872	3.795	0.1223	0.5984	-0.5170
1300 - 2600 - 10	0.3585	0.02466	0.07693	-0.09631	3.087	0.06393	0.3354	-0.3020
1300 - 4800 - 2	0.4898	0.06397	0.2456	-0.1700	0.5579	0.07083	0.2677	-0.1939
1300 - 4800 - 5	0.4411	0.04950	0.1639	-0.1507	0.7043	0.05524	0.1665	-0.2071
1300 - 4800 - 10	0.4304	0.02840	0.09654	-0.1055	0.8667	0.03248	0.1297	-0.1423
standard uncertainty / maximum uncertainty								

Table of Appendix 22: Conversion of methane as well as yields of hydrogen and ethyne along with respective maximum and standard uncertainties for experiments with argon as dilution gas and nominal furnace temperatures of 1400 °C, 1500 °C, and 1600 °C

Set	X_{CH_4} in %				Y_{H_2} in %				$Y_{C_2H_2}$ in %			
1400 - 700 - 2	97.14	0.1821	0.6575	-0.8572	89.17	3.785	10.83	-15.54	47.54	4.285	19.69	-13.07
1400 - 700 - 5	96.55	0.1960	0.7136	-0.8869	92.55	3.295	7.451	-13.89	35.40	3.222	12.70	-10.42
1400 - 700 - 10	95.89	0.2149	0.8147	-0.9734	89.18	3.576	10.82	-14.53	29.23	1.791	7.687	-6.547
1400 - 1400 - 2	91.98	0.5799	2.016	-2.243	86.01	2.499	12.72	-11.27	40.63	2.718	11.63	-8.904
1400 - 1400 - 5	92.20	0.3351	1.265	-1.516	86.68	2.807	13.32	-11.71	32.54	3.839	14.73	-10.13
1400 - 1400 - 10	90.38	0.3799	1.563	-1.915	85.92	3.199	14.08	-13.42	40.68	2.322	10.17	-8.720
1400 - 2600 - 2	74.57	1.027	3.847	-4.573	62.52	2.572	11.29	-9.667	46.41	3.484	14.09	-10.14
1400 - 2600 - 5	75.02	1.027	3.969	-4.836	66.42	2.120	10.10	-9.393	33.08	3.798	15.28	-9.856
1400 - 2600 - 10	73.14	0.8804	3.667	-4.323	63.04	2.183	10.61	-8.865	36.51	2.131	8.647	-7.525
1400 - 3800 - 2	44.92	2.566	9.912	-12.21	33.96	1.575	7.448	-6.134	26.99	2.686	11.69	-7.503
1400 - 3800 - 5	48.22	2.176	8.500	-10.11	37.96	1.175	5.965	-5.091	24.44	2.141	8.957	-6.047
1400 - 3800 - 10	48.43	2.216	8.511	-10.16	40.66	1.323	6.575	-5.581	20.37	1.851	6.908	-5.780
1400 - 6500 - 2	10.72	3.852	14.63	-10.72	5.622	0.3513	1.466	-1.174	2.780	0.4776	1.628	-1.286
1400 - 6500 - 5	11.24	3.319	12.78	-11.24	7.030	0.2444	1.120	-0.9666	4.199	0.5705	2.237	-1.316
1400 - 6500 - 7.1	11.97	3.258	12.66	-11.97	7.972	0.3576	1.560	-1.288	4.704	0.6589	2.605	-1.499
1500 - 1600 - 2	99.06	0.03339	0.1393	-0.1558	90.83	2.326	9.171	-10.36	50.93	3.998	16.28	-12.05
1500 - 1600 - 5	98.35	0.1295	0.4164	-0.5492	91.24	3.471	8.757	-13.63	43.12	4.422	18.86	-12.31
1500 - 1600 - 10	97.81	0.1718	0.5196	-0.7160	92.98	3.453	7.016	-12.94	39.79	2.338	10.15	-7.955
1500 - 2800 - 2	95.41	0.3640	1.152	-1.306	83.40	2.212	10.88	-9.481	59.53	5.671	22.59	-14.66
1500 - 2800 - 5	94.43	0.2947	1.038	-1.284	84.89	2.847	13.97	-11.74	48.13	4.356	16.23	-13.57
1500 - 2800 - 10	93.32	0.2765	1.060	-1.253	85.04	3.055	14.56	-12.18	39.32	2.395	11.66	-6.487
1500 - 4600 - 2	77.00	1.220	3.988	-6.030	63.66	2.637	12.57	-10.41	48.05	3.867	16.13	-12.06
1500 - 4600 - 5	76.16	0.9083	3.571	-4.217	66.06	1.982	9.855	-8.465	40.57	4.016	15.71	-11.09
1500 - 4600 - 10	74.26	1.055	4.046	-4.834	67.89	2.313	11.20	-9.445	35.87	2.090	8.449	-7.358
1500 - 7200 - 2	43.19	2.250	8.638	-10.17	33.95	1.074	5.193	-4.405	25.72	1.686	6.410	-5.782
1500 - 7200 - 5	44.95	2.380	8.706	-10.27	36.86	1.309	5.882	-5.188	22.96	1.803	7.108	-5.233
1500 - 7200 - 6.3	44.59	2.523	9.127	-10.89	37.49	1.281	5.915	-5.173	21.98	1.773	7.164	-5.015
1500 - 9800 - 2	24.57	2.966	10.99	-13.11	16.47	0.6877	2.994	-2.495	9.381	1.633	7.651	-2.320
1500 - 9800 - 3.1	26.69	2.986	10.94	-12.91	17.39	0.7358	3.163	-2.649	10.41	1.896	8.345	-3.073
1500 - 9800 - 5	27.66	2.978	10.84	-12.80	18.58	0.7994	3.423	-2.846	10.49	1.645	7.865	-2.274
1600 - 2000 - 2	99.83	0.008091	0.02845	-0.03537	92.32	2.367	7.679	-10.48	43.43	3.356	13.01	-10.27
1600 - 2000 - 5	99.60	0.02220	0.07924	-0.1001	95.35	3.422	4.648	-14.17	38.23	3.740	15.29	-10.86
1600 - 2000 - 10	99.33	0.03315	0.1224	-0.1491	91.43	3.325	8.566	-13.58	35.17	2.068	8.630	-7.406
1600 - 3350 - 2	99.07	0.07378	0.2319	-0.2636	89.40	2.366	10.60	-9.969	57.31	4.428	17.24	-12.82
1600 - 3350 - 5	98.74	0.05770	0.2113	-0.2563	87.97	2.876	12.03	-11.83	47.97	4.758	18.88	-12.95
1600 - 3350 - 10	98.40	0.08117	0.2846	-0.3522	89.30	3.213	10.70	-12.75	44.23	2.576	10.36	-9.031
1600 - 6500 - 2	81.45	0.7573	2.918	-3.465	68.29	2.759	12.54	-10.77	52.48	5.810	24.72	-13.81
1600 - 6500 - 5	82.21	0.6971	2.550	-3.252	69.83	1.825	9.193	-7.976	45.72	3.391	10.97	-12.37
1600 - 6500 - 7.1	82.18	0.6914	2.506	-3.287	69.98	2.231	10.72	-9.090	43.86	2.538	9.995	-8.812
1600 - 9800 - 2	59.29	2.017	7.080	-8.598	47.85	1.993	8.740	-7.543	36.36	3.667	15.29	-8.967
1600 - 9800 - 3	60.05	1.858	6.565	-7.909	48.56	1.795	8.182	-6.804	35.22	3.389	13.87	-8.471
1600 - 9800 - 5	60.33	1.807	6.464	-7.656	49.63	1.399	6.796	-5.848	32.32	3.298	12.41	-8.945

standard uncertainty / maximum uncertainty

Table of Appendix 23: Yields of ethane and ethene along with respective maximum and standard uncertainties for experiments with argon as dilution gas and nominal furnace temperatures of 1400 °C, 1500 °C, and 1600 °C

Set	$Y_{C_2H_6}$ in %				$Y_{C_2H_4}$ in %			
1400 - 700 - 2	0	0	0	0	0.5509	0.07239	0.2976	-0.2061
1400 - 700 - 5	0	0	0	0	1.254	0.06496	0.2511	-0.2844
1400 - 700 - 10	0	0	0	0	1.885	0.07017	0.3366	-0.2986
1400 - 1400 - 2	0.003151	0.002818	0.01267	-0.003151	0.3387	0.03696	0.1402	-0.1074
1400 - 1400 - 5	0.007131	0.002657	0.00977	-0.005311	0.7959	0.09221	0.3175	-0.2765
1400 - 1400 - 10	0.003977	0.001208	0.00516	-0.002086	1.585	0.1595	0.5790	-0.5276
1400 - 2600 - 2	0.1376	0.04532	0.1862	-0.07365	1.232	0.1476	0.5206	-0.4106
1400 - 2600 - 5	0.02749	0.006741	0.02920	-0.01136	1.144	0.1294	0.4440	-0.4030
1400 - 2600 - 10	0.02853	0.009400	0.03920	-0.01536	1.518	0.1538	0.5256	-0.4911
1400 - 3800 - 2	0.2660	0.07736	0.3459	-0.1262	3.967	0.1605	0.7386	-0.6822
1400 - 3800 - 5	0.1649	0.01776	0.07427	-0.04513	2.857	0.08801	0.4134	-0.4106
1400 - 3800 - 10	0.1384	0.01586	0.06179	-0.04250	2.519	0.09055	0.4541	-0.3552
1400 - 6500 - 2	0.9270	0.04428	0.1973	-0.1617	3.031	0.1666	0.5934	-0.6853
1400 - 6500 - 5	0.6821	0.02523	0.1068	-0.1036	2.867	0.07627	0.3423	-0.3607
1400 - 6500 - 7.1	0.6089	0.02132	0.09258	-0.08971	2.785	0.08949	0.4232	-0.3661
1500 - 1600 - 2	0.003479	0.002441	0.01016	-0.003479	0.2810	0.07570	0.3099	-0.1369
1500 - 1600 - 5	0	0	0	0	0.6696	0.07387	0.2746	-0.2313
1500 - 1600 - 10	0.001202	0.0002669	0.001182	-0.0004535	1.211	0.07445	0.3128	-0.2554
1500 - 2800 - 2	0	0	0	0	0.2670	0.07388	0.2920	-0.1338
1500 - 2800 - 5	0	0	0	0	0.5788	0.06182	0.1852	-0.2175
1500 - 2800 - 10	0.002498	0.0008504	0.003635	-0.001291	1.039	0.03545	0.1485	-0.1637
1500 - 4600 - 2	0.04934	0.01690	0.07327	-0.02672	0.9479	0.1177	0.4334	-0.3426
1500 - 4600 - 5	0.02691	0.009111	0.03837	-0.01430	1.046	0.07002	0.2431	-0.2609
1500 - 4600 - 10	0.02510	0.008578	0.03624	-0.01341	1.275	0.04965	0.2237	-0.2001
1500 - 7200 - 2	0.3427	0.04281	0.1519	-0.1193	4.032	0.1805	0.7601	-0.6905
1500 - 7200 - 5	0.2117	0.03001	0.1057	-0.07852	2.943	0.1001	0.4556	-0.4024
1500 - 7200 - 6.3	0.1984	0.02815	0.09983	-0.07388	2.806	0.09371	0.4372	-0.3801
1500 - 9800 - 2	0.8078	0.1046	0.3865	-0.2635	4.036	0.1247	0.4585	-0.6152
1500 - 9800 - 3.1	0.6309	0.07450	0.2569	-0.2083	3.656	0.1038	0.4171	-0.4985
1500 - 9800 - 5	0.5169	0.05458	0.1695	-0.1747	3.315	0.09535	0.4182	-0.4217
1600 - 2000 - 2	0	0	0	0	0.1753	0.04303	0.1682	-0.08384
1600 - 2000 - 5	0	0	0	0	0.4195	0.05258	0.1898	-0.1564
1600 - 2000 - 10	0	0	0	0	0.7946	0.03957	0.1671	-0.1546
1600 - 3350 - 2	0	0	0	0	0.2050	0.05686	0.2249	-0.1021
1600 - 3350 - 5	0	0	0	0	0.4260	0.05043	0.1781	-0.1457
1600 - 3350 - 10	0	0	0	0	0.7928	0.03918	0.1607	-0.1478
1600 - 6500 - 2	0.02206	0.006038	0.02497	-0.01060	0.7013	0.06283	0.2632	-0.1698
1600 - 6500 - 5	0.01513	0.002919	0.01243	-0.005170	0.7764	0.04094	0.1414	-0.1660
1600 - 6500 - 7.1	0.02524	0.007794	0.03309	-0.01203	0.8567	0.03464	0.1136	-0.1665
1600 - 9800 - 2	0.2088	0.06091	0.2583	-0.09609	2.138	0.1158	0.4077	-0.4603
1600 - 9800 - 3	0.1473	0.04467	0.1919	-0.06619	1.915	0.08474	0.2941	-0.3666
1600 - 9800 - 5	0.1188	0.03763	0.1589	-0.05736	1.794	0.05966	0.2427	-0.2657
standard uncertainty / maximum uncertainty								

Table of Appendix 24: Various information about reaction conditions for with helium as dilution gas (nominal furnace temperature in °C - nominal total standard volume flow in sccm - nominal initial molar fraction of methane in %) I

Set	$\dot{V}_{N,He,0}$ in sccm			$\dot{V}_{N,CH_4,0}$ in sccm			$\dot{V}_{N,tot,0}$ in sccm	$x_{CH_4,0}$ in %
1300 - 3800 - 2	3726	45.0	110.2	75.98	1.8	3.9	3802	1.998
1300 - 3800 - 5	3612	44.4	108.6	188.8	2.3	5.5	3801	4.967
1300 - 3800 - 10	3428	43.5	106.0	379.1	3.5	8.2	3807	9.958
1400 - 2800 - 2	2742	25.9	61.6	55.97	0.6	1.4	2798	2.000
1400 - 2800 - 5	2656	25.3	60.4	139.9	2.0	4.8	2796	5.004
1400 - 2800 - 10	2516	24.4	58.4	280.3	2.8	6.8	2796	10.02
1400 - 3800 - 2	3720	45.0	110.1	76.00	0.7	1.6	3796	2.002
1400 - 3800 - 5	3605	44.4	108.5	190.1	2.3	5.5	3795	5.009
1400 - 3800 - 10	3414	43.4	105.8	379.9	3.5	8.2	3794	10.01
1400 - 6500 - 2	6365	61.4	147.1	129.8	2.0	4.7	6495	1.999
1400 - 6500 - 5	6167	60.1	144.3	325.3	3.1	7.4	6492	5.011
1400 - 6500 - 7.1	6044	59.2	142.6	462.6	4.2	9.9	6507	7.110
1500 - 3800 - 2	3724	45.0	110.1	75.86	1.8	3.9	3800	1.996
1500 - 3800 - 5	3619	44.5	108.7	190.3	2.3	5.5	3809	4.996
1500 - 3800 - 10	3429	43.5	106.0	379.9	3.5	8.2	3809	9.974
standard uncertainty / maximum uncertainty								

Table of Appendix 25: Various information about reaction conditions for with helium as dilution gas (nominal furnace temperature in °C - nominal total standard volume flow in sccm - nominal initial molar fraction of methane in %) II

Set	$p_{R,inlet}$ in bar		$p_{R,outlet}$ in bar		τ in s		# Runs
	start	end	start	end			
1300 - 3800 - 2	1.011	1.011	1.012	1.011	0.0344	0.00516	1
1300 - 3800 - 5	1.011	1.012	1.011	1.012	0.0344	0.00516	1
1300 - 3800 - 10	1.012	1.012	1.011	1.011	0.0343	0.00515	3
1400 - 2800 - 2	1.016	1.016	1.008	1.008	0.0441	0.00623	1
1400 - 2800 - 5	1.019	1.021	1.007	1.007	0.0443	0.00630	1
1400 - 2800 - 10	1.019	1.022	1.017	1.017	0.0443	0.00630	1
1400 - 3800 - 2	1.020	1.020	1.011	1.011	0.0326	0.00487	1
1400 - 3800 - 5	1.021	1.022	1.011	1.011	0.0327	0.00490	1
1400 - 3800 - 10	1.025	1.032	1.020	1.020	0.0329	0.00494	1
1400 - 6500 - 2	1.015	1.015	1.012	1.012	0.0190	0.00270	2
1400 - 6500 - 5	1.014	1.014	1.012	1.012	0.0190	0.00270	1
1400 - 6500 - 7.1	1.014	1.014	1.011	1.011	0.0189	0.00269	1
1500 - 3800 - 2	1.004	1.004	1.003	1.004	0.0303	0.00455	1
1500 - 3800 - 5	1.005	1.007	1.004	1.004	0.0303	0.00454	1
1500 - 3800 - 10	1.008	1.014	1.004	1.004	0.0304	0.00457	1
maximum uncertainty							

Table of Appendix 26: Conversion of methane as well as yields of hydrogen and ethyne along with respective maximum and standard uncertainties for experiments with helium as dilution gas

Set	X_{CH_4} in %				Y_{H_2} in %				$Y_{C_2H_2}$ in %			
1300 - 3800 - 2	27.66	3.305	12.36	-15.12	12.32	1.587	7.041	-3.550	11.94	1.532	6.067	-4.040
1300 - 3800 - 5	28.66	2.920	10.88	-12.89	18.35	0.8927	3.797	-3.124	13.04	1.398	5.659	-3.435
1300 - 3800 - 10	29.27	2.939	10.21	-11.89	18.70	0.7316	2.984	-2.580	11.65	1.146	4.508	-2.839
1400 - 2800 - 2	87.70	0.9724	3.001	-3.366	74.14	2.914	12.10	-10.46	57.62	4.837	18.93	-12.64
1400 - 2800 - 5	88.99	0.5118	1.801	-2.172	83.86	2.660	12.46	-10.53	26.58	2.396	9.766	-6.225
1400 - 2800 - 10	86.88	0.4214	1.605	-1.890	80.41	2.666	11.82	-10.08	27.41	1.570	5.860	-5.223
1400 - 3800 - 2	76.28	1.882	5.872	-6.619	69.57	3.073	12.75	-10.75	58.58	5.830	22.45	-14.94
1400 - 3800 - 5	80.83	0.6809	2.654	-3.125	73.41	2.577	12.89	-9.194	40.84	5.313	20.47	-12.92
1400 - 3800 - 10	80.12	0.9446	3.252	-3.900	68.67	2.379	10.63	-9.061	28.05	1.624	6.188	-5.469
1400 - 6500 - 2	56.21	1.635	6.168	-7.357	43.32	1.898	8.262	-6.779	37.22	2.768	10.43	-8.727
1400 - 6500 - 5	55.31	1.882	6.583	-7.756	43.03	1.484	6.343	-5.613	32.67	3.220	11.62	-8.727
1400 - 6500 - 7.1	53.11	2.015	6.971	-8.200	41.28	1.313	5.711	-5.048	30.27	3.210	11.90	-8.119
1500 - 3800 - 2	98.09	0.1449	0.4613	-0.6041	80.45	3.722	16.87	-13.97	62.50	5.733	24.63	-15.98
1500 - 3800 - 5	97.60	0.1843	0.5617	-0.7102	91.10	2.903	8.896	-11.66	31.61	3.193	11.93	-8.922
1500 - 3800 - 10	96.15	0.2983	0.8543	-1.028	83.84	3.824	13.00	-10.96	37.08	2.410	8.144	-7.226
standard uncertainty / maximum uncertainty												

Table of Appendix 27: Yields of ethane and ethene along with respective maximum and standard uncertainties for experiments with helium as dilution gas

Set	$Y_{C_2H_6}$ in %				$Y_{C_2H_4}$ in %			
1300 - 3800 - 2	0.6523	0.09196	0.3531	-0.2425	5.627	0.2265	0.9929	-0.9298
1300 - 3800 - 5	0.4182	0.05071	0.1705	-0.1483	4.267	0.1423	0.6731	-0.5588
1300 - 3800 - 10	0.3475	0.02663	0.08381	-0.09158	3.583	0.1575	0.7060	-0.4738
1400 - 2800 - 2	0.006659	0.002191	0.008834	-0.003525	0.5848	0.06730	0.2349	-0.1800
1400 - 2800 - 5	0.003452	0.001137	0.004670	-0.001844	0.6314	0.07455	0.2553	-0.2138
1400 - 2800 - 10	0.006802	0.002430	0.01001	-0.003667	1.172	0.04527	0.1889	-0.1664
1400 - 3800 - 2	0.02281	0.007510	0.03050	-0.01212	0.8611	0.0996	0.3526	-0.2677
1400 - 3800 - 5	0.01514	0.004985	0.02053	-0.008105	0.9308	0.1064	0.3549	-0.3201
1400 - 3800 - 10	0.02167	0.007374	0.03103	-0.01094	1.192	0.03440	0.1345	-0.1623
1400 - 6500 - 2	0.1663	0.05841	0.2456	-0.08926	3.324	0.1746	0.6862	-0.6263
1400 - 6500 - 5	0.1450	0.02173	0.07465	-0.05463	2.843	0.09745	0.4158	-0.3706
1400 - 6500 - 7.1	0.1493	0.02249	0.07703	-0.05632	2.846	0.08876	0.3893	-0.3425
1500 - 3800 - 2	0	0	0	0	0.2893	0.08084	0.3377	-0.1474
1500 - 3800 - 5	0	0	0	0	0.3583	0.04527	0.1627	-0.1214
1500 - 3800 - 10	0.0006207	0.0002132	0.0008924	-0.0003158	0.8666	0.03964	0.1089	-0.1365
standard uncertainty / maximum uncertainty								

Table of Appendix 28: Profiles of temperatures related to the thermocouple in wall position (WP) and center position (CP) for a nominal furnace temperature of 1200 °C determined in experiments with argon as dilution gas

$\dot{V}_{N,Ar,nominal}$		95				200				350				685				2000				sccm
$\dot{V}_{N,Ar,actual}$		94.86				200.1				349.2				684.7				2001				sccm
$\overline{p}_{R,inlet}$		1.009				1.015				1.012				1.012				1.024				bar
$\overline{p}_{R,outlet}$		1.003				1.005				1.014				1.000				1.009				bar
z in mm	620	**40**	5	**40**	5	**40**	5	**40**	5	**26**	5	**26**	5	**40**	5	**40**	5	**40**	5	**40**	5	
	600	53		53		47		47		36		36		52		52		56		58		
	580	73		73		57		57		53		54		72		73		86		90		
	560	102		102		71		71		77		80		100		101		126		133		
	540	137		137		91		91		108		113		135		137		176		187		
	520	180		180		116		116		147		153		177		179		234		250		
	500	230		230		147		147		192		200		226		228		299		319		
	480	285		285		186		186		244		254		281		284		370		394		
	460	347		347		232		232		303		314		341		346		446		474		
	440	414		414		287		287		368		381		408		413		524		556		
	420	485		485		352		352		440		453		480		486		604		638		
	400	562		562		426		426		518		531		557		564		684		721		
	380	643		643		512		512		602		615		639		647		764		801		
	360	728		728		609		609		692		704		726		733		841		878		
	340	816		816		718		718		788		797		817		824		915		950		
	320	**907**	7	**907**	7	**840**	10	**840**	10	**889**	8	**896**	10	**911**	8	**919**	10	**981**	6	**1014**	14	
	300	**1001**	7	**1001**	7	**976**	10	**976**	10	**996**	8	**999**	9	**1009**	8	**1017**	10	**1048**	6	**1072**	12	
	280	**1066**	6	**1066**	6	**1054**	7	**1054**	7	**1063**	6	**1064**	6	**1076**	6	**1082**	8	**1101**	5	**1120**	10	
	260	**1123**	6	**1123**	6	**1115**	6	**1116**	6	**1122**	6	**1123**	6	**1128**	5	**1131**	6	**1145**	5	**1154**	7	
	240	**1167**	5	**1167**	5	**1161**	5	**1162**	5	**1166**	5	**1168**	6	**1169**	5	**1171**	5	**1178**	5	**1181**	5	
	220	**1189**	4	**1189**	4	**1186**	4	**1187**	5	**1190**	4	**1190**	4	**1191**	4	**1192**	4	**1194**	4	**1194**	4	
	200	**1202**	4	**1202**	4	**1200**	4	**1200**	4	**1204**	4	**1204**	4	**1204**	4	**1205**	4	**1203**	4	**1200**	4	
	180	**1209**	3	**1209**	3	**1208**	3	**1208**	3	**1211**	3	**1211**	3	**1211**	3	**1212**	4	**1206**	3	**1202**	4	
	160	**1213**	3	**1213**	3	**1212**	3	**1212**	3	**1215**	3	**1215**	3	**1215**	3	**1215**	3	**1206**	3	**1199**	5	
	140	**1215**	3	**1215**	3	**1215**	3	**1214**	3	**1217**	3	**1216**	3	**1217**	3	**1217**	3	**1202**	3	**1190**	7	
	120	**1215**	3	**1215**	3	**1214**	3	**1214**	3	**1217**	3	**1216**	3	**1216**	3	**1216**	3	**1195**	4	**1177**	8	
	100	**1213**	3	**1213**	3	**1212**	3	**1212**	3	**1214**	3	**1214**	3	**1213**	3	**1213**	3	**1184**	4	**1158**	11	
	80	**1208**	3	**1208**	3	**1208**	3	**1208**	3	**1210**	3	**1209**	4	**1207**	4	**1206**	4	**1169**	4	**1135**	13	
	60	**1200**	4	**1200**	4	**1200**	4	**1200**	4	**1202**	4	**1201**	4	**1197**	4	**1195**	5	**1145**	4	1106		
	40	**1186**	4	**1186**	4	**1186**	4	**1186**	4	**1186**	4	**1185**	5	**1179**	4	**1175**	5	1116		**1054**	21	
	20	**1162**	5	**1162**	5	**1161**	5	**1160**	5	**1160**	5	**1157**	6	**1150**	5	**1145**	7	**1068**	6	991		
	0	**1124**	6	**1124**	6	**1118**	7	**1118**	7	**1116**	6	**1112**	7	**1103**	7	**1095**	9	**1001**	7	**913**	30	
	-20	1053		1053		1044		1044		1042		1038		1026		1016		909		818		
	-40	955		955		945		945		945		940		926		915		805		718		
	-60	837		837		827		827		830		826		809		798		693		613		
	-80	707		707		697		697		705		701		680		671		577		507		
	-100	571		571		562		562		574		571		548		540		460		403		
	-120	436		436		429		429		445		442		417		411		349		305		
	-140	308		308		303		303		324		322		295		290		246		216		
	-160	196		196		192		192		216		215		187		184		157		140		
	-180	105		105		103		103		129		128		100		99		86		79		
	-200	42		42		42		42		68		67		41		41		38		37		
	-213	**20**	6	**20**	6	**20**	6	**20**	6	**45**	6	**45**	6	**20**	6	**20**	6	**20**	6	**20**	6	

T_{TC-WP} in °C

T_{TC-CP} in °C

measured
3rd order polynomial fit
smoothed

maximum uncertainty in K

switching point

Table of Appendix 29: Profiles of temperatures related to the thermocouple in wall position (WP) and center position (CP) for a nominal furnace temperature of 1300 °C determined in experiments with argon as dilution gas

$\dot{V}_{N,Ar,nominal}$	340				650				1300				2600				4800				sccm
$\dot{V}_{N,Ar,actual}$	339.4				649.2				1301				2599				4800				sccm
$\overline{p}_{R,inlet}$	1.010				1.009				1.019				1.016				1.013				bar
$\overline{p}_{R,outlet}$	1.010				1.009				1.019				1.013				1.009				bar
z in mm	T_{TC-WP} in °C		T_{TC-CP} in °C		T_{TC-WP} in °C		T_{TC-CP} in °C		T_{TC-WP} in °C		T_{TC-CP} in °C		T_{TC-WP} in °C		T_{TC-CP} in °C		T_{TC-WP} in °C		T_{TC-CP} in °C		
620	**23**	5	**23**	5	**20**	5	**20**	5	**20**	5	**20**	5	**31**	5	**31**	5	**57**	6	**57**	6	
600	35		36		33		33		34		35		50		51		80		82		
580	57		58		57		58		61		63		83		87		118		122		
560	88		90		92		93		100		103		129		135		168		174		
540	127		130		137		139		149		153		185		194		229		238		
520	175		179		191		193		207		213		250		263		300		310		
500	230		236		252		256		273		281		323		340		377		390		
480	292		299		321		325		346		356		402		424		459		474		
460	361		370		395		400		425		437		487		512		545		562		
440	437		446		475		481		508		522		574		602		632		651		
420	518		527		560		566		595		610		663		694		719		739		
400	604		614		647		654		685		701		752		785		804		825		
380	695		704		738		745		775		792		840		874		886		906		
360	790		799		830		837		866		883		926		960		961		981		
340	889		896		923		930		956		972		1007		1039		1029		1046		
320	**991**	8	**996**	9	**1016**	7	**1022**	9	**1043**	7	**1058**	11	**1082**	7	**1111**	14	**1087**	6	**1106**	11	
300	**1096**	8	**1098**	8	**1108**	7	**1113**	9	**1127**	7	**1140**	10	**1150**	6	**1174**	12	**1138**	5	**1134**	6	
280	**1164**	6	**1165**	7	**1170**	6	**1176**	8	**1182**	6	**1192**	8	**1197**	5	**1212**	9	**1177**	5	**1168**	7	
260	**1222**	6	**1223**	6	**1224**	6	**1227**	6	**1234**	6	**1241**	7	**1240**	5	**1246**	6	**1209**	5	**1190**	9	
240	**1262**	5	**1263**	5	**1263**	5	**1264**	5	**1267**	5	**1271**	6	**1269**	5	**1268**	5	**1230**	4	**1198**	12	
220	**1284**	4	**1285**	5	**1284**	4	**1284**	4	**1287**	4	**1288**	4	**1282**	4	**1279**	5	**1238**	4	**1187**	16	
200	**1297**	4	**1297**	4	**1296**	4	**1295**	4	**1297**	4	**1297**	4	**1289**	4	**1287**	4	**1240**	3	1175		
180	**1304**	4	**1304**	4	**1302**	4	**1302**	4	**1303**	4	**1303**	4	**1290**	3	**1287**	4	**1236**	4	**1174**	19	
160	**1308**	4	**1308**	4	**1306**	4	**1305**	4	**1305**	3	**1305**	3	**1289**	4	**1282**	6	**1224**	4	1180		
140	**1309**	3	**1309**	3	**1307**	3	**1307**	3	**1306**	4	**1305**	4	**1284**	4	**1264**	9	**1213**	4	**1177**	14	
120	**1309**	3	**1309**	3	**1306**	3	**1306**	4	**1303**	4	**1302**	4	**1274**	4	**1251**	10	**1197**	4	**1134**	22	
100	**1307**	4	**1307**	4	**1304**	4	**1303**	4	**1299**	4	**1296**	5	**1260**	4	**1230**	13	**1178**	4	**1063**	35	
80	**1303**	4	**1303**	4	**1299**	4	**1298**	4	**1291**	4	**1285**	6	**1243**	4	**1186**	19	**1152**	4	**1011**	43	
60	**1295**	4	**1294**	4	**1290**	4	**1288**	5	**1277**	4	**1268**	7	**1221**	5	**1145**	24	**1133**	5	**918**	61	
40	**1281**	5	**1280**	5	**1274**	5	**1270**	6	**1254**	5	**1235**	10	**1183**	5	**1101**	27	**1092**	5	826		
20	**1256**	5	**1255**	6	**1247**	5	**1242**	7	**1218**	6	**1193**	13	**1138**	7	1030		**1042**	6	736		
0	**1213**	8	**1211**	8	**1201**	8	**1193**	10	**1157**	8	**1124**	16	**1059**	8	**946**	36	**972**	7	648		
-20	1124		1122		1111		1103		1055		1022		964		853		889		564		
-40	1014		1012		1000		992		942		908		856		750		796		483		
-60	885		883		872		864		816		784		739		642		695		407		
-80	746		744		733		725		683		655		618		533		590		336		
-100	601		600		589		583		548		524		498		427		485		272		
-120	459		458		449		444		418		399		382		326		384		214		
-140	326		325		317		313		296		282		275		234		290		163		
-160	209		208		201		199		190		181		182		155		206		120		
-180	114		113		108		106		104		99		107		92		136		87		
-200	48		48		44		43		45		43		55		49		83		62		
-213	**23**	6	**23**	6	**20**	6	**20**	6	**20**	6	**20**	6	**34**	6	**34**	6	**52**	7	**52**	5	

measured
3rd order polynomial fit
smoothed

maximum uncertainty in K

switching point

Table of Appendix 30: Profiles of temperatures related to the thermocouple in wall position (WP) and center position (CP) for a nominal furnace temperature of 1400 °C determined in experiments with argon as dilution gas

$\dot{V}_{N,Ar,nominal}$		700				1400				2600				3800				6500				sccm
$\dot{V}_{N,Ar,actual}$		701.3				1399.0				2603				3795				6501				sccm
$\overline{p}_{R,inlet}$		1.005				1.012				1.031				1.024				1.065				bar
$\overline{p}_{R,outlet}$		1.007				1.000				1.014				1.002				1.036				bar
z in mm	620	**27**	5	**27**	5	**60**	6	**60**	6	**60**	6	**60**	6	**60**	6	**60**	6	**60**	6	**60**	6	
	600	43		43		83		83		84		86		86		89		85		87		
	580	75		76		120		121		123		127		127		133		126		130		
	560	121		122		169		172		174		182		181		191		180		187		
	540	178		180		230		235		237		249		248		261		247		256		
	520	245		248		300		306		310		325		324		341		322		335		
	500	321		325		378		386		390		409		408		429		406		421		
	480	404		409		462		472		477		500		497		523		495		512		
	460	492		499		550		562		568		594		591		620		587		606		
	440	584		592		642		655		661		691		687		719		680		700		
	420	679		687		735		749		756		788		783		817		773		791		
	400	774		783		827		843		849		883		877		912		863		879		
	380	868		877		918		934		940		974		967		1002		948		960		
	360	960		969		1005		1021		1027		1060		1051		1086		1027		1032		
	340	1048		1056		1087		1103		1108		1139		1128		1160		1096		1092		
	320	**1125**	7	**1132**	9	**1162**	7	**1177**	10	**1181**	7	**1210**	14	**1198**	7	**1227**	14	**1155**	6	**1142**	9	
	300	**1211**	7	**1218**	9	**1230**	7	**1243**	10	**1245**	6	**1265**	11	**1250**	6	**1270**	10	**1198**	5	**1165**	12	
	280	**1271**	6	**1275**	7	**1286**	6	**1296**	8	**1294**	6	**1307**	9	**1292**	5	**1299**	7	**1230**	5	**1185**	15	
	260	**1325**	6	**1326**	6	**1332**	6	**1339**	7	**1337**	6	**1342**	6	**1323**	5	**1327**	6	**1261**	5	**1191**	21	
	240	**1360**	5	**1362**	6	**1366**	5	**1370**	6	**1365**	5	**1365**	5	**1338**	5	**1350**	8	**1280**	4	**1208**	22	
	220	**1380**	5	**1380**	4	**1383**	4	**1384**	5	**1379**	4	**1377**	5	**1360**	5	**1358**	4	**1284**	4	1196		
	200	**1391**	4	**1391**	4	**1393**	4	**1393**	4	**1386**	4	**1379**	5	**1362**	4	**1353**	7	**1283**	3	**1171**	32	
	180	**1398**	4	**1397**	4	**1398**	4	**1398**	4	**1388**	4	**1376**	7	**1359**	4	1333		**1284**	4	**1148**	38	
	160	**1401**	4	**1401**	4	**1401**	4	**1400**	4	**1386**	4	**1374**	7	**1351**	4	**1304**	17	1276	1	**1121**	44	
	140	**1402**	4	**1402**	4	**1401**	4	**1400**	4	**1382**	4	**1369**	7	**1337**	4	**1275**	20	**1262**	4	1072		
	120	**1402**	4	**1402**	4	**1399**	4	**1397**	4	**1374**	4	**1358**	9	**1323**	4	**1247**	24	**1248**	4	**1017**	63	
	100	**1400**	4	**1399**	4	**1394**	4	**1392**	5	**1364**	5	1334		**1303**	4	**1210**	28	**1232**	5	971		
	80	**1395**	4	**1394**	4	**1385**	4	**1378**	6	**1342**	5	**1298**	17	**1281**	5	**1176**	32	**1195**	5	**923**	74	
	60	**1387**	4	**1386**	5	**1371**	5	**1359**	8	**1320**	5	**1252**	23	**1253**	5	**1115**	40	**1159**	5	**859**	81	
	40	**1370**	5	**1368**	6	**1348**	5	**1330**	10	**1293**	6	1209		**1215**	6	**1054**	47	**1113**	6	**805**	83	
	20	**1344**	6	**1339**	7	**1311**	6	**1287**	13	**1243**	7	**1144**	32	**1158**	7	**981**	52	1039	7	731	84	
	0	**1299**	7	**1293**	9	**1251**	8	**1216**	17	**1175**	8	**1052**	39	**1086**	8	**876**	61	953	8	656	81	
	-20	1218		1211		1152		1107		1068		951		982		768		855		578		
	-40	1108		1101		1032		986		950		836		869		659		749		499		
	-60	977		971		897		852		820		715		748		552		638		420		
	-80	831		826		751		712		684		591		622		448		526		344		
	-100	680		675		602		570		548		468		497		351		417		271		
	-120	529		525		457		433		416		352		376		262		314		205		
	-140	386		384		322		306		294		247		266		183		221		145		
	-160	259		258		204		196		188		156		170		117		141		95		
	-180	155		155		109		107		102		84		94		66		78		56		
	-200	82		82		45		45		43		36		41		32		35		30		
	-213	**54**	7	**54**	7	**20**	6	**20**	6	**20**	6	**20**	6	**20**	6	**20**	5	**20**	6	**20**	5	

T_{TC-WP} in °C

T_{TC-CP} in °C

measured
3rd order polynomial fit
smoothed

maximum uncertainty in K

switching point

Table of Appendix 31: Profiles of temperatures related to the thermocouple in wall position (WP) and center position (CP) for a nominal furnace temperature of 1500 °C determined in experiments with argon as dilution gas

$\dot{V}_{N,Ar,nominal}$	1600				2800				4600				7200				9800				sccm
$\dot{V}_{N,Ar,actual}$	1600				2800				4597				7194				9780				sccm
$\overline{p}_{R,inlet}$	0.984				1.004				1.016				1.011				1.027				bar
$\overline{p}_{R,outlet}$	0.984				0.996				1.012				1.002				1.009				bar
z in mm	T_{TC-WP} in °C		T_{TC-CP} in °C		T_{TC-WP} in °C		T_{TC-CP} in °C		T_{TC-WP} in °C		T_{TC-CP} in °C		T_{TC-WP} in °C		T_{TC-CP} in °C		T_{TC-WP} in °C		T_{TC-CP} in °C		
620	**24**	5	**24**	6	**30**	6	**30**	6	**37**	6	**37**	6	**66**	6	**66**	6	**94**	6	**94**	6	
600	45		47		54		55		63		63		96		97		126		127		
580	84		88		95		99		107		107		143		143		171		177		
560	139		145		153		160		166		167		203		205		227		239		
540	207		215		224		236		239		240		275		279		294		312		
520	286		297		307		323		323		325		356		363		368		393		
500	375		389		399		419		416		418		445		454		450		480		
480	471		487		498		523		516		519		539		550		536		570		
460	573		591		602		631		620		624		637		649		625		659		
440	677		698		708		741		726		731		736		748		715		747		
420	783		805		816		851		832		837		835		845		804		830		
400	888		911		921		958		936		942		931		938		892		905		
380	990		1013		1023		1061		1036		1041		1022		1024		975		970		
360	1087		1110		1118		1156		1128		1134		1106		1101		1053		1022		
340	1177		1198		1206		1240		1212		1218		1181		1167		1123		1060		
320	**1257**	7	**1278**	13	**1286**	7	**1316**	15	**1288**	7	**1292**	8	**1251**	7	**1223**	13	**1188**		**1079**	31	
300	**1331**	7	**1340**	9	**1346**	6	**1371**	13	**1341**	6	**1348**	8	**1291**	5	**1245**	16	**1230**	5	**1078**	42	
280	**1383**	6	**1394**	9	**1392**	6	**1405**	9	**1383**	6	**1381**	6	**1326**	5	**1274**	18	1266		1094		
260	**1427**	6	**1429**	6	**1433**	6	**1437**	6	**1417**	5	**1415**	6	**1355**	5	**1281**	23	**1296**	5	**1111**	50	
240	**1462**	6	**1463**	6	**1461**	5	**1462**	5	**1440**	5	**1429**	7	**1373**	4	**1301**	22	1321		1101		
220	**1479**	5	**1479**	5	**1475**	5	**1475**	5	**1449**	4	**1444**	6	**1385**	4	1288		**1335**	4	**1088**	65	
200	**1489**	4	**1488**	5	**1482**	4	**1478**	5	**1452**	4	**1441**	7	**1384**	4	**1267**	35	1337		1084		
180	**1494**	4	**1493**	4	**1484**	4	**1482**	5	**1451**	4	**1433**	9	**1384**	4	**1226**	45	**1325**	5	**1099**	60	
160	**1496**	4	**1496**	4	**1484**	4	**1477**	6	**1447**	5	**1421**	12	**1372**	5	**1174**	55	1303		1084		
140	**1497**	4	**1495**	5	**1480**	4	**1469**	8	**1432**	4	**1379**	19	1348		1126		**1284**	4	1056		
120	**1495**	4	**1492**	5	**1473**	5	**1450**	11	**1424**	4	**1335**	28	**1323**	5	**1081**	66	1267		1017		
100	**1491**	4	**1486**	6	**1458**	5	**1426**	13	**1410**	5	**1288**	37	**1306**	4	1035		**1251**	4	**967**	77	
80	**1483**	5	**1475**	7	**1442**	5	**1392**	18	**1384**	5	**1226**	46	**1289**	4	**989**	80	1232		905		
60	**1469**	5	**1454**	9	**1421**	5	**1351**	24	**1359**	5	**1176**	53	**1267**	5	946		**1211**	4	**838**	100	
40	**1448**	5	**1431**	10	**1389**	6	1298		**1320**	6	1093		**1230**	6	**891**	91	**1188**	5	767		
20	**1417**	7	**1389**	14	**1344**	7	**1222**	38	**1265**	7	1005		**1177**	6	825		**1139**	7	693		
0	**1355**	9	**1315**	19	**1282**	8	1127		**1196**	9	909		**1107**	8	751		1065		617		
-20	1254		1203		1179		1017		1085		807		1005		670		972		541		
-40	1130		1077		1058		896		966		702		893		586		864		466		
-60	987		936		922		769		837		596		773		500		747		393		
-80	833		787		776		640		702		493		648		415		625		324		
-100	674		637		628		513		567		394		522		333		503		259		
-120	519		491		483		393		437		302		402		257		386		199		
-140	374		355		348		283		316		219		291		188		277		147		
-160	246		236		230		189		210		148		193		128		183		103		
-180	143		139		134		113		125		93		114		81		106		68		
-200	72		72		67		61		64		54		59		48		54		43		
-213	**44**	7	**44**	7	**42**	6	**42**	6	**38**	6	**38**	6	**36**	6	**36**	5	**34**	6	**34**	5	

measured
3rd order polynomial fit
smoothed

maximum uncertainty in K

switching point

Table of Appendix 32: Profiles of temperatures related to the thermocouple in wall position (WP) and center position (CP) for a nominal furnace temperature of 1600 °C determined in experiments with argon as dilution gas

$\dot{V}_{N,Ar,nominal}$	2000				3350				6500				9800				sccm
$\dot{V}_{N,Ar,actual}$	2006				3349				6493				9810				sccm
$\overline{p}_{R,inlet}$	1.008				1.041				1.066				1.039				bar
$\overline{p}_{R,outlet}$	1.007				1.024				1.036				1.006				bar
z in mm	T_{TC-WP} in °C		T_{TC-CP} in °C		T_{TC-WP} in °C		T_{TC-CP} in °C		T_{TC-WP} in °C		T_{TC-CP} in °C		T_{TC-WP} in °C		T_{TC-CP} in °C		
620	**27**	6	**27**	6	**80**	6	**80**	6	**80**	6	**80**	6	**140**	6	**140**	6	
600	53		55		113		114		112		113		178		180		
580	97		102		162		165		162		165		228		237		
560	159		167		227		233		228		234		290		308		
540	235		246		305		313		308		317		363		391		
520	323		338		394		405		399		411		443		482		
500	422		439		492		506		499		513		529		579		
480	528		549		596		613		604		621		620		678		
460	640		663		704		724		713		732		714		777		
440	755		780		814		837		824		843		808		873		
420	870		896		924		949		932		952		902		963		
400	983		1010		1032		1058		1037		1055		993		1044		
380	1092		1120		1135		1161		1136		1150		1079		1113		
360	1195		1222		1231		1256		1225		1234		1158		1168		
340	1289		1313		1317		1341		1303		1304		1230		1205		
320	**1373**	8	**1398**	14	**1397**	8	**1418**	13	**1370**	7	**1361**	9	**1295**	7	**1221**	22	
300	**1441**	7	**1455**	10	**1453**	7	**1470**	11	**1411**	6	**1387**	11	**1338**	6	**1214**	34	
280	**1488**	6	**1496**	8	**1494**	6	**1503**	8	**1446**	6	**1408**	14	**1373**	5	**1214**	44	
260	**1531**	6	**1537**	8	**1536**	6	**1533**	6	**1477**	5	**1422**	18	**1400**	5	**1240**	44	
240	**1562**	6	**1562**	5	**1559**	5	**1556**	6	**1499**	5	**1441**	19	**1424**	5	**1247**	48	
220	**1578**	5	**1577**	5	**1571**	5	**1565**	6	**1506**	4	**1427**	25	**1422**	4	**1259**	45	
200	**1587**	5	**1586**	5	**1575**	4	**1563**	7	**1505**	4	**1450**	19	**1418**	4	**1238**	49	
180	**1591**	4	**1591**	4	**1577**	4	**1562**	8	**1499**	5	**1427**	25	**1411**	4	1228		
160	**1594**	4	**1593**	5	**1574**	4	**1554**	10	**1484**	5	**1369**	35	**1400**	4	**1209**	53	
140	**1593**	4	**1592**	5	**1568**	5	**1546**	10	**1471**	5	**1316**	45	**1392**	5	**1160**	63	
120	**1591**	4	**1586**	6	**1556**	5	**1538**	10	**1453**	5	**1262**	54	**1373**	5	**1123**	68	
100	**1587**	5	**1579**	7	**1543**	5	**1518**	12	**1437**	5	**1193**	68	**1362**	4	1077		
80	**1578**	5	**1566**	8	**1530**	5	**1476**	20	**1411**	5	**1111**	82	**1348**	5	**1016**	90	
60	**1563**	5	**1544**	10	**1507**	6	**1419**	30	**1381**	5	**1042**	92	**1326**	5	**935**	105	
40	**1543**	6	**1523**	11	**1466**	6	**1332**	42	**1343**	5	947		**1288**	6	850		
20	**1508**	7	**1474**	17	**1418**	7	**1238**	54	**1310**	7	855		1238		763		
0	**1444**	9	1383		**1346**	10	**1129**	63	1242		759		**1158**	8	674		
-20	1336		1268		1221		1003		1144		663		1051		586		
-40	1203		1132		1088		873		1024		568		932		499		
-60	1052		982		940		740		889		475		802		415		
-80	888		825		786		608		744		386		668		336		
-100	720		666		630		480		596		303		533		262		
-120	555		512		479		360		451		227		404		196		
-140	401		370		340		252		318		161		285		138		
-160	265		245		218		160		200		105		182		90		
-180	155		145		119		88		107		61		99		53		
-200	79		76		50		39		43		32		42		28		
-213	**50**	7	**50**	6	**20**	7	**20**	6	**20**	6	**20**	5	**20**	6	**20**	5	

measured
3rd order polynomial fit
smoothed

maximum uncertainty in K

switching point

Table of Appendix 33: Profiles of temperatures related to the thermocouple in wall position (WP) and center position (CP) determined in experiments with helium as dilution gas

$T_{furnace}$	1300		1400		1400		1400		1500		°C
$\dot{V}_{N,He,nominal}$	3800		2800		3800		6500		3800		sccm
$\dot{V}_{N,He,actual}$	3807		2798		3800		6499		3800		sccm
$\overline{p}_{R,inlet}$	1.026		1.021		1.022		1.024		0.997		bar
$\overline{p}_{R,outlet}$	1.025		1.019		1.019		1.019		0.994		bar

z in mm	T_{TC-WP} in °C		T_{TC-CP} in °C															
620	**24**	5	**24**	5	**23**	5	**23**	6	**20**	5	**20**	6	**37**	6	**37**	6	**23**	6	**23**	6
600	45		45		45		46		42		43		64		64		49		51	
580	80		81		83		85		80		82		106		107		92		95	
560	129		131		136		138		134		136		164		165		151		156	
540	190		192		200		204		200		204		234		236		224		230	
520	260		263		276		281		278		283		315		318		309		316	
500	338		342		360		366		364		370		404		408		403		412	
480	423		428		450		458		457		465		500		504		504		514	
460	512		517		546		555		555		564		599		604		610		621	
440	604		610		644		654		656		666		701		707		719		730	
420	696		704		744		754		758		768		803		809		828		840	
400	788		796		842		853		857		869		902		909		935		947	
380	877		886		937		949		954		965		997		1004		1038		1050	
360	962		971		1028		1039		1045		1056		1085		1092		1134		1146	
340	1040		1050		1112		1122		1128		1139		1165		1172		1222		1233	
320	**1113**	6	**1123**	9	**1190**	7	**1200**	9	**1205**	7	**1215**	9	**1239**	7	**1246**	9	**1303**	7	**1316**	11
300	**1169**	6	**1179**	8	**1250**	6	**1256**	8	**1263**	6	**1272**	8	**1286**	6	**1292**	7	**1360**	6	**1364**	7
280	**1216**	5	**1225**	8	**1300**	6	**1305**	7	**1307**	6	**1312**	7	**1324**	5	**1328**	6	**1405**	6	**1409**	7
260	**1257**	5	**1267**	8	**1344**	6	**1346**	6	**1348**	6	**1352**	7	**1358**	5	**1363**	7	**1445**	6	**1449**	7
240	**1282**	5	**1284**	5	**1371**	5	**1374**	6	**1374**	5	**1376**	5	**1380**	5	**1381**	5	**1471**	5	**1472**	5
220	**1296**	4	**1297**	4	**1387**	4	**1387**	4	**1389**	4	**1389**	4	**1391**	4	**1392**	4	**1485**	5	**1485**	5
200	**1303**	4	**1304**	4	**1396**	4	**1396**	4	**1397**	4	**1397**	4	**1397**	4	**1397**	4	**1493**	4	**1492**	5
180	**1307**	4	**1308**	4	**1401**	4	**1400**	4	**1401**	4	**1401**	4	**1399**	4	**1399**	4	**1497**	4	**1496**	4
160	**1309**	3	**1309**	3	**1403**	4	**1402**	4	**1403**	4	**1402**	4	**1398**	4	**1398**	4	**1498**	4	**1498**	4
140	**1308**	4	**1308**	4	**1403**	4	**1403**	4	**1402**	4	**1402**	4	**1394**	4	**1392**	5	**1498**	4	**1498**	4
120	**1305**	4	**1305**	4	**1402**	4	**1401**	4	**1400**	4	**1400**	4	**1386**	4	**1383**	5	**1497**	4	**1496**	4
100	**1299**	4	**1298**	4	**1398**	4	**1398**	4	**1395**	4	**1394**	4	**1372**	5	**1365**	7	**1492**	4	**1491**	5
80	**1286**	4	**1283**	5	**1392**	4	**1390**	5	**1386**	4	**1383**	5	**1347**	6	**1332**	10	**1485**	5	**1483**	5
60	**1268**	5	**1261**	7	**1380**	5	**1378**	5	**1371**	5	**1366**	7	**1305**	7	**1272**	15	**1470**	5	**1466**	6
40	**1233**	6	**1222**	10	**1359**	5	**1353**	7	**1338**	6	**1329**	9	**1242**	7	**1194**	20	**1444**	6	**1435**	9
20	**1174**	7	**1147**	14	**1321**	7	**1307**	10	**1288**	8	**1265**	13	**1159**	9	**1093**	26	**1395**	7	**1383**	11
0	**1091**	8	1064	15	**1250**	8	**1236**	12	1201		1176		**1042**	9	**965**	28	**1320**	9	**1301**	14
-20	992		962		1145		1129		1095		1068		937		850		1205		1186	
-40	879		849		1024		1008		973		945		818		731		1076		1057	
-60	758		730		891		875		840		814		695		614		934		916	
-80	634		608		749		736		702		679		572		501		784		768	
-100	510		488		606		595		564		544		454		395		633		619	
-120	391		374		467		458		431		415		343		298		486		475	
-140	282		270		338		331		308		296		243		212		350		341	
-160	188		180		224		220		201		193		157		139		231		225	
-180	112		108		132		130		115		111		91		83		134		131	
-200	59		58		67		67		56		54		46		45		67		65	
-213	**40**	6	**40**	6	**41**	6	**41**	6	**33**	6	**33**	6	**32**	5	**32**	5	**39**	7	**39**	6

measured
3rd order polynomial fit
smoothed

maximum uncertainty in K

switching point

Appendix D: Fluid material properties and diffusion

Table of Appendix 34: Material properties of argon partly as a function of the temperature

Material property	Function	Source
Molecular weight	$\frac{M_{\mathrm{Ar}}}{\mathrm{g/mol}} = 39.95$	[VDI, 2006], p. Dca 2
Specific heat capacity at constant pressure	$\frac{c_{\mathrm{p,Ar}}}{\mathrm{J/(kg\ K)}} = 520.3$	[VDI, 2006], p. Dca 23
Dynamic viscosity	$\frac{\eta_{\mathrm{Ar}}}{\mathrm{N\ s/m^2}} = 1.6196 \cdot 10^{-6} + 8.1279 \cdot 10^{-8} \cdot \frac{T}{\mathrm{K}} - 4.1263 \cdot 10^{-11} \cdot \left(\frac{T}{\mathrm{K}}\right)^2 + 1.668 \cdot 10^{-14} \cdot \left(\frac{T}{\mathrm{K}}\right)^3 - 2.76 \cdot 10^{-18} \cdot \left(\frac{T}{\mathrm{K}}\right)^4$	[VDI, 2006], p. Dca 31
Thermal conductivity	$\frac{\lambda_{\mathrm{Ar}}}{\mathrm{W/(m\ K)}} = 4.3 \cdot 10^{-3} + 4.7 \cdot 10^{-5} \cdot \frac{T}{\mathrm{K}} - 7.78 \cdot 10^{-9} \cdot \left(\frac{T}{\mathrm{K}}\right)^2$	[VDI, 2006], p. Dca 39

Table of Appendix 35: Material properties of helium partly as a function of the temperature

Material property	Function	Source
Molecular weight	$\frac{M_{\mathrm{He}}}{\mathrm{g/mol}} = 4.0026$	[Mortimer, 1996], p. 745
Specific heat capacity at constant pressure	$\frac{c_{\mathrm{p,He}}}{\mathrm{J/(kg\ K)}} = 5193.1$	[VDI, 2006], p. Dca 23
Dynamic viscosity	$\frac{\eta_{\mathrm{He}}}{\mathrm{N\ s/m^2}} = 3.9223 \cdot 10^{-6} + 6.13 \cdot 10^{-8} \cdot \frac{T}{\mathrm{K}} - 3.1007 \cdot 10^{-11} \cdot \left(\frac{T}{\mathrm{K}}\right)^2 + 1.479 \cdot 10^{-14} \cdot \left(\frac{T}{\mathrm{K}}\right)^3 - 2.84 \cdot 10^{-18} \cdot \left(\frac{T}{\mathrm{K}}\right)^4$	[VDI, 2006], p. Dca 31
Thermal conductivity	$\frac{\lambda_{\mathrm{He}}}{\mathrm{W/(m\ K)}} = 3.4 \cdot 10^{-2} + 4.57 \cdot 10^{-4} \cdot \frac{T}{\mathrm{K}} - 2.1489 \cdot 10^{-7} \cdot \left(\frac{T}{\mathrm{K}}\right)^2 + 1.0071 \cdot 10^{-10} \cdot \left(\frac{T}{\mathrm{K}}\right)^3 - 1.914 \cdot 10^{-14} \cdot \left(\frac{T}{\mathrm{K}}\right)^4$	[VDI, 2006], p. Dca 39

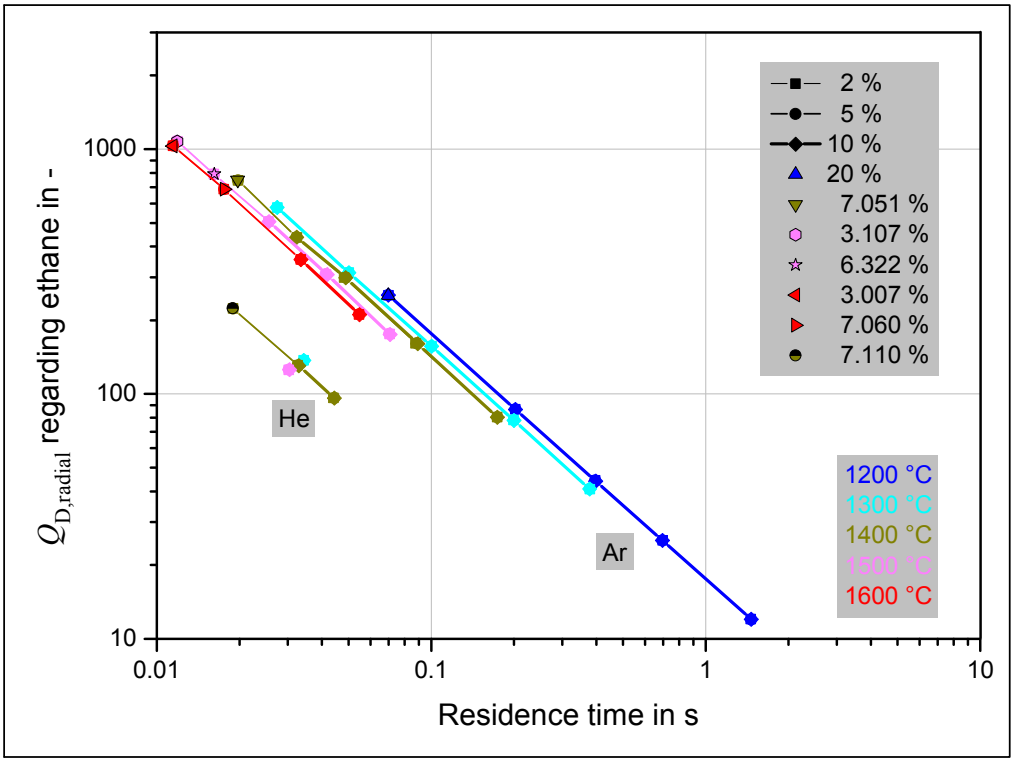

Figure of Appendix 11: Diffusive quotient regarding ethane as a function of the residence time, the nominal furnace temperature, the initial molar fraction of methane, and the dilution gas

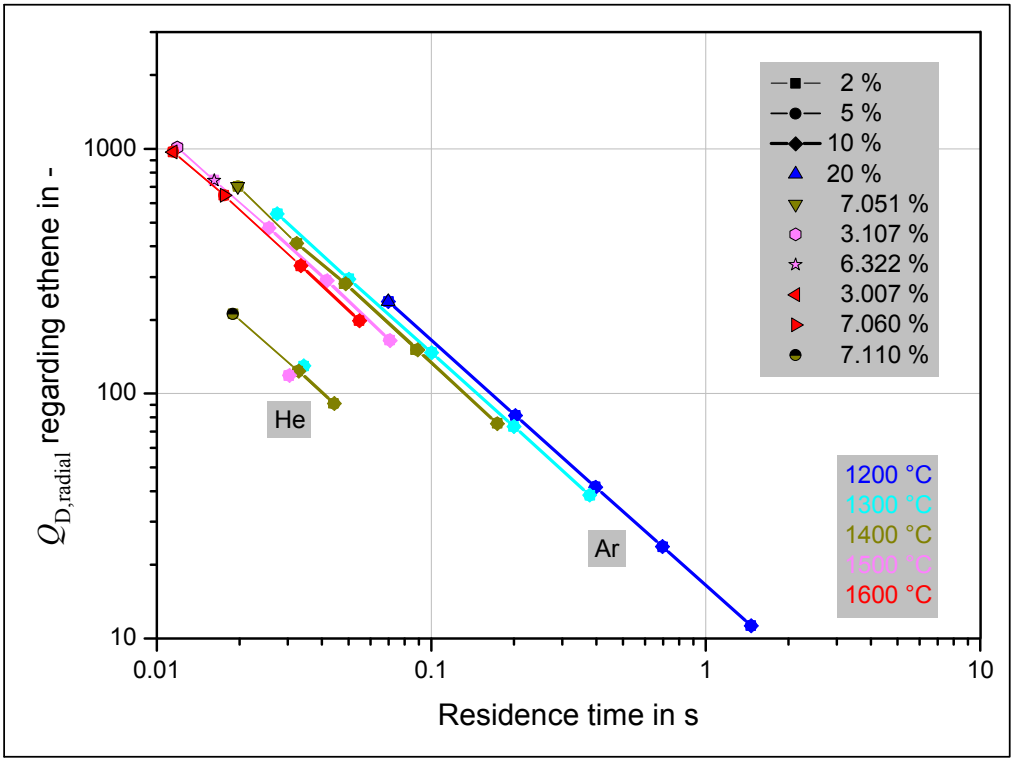

Figure of Appendix 12: Diffusive quotient regarding ethene as a function of the residence time, the nominal furnace temperature, the initial molar fraction of methane, and the dilution gas

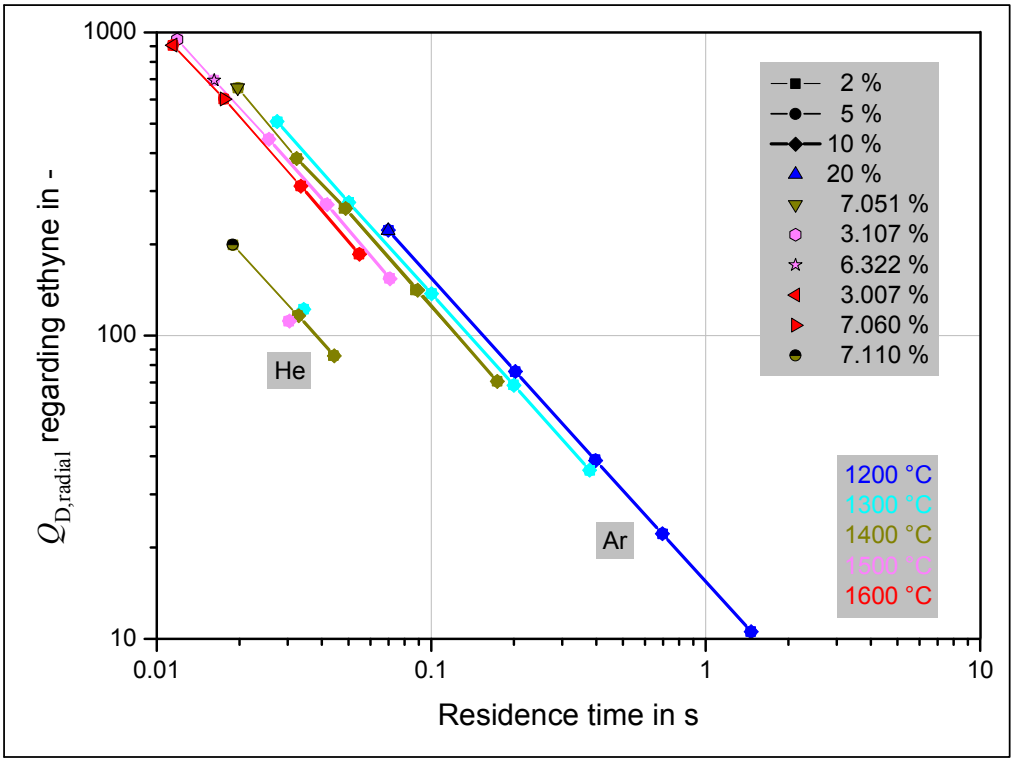

Figure of Appendix 13: Diffusive quotient regarding ethyne as a function of the residence time, the nominal furnace temperature, the initial molar fraction of methane, and the dilution gas

Appendix E: Calculations with ANSYS

Table of Appendix 36: Information about general settings for the calculations with ANSYS 12

Mesh information	
Physical preference Mesh method	CFD Automatic (Patch conforming / Sweeping)
Settings Maximum Body Size Inflation Maximum Layers Transition Growth rate Inflation Algorithm	 4E-04 m 2 Smooth, Transition ratio 0.272 1.2 Pre
Statistics Nodes Elements	 403715 1667453
Domain physics	
Type	Fluid
Material Fluid definition Morphology	Argon Material Library, user defined for reference conditions, pure substance, calorically perfect ideal gas Continuous Fluid
Setting Buoyancy Model Domain Motion Reference Pressure Heat Transfer Model Fluid Temperature Turbulence Model	 Non Buoyant Stationary Reactor inlet pressure Isothermal Reactor inlet temperature Laminar
Boundary physics	
Inlet face (of entrance region) Flow Regime Mass And Momentum Normal Speed	 Subsonic Normal Speed average speed
Outlet face (of entrance region) Flow Regime Mass And Momentum Relative Pressure	 Subsonic Static Pressure 0 bar
Walls (of entrance region) Mass And Momentum	 No Slip Wall
Solver control	
Basic settings Advection Scheme Convergence control Timescale Control Length Scale Option Timescale Factor Convergence Criteria Residual type Residual target Conservation target	 High Resolution Auto timescale Aggressive 1.0 RMS 1E-06 1E-04
Equation Class Settings	Continuity, Momentum
Advanced options	Global Dynamic Model Control

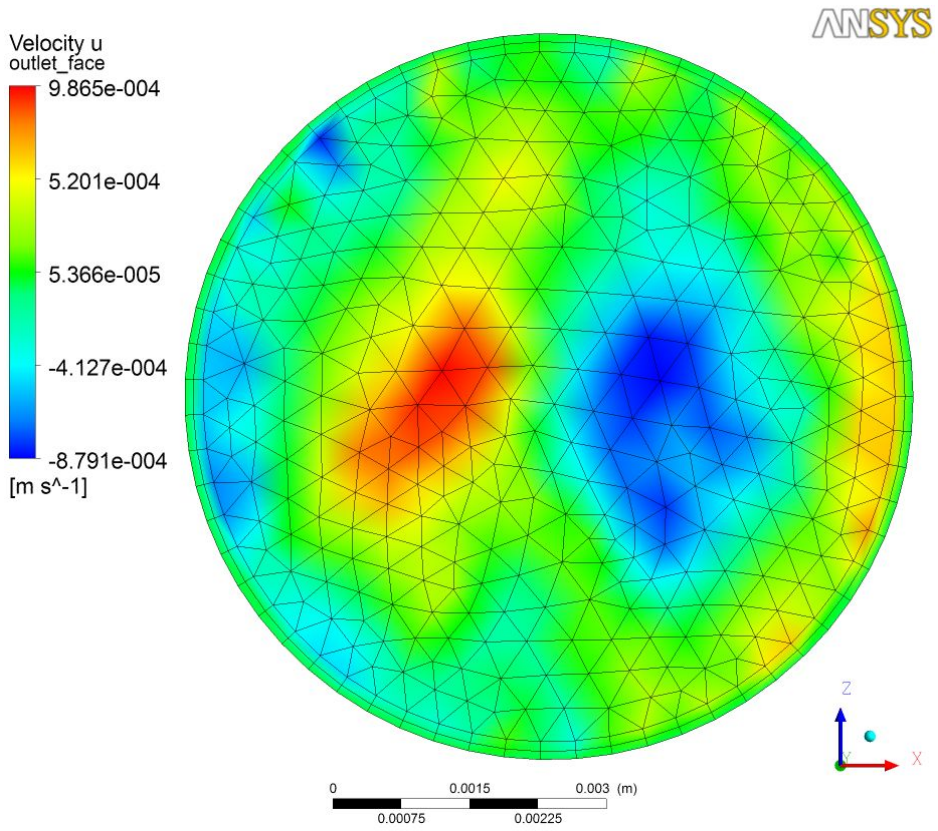

Figure of Appendix 14: Results of flow simulations with ANSYS 12 – Velocity in X-direction (parallel to face) at the reactor inlet for a standard volume flow of 700 sccm Ar

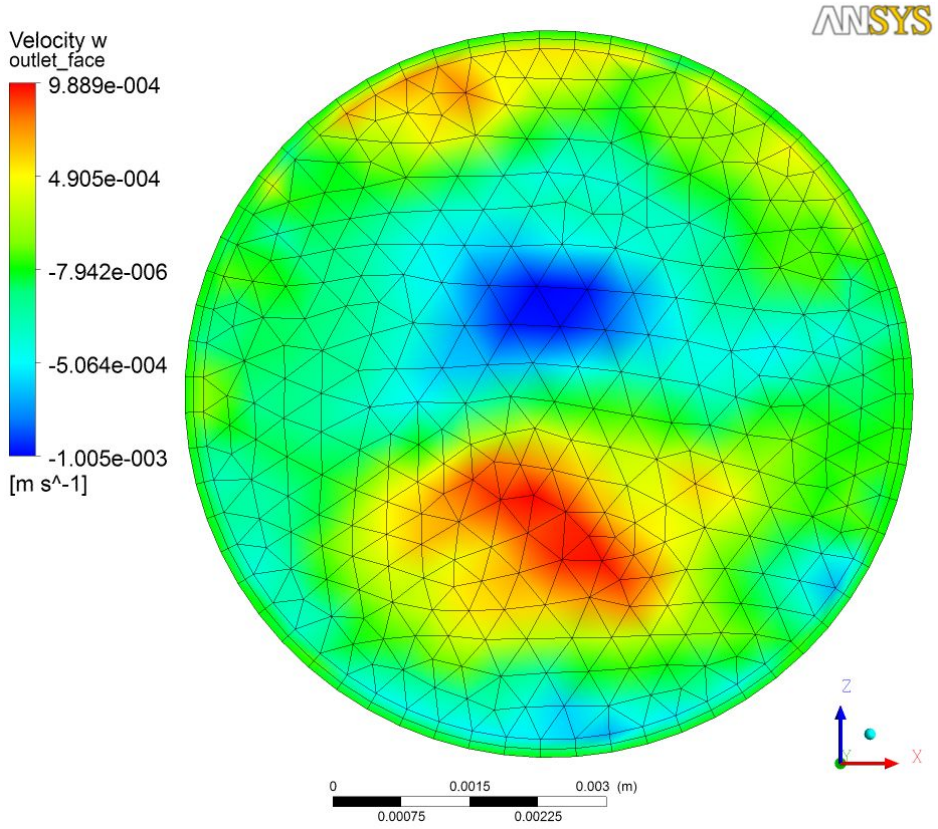

Figure of Appendix 15: Results of flow simulations with ANSYS 12 – Velocity in Z-direction (parallel to face) at the reactor inlet for a standard volume flow of 700 sccm Ar

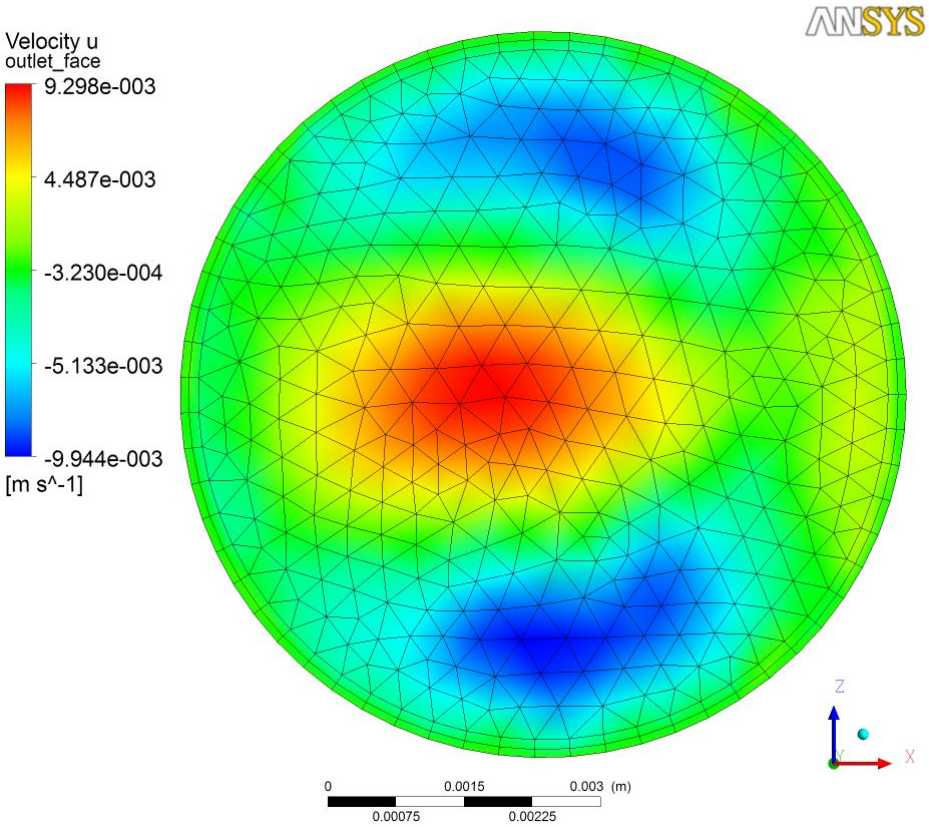

Figure of Appendix 16: Results of flow simulations with ANSYS 12 – Velocity in X-direction (parallel to face) at the reactor inlet for a standard volume flow of 2600 sccm Ar

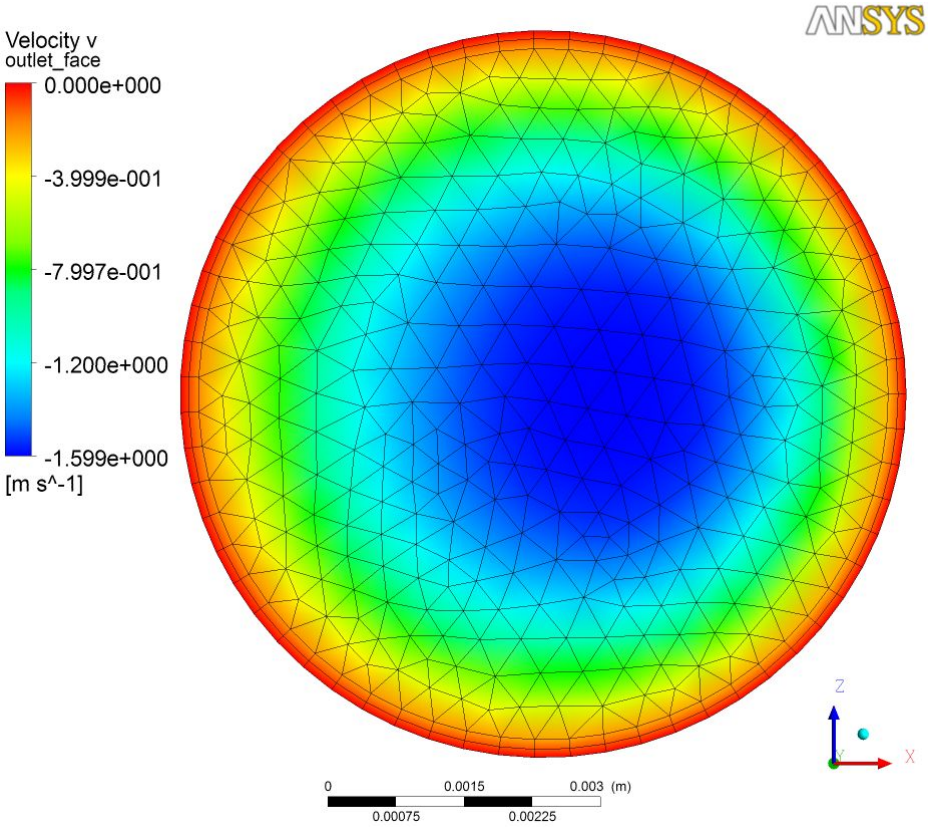

Figure of Appendix 17: Results of flow simulations with ANSYS 12 – Velocity in Y-direction (normal to face) at the reactor inlet for a standard volume flow of 2600 sccm Ar

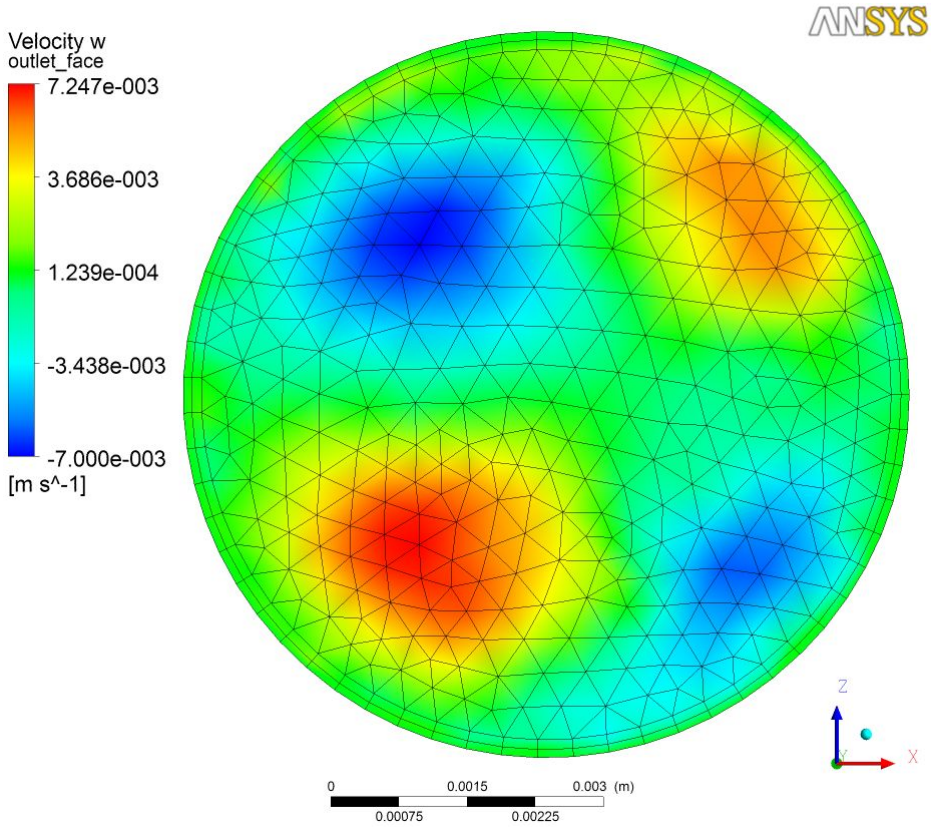

Figure of Appendix 18: Results of flow simulations with ANSYS 12 – Velocity in Z-direction (parallel to face) at the reactor inlet for a standard volume flow of 2600 sccm Ar

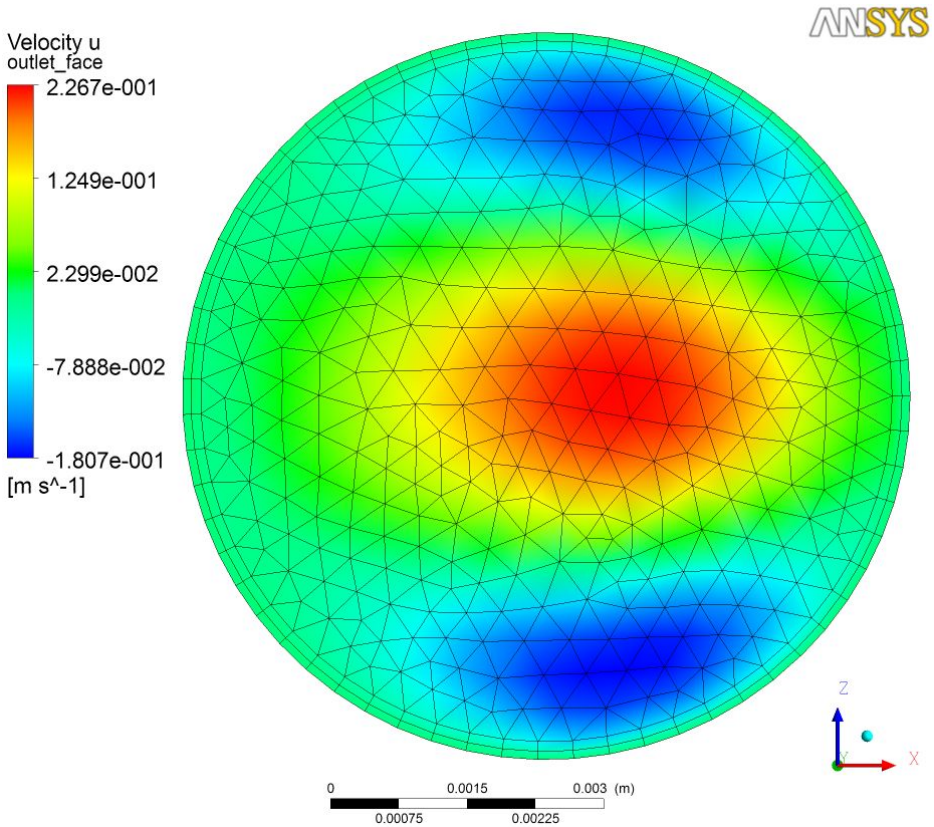

Figure of Appendix 19: Results of flow simulations with ANSYS 12 – Velocity in X-direction (parallel to face) at the reactor inlet for a standard volume flow of 9800 sccm Ar

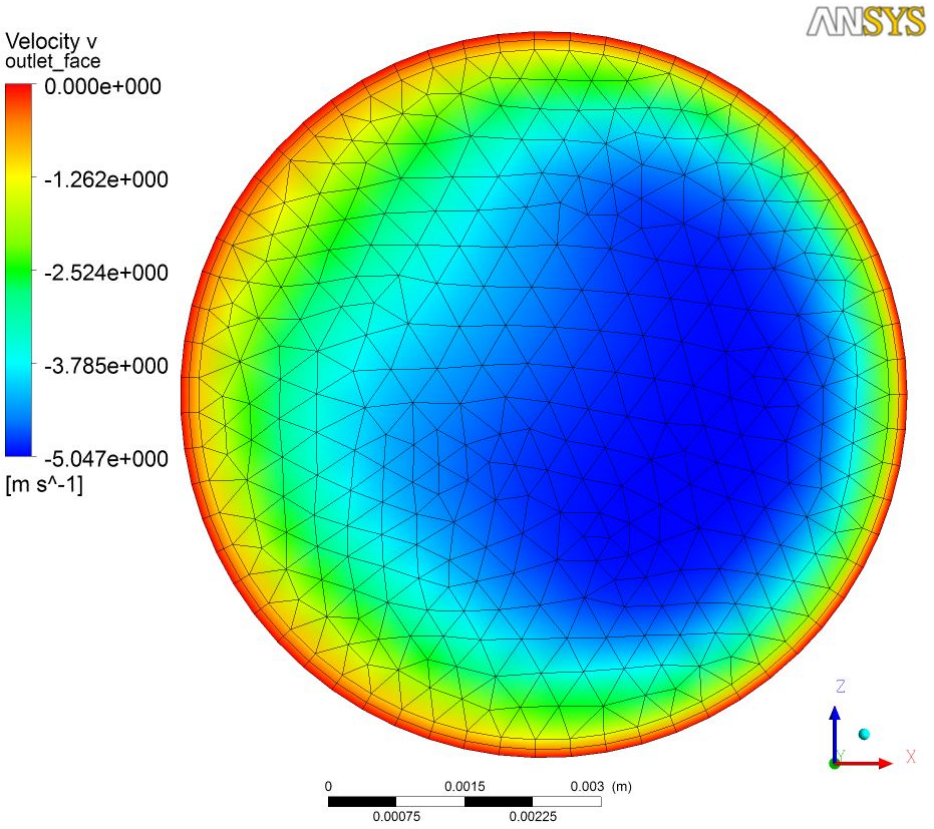

Figure of Appendix 20: Results of flow simulations with ANSYS 12 – Velocity in Y-direction (normal to face) at the reactor inlet for a standard volume flow of 9800 sccm Ar

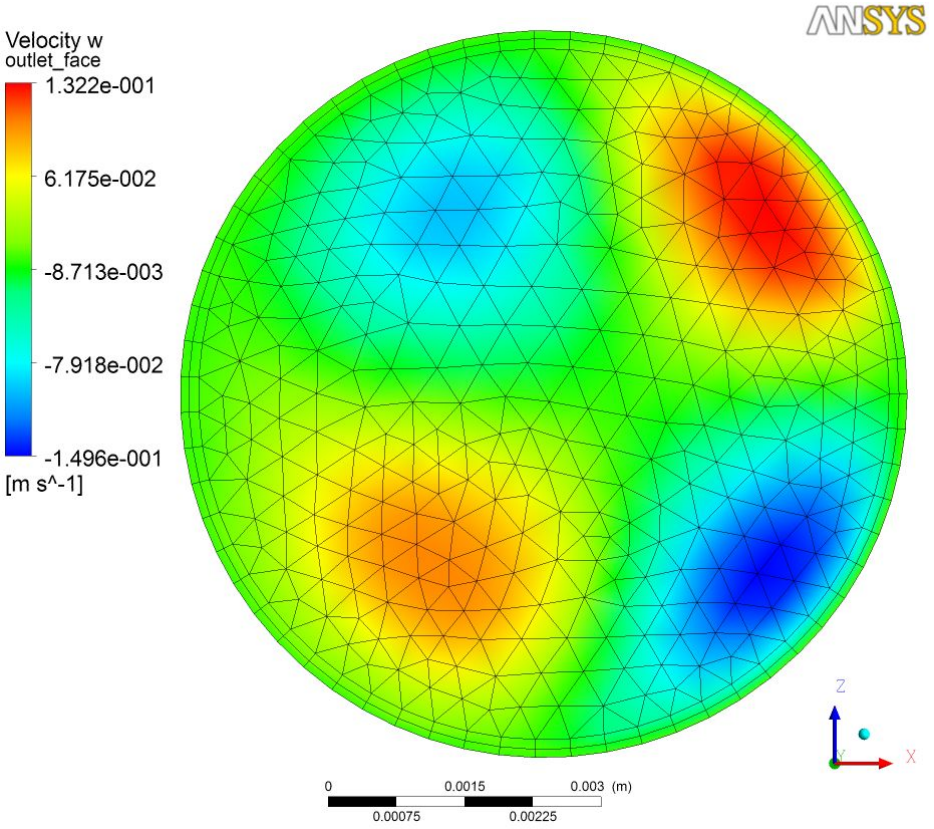

Figure of Appendix 21: Results of flow simulations with ANSYS 12 – Velocity in Z-direction (parallel to face) at the reactor inlet for a standard volume flow of 9800 sccm Ar

Table of Appendix 37: Coefficients of the polynomial fit function for the approximation of averaged velocity profiles at the inlet of the reactor.

$T_{\text{furnace}} / \tau$	k_i in m/(s m^i)						
- set	k_6	k_5	k_4	k_3	k_2	k_1	k_0
5	-1.46961E+15	1.76766E+13	-7.44044E+10	1.18131E+08	-1.23928E+05	3.42689E+01	1.26064E+00
8	-4.40221E+14	4.83776E+12	-1.61002E+10	7.58349E+06	-2.40424E+04	6.62798E+00	8.48611E-01
9	-2.37714E+15	2.97222E+13	-1.33812E+11	2.43183E+08	-2.47299E+05	6.87565E+01	1.68981E+00
10	-3.42516E+15	4.61344E+13	-2.36305E+11	5.05774E+08	-5.46973E+05	1.62766E+02	3.05639E+00
12	-5.53268E+14	6.19635E+12	-2.18588E+10	1.70492E+07	-3.25138E+04	9.05793E+00	9.15241E-01
13	-2.25989E+15	2.84492E+13	-1.29427E+11	2.39223E+08	-2.43357E+05	6.77897E+01	1.58450E+00
14	-2.79340E+15	3.72920E+13	-1.85612E+11	3.84844E+08	-4.06780E+05	1.17127E+02	2.20985E+00
15	-3.81975E+15	4.52614E+13	-2.21302E+11	4.70673E+08	-5.04308E+05	1.60090E+02	3.30858E+00
16	-8.18284E+14	9.31907E+12	-3.45001E+10	3.53003E+07	-5.18058E+04	1.44728E+01	1.15986E+00
17	-2.68651E+15	3.39121E+13	-1.54905E+11	2.88083E+08	-2.93237E+05	8.17667E+01	1.87827E+00
18	-3.15818E+15	4.25351E+13	-2.17571E+11	4.64999E+08	-5.02286E+05	1.49323E+02	2.79716E+00
19	-5.07327E+15	5.85432E+13	-2.79832E+11	5.88089E+08	-6.20250E+05	1.97535E+02	4.02807E+00
20	-1.16594E+16	1.23838E+14	-5.35837E+11	1.06155E+09	-1.00631E+06	3.28436E+02	5.05363E+00
21	-1.49427E+15	1.77358E+13	-7.26584E+10	1.07640E+08	-1.17152E+05	3.25357E+01	1.42472E+00
22	-2.67737E+15	3.51676E+13	-1.70303E+11	3.42289E+08	-3.55471E+05	1.00493E+02	1.95438E+00
23	-3.77435E+15	4.48292E+13	-2.19843E+11	4.68526E+08	-5.02414E+05	1.59972E+02	3.29918E+00
24	-1.17506E+16	1.24183E+14	-5.33103E+11	1.05118E+09	-9.86948E+05	3.22354E+02	4.74821E+00

Appendix F: Calculations with COMSOL Multiphysics

Table of Appendix 38: Information about general settings for the calculations with COMSOL Multiphysics

Basics	
Geometry	2D, axial symmetry
Modus of application Fluid flow Standard type of element Type of analysis Model of turbulence Heat transfer Standard type of element Type of analysis Model of turbulence	 Weakly compressible Navier-Stokes Lagrange - P_2 P_1 Stationary None General heat transfer with disabled radiative heat transfer Lagrange - P_2 J_1 Stationary None
Mesh information	
Settings Predefined mesh size Method of refinement Level of refinement	 Normal Regular 3
Statistics Nodes Elements Degrees of freedom	 187189 366912 (triangular) 1690584
Domain condition	
Fluid Material Density Heat transfer	 Argon or helium (user defined material properties) Function of temperature and pressure Convection
Reactor wall and thermocouple Material Density Specific heat capacity at constant pressure Heat transfer	 AL23 3825 kg/m^3 900 J/(kg K) Conduction
Boundary conditions	
Inlet face of fluid domain	Velocity profile provided Temperature provided
Outlet face of fluid domain	Pressure provided Convective flux
Inner face of reactor wall	No-slip wall Temperature provided
Outer face of thermocouple	No-slip wall Temperature linked to temperature variable
Other faces	No-slip wall Thermal insulation
Solver control	
Type of analysis Linear solver of equations Convergence Criteria Relative accuracy Newton damping	Stationary Direct (UMFPACK) 1E-06 activated

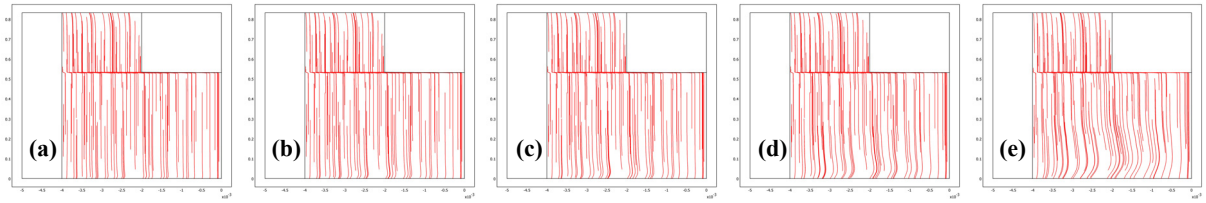

Figure of Appendix 22: Results of COMSOL Multiphysics calculations based on a simplified temperature profile for the wall of the reactor concerning flow lines for different standard volume flows of argon and a nominal furnace temperature of 1200 °C: 95 sccm (a), 200 sccm (b), 350 sccm (c), 685 sccm (d), and 2000 sccm (e)

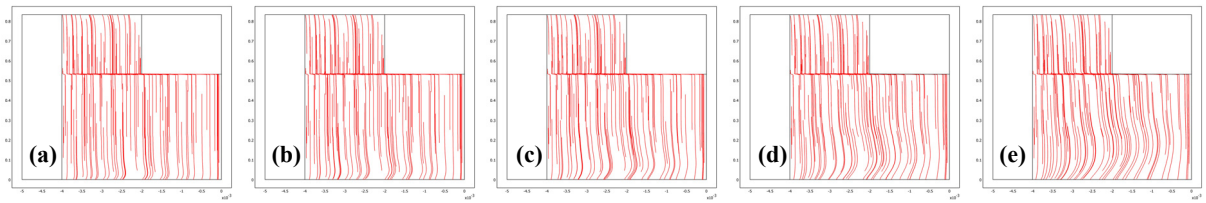

Figure of Appendix 23: Results of COMSOL Multiphysics calculations based on a simplified temperature profile for the wall of the reactor concerning flow lines for different standard volume flows of argon and a nominal furnace temperature of 1300 °C: 340 sccm (a), 650 sccm (b), 1300 sccm (c), 2600 sccm (d), and 4800 sccm (e)

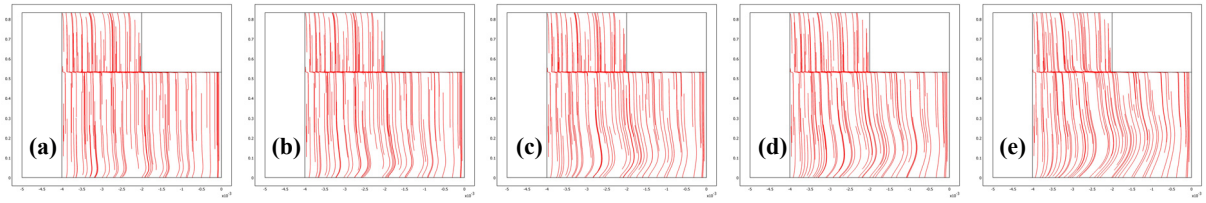

Figure of Appendix 24: Results of COMSOL Multiphysics calculations based on a simplified temperature profile for the wall of the reactor concerning flow lines for different standard volume flows of argon and a nominal furnace temperature of 1400 °C: 700 sccm (a), 1400 sccm (b), 2600 sccm (c), 3800 sccm (d), and 6500 sccm (e)

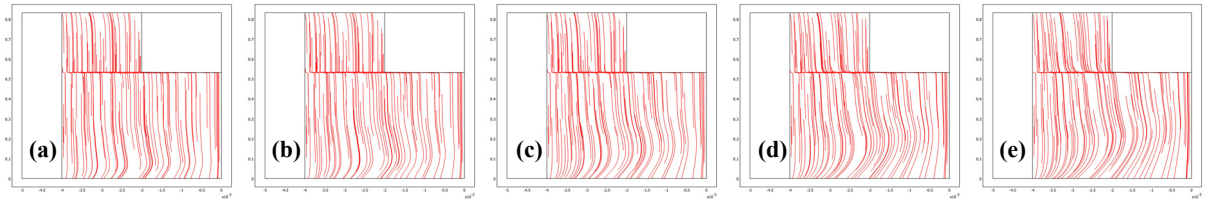

Figure of Appendix 25: Results of COMSOL Multiphysics calculations based on a simplified temperature profile for the wall of the reactor concerning flow lines for different standard volume flows of argon and a nominal furnace temperature of 1500 °C: 1600 sccm (a), 2800 sccm (b), 4600 sccm (c), 7200 sccm (d), and 9800 sccm (e)

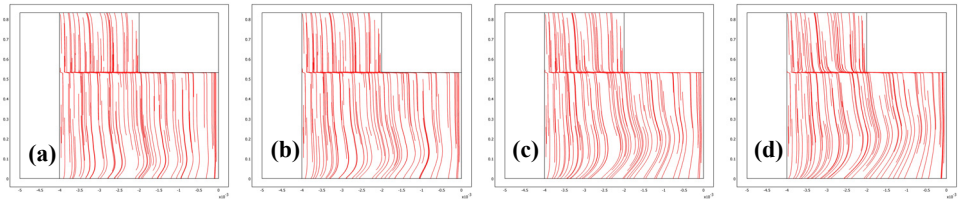

Figure of Appendix 26: Results of COMSOL Multiphysics calculations based on a simplified temperature profile for the wall of the reactor concerning flow lines for different standard volume flows of argon and a nominal furnace temperature of 1600 °C: 2000 sccm (a), 3350 sccm (b), 6500 sccm (c), 9800 sccm (d)

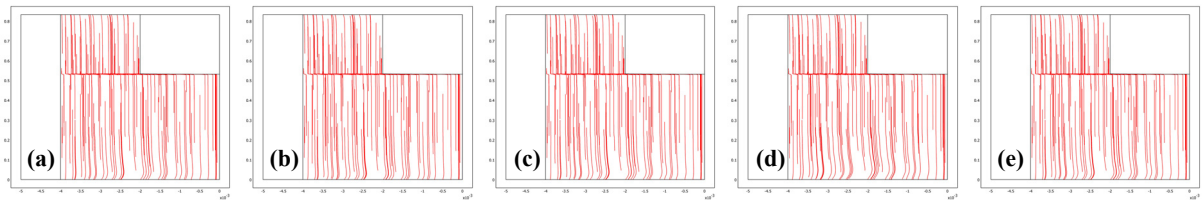

Figure of Appendix 27: Results of COMSOL Multiphysics calculations based on a simplified temperature profile for the wall of the reactor concerning flow lines for different sets of standard volume flow of helium and nominal furnace temperature: 1300 °C - 3800 sccm (a), 1400 °C - 2800 sccm (b), 1400 °C - 3800 sccm (c), 1400 °C - 6500 sccm (d), and 1500 °C - 3800 sccm (e)

Table of Appendix 39: Coefficients of the polynomial fit function for the approximation of fractions of the molar flow at the inlet of the reactor present 5 mm downstream the tip of the thermocouple in particular nested tube reactors (NTR) of region B.

Gas	NTR	k_i in $(s/mol)^i$			
		k_3	k_2	k_1	k_0
Ar	1	-2.0556E+05	3.7537E+03	-1.1197E+01	1.3511E-01
	2	-3.5574E+05	4.6347E+03	-1.3581E+01	3.2845E-01
	3	3.1172E+05	-4.4580E+03	1.0098E+01	3.6014E-01
	4	2.4958E+05	-3.9304E+03	1.4679E+01	1.7630E-01
He	1	-	-9.7174E+01	-2.4543E-01	1.3266E-01
	2	-	-1.2551E+02	-3.8322E-01	3.2631E-01
	3	-	8.9136E+01	1.6390E-01	3.6212E-01
	4	-	1.3355E+02	4.6474E-01	1.7891E-01

Appendix G: Optimization tool and results of kinetic evaluation

Table of Appendix 40: Information about the optimization tool used for the determination of kinetic parameters

Optimization tool Solver Algorithm Algorithm settings Subproblem algorithm	Optimization Toolbox 4.0 embedded in MATLAB Version 7.6.0.324 (R2008a) “lsnonlin“ (Nonlinear least squares) Large scale Cholesky factorization
Stopping criteria X tolerance Function tolerance	 1E-06 (default) 1E-06 (default)

Approximated derivates
  Finite differences
  Minimum perturbation
  Maximum perturbation
	
	1E-08 (default)
	0.1 (default)

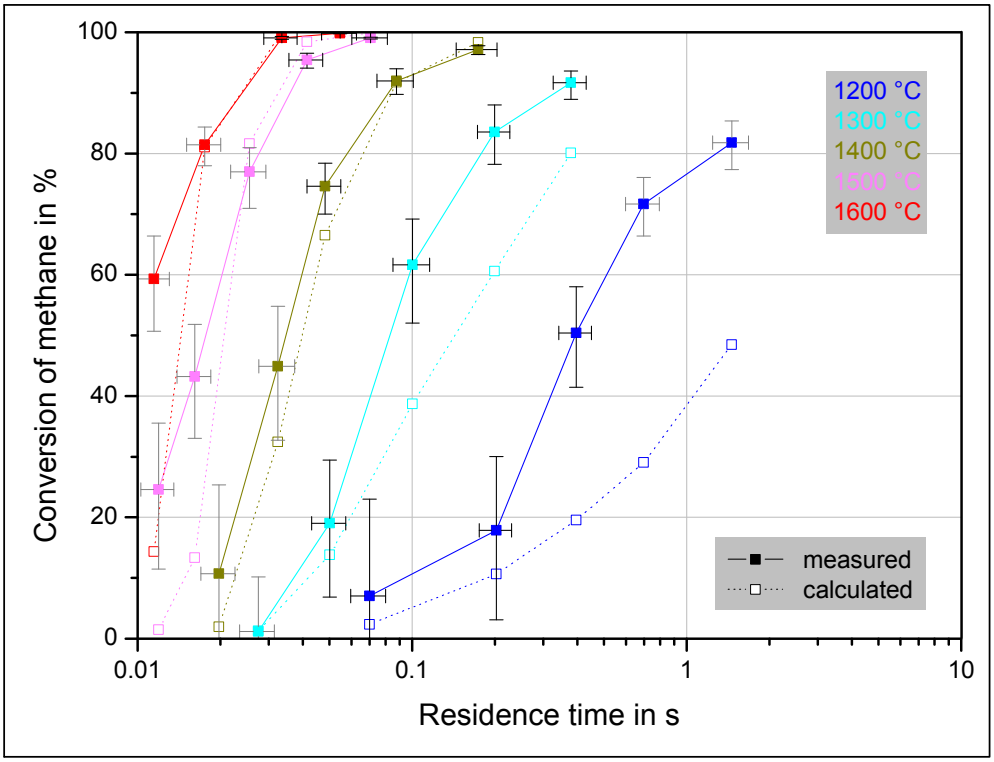

Figure of Appendix 28: Comparison of experimentally determined conversion of methane (as a function of the residence time and the nominal furnace temperature) with calculated values employing reactor model 5 NTR and respective best fit kinetic parameters. 2 % initial molar fraction of methane in argon. Indicators of uncertainty refer to maximum uncertainty (black: used for kinetic evaluation, gray: not used for kinetic evaluation).

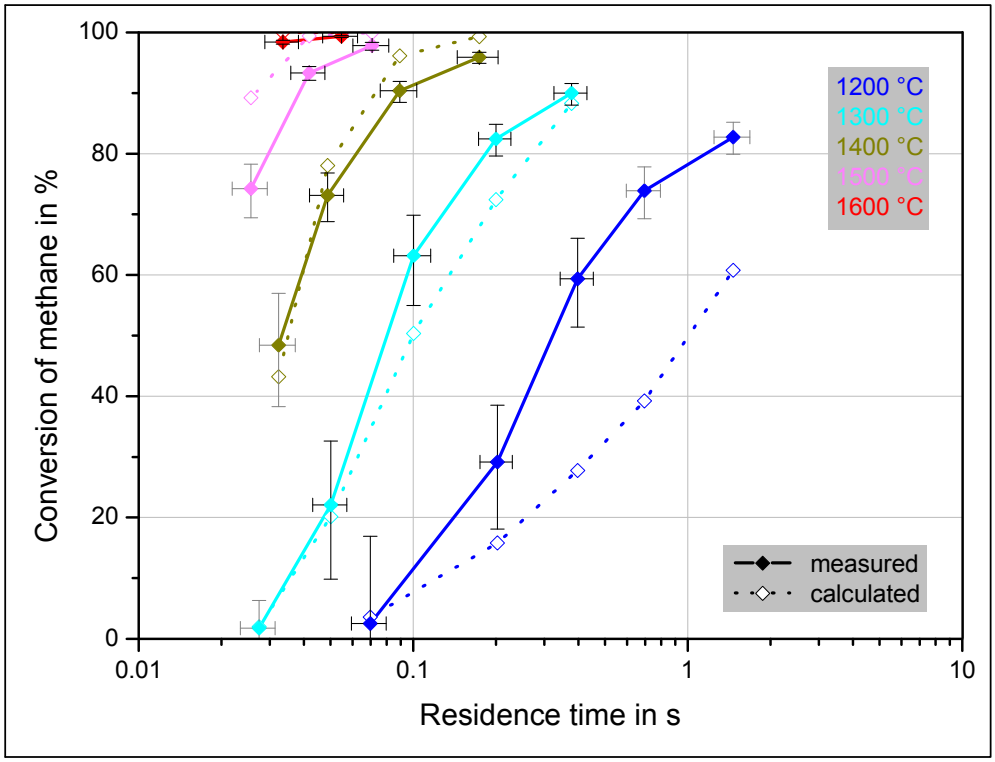

Figure of Appendix 29: Comparison of experimentally determined conversion of methane (as a function of the residence time and the nominal furnace temperature) with calculated values employing reactor model 5 NTR and respective best fit kinetic parameters. 10 % initial molar fraction of methane in argon. Indicators of uncertainty refer to maximum uncertainty (black: used for kinetic evaluation, gray: not used for kinetic evaluation).

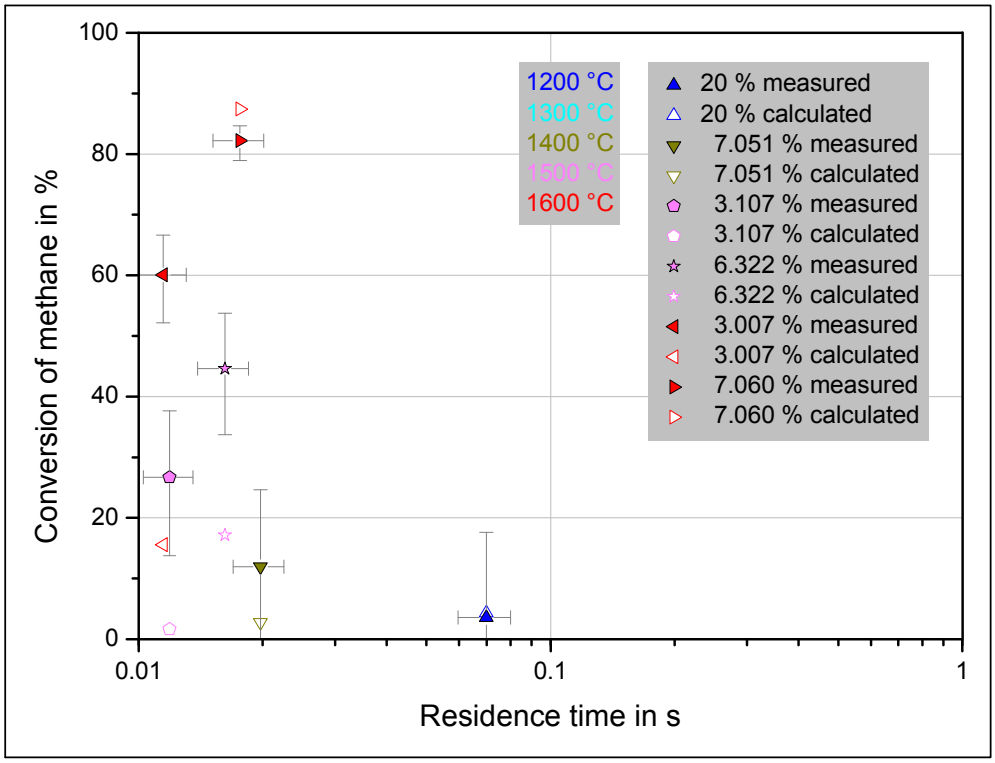

Figure of Appendix 30: Comparison of experimentally determined conversion of methane (as a function of the residence time and the nominal furnace temperature) with calculated values employing reactor model 5 NTR and respective best fit kinetic parameters. Diverse initial molar fractions of methane in argon. Indicators of uncertainty refer to maximum uncertainty (black: used for kinetic evaluation, gray: not used for kinetic evaluation).

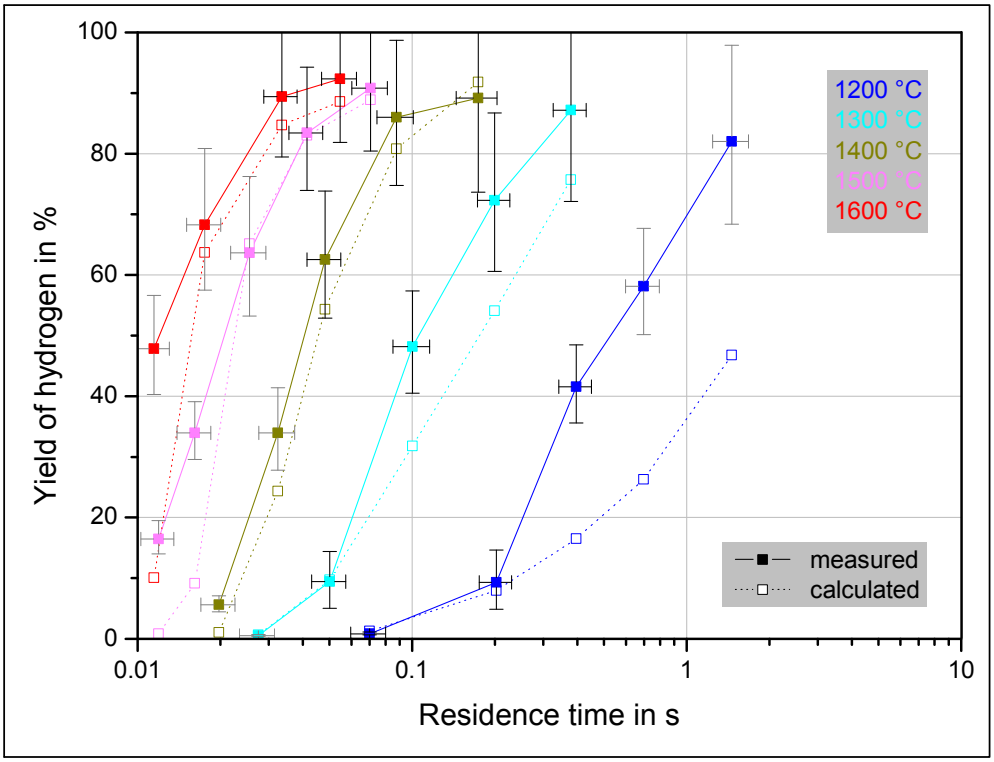

Figure of Appendix 31: Comparison of experimentally determined yield of hydrogen (as a function of the residence time and the nominal furnace temperature) with calculated values employing reactor model 5 NTR and respective best fit kinetic parameters. 2 % initial molar fraction of methane in argon. Indicators of uncertainty refer to maximum uncertainty (black: used for kinetic evaluation, gray: not used for kinetic evaluation).

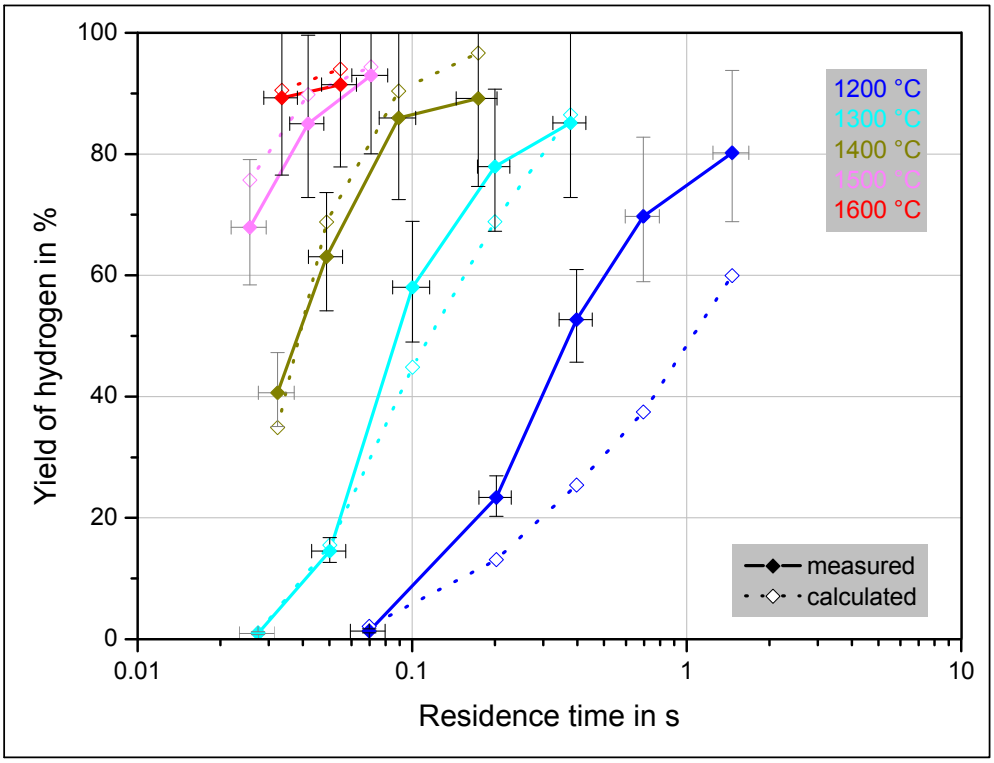

Figure of Appendix 32: Comparison of experimentally determined yield of hydrogen (as a function of the residence time and the nominal furnace temperature) with calculated values employing reactor model 5 NTR and respective best fit kinetic parameters. 10 % initial molar fraction of methane in argon. Indicators of uncertainty refer to maximum uncertainty (black: used for kinetic evaluation, gray: not used for kinetic evaluation).

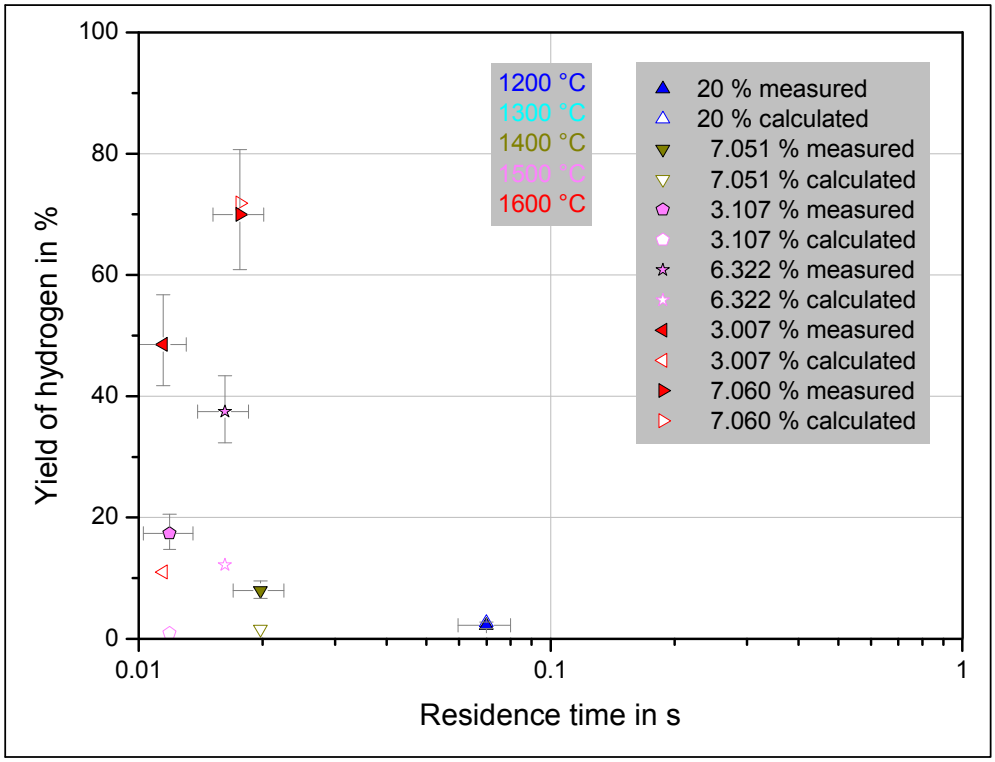

Figure of Appendix 33: Comparison of experimentally determined yield of hydrogen (as a function of the residence time and the nominal furnace temperature) with calculated values employing reactor model 5 NTR and respective best fit kinetic parameters. Diverse initial molar fractions of methane in argon. Indicators of uncertainty refer to maximum uncertainty (black: used for kinetic evaluation, gray: not used for kinetic evaluation).

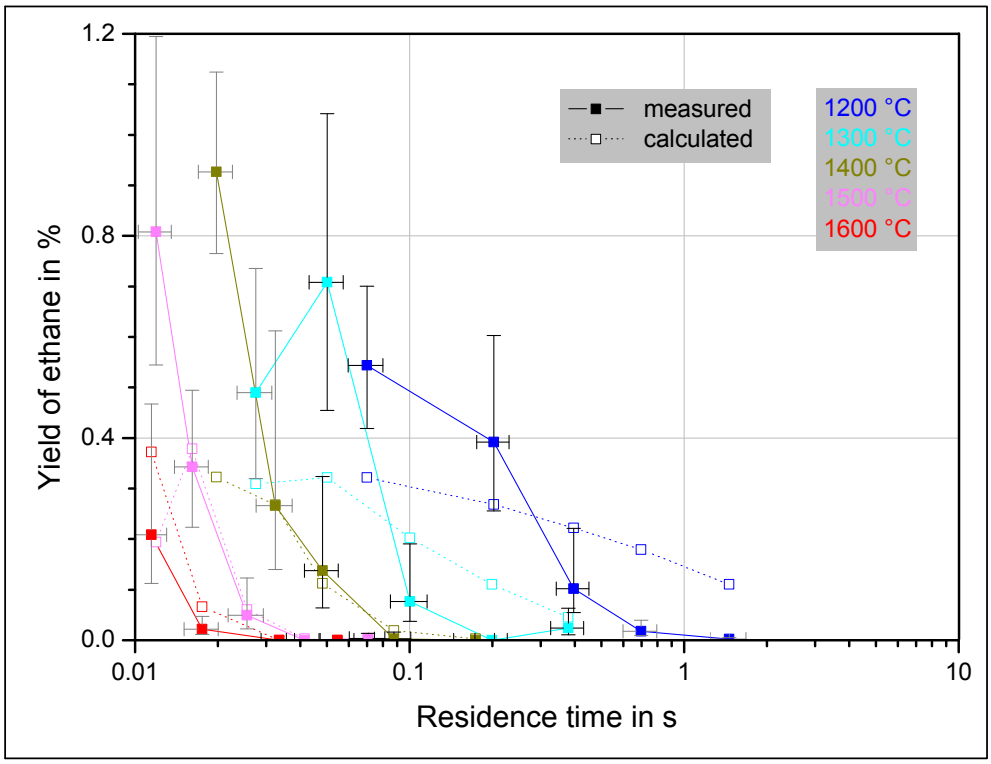

Figure of Appendix 34: Comparison of experimentally determined yield of ethane (as a function of the residence time and the nominal furnace temperature) with calculated values employing reactor model 5 NTR and respective best fit kinetic parameters. 2 % initial molar fraction of methane in argon. Indicators of uncertainty refer to maximum uncertainty (black: used for kinetic evaluation, gray: not used for kinetic evaluation).

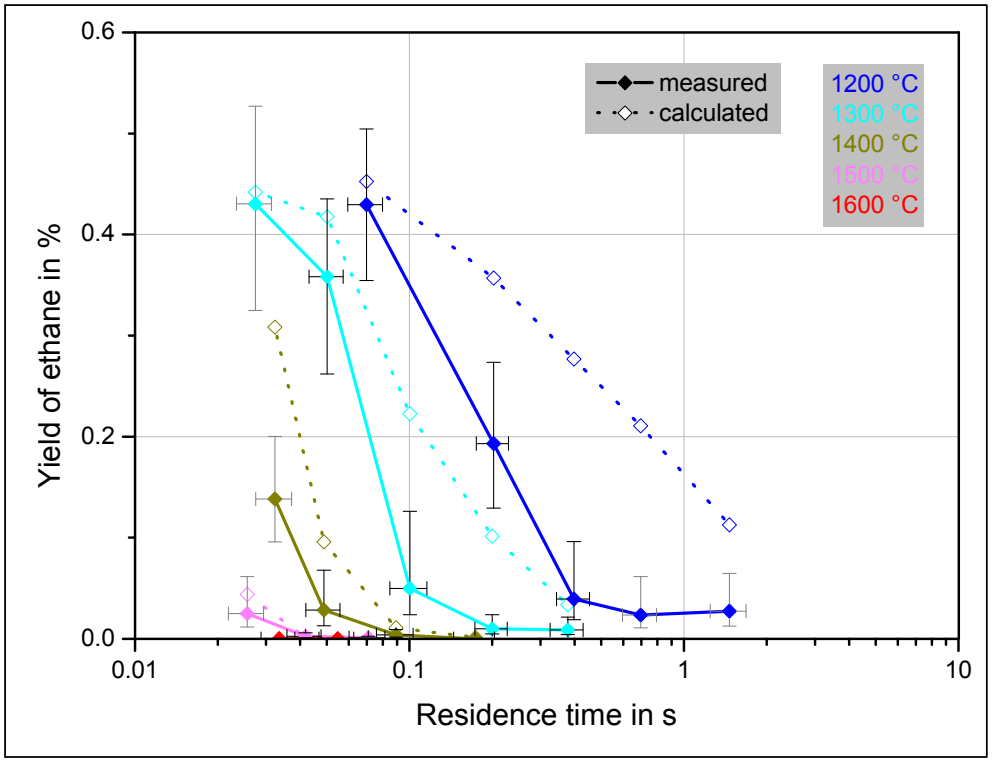

Figure of Appendix 35: Comparison of experimentally determined yield of ethane (as a function of the residence time and the nominal furnace temperature) with calculated values employing reactor model 5 NTR and respective best fit kinetic parameters. 10 % initial molar fraction of methane in argon. Indicators of uncertainty refer to maximum uncertainty (black: used for kinetic evaluation, gray: not used for kinetic evaluation).

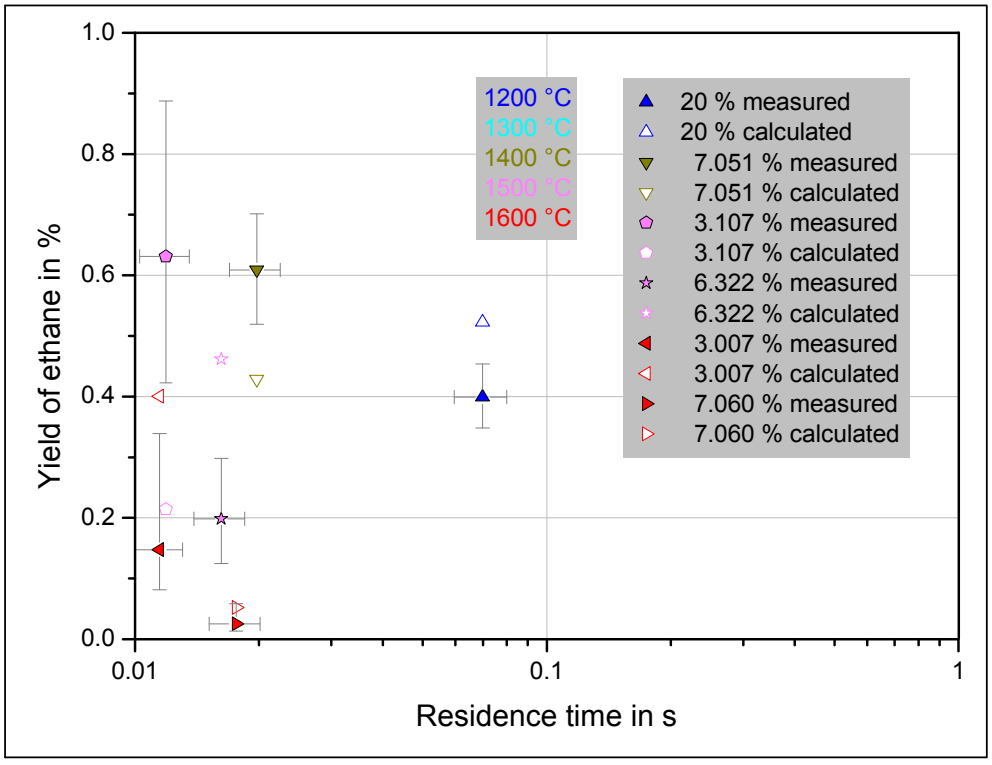

Figure of Appendix 36: Comparison of experimentally determined yield of ethane (as a function of the residence time and the nominal furnace temperature) with calculated values employing reactor model 5 NTR and respective best fit kinetic parameters. Diverse initial molar fractions of methane in argon. Indicators of uncertainty refer to maximum uncertainty (black: used for kinetic evaluation, gray: not used for kinetic evaluation).

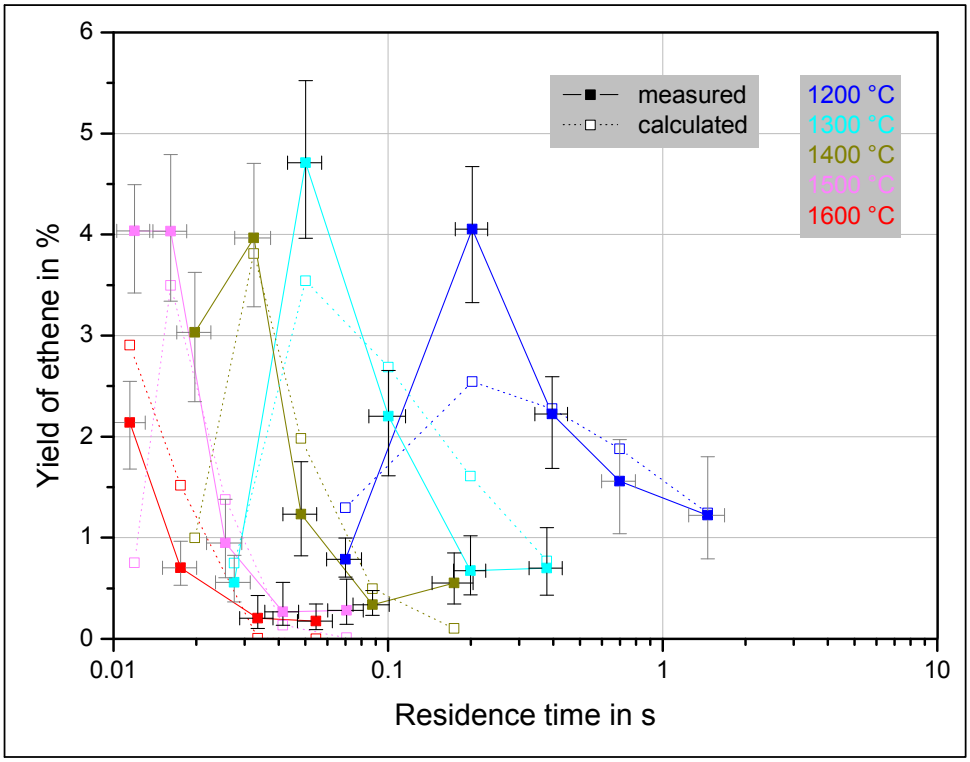

Figure of Appendix 37: Comparison of experimentally determined yield of ethene (as a function of the residence time and the nominal furnace temperature) with calculated values employing reactor model 5 NTR and respective best fit kinetic parameters. 2 % initial molar fraction of methane in argon. Indicators of uncertainty refer to maximum uncertainty (black: used for kinetic evaluation, gray: not used for kinetic evaluation).

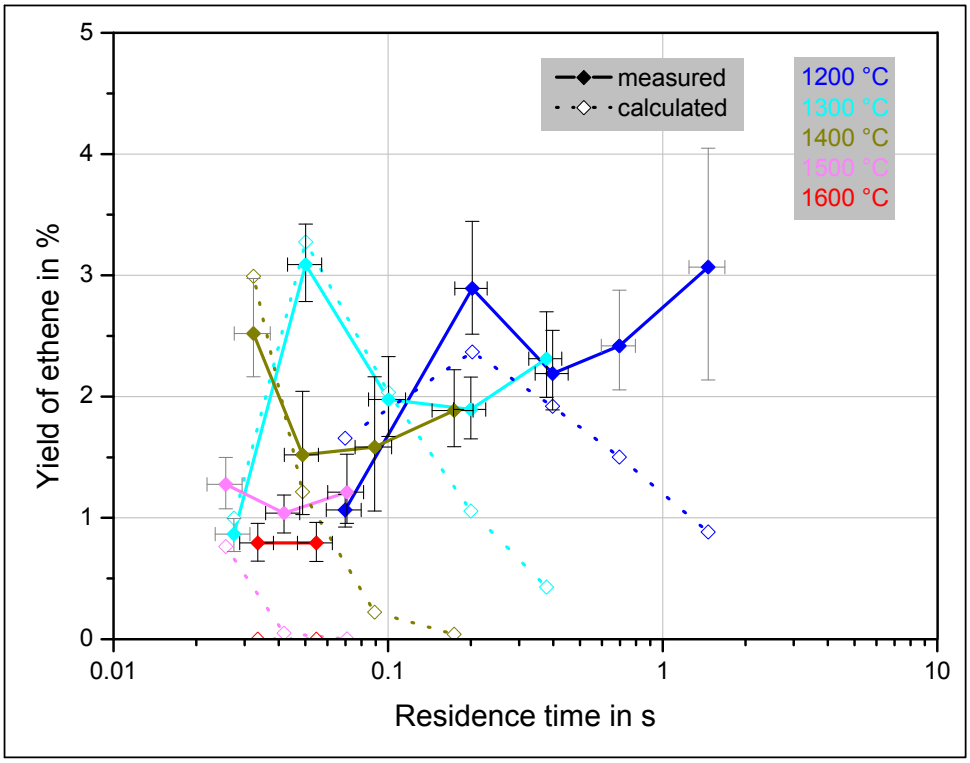

Figure of Appendix 38: Comparison of experimentally determined yield of ethene (as a function of the residence time and the nominal furnace temperature) with calculated values employing reactor model 5 NTR and respective best fit kinetic parameters. 10 % initial molar fraction of methane in argon. Indicators of uncertainty refer to maximum uncertainty (black: used for kinetic evaluation, gray: not used for kinetic evaluation).

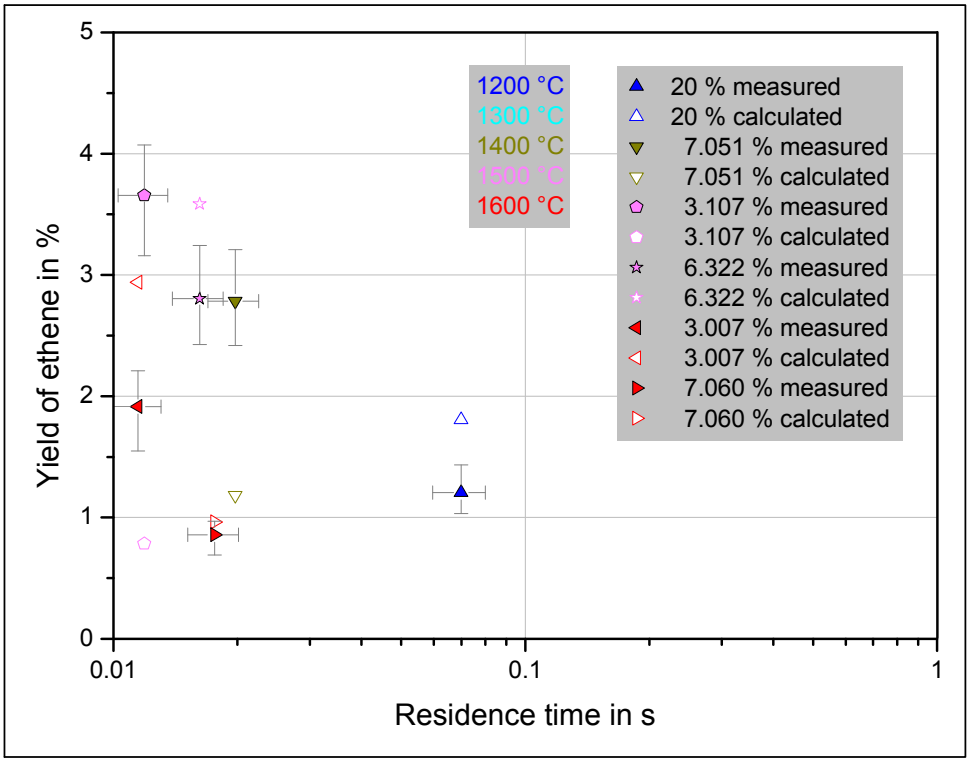

Figure of Appendix 39: Comparison of experimentally determined yield of ethene (as a function of the residence time and the nominal furnace temperature) with calculated values employing reactor model 5 NTR and respective best fit kinetic parameters. Diverse initial molar fractions of methane in argon. Indicators of uncertainty refer to maximum uncertainty (black: used for kinetic evaluation, gray: not used for kinetic evaluation).

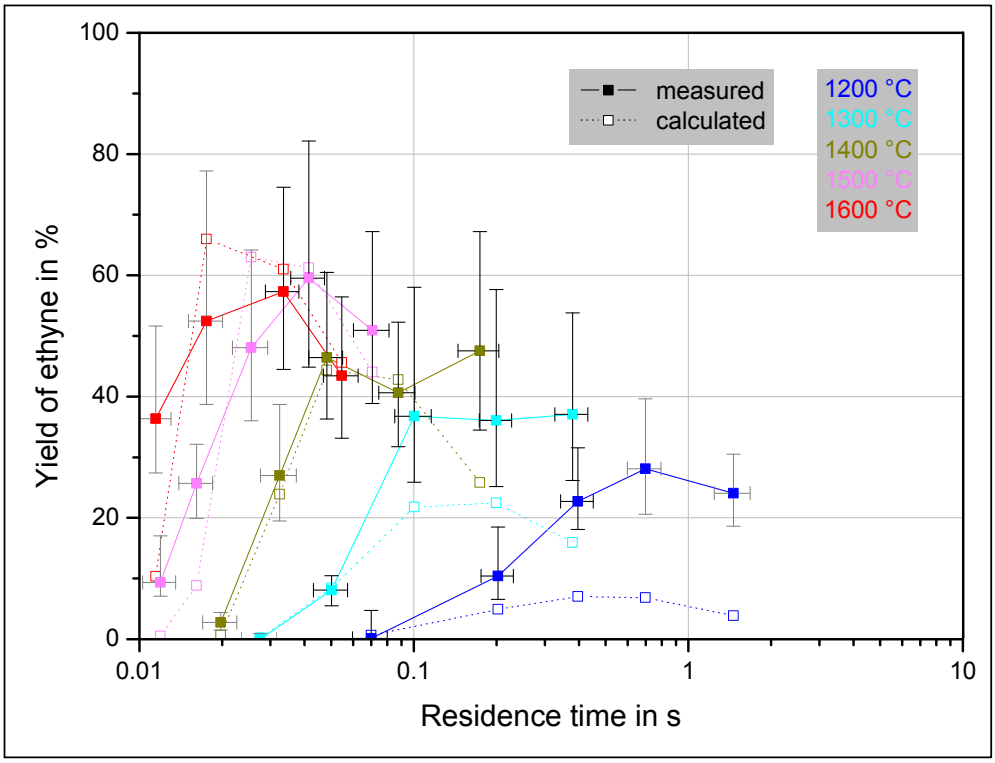

Figure of Appendix 40: Comparison of experimentally determined yield of ethyne (as a function of the residence time and the nominal furnace temperature) with calculated values employing reactor model 5 NTR and respective best fit kinetic parameters. 2 % initial molar fraction of methane in argon. Indicators of uncertainty refer to maximum uncertainty (black: used for kinetic evaluation, gray: not used for kinetic evaluation).

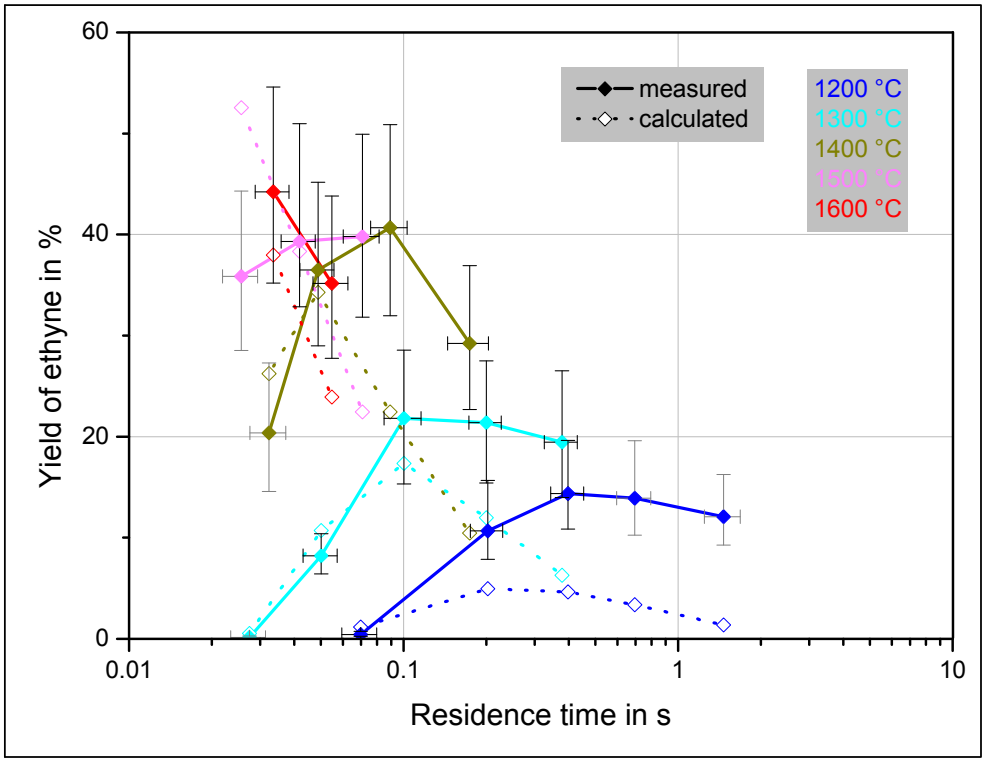

Figure of Appendix 41: Comparison of experimentally determined yield of ethyne (as a function of the residence time and the nominal furnace temperature) with calculated values employing reactor model 5 NTR and respective best fit kinetic parameters. 10 % initial molar fraction of methane in argon. Indicators of uncertainty refer to maximum uncertainty (black: used for kinetic evaluation, gray: not used for kinetic evaluation).

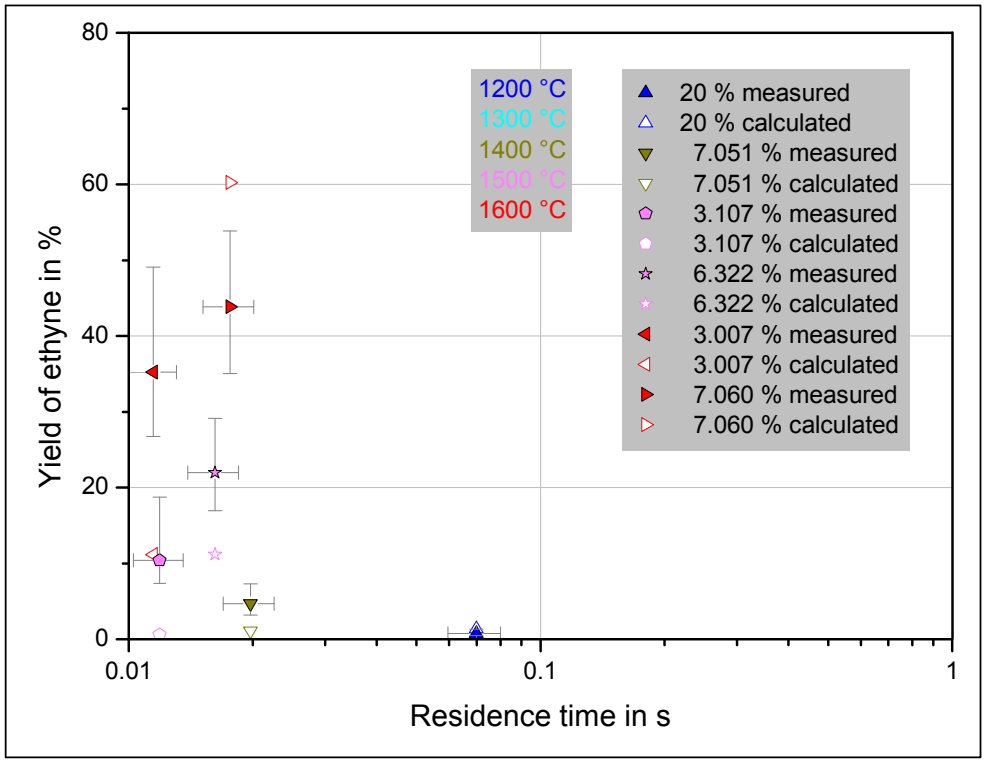

Figure of Appendix 42: Comparison of experimentally determined yield of ethyne (as a function of the residence time and the nominal furnace temperature) with calculated values employing reactor model 5 NTR and respective best fit kinetic parameters. Diverse initial molar fractions of methane in argon. Indicators of uncertainty refer to maximum uncertainty (black: used for kinetic evaluation, gray: not used for kinetic evaluation).

Table of Appendix 41: Covariance matrix calculated based on the best fit kinetic parameters for model 5 NTR

$Cov(\psi)$	1	2	3	4	5	6	7	8	9	10	11	12	Related to
1	3.29 E+00	1.15 E-01	8.14 E-03	1.43 E-01	1.27 E-02	3.86 E-03	5.56 E-01	2.86 E-02	5.57 E-03	-1.39 E-01	-2.94 E-04	5.61 E-03	$E_{a,1}$
2	1.15 E-01	4.02 E-03	3.05 E-04	4.05 E-03	4.45 E-04	1.45 E-04	1.53 E-02	8.82 E-04	2.03 E-04	-4.92 E-03	-2.38 E-05	1.83 E-04	$\log(k_{0,1})$
3	8.14 E-03	3.05 E-04	5.05 E-05	-7.35 E-04	2.97 E-05	2.10 E-05	-2.34 E-03	-3.47 E-05	2.24 E-05	-3.60 E-04	-1.13 E-05	2.46 E-06	m_1
4	1.43 E-01	4.05 E-03	-7.35 E-04	8.79 E+01	3.20 E+00	1.57 E-02	4.36 E-01	-2.21 E-02	-7.54 E-03	1.22 E-03	3.77 E-03	4.04 E-03	$E_{a,2}$
5	1.27 E-02	4.45 E-04	2.97 E-05	3.20 E+00	1.22 E-01	2.42 E-03	5.52 E-03	-1.15 E-03	-2.70 E-04	-7.56 E-04	9.96 E-05	1.38 E-04	$\log(k_{0,2})$
6	3.86 E-03	1.45 E-04	2.10 E-05	1.57 E-02	2.42 E-03	6.30 E-04	-2.41 E-03	-8.36 E-05	2.19 E-06	-3.05 E-04	-8.13 E-06	3.59 E-06	m_2
7	5.56 E-01	1.53 E-02	-2.34 E-03	4.36 E-01	5.52 E-03	-2.41 E-03	9.88 E+00	3.45 E-01	3.66 E-03	3.61 E-02	9.32 E-03	9.36 E-03	$E_{a,3}$
8	2.86 E-02	8.82 E-04	-3.47 E-05	-2.21 E-02	-1.15 E-03	-8.36 E-05	3.45 E-01	1.29 E-02	4.85 E-04	2.20 E-04	2.97 E-04	3.39 E-04	$\log(k_{0,3})$
9	5.57 E-03	2.03 E-04	2.24 E-05	-7.54 E-03	-2.70 E-04	2.19 E-06	3.66 E-03	4.85 E-04	1.61 E-04	-4.70 E-04	-5.23 E-06	1.40 E-05	m_3
10	-1.39 E-01	-4.92 E-03	-3.60 E-04	1.22 E-03	-7.56 E-04	-3.05 E-04	3.61 E-02	2.20 E-04	-4.70 E-04	1.39 E+01	4.81 E-01	-3.68 E-02	$E_{a,4}$
11	-2.94 E-04	-2.38 E-05	-1.13 E-05	3.77 E-03	9.96 E-05	-8.13 E-06	9.32 E-03	2.97 E-04	-5.23 E-06	4.81 E-01	1.77 E-02	-2.82 E-04	$\log(k_{0,4})$
12	5.61 E-03	1.83 E-04	2.46 E-06	4.04 E-03	1.38 E-04	3.59 E-06	9.36 E-03	3.39 E-04	1.40 E-05	-3.68 E-02	-2.82 E-04	1.12 E-03	m_4

$$E_a \text{ in } \frac{\text{kJ}}{\text{mol}},\ k_0 \text{ in } \frac{1}{\text{s}} \cdot \left(\frac{\text{mol}}{\text{m}^3}\right)^{(1-m)},\ m \text{ in } -$$